Development of Biomaterials for Neural Tissue Engineering

Paige Alexandra Walczak

Doctor of Philosophy

Aston University

January 2024

©Paige Alexandra Walczak, 2024.

Paige Alexandra Walczak asserts her moral right to be identified as the author of this thesis. This copy of the thesis has been supplied on condition that anyone who consults it is understood to recognise that its copyright belongs to its author and that no quotation from the thesis and no information derived from it may be published without appropriate acknowledgement.

Thesis summary

Tissues are the building blocks of organs, comprised of cellular and acellular components. The acellular extracellular matrix (ECM) acts to simultaneously provide biological and physical support to cells and drive tissue function. The complex interconnected nature of biochemical & physiomechanical features of human tissue enables maintenance of dynamic architectures, capable of supporting function throughout human lifetimes. When we consider the incredible structural *and* functional complexity of the human brain, we can only infer that the interconnectedness of features is even more delicately balanced.

Recreating complexity of the human CNS in the form of model systems is an invaluable tool for furthering scientific knowledge, in areas including tissue development, pathogenesis, and therapeutic testing. Improved *in vitro* modelling of the human brain is a particularly powerful tool when we consider the unsuitability of existing models and severity of unmet clinical needs i.e. distinct lack of treatments for neurodegenerative disease. Development of advanced *in vitro* models of the human CNS is hampered by obscurity surrounding neurophysiology and pathogenesis, particularly the importance of the ECM.

Researchers now recognise a multidisciplinary approach is necessary to understand and reproduce complexity of the CNS, utilising biology, chemistry, physics, mathematics, engineering & other fields i.e. material science to develop “soft solid” hydrogel biomaterials to mimic mechanical behaviour of the brain.

This project looks to enable engineering of neural tissue via development of hydrogel biomaterials that are capable of mimicking structural and architectural complexity of the CNS. Research here demonstrates suitability of HAMA hydrogels for neural tissue engineering, with biological relevance of HA/laminin components and retained cell viability, alongside replication of biomechanical properties of the CNS. Novelty of work herein arises from the balancing of biological and mechanical properties to develop a tuneable hydrogel system, highlighting potential for further tailoring via additional biofunctionalisation or structuring via bioprinting.

Magnetic Resonance Imagery of the brain that wrote this thesis on development of brain biomaterials.

Keywords: Tissue Engineering, Biomaterials, Hydrogels

Acknowledgements

I would like to thank Dr Eric Hill for his academic and personal support, providing ideas, preventing meltdowns and being a genuine friend. Your enthusiasm for science has provided endless inspiration.

I also want to thank the lifETIME Centre for Doctoral Training for their financial, academic and pastoral support. Michelle and Aimee, thank you for tirelessly supporting us all, smiling as you do. Special thanks to Professor Matt Dalby for all your encouragement and wisdom. Also thank you to my CDT cohort; the original lifetime. We have grown so much in 4+ years and I cannot wait to celebrate our collective success in 40 years. To the younger cohorts, thank you for ensuring I did not forget what tequila tasted like.

Thank you Megan, your positivity, friendship and unwavering support has motivated me on the darkest of Mondays. Georgia, your company and laughter kept me smiling during the most tiresome training sessions. Hannah, thank you for the invaluable life advice and being my twin in almost every way. I would not be the person I am today without you, I truly feel I found a family in you three.

Michael, Olivia and Taylor, thanks for sticking by me through the cancelled plans and complaining. Thank you for reminding me nothing makes me happy quite like a few hours with my closest friends.

Chad, Kyle and Luke, you didn't really contribute but I'm proud of you anyway.

Last but never least; I need to thank my grandparents, Diane and Paul. Without your support I would never have made it this far. I can never repay the love and energy you invested in me, but dedicating my doctorate to you is a good start.

Contents

List of abbreviations

2D - Two-dimensional

2PP - 2-Photon-Polymerisation

2.5D - “quasi-3D”

3D - Three-dimensional

AD - Alzheimers Disease

ANOVA - Analysis Of Variance

APOE - Apolipoprotein E

ALM - Additive Layer Manufacturing

BDNF - Brain-derived Neurotrophic Factor

CNS - Central Nervous System

CS - Chondroitin Sulphate

DAPI - 4′,6-diamidino-2-phenylindole

DI - Deionised

dH_2O - Distilled water

ddH_2O - Double distilled water

DTT - Dithiothreitol

DMSO - Dimethyl

DNA – Deoxyribonucleic Acid

ECM - Extracellular Matrix

EDAC - N-(3-Dimethylaminopropyl)-N′-ethylcarbodiimide hydrochloride

ESC - Embryonic Stem Cell

FBS - Foetal Bovine Serum

FRESH - Freeform Reversible Embedding of Suspended Hydrogels

G’ - Elastic modulus

G’’ - Viscous modulus

GG - Gellan Gum

GABA - Gamma-aminobutyric acid

GAG - Glycosaminoglycan

GDNF - Glial cell-derived Neurotrophic Factor

GECI - Genetically-encoded Calcium Indicator

GFP - Green Fluorescent Protein

HA - Hyaluronic Acid

HA-CHO - Aldehyde Hyaluronic Acid

HAMA - Hyaluronic Acid Methacrylate

Hz - Hertz (unit of frequency)

HS - Heparin Sulphate

IKVAV - Peptide formed of Isoleucine, Lysine, Valine, Alanine and Valine

ICC - Immunocytochemistry

IPSC - Induced Pluripotent Stem Cell

LAP - Lithium phenyl-2,4,6-trimethylbenzoylphosphinate

LVR - Linear Viscoelastic Region

MEA - Multielectrode Array

MMP - Matrix Metalloproteinase

MTT - 3-(4,5-dimethyl-2-thiazolyl)-2,5-diphenyl-2H-tetrazolium bromide

NMR - Nuclear Magnetic Resonance

NMM - Neural Maintenance Media

NPC - Neural Progenitor Cell

NSC - Neural Stem Cell

OOAC - Organ-on-a-chip

PBS - Phosphate Buffered Saline

PEG - Polyethylene Glycol

P/S - Penicillin/Streptomycin

PNN - Perineuronal Net

RGD - Peptide formed of Arginine, Glycine and Aspartic Acid

RT - Room Temperature

SD - Standard Deviation

SEM - Standard Error of the Mean

SHAPE - Self-Healing Annealable Particle-Extracellular matrix

SLAM - Suspended Layer Additive Manufacture

TCP - Tissue Culture Plastic

UV - Ultraviolet radiation

VEGF - Vascular Endothelial Growth Factor

1. Introduction

1.1. Neurodegenerative Disease

While causes of neurological disorder are multifaceted, neurodegenerative disease commonly occurs due to old age and are characterised by progressive deterioration of nervous tissue and executive function over time. Accumulation of environmental damage (i.e. alcoholism, poor diet, vascular damage, trauma, smoking etc.) alongside age-associated changes (i.e. metabolic dysfunction, reduction in repair) facilitates acceleration of neurodegenerative disease states within the Central Nervous System (CNS). Interestingly, the modern lifestyle is linked to chronic systemic low-grade inflammation, due to factors such as a pro-inflammatory diet and sedentary lifestyle, contributing to metabolic dysfunction (Monteiro and Azevedo, 2010, Mundula et al., 2022). Increased incidence of dementias may be attributed to people living longer, yet life expectancy in western countries is declining, thought to be partially due to the inflammatory nature of modern life (Ahmad et al., 2022, Christ and Latz, 2019).

1.1.1. Alzheimer's Disease

Alzheimer's disease (AD) was the leading cause of dementia in 2020 with over half a million confirmed diagnosis' in England alone with an estimated cost of £26 billion each year in the UK (Lewis, 2014, NHS, 2020). AD is a progressive neurodegenerative disease leading to cognitive decline and the onset of dementia. Cases typically begin asymptomatically, or with minor learning or planning deficits, progressing to moderate disease effecting spatial awareness and language. In later stages of the disease serious impairments occur in executive function, perception and behaviour (Long and Holtzman, 2019). While various pathologies underlie AD, deposition of β-amyloid (Aβ) plaques and neurofibrillary tangles of Tau, are heavily implicated. Research has gone on to propose dementias such as AD are a result of various concurrent pathological states, involving a multitude of abnormal functions within the brain (Coulthard and Love, 2018). By utilising a combination of experimental diagnostic techniques, it may be possible to identify neurodegeneration earlier, or aid in the monitoring of treatments. Unfortunately, *post-mortem* histopathology is required for a definitive diagnosis, meaning clinicians must carefully evaluate patients' history, symptoms and diagnostic features in order to rule out alternative diagnoses. Risk factors associated with this disease are commonly lifestyle related; poor diet, sedentary lifestyle and alcohol abuse correlate with poor vascular health, diabetes and existing cognitive impairment i.e. stroke. Such environmental factors contribute to the development of AD (van Praag, 2018). Conversely, a family history can be indicative of a genetic predisposition to the Further characterisation is needed to identify AD-associated genes and their implications for neurodevelopment.

Four approved treatments for AD are available within the European Union, namely three acetylcholinesterase inhibitors (AChE inhibitors) and one N-methyl-D-aspartate receptor antagonist (memantine). Well-established AChE inhibitors are donepezil, galantamine, and rivastigmine, working to reduce memory symptoms of the disease by inhibiting enzyme activity and preventing degradation of acetylcholine (McGleenon et al., 1999). Memantine treats moderate to severe cases, acting in a cholinergic-independent manner. This novel approach looks to inhibit glutamate activity found in the neurodegenerative brain; competitively binding glutamate receptors reduces abnormal glutamate activity, offering some protection to cells within the brain from excessive glutamate stimulation (Matsunaga et al., 2015). Current treatments such as cholinesterase inhibitors and behaviour modifying drugs cannot cure the AD pathology, but rather look to manage symptoms of the disease, by reducing/slowing memory loss associated with neuronal death and treating hallucinations/confusion associated with the diagnosis. With little progress in AD treatments in over a decade, future approaches are looking to treat and prevent the disease via targeting of AD associated proteins, inflammatory responses and cell-cell interactions (Cummings et al., 2019, Long and Holtzman, 2019, Zotova et al., 2010). Monoclonal antibodies (mAbs) targeting Aβ oligomers, promoting clearance of the protein from the brain have shown some promise. However, overall lack of significant improvement in symptoms is thought to be due to the stage at which treatment is received. Late stage AD presents with extensive accumulation of Aβ, meaning the pathological state is irrevocably established and anti-Aβ mAb therapy is often ineffective due to targeting of oligomers and not disease-associated plaques (van Dyck, 2018, Panza et al., 2019). Whats more, deposition of Aβ is observed in cognitively healthy individuals, raising further questions into treatment efficacy (Panza et al., 2019). It is highly likely that treatment of dementias such as AD will require a multi-pronged approach, utilising targeted and general therapies, in order to address the multiple concurrent protein abnormalities in AD. While multiple strategies are theorised, very few therapeutics make it to clinical trials, with the success rate for advancing to the next stage of trials also very low. From 2002 to 2012, the success rate for approval of treatments for AD was 0.4%, the lowest for any therapeutic field (Cummings et al., 2014). While this figure remains remarkably low, approval of the antibody treatment aducanumab provided great hope; however, scepticism around efficacy of the treatment remains staunch (Blaikie et al., 2022, Kim et al., 2022).

Translation of preclinical success to clinical trials is particularly low for models of the CNS (Dhir et al., 2020, Dragunow, 2020, Marshall et al., 2023). This is particularly true for models of neurodegenerative states, with preclinical models failing to account for the multifactorial nature of age-associated degenerative disease *in vivo* (Dragunow, 2020). Development of multifactorial human-specific models of CNS disease would provide invaluable support to the

search for neurodegenerative disease treatments, circumventing the need for expensive and time-consuming animal testing, ensuring ineffective treatments are identified earlier and only those treatments holding promise are taken forward to trial. Bespalov *et al.* (2016) take this further, suggesting improved translation hinges upon increased importance of data robustness and generalization (Bespalov et al., 2016). Tissue engineering tools, such as hydrogel biomaterials, bioprinting and chemical functionalisation, are explored within this thesis, to contribute to the development of an advanced *in vitro* model of neural tissue. This modelling of neural tissue outside the human body is an invaluable tool for understanding the neurological development, but also the progression of neurodegenerative states.

1.2. Disease Modelling

1.2.1. Modelling (Patho)Physiology

Modelling tissue outside the human body is an invaluable tool for understanding the physiological development of various organs, but also the progression of disease states. *In vivo* studies utilise experimentation within a living organism, be that human or animal. Whereas *ex vivo* procedures occur removal of tissue for *in vitro* culture outside a living organism, *in vitro* meaning culture outside a living organism, however sources of culture material are predominantly from repositories. Modelling of disease states via animal *ex vivo* and *in vitro* studies enables investigation of potential treatments, providing a convenient platform for determining toxicity or efficacy of therapeutics, without detrimental effects to human life. By utilising disease-specific models, treatment can be tailored to specific pathological states. In order to create such advanced models, continual research is needed to identify and incorporate central hallmarks of disease.

Physiology is the basis for tissue (dys)function, with biochemical composition, hierarchical patterning and structural architecture responsible for guiding not only cellular processes but the dynamic mechanical behaviour of living tissues (Coppari et al., 2021, Eltom et al., 2019). Unfortunately recapitulating the complex interplay of these features within the human body is near impossible, compounded by the fact that no two humans are the same. This genetic and phenotypic variability within the human species is advantageous for evolution; however, this adds additional complexity when modelling systems. Nevertheless, a generalised “roadmap” for tissue development is consistent among individuals i.e. a circulatory system encompassing a four-chambered heart, and enables creation of generalised models. Model systems should therefore look to encompass as many of these features as possible, in order to provide functional outputs most representative of the human condition *in vivo*.

1.2.2. *In Vivo* Modelling

Mammalian models are the current 'gold standard' when testing potential therapeutics, as *in* vivo systems possess much of the complexity found within the human body e.g. organ architecture, multicellular composition, Extracellular Matrix (ECM) complexity, cell-cell, cell-ECM and interconnecting organ systems.

Vertebrate species are commonly employed within scientific research, due to their availability but also similarity to human physiology (Taylor and Alvarez, 2019). With testing on humans reserved for the latest stages of clinical testing, much animal testing relies upon the use of small mammals e.g. rodents for early-stage primary testing. The use of rodent *ex vivo* sliced or *in vitro* dissociated cultures for modelling human tissue is common, allowing for models possessing almost all of the elements observed *in vivo* (Grainger et al., 2018). Within the EU, vertebrates are estimated to make up 93% of all animals utilised for research (Taylor and Alvarez, 2019). However, the UK Home office (2023) estimates use of cats, dogs, horses and non-human primates within scientific research is the lowest it has been since the 1980s, comprising only 0.97% of animal testing procedures in 2022. This shift is indicative of a wider change within animal research to adopt the 3 R's framework; Replacement, Reduction and Refinement of methods in order to enable more ethical use of animals within scientific research (NC3Rs, 2023).

Validity of such approaches to model human tissue is called into question due to issues such as a lack of species specificity (van Norman, 2019). Thus resulting in inaccurate determination of therapeutic responses due to differences in mechanisms of action between species. Development of *in vitro* models of disease is increasingly important as a means to overcome hurdles associated with *in vivo* models.

1.2.3. *In Vitro* Modelling

Artificial *in vitro* cultivation of cells enables biomimicry of naturally occurring cell behaviour and tissue formation. The type and source of cells used depends on the research objective (with the aim of selecting a cell line with appropriate biological relevance) and the ability of cells to proliferate *in vitro* to enable experimentation. *Ex vivo* culture enables *in vitro* culture of tissues containing many of the multiscale biochemical and physiomechanical features seen *in vivo*. Alternatively, *in vitro* cultures of organoids and primary disaggregated tissues goes a way to recreate some of the 3D architecture however lack physiological patterning seen in living tissues. Cell culture enables generation of *in vitro* models of tissue, with greater control over specific cell fates and wider tissue development.

Immortalised cells, despite their name, do not proliferate indefinitely but do contain genetic changes enabling them to elude senescence and undergo division for prolonged periods. While immortalised lines are cheap and easy to obtain from cancerous tissues or intentional induction, such cell lines often fail to display “normal” cell behaviour, possessing genetic abnormalities and functional differences not observed *in vivo*. An infamous immortal line is the HeLa cell line, derived from human cervical cancer in 1951, over time recognised as displaying extensive chromosomal instability and vast genetic differences between lines (Frattini et al., 2015, Tang, 2019). Tumour derived cells may provide an ideal primary source of cells when generating cancer models, with primary tumour samples shown to retain heterogeneous disease markers that may be lost in cell lines (Pastor et al., 2010). Despite the potential for generation of patient and disease-specific models, the unpredictable and uncontrollable nature of immortalised cells, from any source, is an unarguable limitation.

Alternatively, the use of stem cells is ideal due to their propensity to differentiate into almost any cell type. Stem cells are derived from embryonic (ESCs), placental or adult tissue. However, each possesses its own unique features e.g. adult stem cells possess a reduced differentiation capability when compared to ESCs. The self-renewal and differentiation capacity of these unique cells, combined with the development of induced pluripotent stem cell (Cuomo et al., 2020) technology, allows for creation of both ‘healthy’ and ‘diseased’ models (Takahashi and Yamanaka, 2006). IPSC technology overcomes problems associated with embryonic cells, such as ethical issues and a reduced reprogramming ability. This approach also enables creation of patient/disease-specific models as iPSCs can be made from almost any adult cell, with simple procedures to obtain somatic cells such as skin cells through biopsy. Reprogramming of somatic cells occurs following induced expression of Yamanaka transcription factors OCT4, KLF4, SOX2, and C-MYC (Takahashi and Yamanaka, 2006). However, resetting of somatic cells to an embryonic-like state results in a loss of biological features necessary for modelling age-associated disease states, such as neurodegeneration (Mertens et al., 2018). Nevertheless, iPSCs are thought to retain an “epigenetic memory” that favours previous cell fates (Lee et al., 2020a, Mertens et al., 2018). Epigenetic mechanisms, such as DNA methylation or histone modification, act to supress/activate gene transcription without influencing DNA, altering expression and cell behaviour. Within iPSCs, this may present as bias towards differentiation towards original cell type despite apparent reprogramming to pluripotent states.

When culturing cells for integration into a tissue model, environmental cues influence cellular behaviour and differentiation. When culturing primary or immortalised cells, there is reduced potential for tailored differentiation, as cultures commonly display mature phenotypes and are unable to differentiate. On the other hand, environmental control of stem cells is of greater

importance as these remarkable cells can enter into multiple lineages, such as glial and neuronal subtypes, in response to environmental cues. Soluble factors within tissue culture media act as biochemical factors that can influence differentiation, maturation and proliferation of stem cells. For example, differentiation of iPSCs to cortical neural progenitors is initiated by culturing iPSCs in the presence of Rock inhibitor Y-27632, with additional compounds such as B-27 and SB-431542 added at later days (Paşca et al., 2015, Song et al., 2019). Rock inhibition is particularly important as a means to regulate basal spreading activity during rosette morphogenesis (Townshend et al., 2020). Physical and mechanical factors can also influence differentiation via a variety of mechanisms such as mechanosensing of stiffness, modulation of adhesion, alternations to cytoskeletal arrangement, etc. Creating a model with tissue-specific cell types, mechanical properties, ECM and cell-cell interaction is vital in order to produce a reliable model (Pearce et al., 2017).

1.2.4. *In Vitro* Tissue Engineering

Tissue engineering is a multidisciplinary field that looks to engineer living tissue by integrating biology, medicine, chemistry, physics, materials science and various engineering disciplines. Crude references to the field have existed for thousands of years within mythology, alongside practical development of biomaterials for wound healing, transplantation and prosthesis (Kaul and Ventikos, 2015, Vacanti, 2006). The term “tissue engineering” as we know it was coined in the late 20th century, gaining immense traction well into the 21st century, as researchers began to recognise the power of potential applications (Kaul and Ventikos, 2015, Viola, 2003). The field was suggested as a means to develop biological substitutes, in

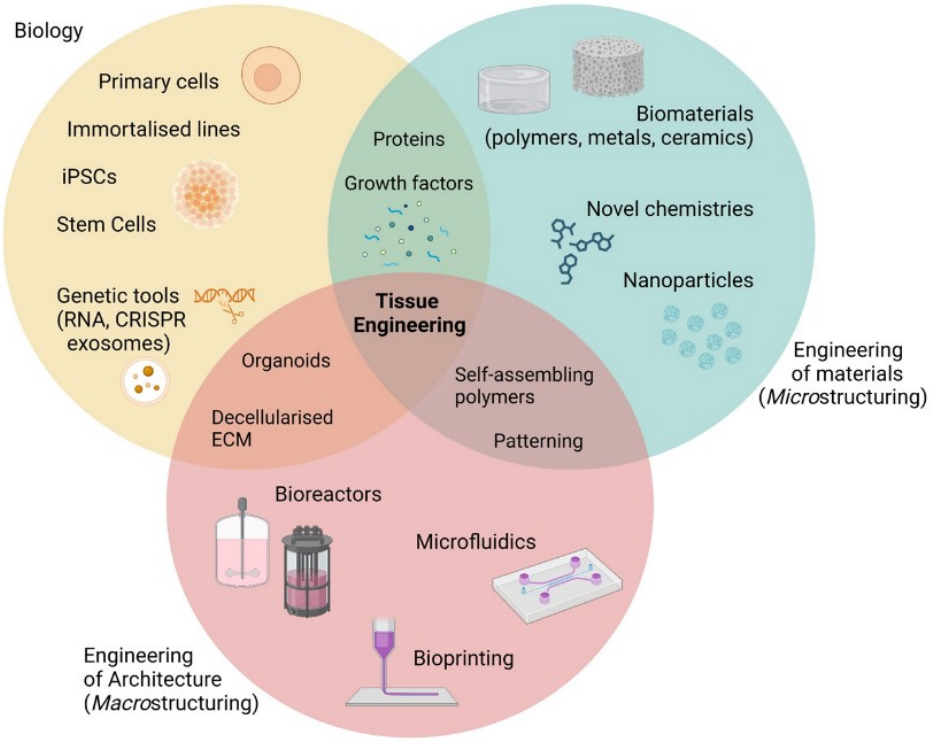

Figure 1. The Tissue Engineering toolkit can be grouped by discipline (biology, chemistry, materials science, mechanical engineering etc.) but also by scale (sub/cellular, microstructure, macrostructure).

order to restore or replace pathologically altered tissue architectures (Safinsha and Mubarak Ali, 2020, Vacanti, 2006). However, the field is more recently utilised to develop of model systems, contributing to expanding understanding of structure-function relationships in physiological and pathophysiological tissue.

Tissue engineers combine cells, biomaterials and additional factors (Figure 1) to generate functional tissues. This engineering of artificial tissue is challenging as naturally occurring human tissues contain a myriad of features or “signals” that cross disciplinary boundaries. For instance, biologists may focus on environmental factors to support cell viability and functions, whereas materials scientists or engineers may be more concerned with replicating mechanical behaviours of tissue i.e. stiffness, stress-relaxation. Specifically, inclusion of fibrillary matrix proteins within hydrogel biomaterials can support cell culture, but will also alter to mechanical properties. Untangling cross talk of signals is especially challenging when we begin to look at tissues with complex 3D structure-function relationships such as the CNS.

Tools used depend upon application and desired outputs. Huge focus is given to the design and processing of biomaterials (Section 1.2.4.2 and 1.4.2) to provide optimal environmental conditions that support cell processes and guide tissue formation. However, increasing attention is now given to engineering technologies as a means to assimilate multiscale cues, as a way of replicating the hierarchical architecture of naturally occurring tissues. Methods of engineering the wider architecture of the tissue model includes the integration of bioreactor systems, such as microfluidic devices, but also structuring via bioprinting.

The term bioreactor encompasses any device or system that provides an additional level of environmental control when cultivating cells and tissues. Typically, they mimic optimal conditions for growth; however, parameters may be modified to address specific experimental questions. Microfluidic devices enable manipulation of fluidics at a micro to nanolitre scale, with integration of cells yielding organ-on-a-chip (OOAC) technology, whereby the chip itself acts as a bioreactor. OOAC technology is gaining interest among researchers, particularly tissue engineers, with recent reports indicating the OOAC market will grow with a compound annual growth rate of 30% by 2031 (Deshmukh, 2022). A variety of OOACs exist, for various tissues in both healthy and diseased states (Aref et al., 2018, Jang et al., 2019, Kim and Ingber, 2013, Park et al., 2015, Sontheimer-Phelps et al., 2019, van den Berg et al., 2019). Combining OOACs may lead to production of multi-organ microfluidic systems, otherwise known as body-on-a-chip technology (Liu et al., 2019, Leung et al., 2022). Advancements may include creation of personalised OOACs for precision medicine, for example incorporation of patient microbiota for gut-on-a-chip technology (van den Berg et al., 2019, Tan and Toh, 2020). Integration of sensors is suggested for real-time monitoring of cell behaviour,

specifically for electrophysical assessment of rapid neuronal activity (Kamudzandu et al., 2019, Ma et al., 2022, Obien et al., 2014). Reviews provide novel OOAC case studies and critically evaluate typical cell sources, materials and modifications, manufacturing techniques and end-point outputs (Leung et al., 2022, Wu et al., 2020, Osório et al., 2021).

OOAC devices can include numerous components, including but not limited to cells, biomaterials, controlled fluid flow, physical or biochemical patterning (Section 1.4.2.2-6), alongside functional components such as sensors. Spatiotemporal over the cellular microenvironment is achieved via modulation of input parameters, with precise control of fluid dynamics one of the main advantages of this type of bioreactor system; continuous and peristaltic perfusion systems ensure tailored baseline of nutrient delivery and waste removal. This approach is not only more a more convenient alternative to traditional feeding regimes, but is also more biologically relevant, with shear stress from perfusion regimes known to promote functionality of junction proteins found within cellular junctions (Potjewyd et al., 2018, Shimizu et al., 2020). Miniaturisation of devices enables the use of small sample volumes; resulting in reduced reagent consumption, reduced waste, improved reaction control, potential for high throughput screening when used in conjunction with automated systems. Automated and integrated microfluidic systems allow for computational control over sensors and actuators, decoding and influencing cellular responses in real-time. A combination of several analytical techniques in a microfluidic device, including electrical, enzymatic, fluorescent, and immunological assays, allows the simultaneous testing of multiple variables, such as cell viability, phenotype, secreted factors, and metabolites (Castiaux et al., 2019, Leung et al., 2022).

1.2.4.1. Bioprinting

Bioprinting is a bottom-up approach that enables geometrically controlled assembly of complex 3D structures, with inclusion of functional elements producing scaffolds that encompass mechanically and biologically relevant cues (de la Vega et al., 2019, Ouyang et al., 2020). 3D computer modelling software translates the construct into digital format, with the general structure then broken down into individual “building blocks”. Bottom up approaches whereby “building blocks” are built bottom-up is preferred when printing designs with multiple components (Ouyang et al., 2020). Extrusion based methods of 3D bioprinting are popular due to high control over construction, alongside improved availability and understanding of computer aided design and freeform fabrication techniques (Billiet et al., 2012, Cadena et al., 2021, Ozbolat and Hospodiuk, 2016).

Bioprinting relies on the development of bioinks; specialised materials capable of supporting cells via physical materials (e.g. polymers) and functional components (e.g. ECM proteins,

growth factors etc.) Incorporation of iPSCs into bioink formulations lends the concept towards creation of heterogeneous models, with potential for disease models via inclusion of iPSCs possessing diseased genotypes (Gu et al., 2017, Loai et al., 2019, Walus et al., 2020). The use of organoids within a bioink is suggested to hold promise as a method of organ printing to produce self-organising organ constructs containing built-in vascular networks (Mironov et al., 2009). Hydrogels are widely used as bioinks in 3D printing of tissue-engineered constructs due to their biocompatible, dynamic and tuneable characteristics. Extrusion printing of hydrogel bioinks is an advancement upon traditional scaffolds, which allows for greater control over spatial features (Kaplan et al., 2020).

Figure 2. Example of additive layer manufacturing approach to 3D printing, enabling generation of macroscale structures via extrusion of a singular filament into a lattice structure (left to right; side view, birds eye view, final construct). Fusion of printed material enables production of a monolithic constructs.

It is vital to select a printing material with viscous and fluid behaviour relevant for the chosen application; when printing tissue, a balance must be found to ensure the material possesses a low enough viscosity to ensure layer integration and relevant stiffness, with a high enough viscosity to prevent the structure collapsing. Unfortunately, such a balance is hard to achieve when printing low-viscosity bioinks comprised of hydrogel-precursor. Unfortunately, “soft” hydrogel constructs commonly necessary for mimicry of ECM are often unable to maintain shape following extrusion printing. As such, lattice structures are favoured as a means to provide stabilisation to printed constructs (Figure 2). This approach of stacking filaments (Figure 2) to produce 3D structures is an example of additive layer manufacturing (ALM). It is suggested that printing of low-viscosity material into complex shapes requires a secondary sacrificial gel to provide mechanical support (Brunel et al., 2022, Luo et al., 2019, Moxon et al., 2017, Senior et al., 2019). An adaptation of the ALM method is Suspended Layer Additive Manufacture or SLAM (Figure 3); whereby injection of the bioink into a fluid gel support allows for printing of low-viscosity biopolymers (Moxon et al., 2017, Senior et al., 2019). This method of using a support phase and injectable phase has been coined an aqueous two-phase system (ATPs), with potential support matrices including viscous oils, elastomers and gels (Luo et al., 2019). In the case of SLAM, displacement and rapid restructuring of the fluid gel occurs following injection of the bioink (Cooke et al., 2018). Agarose and gellan gum are popular

support phase materials as these substrates are capable of providing mechanical support, but also allow for entrapment of biologically active molecules (Compaan et al., 2019, Senior et al., 2019). Modifications to this method include FRESH (Freeform Reversible Embedding of Suspended Hydrogels) and SHAPE (Self-Healing Annealable Particle-Extracellular matrix) (Hinton et al., 2015, Kajtez et al., 2022).

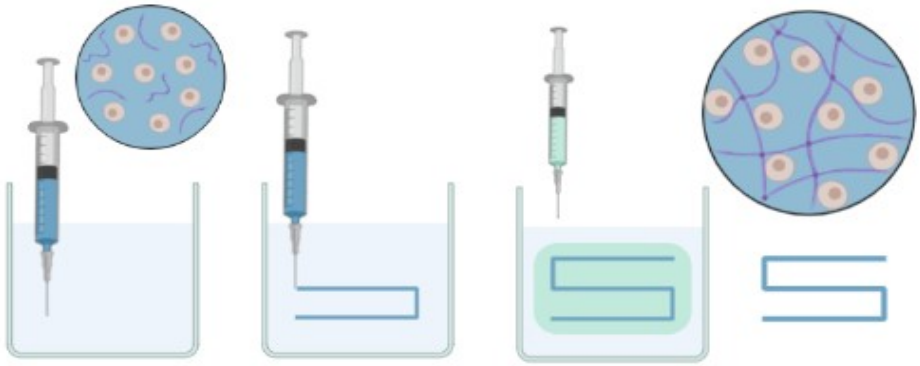

Figure 3. Stages of SLAM. Extrusion of polymer bioink containing cells into desired shape. Addition of cross-linking agent. Removal of the support phase to produce self-supporting cell-laden construct.

This approach allows distinct layer formation and ensures the printed structure does not collapse under its own weight prior to gelation. This approach is discussed within the context of structural patterning later (Section 1.4.2.6). Gelation may occur following addition and perfusion of a cross-linking agent. Alternatively, this approach can be adapted, with use of a support bath already containing the cross-linking agent allowing for printing of structures with almost immediate gelation. Alternatively, light-based crosslinking approaches may be employed, however penetrance of UV is difficult to measure. In order to utilise conventional or adapted SLAM methods, careful consideration is given to a materials mode of gelation and polymerisation kinetics, to allow for good resolution of printed constructs.

Researchers therefore must carefully consider the technical and practical requirements of their tissue engineered system and optimise cells, biomaterials, processing conditions and other extraneous factors in order to promote compatibility of variables and desirable outputs e.g. high cell viability, printable biomaterial etc.

1.2.4.2. Biomaterials

A biomaterial is a material that has been modified to interact with biological systems, often exploiting advantageous characteristics for a chosen application. Mechanical (stiffness, porosity, degradation) and biological (biocompatible, bioactive) properties will have a dramatic effect on cell behaviour and must be evaluated against the suitability of the material for use within research (cost effectiveness, ease of use, readily available, measurable outputs).

Traditional plastic two dimensional (2D) vessels possess stiffness for cell culture are several orders of magnitude stiffer than tissues *in vivo* (Sigma-Aldrich, 2021), which has been shown to induce cellular stress (Watson et al., 2017). Tissue engineers propose the improvement of

biomaterials as a means to develop advanced 3D models capable of supporting cell growth but also actively influencing cell behaviour. Examples of biomaterials include metals, ceramics, glass, plastics and polymers, to produce a variety of geometries (e.g. solid structures, fibres, gels) for integration with biological systems. A 3D tissue engineered approach utilising planned biomaterial scaffolds alongside engineering techniques is thought to be the best hope of recreating functional tissues *in vitro* (Cukierman et al., 2001).

Developing biomaterials for 3D culture is essential for accurately replicating the intricate architecture of human tissues, especially within the CNS. Gels, specifically hydrogels, are the focus of work herein due to their suitability when modelling soft tissues. Well established applications of hydrogels include contact lenses, wound dressings, incontinence products and drug delivery systems (Caló and Khutoryanskiy, 2015). While hydrogel scaffolds alone can provide mechanical support to injury sites, they can be exploited to entrap, protect and deliver therapeutics (e.g. cells, growth factors, proteins, small molecules, drugs) to injury sites, with known degradation kinetics allowing for temporal control over therapeutic delivery (George et al., 2019, Jayakumar et al., 2020). As time progresses, characteristics of these novel materials are becoming better understood, enabling the use of modified hydrogels such as fluid-gels; shear-thinning properties of fluid gels allow for delivery of therapeutic drugs to the eye (Hill et al., 2018). While the use of hydrogels within biomedical sciences is not new, recent work has suggested hydrogels are well suited for tissue engineering applications due to their biocompatible, easily modifiable and injectable nature (Billiet et al., 2012, Cooke et al., 2018). Hydrogel biomaterials are therefore of great interest within the field of neural tissue engineering (Section 1.4.2), with compositional, structural and functional complexity necessary to support functional development of CNS models *in vitro*.

1.3. Neural Modelling

1.3.1. *In Vivo* Modelling

Due to the lack of available and abundant living human neural tissue, animal models are essential when modelling the human CNS. Furthermore, the use of non-human systems is especially necessary when testing CNS therapeutics, due to sensitivity of the organ and possibility of life changing damage. These *in vivo* models therefore provide invaluable insight into the complexities of brain development, homeostasis and dysfunction. Various species are employed depending on the experimental question at hand. Zebrafish, noted for their transparent embryos enabling whole-brain imaging, are particularly useful for assessing neurodevelopment (Schmidt et al., 2013). At the other end of the scale, non-human primates are utilised due to their behavioural and physiological similarity to humans; however, undertaking of non-human primate studies must be adequately justified to ensure scientific

benefit outweighs harm (Capitanio and Emborg, 2008). Small rodents are advantageous due to their small size, short gestational period, ease of maintenance and low cost (Ranjan et al., 2018). Reviews below highlight various methodologies for modelling neuropathologies with rodents.

Mouse or rodent models can be used to study CNS dysfunction and disease via induction of pathological states. For Alzheimers this is achieved via introduction of disease-associated proteins, such as mutant tau or amyloid precursor protein, leading to tau aggregation or amyloid plaque formation, and ultimately neurodegeneration. Typically, genetic engineering is employed to induce mutant expression, however direct injection of mutant proteins may also be carried out (Yokoyama et al., 2022). Genetic modification, via whole organism or cell-specific gene knock-outs, viral vectors and CRISPR-Cas9 technology, can be used to modify tissue phenotype in order to replicate key features of neuropathological states (Navabpour et al., 2020, Yadav and Purow, 2024). Post-transcriptional gene silencing, via RNAs, is an alternative method of modifying expression that can provide spatiotemporal control (Navabpour et al., 2020). Reviews highlight specific genetic modifications and mouse models for creating models of Alzheimers, Parkinson's, frontotemporal dementia or amyotrophic lateral sclerosis (Dawson et al., 2018, Yokoyama et al., 2022). Alternative approaches include immunisation against various myelin proteins (e.g. MOG_{35-55} mutation), to reproduce inflammatory demyelination of the CNS seen within autoimmune-mediated diseases such as multiple sclerosis (Kipp et al., 2017). Additional alternative methods include physical injury or electrical overstimulation, to recreate conditions such as traumatic brain injury or epilepsy (Kandratavicius et al., 2014, Xiong et al., 2013). Another common option for inducing seizure activity is short-term exposure of animal brains to toxins (namely chemoconvulsants) as a means to promote epileptic phenotypes in vivo, providing insight into epilepsy development (Losi et al., 2016). This may suggest that the most appropriate methodology for inducing disease *in vivo* would be that which most closely mimics disease progression *in vitro* i.e. long-term study of genetically modified animals to recreate complex neuropathologies/neurodegenerative states developed over human lifetimes.

Slicing of brain tissue from *in vivo* model systems enables *ex vivo* interrogation via *in vitro* techniques such as fluorescence microscopy, electrophysiological measurement (Section 1.3.3) and eventual histopathological examination. This approach is praised for bridging the gap between in vivo and in vitro model systems, although is not without limitation (AlaylioĞlu et al., 2020). Brain slices are unique in their ability to retain many spatiotemporal features of *in vivo* biology, including elaborate tissue architecture, interactive cell types and functional neural circuitry, while enabling experimental access. For example, treatment of slices can induce neural network seizure activity is possible via electrical simulation, perfusion of drugs,

toxins or ionically modified solutions (Losi et al., 2016). Brain slices obtained from postnatal rats can be maintained *in vitro* for weeks, undergoing maturation similar to that seen *in vivo* (Cho et al., 2007). This allows for physiological and pharmacological assessment of neural tissue, providing detailed insight into dynamic processes such as neuronal activity and synaptic transmission. Retaining functional activity of *ex vivo* neural culture enables real-time imaging of cell processes via fluorescence microscopy or high-resolution confocal microscopy. Injection, or induced expression, of fluorescent markers may provide valuable insight into spatiotemporal distribution of functional activity and morphological components. Fluorescent and confocal imaging methods can also be adapted to *in vivo* imaging as a means to place findings within the context of unaltered physiological activity (Kerr and Denk, 2008).

The slicing method is particularly advantageous when examining tissue from genetically modified or treated sources, allowing invasive interrogation of these processes. Glioblastoma is one condition which has been extensively studied via treatment of *ex vivo* slices with diseased proteins/cells, and slicing of *in vivo* diseased tissue, either natural or genetically-modified in origin (Yadav and Purow, 2024). Slice models of Alzheimers are typically achieved via *in vivo* growth of mice that have been genetically modified for pathological amyloid expression (Croft and Noble, 2018, Yadav and Purow, 2024). Direct exposure of mouse hippocampal slices to beta-amyloid has shown to result in neurotoxicity and reduced plasticity, accompanied by increased amyloid plaque deposition (Cho et al., 2007). Interestingly, immature slices were shown to be resistant to beta-amyloid-induced neurotoxicity (Bruce et al., 1996). While this has interesting implications for AD-associated toxicity in “mature” hippocampal networks taken from young animals, this may not relate to the long-term maturity observed within humans *in vivo*, and thereby translation to human neurodegenerative disease is limited. Slicing of organoids may overcome difficulties with diffusion and hypoxia associated with traditional organoid culture (Aili et al., 2024). This approach enabled investigation of the autism susceptibility gene DISC1 via generation of neocortical organoids, with subsequent slices showing abnormal cortical layer formation (Qian et al., 2020).

CNS tissue slices are indeed a valuable tool for exploring neurodevelopment and neuropathological mechanisms, alongside testing of potential therapeutics; however, limitations such as mechanical damage during slicing and loss of native tissue architecture are unavoidable. As such, researchers may look to utilise non-invasive *in vivo* techniques such as magnetic resonance imaging (Li et al., 2017), positron emission tomography (PET) and multi-photon microscopy, which are gaining attention due to novel advancements (e.g. Increased resolution due to novel probe design) (Kastelik-Hryniewiecka et al., 2021, Kerr and Denk, 2008, Xu et al., 2024).

Late-stage failure rates of clinical trials are significantly higher for neurological therapeutics, thought in part to be due evolutionary obstacles preventing developing animal models that accurately predict responses of human tissue (Cummings et al., 2019, Pankevich et al., 2014). Inherent differences between non-human animal and human brains, during disease and development, may hinder interpretation and translation of biological features to cognitive deficits. While genetic modification can enable the creation of diseased models, these conditions do not always translate into the human disease state (LaFerla and Green, 2012, Ranjan et al., 2018). For example, populations of transgenic mice used for testing do not display the variability and complexity seen in wider human populations (Cuadrado-Tejedor and García-Osta, 2014, Ranjan et al., 2018). Researchers should therefore look to clarify the mechanism by which genetic modification produces models of neurodegeneration, and validate such models via comparison to non-human primates (Yokoyama et al., 2022). Inducing a valid and reliable disease phenotype is difficult as causes of neurodegeneration are not completely understood, with animal models failing to display all of the hallmarks of naturally occurring AD in humans (Dawson et al., 2018). Furthermore, modelling of long-term disease progression over decades is difficult as animal lifespans are not as long as that of humans, preventing relatable accumulation of environmental damage.

An additional criticism of *in vivo* animal modelling is the inability to accurately evaluate psychological and behavioural effects of potential therapeutics, a necessary output when testing compounds to treat neurodegenerative disease and resultant psychiatric dysfunction. Crude experiments exist to measure psychological outputs, i.e. behavioural despair tests to assess low mood, however the inability of animals to not only process complex emotion, but also provide feedback on psychological side-effects is a fundamental limitation.

1.3.2. Neurophysiology

The mammalian central nervous system is unique in its ability to instil consciousness and higher-order thought processes, with evolution of modern *Homo sapiens* resulting in advanced cognitive ability of the modern human CNS (Miller et al., 2019, Vanderhaeghen and Polleux, 2023). Unfortunately, understanding this organ in its entirety is impossible due to complexity, inaccessibility and sensitivity to external interference. Biological features of the brain can be separated into cellular and acellular components. The brain has over 100 functionally distinct regions, containing over 85 billion neurons and over 61 billion supportive glial cell types (Vanderhaeghen and Polleux, 2023). Non-neuronal glial cells (microglia, astrocytes, and oligodendrocytes) are important, as these cells are crucial for regulating numerous cellular processes and guiding neuronal network formation (Bayraktar et al., 2020, Molyneaux et al., 2007).

It is thought the intricate organisation of supportive cell types is partly responsible for higher-thought processes in mammals; with only humans and primates displaying a particular population of cortex layer 1 interlaminar astrocytes (Oberheim et al., 2006). The cortex is the largest and outermost region of the brain and is responsible for processes such as memory, attention, and perception. This region of the brain is estimated to contain over 16 billion neurons (Hodge et al., 2019). Evolution of the human cortex is thought to be responsible for our unmatched cognitive capacity, with enlargement of this region linked to expansion and increased functionality of supportive cell populations (Oberheim et al., 2009, Robertson, 2014). While the human brain is not the largest mammalian brain, complexity and relative size of the neocortex and corpus callosum is thought to drive emergence of advanced cognitive function (Miller et al., 2019).

Nevertheless, neuronal populations are the foundation for electrical network activity, and the mature cortex predominantly contains two types of neuron; projector or excitatory neurons utilise glutamate as a neurotransmitter and account for 80%, with local circuit or inhibitory neurons responding to Gamma-aminobutyric acid (GABA) and accounting for roughly 20% (Rubenstein, 2011). When examining a section of cortex via immunohistochemistry, distinct layers of cell populations and varying ECM compositions are observed (Figure 4). These layers form during development whereby after deposition of the first layer, layers 6-2 form in an inside out manner, with six preceding five and so on. Positioning of both neuronal and glial cells within the cortex has a profound effect on gene expression profiles and resultant phenotypes; thought to be due to a range of cellular interactions with other cells, matrix proteins and small molecules (Bayraktar et al., 2020, Molyneaux et al., 2007).

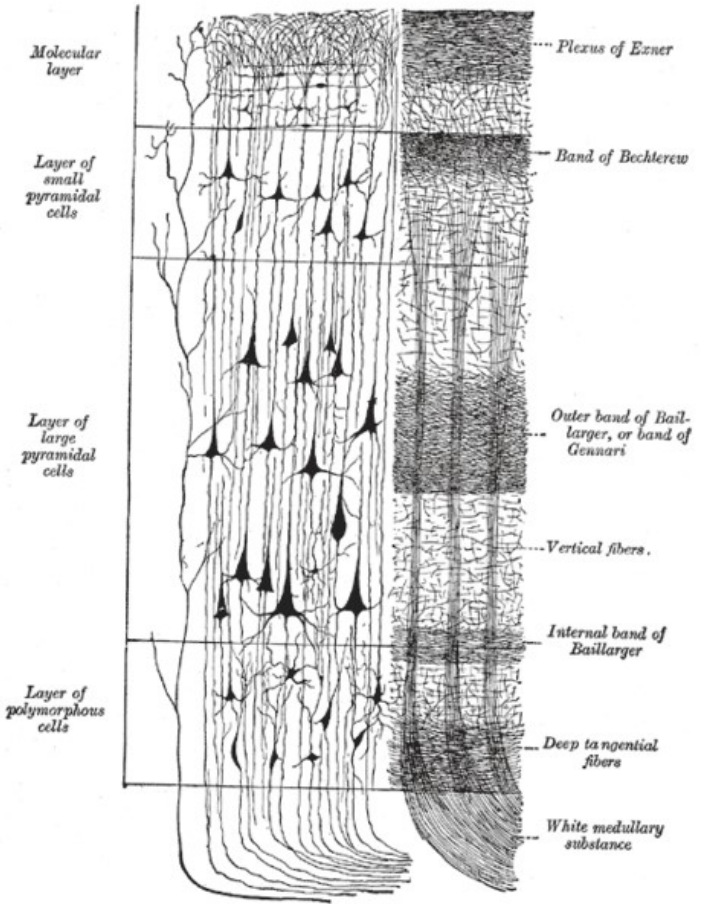

Figure 4. Cerebral cortex. Cellular and nervous fibres (left to right) (Gray, 1858). Image available in the public domain, CC0.

Structurally, the cerebral cortex comprises a small 2-5 mm layer of grey matter around the outer surface of the brain, with large surface area due to the formation of ridges and indentations, defined as individual gyrus and sulcus. This folding occurs during development, in a process coined as gyrification, enabling increased volume of cells to fit within the skull. Gyri form a generalised pattern in most humans, enabling division of the brain into two hemispheres that possess marked differences in cytoarchitecture and neurotransmitter composition, thought to be due to differences in function depending upon region, as well as across species and individuals (Hutsler and Galuske, 2003). Gyrification enables segmentation of the cortex into four anatomically defined areas. Frontal, parietal, occipital and temporal lobes comprise the forebrain, sitting on the central midbrain and hindbrain located at the base of the skull. Recent computational dynamic modelling found that degree of folding is fundamental in the mechanical response of brain tissue (Sáez et al., 2020).

1.3.2.1. Neurogenesis

During development, spatiotemporal secretion of soluble proteins, growth factors, hormones, cytokines, proteases, matrix proteins, lipid mediators and genetic material plays an important role in guiding fundamental cellular and tissue processes (Miller et al., 2019). Secretion is fundamental as a means to establish gradients of proteins, small molecules, hormones etc. during development and into adulthood. These gradients in the local environment influence cell behaviour, for example migration along a soluble concentration gradient is known as chemotaxis. Small molecule gradients are particularly important when ensuring complex patterning of tissues, with transcription factor and mRNA expression and distribution heavily implicated in organisation of the cortex during development and adulthood (Caviness et al., 2009). A myriad of patterning molecules are thought to regulate spatial organisation of various cell types within the cortex (Rubenstein, 2011). Secretion of ECM proteins is also essential to guide migration, with an intricate network of adhesion proteins, such as α-laminin, guiding patterning and remodelling of the wider tissue architecture (Merryweather and Roach, 2017). Alternatively, reelin is a matrix protein with great tissue-specificity, implicated in neuronal migration and cortical organisation (Frotscher, 2010). Abnormal reelin activity is also associated with a variety of neurodegenerative diseases, specifically AD (Liu et al., 2013).

1.3.2.2. Extracellular Matrix

ECM of the brain is a complex and dynamic network composed of proteins, glycoproteins, and polysaccharides that provide structural support and biochemical signalling to cells. It includes components like collagen, laminin, fibronectin, and proteoglycans, which help maintain tissue integrity, facilitate cell adhesion and migration, and play crucial roles in neurodevelopment, synaptic function, and repair processes following injury. ECM of the CNS is unique in that it

contains reduced fibrous proteins and more proteoglycans than other tissues, regulating adhesion-based processes such as attachment, migration and neurite extension (Ruoslahti, 1996). Retention of the proteoglycan protein core within cell membranes enables retention and regulation of growth factors by sulphated glycosaminoglycan (GAG) extensions (Simsa et al., 2021). Sulphated GAGs include chondroitin sulphate (CS), heparin sulphate (HS), keratin sulphate (KS), whereas hyaluronic acid (HA) is a non-sulphated GAG that is not bound to a core protein. CS contributes to ECM integrity and regulates neuronal growth and synaptic plasticity, encompassing the family of four lectican proteins that bind HA; with neurocan and brevican exclusively expressed in neural tissue (Miyata and Kitagawa, 2017). HS supports survivability of cells within the ECM by facilitating signalling from growth factors (Tomaszewski et al., 2021). This is particularly important when we consider the importance of growth factors, such as BDNF, for guiding neural development (Section 1.4.1.1). HA provides fundamental support via interaction with various matrix proteins but also possesses a high capability for water binding, ideal for CNS tissue (Rauti et al., 2020, Simsa et al., 2021).

Additionally, collagens, such as Collagen IV and VI are essential for maintaining structural integrity and functionality of the CNS ECM. Collagen IV is primarily located in the basal lamina of the blood-brain barrier and surrounding nerve cells, where it provides structural support and regulates cell adhesion and permeability. Collagen VI is found in the pericellular matrix around neurons and glial cells, contributing to ECM stability, facilitating cell interactions, and playing a role in neuronal development and repair processes following injury. Such structural support is vital for formation of the basement membrane and integrity of the blood-brain barrier.

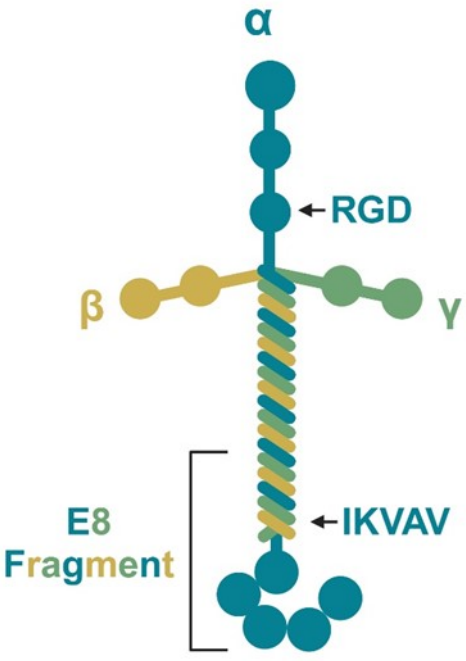

Figure 5. Schematic of heterotrimeric structure of laminin. Functional RGD and IKVAV sequences are found on the α-chain, whereas the E8 fragment spans C-terminal regions of α, β and γ chains. Created with Biorender.com.

Alongside providing structural support to cells, adhesion proteins within the CNS mediate cellular interaction with the ECM. Laminin is a crucial adhesion glycoprotein, bound within the basement membrane to guides adhesion, migration and differentiation of precursor cells during CNS development. Laminin binds to cells via integrin binding of adhesive motifs (Figure 5), such as RGD (arginine-glycine-aspartic acid) or IKVAV (Isoleucine-lysine-valine-alanine-valine) sequences (Farrukh et al., 2017, Hyysalo et al., 2017).

Alternatively, glycoproteins such as fibronectin and vitronectin are found in both ECM and plasma. Fibronectin exists as a dimer, playing a significant role in neuronal guidance and network plasticity. Specifically, the RGD and PHSRN (Proline-Histidine-Serine-Arginine-Asparagine) motifs, binds integrins on neuronal and glial cells, regulating processes such as axon guidance and synapse remodelling (Trujillo et al., 2019). Vitronectin is a less abundant adhesion protein, existing primarily as a monomer, guiding ECM (re)structuring via adhesion at multiple binding sites (Ruzha et al., 2022). Distribution, isoform and functionality of such proteins, within the CNS and wider body, differs greatly; while laminin and fibronectin are abundant and functionally diverse, vitronectin plays a localised role in tissue maintenance.

Given the secretome of a given cell changes depending on the origin and environmental stimuli (Daneshmandi et al., 2020), a feedback loop exists whereby acellular and cellular components are in constant communication to dynamically shape the local microenvironment. The result is a highly heterogeneous polymeric network comprised of innumerable protein-protein interactions, acting to provide physical and biochemical support to cells of the CNS. The importance of this support networks becomes clear when we recognise formation perineuronal nets (PNNs) around parvalbumin-expressing inhibitory neurons, with specific condensation of ECM to modulate synaptic plasticity (Abdeen et al., 2016, Miyata and Kitagawa, 2017, Rauti et al., 2020). Further research is needed inr order to understand the complex mechanisms that underpin elaborate ECM arrangement and composition, with spatiotemporal differences observed in both homeostasis and disease (Abdeen et al., 2016, Rauti et al., 2020, Ueno et al., 2019). This challenge is compounded by the fact the brain undergoes continual remodelling via metalloproteinases (MMPs), driving not only structural changes but plasticity of neuronal networks (Simsa et al., 2021).

1.3.2.3. Mechanical properties

It is widely accepted that the brain does not behave as liquid or solid, rather has viscous and elastic properties, commonly seen in highly hydrated tissues comprised of heterogeneous polymer networks such as ECM (Libertiaux and Pascon, 2009). Lack of fibrillary ECM proteins within the brain results in reduced elastic modulus compared to other tissues, alongside unique viscoelastic behaviour (Kim and Choi, 2019). This suggests elaborate structure-function relationships underpin distinctive mechanical behaviour (Simsa et al., 2021). High water retention may have a part to play in the unusual viscoelastic behaviour of the brain, with solid ECM of the brain is estimated to contribute to only 20% of its final weight, far lower than other tissues. Furthermore, mechanical properties vary depending on the depth, position, and cytoarchitecture of tissue analysed (Murphy et al., 2019). For example, white matter was observed to be stiffer than grey matter (Bartlett et al., 2020, Budday et al., 2015). Differences

in mechanics are observed in disease states, with reduced stiffness in AD (Murphy et al., 2011). Exact stiffness of the brain is estimated based on measurement technique, with approximations around ~0.5-10 kPa (Leipzig and Shoichet, 2009, Libertiaux and Pascon, 2009, Murphy et al., 2019, Murphy et al., 2011, Pogoda et al., 2014).

Mechanical cues, such as ECM stiffness, within the local microenvironment are detected by cells in a process known as rigidity mechanosensing (Janmey and McCulloch, 2007). Cells sense substrate elasticity by gauging resistance to the adhesion forces cells exert on their surroundings (Chaudhuri et al., 2016). Mechanotransduction is a function of ligand binding and tension on integrins, resulting in cytoskeletal rearrangement and downstream signalling. (Di et al., 2023, Petzold and Gentleman, 2021, Pogoda et al., 2014)The external environment may be ligands present within the ECM or displayed on nearby cells Nevertheless, signal-ligand interaction may be mechanical or biochemical in nature, with transduction of such signals along key intracellular signalling pathways resulting in changes to environmental stimuli. Cells favour differentiation down specific lineages in response to mechanosensing of elasticity or stiffness of the surrounding matrix (Allen et al., 2012, Wen et al., 2014). Interestingly, cells may display a “mechanical memory”, with long-term culture on a stiff substrate leaving a “permanent imprint” that alters cellular behaviour proceeding this (Kim and Choi, 2019). Kim and Choi propose cells that undergo prolonged (i.e. beyond 7 days) culture on stiff substrates retain a “memory” of mechanical features (Kim and Choi, 2019), While the exact mechanism of this “memory imprint” is unclear, this could possibly be due to cytoskeletal interaction with surrounding ECM (e.g. repeated stretching) resulting in changes to gene expression. Emerging theories into mechanical memory postulate long-term mechanical memory in cells is influenced by transcriptional activity and epigenetic plasticity, rather than solely by adhesion-based signalling (Mathur et al., 2020). Such theories suggest cells undergo transcriptional reinforcement of cytoskeletal signalling pathways, with prolonged exposure leading to decreased epigenetic plasticity as cells “forget” mechanical features not present. This reduced epigenetic plasticity impedes transcriptional changes necessary for adapting to new environments, resulting in the cell displaying a “mechanical memory” favouring previous environment. Researchers should therefore carefully consider all environments which cells are cultured in, long before incorporation into *in vitro* biomaterials or systems, in order to promote desirable phenotypes.

Stiffness, or alternatively elasticity, favours specific lineages by recapitulating the cells natural environment i.e. soft hydrogel substrates around 1 kPa promote neurogenesis; however, differentiation of glial cells is favoured on materials with an elastic modulus around 0.5-10 kPa (Merryweather and Roach, 2017, Pek et al., 2010, Leipzig and Shoichet, 2009). Alternatively, physical cell-cell communication enables indirect relaying of environmental signals and

coordination of cell behaviour (Abdeen et al., 2016). Consideration of such physical and mechanical cues (layered arrangements, stiffness) is vital when looking to recreate the CNS niche *in vitro*.

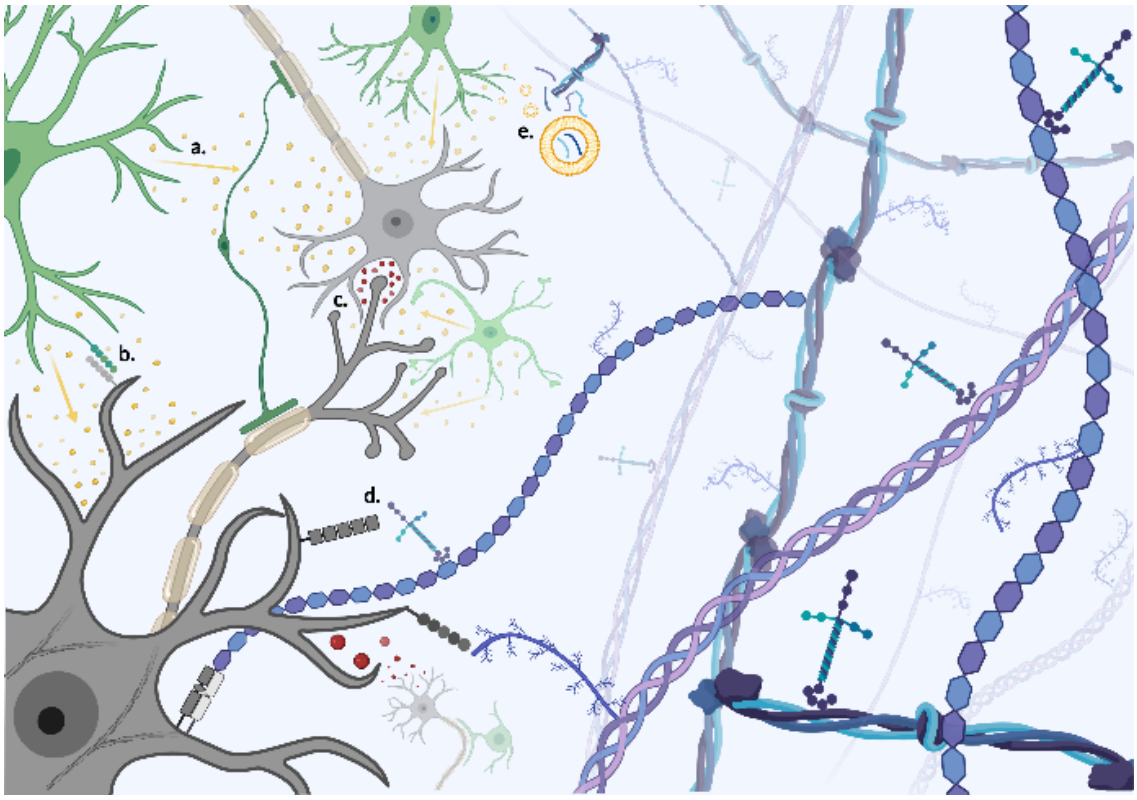

Figure 6. Taken with permission from Walczak et al. 2021. "Complex cell–cell and cell–matrix interactions drive tissue construction and network formation. Heterogeneous cellular interaction is simplified to show neuronal (grey) and non-neuronal (green), here limited to myelinating oligodendrocytes, astrocytes and microglia. 6A) Paracrine cell signalling. 6B) Contact dependent cell–cell signalling. 6C) Neuronal signalling. Dynamic cell–matrix interactions produce a tissue specific microenvironment with multiscale hierarchical features both biochemical and biophysical in nature. 6D) Direct cell–matrix interaction leading to induction of intracellular signalling cascades, with mechanosensing of matrix proteins acting upon the internal cytoskeleton of the cell to evoke a biophysical response. 6E) Cells degrade matrix components e.g. collagen triple helices and branched proteoglycans, to remodel the local microenvironment."

While biological and physical characteristics of the cortex microenvironment can be imprecisely separated, the interconnected nature of cellular and acellular components guarantees that a singular feature cannot be altered without influencing the other. The interconnected and dynamic nature of tissues *in vivo* can be attributed to this continual tissue "cross talk", driving spatiotemporal modification of ECM composition and structure, alongside cell behaviour (Figure 6). This is particularly true of the human brain whereby billions of cells are in constant communication to drive not only conscious behaviour of the entire organism, but also multi-scale changes in tissue architecture and composition. The dynamic remodelling of neuronal networks is known as pruning, and is vital in maintaining biomechanical support and electrophysiological activity of the CNS.

1.3.3. Electrophysiology

Electrical activity of the CNS is a fundamental tissue function, driving conscious thoughts but also unconscious bodily functions. Electrical signals travel through neuronal networks throughout the brain, via propagation of action potentials. The phospholipid bilayer structure of cell membranes allows tight control of what enters/leaves the cell, enabling generation of electro-chemical charges by limiting movement of charged particles or ions. While neurons are electrically active, transmission and electrical signalling are biochemical processes existing within neuronal networks.

While intracellular and extracellular charge is generally neutral, a slight charge difference occurs at the membrane surface, this is known as the resting membrane potential. In response to stimuli, gated-channel proteins within the cell membrane promote movement of charged ions, generating an electrochemical wave that travels along neuronal axons. As the signal reaches a pre-synaptic terminal, neurotransmitters are released into the synaptic cleft following opening of calcium channels, binding to receptors on nearby cells to promote or inhibit signal propagation. The frequency of action potentials varies, with many neurons emitting tens of action potentials per second, whereas other network areas may be inactive for minutes at a time.

Analysis of electrical activity is paramount when generating *in vitro* neuronal networks, and is made possible by various techniques. The patch clamp method is the current “gold standard” for quantifying ionic currents of individual cells or pieces of membrane, but is labour intensive and requires a high level of precision and expertise to carry out (Grainger et al., 2018, Annecchino and Schultz, 2018). This invasive approach employs a glass pipette to measure ionic currents at a single-cell level, providing high spatiotemporal resolution but evoking cellular damage and providing little insight into wider tissue electrophysiology. The use of invasive electrodes can provide precise real-time insight into electrical activity, with emerging techniques demonstrating the versatility of this approach for in vivo imaging (Kerr and Denk, 2008). Alternatively, inclusion of Multielectrode Arrays (MEAs) yields quantitative information regarding electrical activity, signal potentiation and drug responses (Obien et al., 2014). This approach is non-invasive and collects electrical activity data from numerous cells via direct cell-electrode contact, converting extracellular ionic voltage fluctuations into electronic signals to provide an indication of network connectivity/dynamics. . Incorporation of electronically functional components such as conductive materials or MEAs allows for better integration of nervous tissue within *in vitro* scaffolds (Liu, 2018). While MEAs hold great potential for automated high-throughput applications, this approach generates vast amounts of data,

requiring extensive processing to determine valid experimental endpoints and translate this into comprehensible results.

Alternatively, calcium fluxes provide more qualitative data better indicative of whole network function (Lin and Schnitzer, 2016). Calcium imaging is a non-invasive approach that requires addition of indicators, which can be chemical or genetically encoded calcium indicators (GECIs) (Hendel et al., 2008). This approach provides good spatial resolution, however may lack temporal precision due to the kinetics of dye responses. Loading of cells with fluorescent dyes illuminates intracellular Ca^{2+} and calcium-mediated neurotransmitter release, providing non-invasive insight into electrical activity of a neuronal network (Grainger et al., 2018). Genetically encoded voltage indicators (GEVIs) are an emerging alternative method that enables superior spatial visualisation across scales (cellular, neuronal network, whole brain regions) compared to GECIs (Aseyev et al., 2023, Zhu et al., 2021). Application of GECIsis limited by exposure toxicity and background fluorescence, whereas the use of GECI/GEVI technology allows for cell specific visualisation without the problems associated with chemical counterparts (Peterka et al., 2011). Incorporation of GECIs/GEVIs within engineered constructs will therefore allow for sustainable optical interrogation of neuronal network electrical activity.

Answering the question of how to measure electrophysiological activity *in vitro* largely depends on experimental outputs and biological variables being assessed. The patch-clamp technique offers high temporal and spatial resolution, enabling precise measurements of individual ion channel activity and various ionic currents, although it is labour-intensive, low-throughput, and may be damaging to cells. Conversely, GECI and GEVI methods allow for higher throughput and non-invasive real-time monitoring of multiple cells simultaneously, though they suffer from lower resolution and potential discrepancies in signal interpretation due to dye-related issues (Zhu, 2021). Electrode arrays facilitate large-scale network analysis with a relatively non-invasive approach, but they provide lower resolution and may struggle with signal clarity due to noise and the limitations of surface measurements. Ultimately, the choice of method hinges on the specific experimental goals, with combinations of techniques often yielding the most comprehensive insights into electrophysiological activity.

The use of guidance systems to promote neuronal network formation is one approach that looks to exert greater control and promote creation of functional circuits with well-defined geometries, in order to recreate complex networks observed *in vitro*. Triangular micropatterning within a microfluidic device is one patterning known to create bottlenecks of neurons and enable directional guidance of neurites, with Ca^{2+} propagation efficiency positively correlated to the amount of triangles within the microfluidic system (Gladkov et al.,

2017). These guidance systems rely on integration of environmental prompts to promote desired spatial configuration of cellular focal adhesions and influence cell behaviour; in the case of the cortex, patterning of the culture scaffold can guide neuron alignment and neurite outgrowth, producing neuronal circuits with defined pathways (Merryweather and Roach, 2017). Formation of such pathways is essential to inducing and maintaining electrical functionality of a neuronal network. By guiding neurite extension, it is therefore possible to recreate linear pathways observed between cortex layers, as well as the creation of nonlinear "loops" within the network. The introduction of such feedback loops within a model of neuronal tissue is fundamental to accurately modelling neuronal network dynamics, with incorporation of MEAs allowing for quantification of the effect these feedback circuits have on electrical outputs of the system (Potter et al., 2014).

1.4. Neural Tissue Engineering

While the field of tissue engineering is ever expanding, the majority of success has been demonstrated in the generation skin, cartilage or bone mimetics for transplantation (Kaul and Ventikos, 2015). Engineering of neural tissue is lacking, partly due to the lack of knowledge surrounding native tissue architecture and function, limiting translation to *in vitro* research (Pankevich et al., 2014).

1.4.1. *In Vitro* Cell Culture

1.4.1.1. 2D Culture

Models composed of primary cells obtained from human sources is unrealistic, due to sensitivity of mature neuronal cells and lack of available living human tissue in sufficient quantities required for large scale testing. Animal models are suggested as a means for modelling complex tissues; however, lack species specificity necessary for tailored modelling (Section 1.2.2). Alternatively, immortalised neuroblastoma cell lines such as mouse N1E-155 or human SH-SY5Y offer alternative neural culture platforms with the ability to produce *in vitro* platforms for high-throughput testing. SH-SY5Y cells (Sigma-Aldrich, UK, 86012802) are a sub-line of bone marrow biopsy-derived line SK-N-SH, displaying dopamine-β-hydroxylase activity and can convert glutamate to the neurotransmitter Gamma-aminobutyric acid. SH-SY5Ys transfected with GFP and mCherry fluorescent proteins were used in this project (George et al., 2018).

IPSCs are an invaluable tool for tissue engineers (Section 1.2.3). IPSC technology is particularly useful within neural tissue engineering by enabling generation of neural stem cells (NSCs) in large quantities needed for *in vitro* research, with potential to generate multiple cell types from the same source. The ability to generate multiple cell types from the same source enables creation of co-culture models with increased relevance to development *in vivo*.

Generating models containing various cell types is particularly important for the CNS as supportive cells such as astrocytes support neuronal network function (Section 1.3.2).

With the discovery of iPSC technology came increased attention toward generation of previously “unavailable” cell types, such as neural stem cells and neurons. Specifically, researchers found that partially differentiated foetal NPCs could be reverted to an embryonic-like pluripotent state via induction of OCT4 transcription factor, building upon previous work that required multiple factors to evoke the same response (Kim et al., 2009). Increased availability of pluripotent cells therefore led to increased focus on differentiation protocols, as a means to produce differentiated cells such as neurons.

Some of the earliest research surrounding neural induction of pluripotent cells found synergistic inhibition of SMAD signalling via Noggin and SB431542 produced highly efficient (>80%) conversion of human embryonic cells to neural subtypes, with application of this protocol to human iPSCs confirming robustness of the protocol (Chambers et al., 2009). Advancing upon this, Morizane et al. found dual SMAD inhibition, utilising Dorsomorphin instead of Noggin, was more efficient when inducing neural differentiation and increased survival (Morizane et al., 2011). Work later went on to find retinoids, such as retinoic acid, further improve efficiency of neural induction from iPSCs (Shi et al., 2012). These methodologies produce neural rosettes similar to those observed during neurogenesis *in vitro* (Galiakberova and Dashinimaev, 2020, Townshend et al., 2020). Small molecules are another means to accelerate production of neural cells from pluripotent precursors (Qi et al., 2017, Reinhardt et al., 2013). Neuronal differentiation from such iPSC-derived neural precursor cells involves a series of tightly regulated processes that guide these progenitor cells to develop into differentiated cells such as mature neurons. This transformation is influenced by intrinsic factors, such as transcription factors, and extrinsic signals from the surrounding environment, which together orchestrate the maturation of neuronal characteristics and functions. Optimisation of induction and differentiation protocols over time has led to various methodologies for generation of neural subtypes (such as specific neuronal populations, astrocytes, glial cells etc.) each with their own advantages (Engle et al., 2018, Galiakberova and Dashinimaev, 2020). 3D culture systems for neural induction and differentiation of iPSCs have shown to produce neural tissues with greater structural similarity to neural tissues *in vivo*, however this approach is not without limitations (Section 1.4.1.2).

Yagi *et al*. (2011) were the first to demonstrate the capability to generate iPSCs from familial AD patients, leading to the creation of a 2D cell model possessing mutations in PSEN1 and PSEN2 and presenting with elevated Aβ42 secretion (Yagi et al., 2011). This work was expanded upon to produce many familial and sporadic models of AD, however such models

remain inadequate due to inconsistency and inaccuracy of AD hallmarks (Section 1.1.1) (De Strooper and Karran, 2016, Ranjan et al., 2018). This may be attributed to concurrent pathological states found within neurodegenerative brains (Coulthard and Love, 2018). An emerging novel approach that may overcome this is the use of disease-susceptible iPSCs alongside environmental stimuli to investigate dysregulated inflammatory processes within the brain that may underlie multiple pathological states (Summers et al., 2024). Reviews highlight the breadth of neurodegenerative disease modelling applications when utilising iPSC technology (Bordoni et al., 2018, Engle et al., 2018, Mertens et al., 2018). Pluripotent stem cell repositories are now established and reliable sources of defined cell types that require little to no modification, with the Coriell Institute, the European bank for iPSCs, the Riken Bioresource Centre and others known to distribute AD-specific and control stem cell lines (Engle et al., 2018). Unfortunately, the use of iPSCs to model AD is not perfect. Reprogramming of somatic cells into a pluripotent state induces rejuvenation of the whole cell, reversing some effects of aging. This lack of "aged" cells, accompanied with clonal selection of the fittest and most robust iPSC colonies, means the cells most suited to model age-associated diseases such as AD are commonly not selected for use within a model (Mertens et al., 2018). Furthermore, "epigenetic memory" of reprogrammed cells means iPSCs may retain features such as DNA methylation, favouring differentiation into specific lineages and restricting others (Lee et al., 2020a). While these cells are not without limitations, favourable culture of stem cells allows for formation of organised 3D neuronal tissues that successfully recapitulate cellular and molecular processes involved in the human brain (Yoon et al., 2019).

The power that small molecules hold over cellular behaviour means special consideration to media composition must be given when looking to create and maintain functional neuronal networks. Traditional basal media was found to actually impair neurophysiological function (Bardy et al., 2015). In order to combat this, various institutions have created their own specialised neurobasal media with increased biological relevance (Grainger et al., 2018). Artificial cerebrospinal fluid (aCSF) best mimics *in vivo* conditions due to optimal concentrations of salts, phosphate buffers and energy sources. BrainPhys-basal medium contains concentrations of inorganic salts similar to that of ACSF, while promoting firing of action potentials and forming of synaptic junctions (Bardy et al., 2015). Employing a culture media with superior biological relevance will go a long way to improve reliability and validity of tissue engineered neuronal networks *in vitro*.

Inclusion of growth factors such as BDNF acts to promote cell viability whilst supporting neuronal differentiation of SH-SY5Ys (Hromadkova et al., 2020, Kim, 2014, Kovalevich and Langford, 2013, Ligorio and Mata, 2023) (Methods 3.1.3). BDNF supports neurogenesis and cell survival via binding of tropomyosin-related kinase receptors, inducing transmission of

intracellular signals responsible for guiding synaptic plasticity (Binder and Scharfman, 2004). Interestingly, dysregulation of BDNF pathways is implicated in neuropathological states, such as human AD (Aarons et al., 2019, Jiao et al., 2016). With BDNF shown to exert neuroprotective effects against tau and amyloid-β-induced toxicity in model systems (Jiao et al., 2016, Kim, 2014). Inclusion of growth factors is an attractive avenue for supporting viability of tissue-engineered constructs, with potential for dysregulation of growth factor activity as a means to induce diseased conditions *in vitro.*

Currently the majority of *in vivo* models are 2D; however, 3D architecture and interaction is important to consider when mimicking complex tissues, such as the CNS. Two-dimensional approaches fail to induce the elaborate spatial morphologies observed within the human brain, with fundamental differences in cell interaction when comparing between 2D and 3D culture (Cukierman et al., 2001).

1.4.1.2. 3D Culture

3D culture techniques enable creation of *in vitro* models of the CNS with superior biological relevance, with an additional dimension of features that may present novel phenotypic markers of disease (Fatehullah et al., 2016). Pluripotent cells can spontaneously create 3D aggregates, neurospheres and organoids (Song et al., 2019, Lancaster et al., 2017). These self-organising structures are of particular interest to researchers as they are capable of recreating the complex spatial morphology of a variety of tissues: the gut, intestine, retina, kidneys, liver, heart and even the human brain (Fligor et al., 2018, Kumar et al., 2019, Lancaster et al., 2017, Lee et al., 2008, Merker et al., 2016, Prior et al., 2019). IPSC-derived organoids are established as a means to recreate the biophysical spatial environment of the CNS, promoting culture of both neuronal and glial cell types (Lancaster et al., 2013, Li et al., 2017, Velasco et al., 2019). Cerebral organoids surpass existing methods in terms of 3D cellular layering, structural folding, and network activity (Fatehullah et al., 2016, Lancaster et al., 2013, Li et al., 2017, Trujillo et al., 2019). This approach is used to model neurological diseases such as Alzheimer's disease and glioblastoma (Gonzalez et al., 2018, Lancaster et al., 2013, Nassor et al., 2020, Ogawa et al., 2018). Aili *et al*. provide an up to date summary organoid methods for modelling neurodegenerative disease (Aili et al., 2024). Sadly, organoid protocols face issues with complexity and reproducibility. While homogenous cultures are less biologically relevant, increasing heterogeneity is associated with poor reproducibility due to increasing complexity (Fagerlund et al., 2020, Fedorchak et al., 2021, Kelava and Lancaster, 2016, Kim et al., 2021). Methods to reduce variability rely on bioengineering of organoids and guiding cell fates via small molecules, genome editing, scaffolds, micropatterning, microfabrication

techniques and organoid fusion (Fedorchak et al., 2021, Kelava and Lancaster, 2016, Lancaster et al., 2017, Song et al., 2019, Velasco et al., 2019, Yoon et al., 2019).

Production of tissue in the form of miniature organs is particularly useful with fusion of two or more interconnecting organoids to create complex structures comprised of cells from various lineages, known as assembloids (Paşca, 2019). Assembloid technology is at the forefront of research, with existing organoid models often failing to produce structures that can accurately replicate whole organ architecture. The creation of organ models with interconnected cell types, such as vasculature, would be a major step towards producing representative *ex vivo* models. Sadly, existing organoid approaches display maturation levels far below that required to model adult phenotypes (Takasato et al., 2015). Incorporation of spheroids within spinning bioreactors has shown promote growth of neuronal aggregates when compared to planar culture (Qian et al., 2016). Unfortunately, bioreactor capacity restricts yield of organoid products. Size of organoids is also limited by perfusion of metabolites, with necrotic cores developing in larger organoids due to inadequate waste clearance and lack of nutrient perfusion. This concept also extends to perfusion of therapeutic compounds, with decreased infiltration of drugs to innermost parts of the organoid as size increases. While 3D aggregate or spheroid techniques display superior intercellular communication and ECM development, these approaches are unreliable and yield considerable variation between methodologies; guided patterning approaches when producing brain organoids compares to self-organising structures (Velasco et al., 2019, Yoon et al., 2019).

Assessment of morphology and functional activity requires disassembly of the organoid via slicing, enzymatic disruption and fixing/staining, forcing scientists to analyse changes via sampling of media or expensive 3D optical approaches (Wysmolek et al., 2022). If these hurdles are overcome, assembloid models could replace animal counterparts as the widespread standard for disease modelling, drug testing etc. The use of advanced culture techniques or bioreactors enables induction of optimal environmental conditions across three dimensions, with shaking or spinning bioreactor platforms providing physiologically relevant flow conditions and enabling better diffusion of metabolites.

Microfluidic devices are proposed as a means to address problems with aggregation based 3D culture techniques, while enabling interrogation of the model (Fedorchak et al., 2021, Ranjan et al., 2018). Microfluidics may be invaluable when modelling neural tissue, with microscale topographies guiding neuronal network formation while providing an indication of electrophysiological activity (Gladkov et al., 2017, Kane et al., 2019, Peyrin et al., 2011, Yoon et al., 2019). Versatility of microfluidic systems enables incorporation of multiple culture techniques; Park *et al*. were the first to incorporate neurospheres within a microfluidic system

to model neurodegenerative disease, demonstrating a flow-based system enhances favourable outcomes such as spheroid size, neurite extension, etc. (Park et al., 2015). Researchers are starting to recognise microfluidics as a versatile yet powerful for guiding neural tissue formation (Fedorchak et al., 2021, Liu et al., 2019, Ranjan et al., 2018). Kamudzandu et al. utilised lithographic methods, alongside chemical modification, to produce a microfluidic platform that acted as a brain OOAC, with defined microchannels that guided network connectivity of basal ganglia neurons (Kamudzandu et al., 2019). Brain OOAC models capitalise on the customisable and controllable nature of microfluidics to produce systems capable of recreating core features of the CNS (Servais et al., 2024).

OOACs can contain multiple cell types, due to the potential for physical segregation whilst enabling cell-cell interactions (e.g. via membranes, perfusion systems etc. (Bang, 2019 #654). This is important when we consider the diverse multicellular interactions occurring within the CNS. Microglia are a commonly overlooked immune cell that exhibit diverse functions to mediate inflammation within the brain, dependent upon their state of activation (Ahmad et al., 2022, Gilmour et al., 2019, Lanjewar and Sloan, 2021). While it is important to include multiple cell types found within the CNS *in vivo*, OOAC features should be designed to promote desired cell behaviour; activation and plasticity of primary microglia can be manipulated via exposure to various microstructures within OOAC systems (Amadio et al., 2013). Development of disease-specific brain OOACs can be carried out by incorporating disease-specific cells (e.g. neural stem cells from a Parkinson's patient) or via the addition of pathological features (e.g. inclusion of amyloid-beta within the perfusion system) (Kane et al., 2019, Park et al., 2015). Debate exists over the truly 3D nature of microfluidic or OOAC devices, with cells often growing on 2D surfaces within the system, prompting the label of "2.5D" or "quasi-3D". Use of suspension cells or biomaterials may overcome this (Liu et al., 2019). An alternative approach may be inclusion of aggregates such as spheroids or organoids, producing "milifluidic bioreactors" containing elaborate 3D tissue architectures and extraneous features such as fluid flow (Park et al., 2015, Qian et al., 2016).

In an entirely novel approach, Materne *et al*. produced a multi-OOAC whereby neurospheres were cultured alongside liver spheroids to investigate metabolic activity (Materne et al., 2015). While body-on-a-chip technology is not a new concept, inclusion of CNS tissue is typically limited to models of the blood brain barrier (Amirifar et al., 2022). This is problematic when we consider neural processes are fundamental in controlling function of individual organs, the immune system, metabolism and nutritional state (Jin et al., 2024). Integration of iPSC technology within concurrent OOACs, each with organ-specific outputs, could be invaluable in the development of patient specific body-on-a-chip systems. Such systems would be invaluable in recreating disease states such as neurodegeneration, diabetes etc., whereby

widespread accumulation of inflammation contributes to pathogenesis. Reviews outline recent brain OOAC (brain-on-a-chip) advancements and highlight future perspectives, such as incorporation of biomaterials and bioprinting approaches (Amirifar et al., 2022, Bang et al., 2019, Servais et al., 2024).

Bioprinting allows for structuring of neural tissue *in vitro*, due to the controllable and customisable printing process. This bottom-up approach of structuring tissues *in vitro* is particularly useful when creating multicomponent systems with complex architectures, such as neuronal tissue (Ouyang et al., 2020). Bioprinting for PNS applications has shown great success, whereas translation of this approach to model the CNS is still in its infancy (Kamudzandu et al., 2019, Loai et al., 2019). Nevertheless, bioprinting is now highly reproducible due to automation, and enables high spatial control that is crucial when recreating the complexity of neural networks or brain regions.

Hydrogels are preferred when bioprinting neuronal tissue via ALM methods, due to their low-viscosity properties enabling recreation of a “soft” microenvironment necessary for modelling the CNS (Cadena et al., 2021, Chimene et al., 2020, de la Vega et al., 2019, Potjewyd et al., 2018). Examples of hydrogel bioinks used in neuronal modelling are predominantly natural biopolymers with inherent biological activity such hyaluronan, however some synthetic polymers such as PEG, have also been used (Bedir et al., 2020, Potjewyd et al., 2018). Hyaluronic acid presents as ideal bioink with the ability to retain water, with greatest density of chains at the centre with fluid-filled edges, resulting in favourable viscoelastic behaviour for printing (Cowman et al., 2015).

One of the earliest neuronal bioprinting techniques produced a model of neuronal tissue via inkjet printing of a collagen based hydrogel bioink containing neural stem cells (NSCs) and incorporation of a secondary fibrin based gel containing vascular-endothelial growth factor (VEGF), which prompted sustained release of VEGF from NSCs within the collagen scaffold (Lee et al., 2010). Direct-write printing of human neural stem cells (NSCs) within a natural polysaccharide-based bioink led to the production of neural mini-tissue structures, demonstrating that in situ differentiation of human cells within a printed hydrogel scaffold would be a viable approach for modelling nervous tissue (Gu et al., 2016). Recent advances show bioprinting to be particularly advantageous as means for precise positioning of NSC-laden hydrogels on top of electrodes for assessment of electrical output of neuronal networks (Kapr et al., 2021).

Bioinks can also be tailored to contain different cell types (neurons, astrocytes, glial cells etc.), different biochemical cues (e.g. BDNF growth factor) and specialised material formulations. Bioinks for neural bioprinting are continually evolving, exploiting iPSC technology and an

increased understanding of biochemical features of the CNS, to create specialised formulations capable of recapitulating a myriad of environmental cues (Chimene et al., 2016, Sokolovski et al., 2018, Walus et al., 2020). Reviews evaluate 3D bioprinting approaches for neural tissue engineering, with special consideration given to bioink formulation and mechanical properties(Cadena et al., 2021, de la Vega et al., 2019, Hospodiuk et al., 2017, Potjewyd et al., 2018, Qiu et al., 2020).

1.4.2. Biomaterials for *In Vitro* Neural Culture

Development of biomaterials for 3D culture is essential when looking to recreate human tissues *in vitro*. This is especially true for the CNS, which displays extraordinary 3D architectural complexity, underpinning convoluted structure-function relationships that drive human thought and behaviour.

The need to develop 3D biomaterials for neural culture is exemplified by recent research that shows inadequacy of 2D approaches resulting in reduced maturation and organisation of glial cell types *in vitro* (Lanjewar and Sloan, 2021). With abnormal inflammatory morphologies observed within 2D astrocytes and microglia when compared to 3D *in vivo* counterparts (Watson et al., 2017). Researchers are therefore looking for novel techniques and biomaterials in order to address this need. Metals and ceramics are generally avoided when modelling soft tissues due to biological (no biological activity) and mechanical (extreme stiffness) incompatibility. However, carbon based materials such as graphene and carbon nanotubes have been incorporated into neuronal models due to their flexible and conductive nature, enabling both induction and recording of electrical activity (Boni et al., 2018, Magaz et al., 2021, Tiwari et al., 2020). Silk is also a novel biomaterial found to be suitable for neural culture due to its low elastic modulus and high water content that lends itself easily to combination with other materials/techniques (Rauti et al., 2020). Lancaster *et al*. used microfilaments as floating scaffolds for brain organoids, highlighting that a combinatorial approach, utilising a variety of structures such as sponges, fibres and hydrogels, can best support cell growth (Lancaster et al., 2017). Hydrogels are also suggested as a means to reduce variability during organoid culture, with dynamic regulation of biochemical and physiochemical cues guiding cellular processes during organoid development (Liu et al., 2019). Use of biocompatible and bioactive polymers to form hydrogels has gained popularity within neural tissue engineering due to their “cell friendly” nature, versatility, capability for modification and generation of biomimetic stiffness.

1.4.2.1. Hydrogels

Hydrogel scaffolds are capable of supporting living cells due to their high water content and porous structure, allowing diffusion of molecules to facilitate chemical signalling, as well as

the solid-phase polymer network providing important mechanical and spatial cues. In order to understand the difference between gels and hydrogels, one must first understand the terms Sol and Gel. Sol has long been described as “a fluid colloidal system of at least two components, e.g. a protein sol” (Everett, 1972). Sol-gel processing is the name given to the wet chemical method of producing solid materials (such as hydrogels) from small molecules; monomers are processed into a colloidal system as an antecedent to continuous network formation (Figure 7). If the molecules or particles composing the solid-phase are hydrophilic and the liquid phase is water, the gel is a Hydrogel. Hydrostatic pressure creates a monolithic structure with increased viscosity and elasticity, causing solid-like behaviour of the system that offers a degree of protection to cells encapsulated within (Colombe Dromel et al., 2020).

Hydrogels can be natural or synthetic in origin; natural polymers include gellan gum (GG), alginate, agarose, collagen, dextran, cellulose, hyaluronic acid, chitosan and carrageenan. Natural hydrogels are superior for tissue engineering applications due to their biocompatibility, biodegradability, hierarchical structure and bioactivity (Liu et al., 2019, Rauti et al., 2020). Synthetic counterparts, such as polyethylene glycol (Barros et al., 2019), have tuneable chemical and mechanical characteristics, but possess limitations such as areas of phase separation and reduced biological activity (de la Vega et al., 2019, Gulrez et al., 2011, Jia and Kiick, 2009, Zhu and Marchant, 2011). Natural polymers such as GG are favoured for tissue engineering applications due to tuneable mechanical properties, low antigenicity, ease of production and propensity for molecule/protein encapsulation (Muthukumar et al., 2019). Matrigel™ (Corning, 2020) is one example of a hydrogel scaffold comprised of natural matrix proteins and small molecules that promote cell viability (Corning, 2020, Liu et al., 2019). However, inconsistency in production leads to inter-batch variation, an undesirable trait when looking to tightly control scaffold composition (Aisenbrey and Murphy, 2020). In summary, hydrogels can be defined as permissive or promoting, depending upon their interaction with cell and degree of biofunctionality they provide during 3D culture (Tibbitt and Anseth, 2009). Permissive hydrogels, typically made from synthetic materials, provide a basic 3D environment that supports cell survival but do not enhance or guide cellular functions due to the absence of bioactive signals. In contrast, promoting hydrogels, typically derived from natural materials, are biocompatible and bioactive, actively promoting cell-ECM interaction. Of course, modification or integration of polymers could imbue resultant hydrogel constructs with both permissive and promoting features. DeForest and Anseth expand upon this early discussion, emphasizing how these promoting hydrogels can generate tailored microenvironments that specifically affect cell fate (DeForest and Anseth, 2012).

Decellularised ECM is suggested as an alternative promoting polymer for encapsulation of brain organoids; however, retention of all ECM components during processing is problematic (Simsa et al., 2021). Use of tissue-specific ECM has been shown to accelerate and enhance neuronal network formation within a neuron-glia co-culture (Lam et al., 2019). This study was based on 2D coating of MEAs, with alternative studies suggesting 3D encapsulation of neuronal networks within native-ECM hydrogels may in fact inhibit neuronal growth (Rauti et al., 2020). Despite contradictory research and processing inconsistency, ECM-based biomaterials are advantageous in their ability to instil a greater degree of native biochemical features; enrichment of collagen hydrogels with foetal brain tissue-derived ECM enhanced functional differentiation of NSCs (Sood et al., 2019). Hydrogels can be classified as permanent or reversible, dependent on the mode of cross-linking or gelation. Typically, natural

Author(s)	Year	Cell type	Polymer	Conc	Method of X-linking	Dose
Linville et al.	**2020**	iPSC-BMECs	Col + Matrigel	6 + 1.5 mg/mL	37°C	N/A
Broguire et al.	**2019**	Rat DRG neuron	PEG	1.5%	Micheal addit. (HA/MA)	0.5 + 2%
Sood et al.	**2019**	iPSC-NSCs	Col	3 mg/mL	37°C	N/A
Bonnesoeur et al.	**2020**	Human GBM cells	HA	N/A	Genipin	0.01-1%
Long et al.	**2020**	Mouse NSCs	PNIPAM	15.74 µmol	PEG + BISAM	23 + 0.1 µmol
Moxon & Hooper.	**2017**	SH-SY5Ys	GG + Col	0.5% + 4-1:1	$CaCl_2$ + 37°C	100 mM
Lam et al.	**2019**	Rat cortical neuron	Col	1 mg/mL	37°C	N/A
Distler et al.	**2020**	N/A	Gelatin + Alginate	0.5-1%	4°C + $CaCl_2$	1 M
Farrukh et al.	**2017**	Primary NSC	Polyacrylamide		BISAM	0.04-17 mg/mL
Koivisto et al.	**2017**	iPSC-neurons	Gellan gum	4 parts	Spermidine/spermine	25 parts
Moxon et al.	**2019**	iPSC-cortical neurons	Alginate + Col	2.5 + 10 mg/ml	$CaCl_2$ + 37°C	150 mM
Hartmann et al.	**2023**	iPSC-NPCs	Alginate	1%	$CaCl_2$	90 mM

Table 1. Recent hydrogel biomaterials for neural modelling. IPSC (induced Pluripotent Stem Cell), BMEC (Bone Marrow Microvascular Endothelial Cell), NSC (Neural Stem Cell), DRG (Dorsal Root Ganglion), GBM (Glioblastoma), NPC (Neural Precursor Cell), PEG (Poly-ethylene Glycol diacrylate), GG (Gellan Gum), HA (Hyaluronic Acid Col (Collagen), PNIPAM (Poly(N-isopropylacrylamide), BISAM (N,N'-Methylenebisacrylamide).

polymer polymerisationwill be due to reversible physical interactions such as hydrogen bonds or van der Waals, whereas synthetic polymers rely on chemical crosslinking occurs through covalent bonding. Physical crosslinking of natural polymers is typically preferred amongst researchers due to low toxicity, low cost and ease of use. However, chemical modification is a powerful tool for equipping a chosen polymer with functional or modify crosslinking approach groups (Section 1.4.2.3 and 1.4.2.6). Limiting toxicity of crosslinking approach is fundamental for neural tissue engineering, with sensitivity of neuronal cells.

Table 1 highlights a range of hydrogels for neural modelling, exploiting a range of cell sources, biomaterials and additional factors. Reviews highlight chemical (photopolymerisation, Michael addition, esterification), physical (ionic gelation, hydrogen bonding, thermoresponsive gelation) and self-assembly techniques of polymerisation can be utilised for polymers such as PEG, alginate, gelatin, collagen, hyaluronic acid, fibrin, amongst others, for applications such as neural regeneration, cell/drug delivery and disease modelling (George et al., 2019,

Madhusudanan et al., 2020). While polymers such as PEG are commonly used for neural tissue engineering, modification of resultant hydrogels can instil the polymeric system with advantageous and potentially novel biomechanical and biochemical properties.

1.4.2.2. Physical Modification

Gels can exhibit a variety of unusual mechanical characteristics dependent on their physical processing following the creation of a colloidal system (Hill et al., 2018). The type of processing techniques utilised will greatly influence physical properties of the final hydrogel.

Granular hydrogels comprised of micro-gelated (microgel) hydrogel particles display shear thinning behaviour, due to dense packing of microgels within the liquid phase (Muir et al., 2021). Methods of microgel fabrication vary but commonly rely on separation or mechanical fragmentation of bulk hydrogel during or directly following gelation. Granular hydrogels are unique in that the crosstalk of biochemical and physical features is somewhat limited due to their enhanced bi-phasic nature; mechanical properties depend upon bulk interaction of hydrogel particles and interstitial space enables diffusion of biochemical factors, with microgel interfaces promoting cell-cell interaction (George et al., 2019, Muir et al., 2021).

Fluid gels are a distinctive example of hydrogels comprised of microgellated particles; exposure to shear forces during hydrogel gelation generates reversible hydrogels. Often coined “fluid” or “sheared” gels as they possess pockets of gelation, with filamentous protrusions extending from floccs of colloids, which interact to form solid material (Figure 7) until sheer force is applied (Cooke et al., 2018, Norton et al., 1999, Fernández Farrés et al., 2014). Unlike homogenous hydrogels, fluid gels possess pockets of gelation with fluid-rich areas of weak interaction existing between them (Fernández Farrés et al., 2014). Modulation of shear conditions also enables modification of shape i.e. spherical vs cylindrical particles (Fernández Farrés et al., 2014).

Shear-thinning behaviour of fluid gel material lends to use within extrusion-based systems, but also enables their use as supportive structures for bioprinting (Chapter 6) (Cooke et al., 2018, George et al., 2019, Kajtez et al., 2022). Alternatively, phase separation is a technique that exploits water organising properties of polymers, enabling production of unique

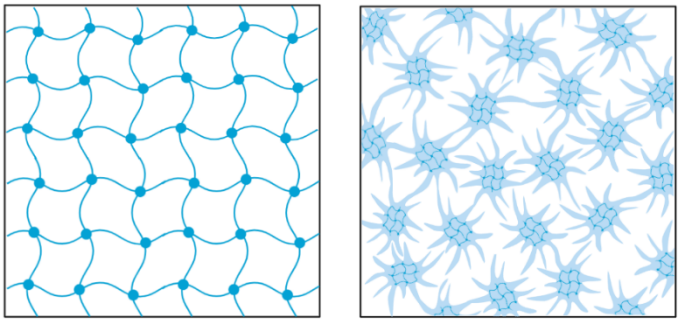

Figure 7. Representative images of gel structures. (Bartlett et al., 2020) Hydrogels undergo cross-linking to form polymer chains with tight junctions, resulting in a stable gel. (Right) Reversible or “fluid” gels contain pockets of tightly connected polymers with weak interaction between them. In static conditions, this resembles a permanent gel but upon application of sheer force, these weak bonds are broken and the gel becomes fluid.

injectable hydrogels with pores ranging from 0.5 to 50 µm (Broguiere et al., 2019). This methodology enables cell friendly generation of interconnected pores after injection, lending the system to use for extrusion systems such as bioprinting.

Approaches outlined here often enable physical separation of solid and liquid phases, enabling greater diffusion of biochemical factors. This physical entrapment of factors of interest (i.e. cytokines, growth factors, proteins) within hydrogels is a common method utilised by researchers to expose cells to guidance cues, relying on passive diffusion. Diffusion therefore relies upon physical and mechanical features of the hydrogel such as pore size, surface area etc. (He et al., 2020). Researchers often utilise this approach to mimic aggregation of soluble factors (e.g. amyloid, tau) in disease states (Fernández Farrés et al., 2014, Ranjan et al., 2018).

Environmental cues within hydrogels for CNS modelling include not only the presence of biochemical molecules (growth factors, proteins, small molecules) and bulk material properties (stiffness, conductivity, porosity), but also more complex heterogeneous aspects such as multicomponent structuring, dynamic or stimuli-responsive properties, and multiscale spatiotemporal topographical patterning to modulate cell behaviour.

1.4.2.3. Chemical Modification

Biomaterials often require modification in order to encompass the physical (e.g. structural, architectural, mechanical etc.) and biochemical cues necessary for biomimicry of *in vivo* tissue environments. While natural polymers, such as collagen or HA, possess intrinsic advantages as tissue culture biomaterials, modification of synthetic polymers allows for increased biological function (Almany and Seliktar, 2005). Chemical modification of natural polymers enables better control over physical characteristics e.g. methacrylation of gelatin polymer to enable photopatterning and bioprinting (Mirek et al., 2023, Nichol et al., 2010, Pereira et al., 2023, Xu et al., 2020).

Modification can occur by direct binding or indirect conjugation of binding domains, via “click chemistry” (Chimene et al., 2020, Jensen et al., 2018, Palmese et al., 2019, Willerth, 2017, Mauri et al., 2016). Recent work by Garrido *et al*. (2023) took this further, inducing anisotropic patterning of stiffness-degradation profiles by utilising a dual-crosslinking approach (Garrido et al., 2023). Barros *et al*. integrated functional proteins into a hydrogel via the addition of an N-terminal agrin domain, exploiting high affinity interactions between laminin and N-terminal groups. Biopolymer networks comprised of polysaccharides often possess negative carboxyl groups (symbolized as COO^-), which can interact with positively charged amino groups on proteins, forming a strong covalent peptide bond between the two groups (Barros et al., 2019). Mauri *et al*. demonstrate that some chemical cross-links, including ester or hydrazone bonds,

are not always stable enough to prevent degradation (Mauri et al., 2016). Alternatively, researchers may choose to exploit chemically or enzymatically degradable cross-links to create dynamic 'smart' materials possessing controlled release systems capable of guiding cell processes such as migration that rely on spatiotemporal heterogeneity of environmental cues (He et al., 2020, Mantha et al., 2019, Palmese et al., 2019, Wei et al., 2019, Willerth, 2017). Possibilities for chemical modification of hydrogel biomaterials are innumerable, limited only by choice of polymer and the requirements necessary for specific application (Xu et al., 2018).

1.4.2.4. Functionalisation

Functionalisation, in the broadest sense, equips a system with increased functionality. Within tissue engineering, the term functionalisation often refers to introduction of additional components within a culture system or biomaterial in order to realise additional functionality. Chemical biofunctionalisation relies on covalent binding of biological factors, such bioactive proteins to promote cell adhesion or mimic disease states of the ECM. Compared to physical entrapment or addition of soluble biologically active factors, this approach prevents leaching of unbound molecules from the hydrogel biomaterial.

Chemical modification becomes increasingly important when ligand interaction relies on specific arrangement of cytoskeletal proteins; clustering of focal adhesions and transmembrane integrins will influence cell responses via activation of intracellular signalling cascades (Abdeen et al., 2016). When looking to incorporate elements within a hydrogel, the method of cross-linking the functional group to the solid-phase polymer network must be adequate to prevent temperature/pH/enzymatic hydrolysis, with physical entrapment of proteins within the gel often failing to ensure long-term retention. One method of controlling retention kinetics is modification of hydrogel pH, encouraging retention of growth factors via promotion of electrostatic or van der Waals interactions (He et al., 2020). Advanced methods of biofunctionalisation look to generate (spatio)temporal patterns of biofunctional features known to influence cell behaviour and tissue formation, such as protein gradients (Section 1.4.2.6) (Primo and Mata, 2021).

Functionalisation of hydrogels with additional ECM proteins or growth factors allows for creation of biomimetic scaffolds that promote cell-material interaction (Chimene et al., 2020, Willerth, 2017, Zhu and Marchant, 2011). Incorporation of ECM proteins and binding peptides provides both structural and functional support to cells, acting to sequester additional cell-secreted ECM components and thus better recreate the native cellular environment (Dobre et al., 2021, Tomaszewski et al., 2021). For example, development of HA-based hydrogels functionalised with dopamine are shown to bind and retain BDNF *in vitro* (Samanta et al.,

2022). An underestimated factor when carrying out chemical modification of hydrogels is spacing of functionalised components, with optimal spatial patterning of components such as adhesion proteins vital for promoting cell-ligand interaction and ultimately adhesion (Abdeen et al., 2016). Integration of proteins or small peptides (Laminin/IKVAV, fibronectin/RGD) is shown to promote attachment and survival in neuronal tissue engineering (Barros et al., 2019, Dobre et al., 2021, Farrukh et al., 2017, Fonseca et al., 2020, Koivisto et al., 2017, Lozano et al., 2015, Long et al., 2020, Li et al., 2018, Perera et al., 2019, Kapr et al., 2021). IKVAV is known to bind several cell membrane integrins (Aydeger et al., 2023); specifically β1-integrins found within focal adhesions, promoting differentiation to neuronal phenotypes (Farrukh et al., 2017).

Inclusion of CNS-specific laminin isoforms is one method utilised by researchers to imbue improved adhesion characteristics of hydrogels for neural culture (Dragunow et al., 2000, Hartmann et al., 2023). Hartmann *et al.* incorporated the L111 isoform of laminin within alginate hydrogels, supporting neural network formation and activity up to 206 days in culture; with L111 hydrogels showing increased network activity, synchronicity and maturation compared to 2D and non-functionalised alginate controls (Hartmann et al., 2023). Interestingly, the L111 isoform is not commonly found in the adult CNS, but is known to guide neurite extension *in vitro* via integrin signalling and downstream activation of C-Jun (Dragunow et al., 2000, Weston et al., 2000). The 511 isoform of laminin in suggested to display greater CNS-specificity (Hirano et al., 2021). Research has gone on to show that isoforms containing the α-5 chain are superior support to neuronal networks *in vitro* (Hyysalo et al., 2017). Importance of the α-chain of laminin is exemplified by the fact that both RGD and IKVAV sequences are found here (Tashiro et al., 1989).

Another protein that holds great potential when creating models of brain tissue is reelin. This protein holds great promise as a functional element of neural development models, as it is heavily implicated in neuronal migration and cortical organisation (Frotscher, 2010), due to association with increased tau tangles and abnormal ApoE signalling pathways (Liu et al., 2013). This demonstrates the capability to create not only tissue-specific hydrogel scaffolds, but also induction of disease-specificity.

HA however is found within ECM throughout the body, however HA polymers specifically do not promote cell binding and can even inhibit neurite extension (Rauti et al., 2020). Perera *et al.* chemically functionalise HA hydrogels with short peptide sequences found in laminin via covalent binding; inclusion of Leucine-arginine-glutamic acid (LRE) peptide alongside IKVAV sequences results in cumulative cell binding effects, as LRE promotes behaviours such as axon guidance that are not stimulated by IKVAV (Perera et al., 2019). Interestingly, chemical

modification of HA occurs during inflammation under physiological conditions, whereby concentration increases and covalent attachment of plasma proteins alters biophysical characteristics of the polymer network (Cowman et al., 2015). In this respect, chemical functionalisation may be a useful avenue for inducing dysfunction or disease states of ECM.

The synthetic nature of PEG means limited protein binding sites exist for cellular attachment, necessitating the need for functionalisation (Choi et al., 2019). Research has shown functionalisation of PEG hydrogels with laminin promotes neural cell proliferation and neurite extension (Barros et al., 2019, Li et al., 2018). With Li *et al.* also showing that tethering of neurogenic differentiation factors (such as interferon-γ) support NSC differentiation without the need for additional media supplements (Li et al., 2018). In an alternative approach, PEG was utilised as a crosslinker for generation of IKVAV-functionalised hydrogels for neural culture (Long et al., 2020). Immobilisation of various proteins on PEG surfaces via generation of gradients within microfluidic systems is suggested as a means for production of overlapping parallel and orthogonal gradients of functional components (Cosson et al., 2009). Such elaborate techniques may be invaluable when looking to incorporate synthetic PEG polymers within hydrogel constructs for neural tissue engineering.

1.4.2.5. Multicomponent Hydrogels

Dynamic heterogeneous hydrogels require increased complexity and multiple components to enhance biophysical functionality of the material. Hybrid materials address limitations of homogenous hydrogel scaffolds, improving the range of applications (Liu et al., 2019, Palmese et al., 2019). As naturally occurring ECM is comprised of a multitude of polymeric networks at various scales, this suggests that hybrid multicomponent frameworks are the most promising avenue when creating biomimetic scaffolds for tissue engineering (Palmese et al., 2019).

Hybrid hydrogels extend beyond mixing of polymers and crosslinking approaches, to inclusion of multiple materials such as fibrillary, granular, crystalline and particulate components. Granular features have shown to support infiltration of cells and vascularisation, a vital consideration when we consider the CNS to be a highly vascularised tissue (George et al., 2019). Conductivity is another important consideration for CNS biomaterials. Inclusion of carbon components (crystals, nanotubes, wires, sheets, nanoclays) improves conductivity and promotes network functionality (Boni et al., 2018, Chimene et al., 2020, Koivisto et al., 2017, Liu, 2018, Tiwari et al., 2020), and have been shown to regulate cellular differentiation and network stabilisation (Sood et al., 2019, Trujillo et al., 2019). Inclusion of conductive components enables integrated analysis of neuronal network activity (Castiaux et al., 2019).

Several studies have employed a combination of concurrent biophysical features such as electrical and mechanical stimulation, to produce dynamic culture systems capable of

promoting neural alignment and neurite extension (Magaz et al., 2021, Shahin-Shamsabadi and Selvaganapathy, 2020). Stimuli-responsive hydrogels respond to chemical or physical stimuli, including light, magnetic/electric fields, shear forces, temperature, pH, ions, chemicals, drugs, enzymes etc. (Mantha et al., 2019). Through modification of stimuli, it is possible to fine-tune mechanical properties such as stiffness, swelling, gelation and degradation kinetics. The type of stimuli and response utilised is highly dependent upon the desired application; however, temperature and pH are highly investigated, as these stimuli possess the greatest biological relevance (Mantha et al., 2019). Dynamic 'smart' biomaterials also provide spatiotemporal control over delivery of biochemical cues, with chemically and enzymatically degradable cross-links enabling a range of applications (Fonseca et al., 2020, He et al., 2020, Palmese et al., 2019). Alternatively, drug-releasing agents such as nanoparticles or gel droplets can be included within hydrogel formulations to function as controlled release systems (He et al., 2020). Multiphase release systems are needed, to ensure sequential and spatiotemporal delivery of biochemical cues similar to naturally occurring tissues *in vivo* (Wei et al., 2019). Ultimately, development of hydrogels with a combination of multiphase, dynamic and stimuli-responsive properties is the ideal approach to modelling complex living tissues *in vitro* (Shahin-Shamsabadi and Selvaganapathy, 2020).

1.4.2.6. Patterning of Hydrogels

Biochemical and structural patterning of hydrogel scaffolds across multiple axes provides micro to nano scale control over surface topography, guiding cellular processes and ultimately tissue formation (Coppari et al., 2021, Merryweather and Roach, 2017). A recent review by Primo *et al*. categorise patterning approaches according to the technique utilised; light-based, chemical, microfluidic, printing or non-contact forces (i.e. self-assembling peptides) (Primo and Mata, 2021). Physical patterning of cell substrates is a powerful tool for influencing cell behaviour, with microscale variation in substrate rigidity and size of patterns implicated in cell lineage commitment (Biggs et al., 2017, Knight et al., 2018). Fabrication techniques such as electrospinning of fibrous scaffolds or structural patterning of parallel grooves have shown to mimic *in vivo* ECM topographies to induce axis alignment (Boni et al., 2018, Coppari et al., 2021, Roach et al., 2013). Inducing desirable cell shape via patterning of biomaterials is shown to induce specific cell behaviours such as arrangement of cytoskeletal proteins, but also epigenetic modifications (Abdeen et al., 2016). Lithographic techniques enable creation of multiscale physical features, providing biophysical (and thereby biochemical) signals to cells (Primo and Mata, 2021). This is important when we consider neuronal axons tend to grow along ridges on 2D nano-patterned hydrogel scaffolds, indicating a preference for adhering to elevated surfaces, although the underlying mechanism is not yet understood (Madhusudanan et al., 2020). Bioprinting offers a customisable and controllable tool for physical patterning of

hydrogels in 3D (Section 1.4.1.2), overcoming limitations with 2.5D approaches such as soft lithography. Printing approaches enable defined spatial distribution and wider patterning within the printed construct, while specialised bioinks provide localised delivery of biochemical signals. 3D printing technology is favoured for patterning of hydrogels due to the potential for printing elaborate architectures, versatility of ink materials and ever-increasing precision leading to increased resolution of printed features (Primo and Mata, 2021).

Extrusion bioprinting is one 3D approach favoured for its ease of use and customisable nature, however limited resolution and bioink requirements (printability vs mechanical suitability etc.) limits implementation (Ozbolat and Hospodiuk, 2016). Extrusion-based approaches may be unable to replicate minute architectural patterning seen within native brain tissue, however this approach has shown to be beneficial in recreating bulk tissue features, such as laminar layering seen within the cortex *in vivo* (Yan et al., 2024). Extension of the model to include patient-derived astrocytes and neurons provided valuable insight into neurodegenerative disease (Yan et al., 2024). One approach to improving resolution of extrusion-printed features is inclusion of a support phase such as the fluid-gel support bed in SLAM bioprinting (Section 1.2.4.1., Figure 3), in order to limit distortion of printed patterns. Methods of supporting 3D bioprinted constructs (such as SLAM) become increasingly relevant when looking to pattern complex structures, such as highly vascularised tissue (Budharaju et al., 2024). Such supportive approaches may provide neural tissue engineers with an opportunity to achieve high-resolution patterning of extrusion-bioprinted constructs without compromising on mechanical properties (Brunel et al., 2022).

In order to achieve high-resolution patterning at the microscale, researchers have modified and built upon existing printing approaches. Modifications include ultrasound-assisted bioprinting in order to exert control over single cell alignment within extrusion-bioprinted alginate scaffolds (Chansoria and Shirwaiker, 2019). . Abelseth *et al*. developed a modified extrusion bioprinting system, whereby microfluidic patterning of bioinks enabled 3D bioprinting of iPSC-derived neural aggregates (Abelseth et al., 2019). Combination of melt electro-writing and extrusion printing into a singular biofabrication process enabled production of gelatin hydrogels with defined spatial distribution of cells and melted polycaprolactone fibres (de Ruijter et al., 2019). Alternatively, light-based approaches, such as two-photon polymerisation, allow better resolution of physical patterns on the micro to nanoscale; however often require transparent materials (Applegate et al., 2015, Liao et al., 2020, You et al., 2018). Another novel combinatorial approach by Lee *et al*. combines digital light projection 3D-printed micromesh scaffolds with sequential hydrogel patterning to produce mesoscale hydrogel structures for various tissue-engineering applications (Lee et al., 2022). Research highlights a dual-crosslinking approach, chemical then light-based, to pattern mechanogradients within

hydrogels (Garrido et al., 2023, Khoshakhlagh and Moore, 2015). Literature here may suggest that 3D bioprinting techniques should be optimised to ensure incorporation of multiscale cues, both biophysical and biochemical in nature.

Photopatterning is also a well-established method of patterning biologically active growth factors, proteins and peptides into hydrogel scaffolds (Primo and Mata, 2021, Yu et al., 2020, Paone et al., 2023). Researchers are now beginning to recognise the power of UV light when controlling shape and distribution of stiffness changes, simultaneous to functionalisation; the combination of variable stiffness and laminin 511 functionalisation allowed for tailored differentiation of iPSCs towards all three germ fates (Wang et al., 2024). Alternatively, chemical modification (Section 1.4.2.3) of precursors enables production of hydrogel constructs with precise spatial distribution of physiomechanical or biochemical factors. A specific example of chemical modification to pattern hydrogels is the incorporation of high-efficiency click reactions; thiol-ene click reactions can be exploited produce distinct spatial patterns, of fluorescent dyes or proteins, within hydrogels (Yigit et al., 2011). Wang et al. developed an extrusion bioprinting system whereby hydrogels comprised of interpenetrating networks were modified to contain dynamic covalent crosslinks, enabling further crosslinking (photostiffening) or thiol-ene functionalisation (photopatterning) (Wang et al., 2018). Photopatterning and chemical modification has also been used in conjunction to support formation of segregated cell populations and microchannels within a microfluidic device to study network connectivity (Kamudzandu et al., 2019).

Point source diffusion methods, such as sink and source systems, allow for diffusion of soluble factors across a hydrogel scaffold in order to study the effect of soluble molecule gradients on cell behaviour (Xu et al., 2018). Creation of an immobilised gradient, i.e. proteins covalently bonded to the hydrogel solid-phase network, allows for investigation of cellular behaviour in response to specific concentrations of immobilised substances. Methods of creating substrate-bound gradients in hydrogel scaffolds often rely upon soluble diffusion of the substance followed by an additional polymerisation step to “trap” molecules within the hydrogel structure (Ricoult et al., 2015). Entrapment of hydrogel matrices’ within a microfluidic device as a means to generate protein distribution gradients demonstrated great success, enabling formation of multiple overlapping gradients by exploiting differential binding schemes (Cosson et al., 2009). Microfluidics enable creation of devices with microchannels and segregated compartments (Fernandes et al., 2021, Liu et al., 2019); as well as enabling tight control over microscale features via precise biochemical patterning of organoids and hydrogel scaffolds (Fedorchak et al., 2021, Primo and Mata, 2021).

Heterogeneous distribution of such physical and biochemical cues within hydrogels is invaluable when investigating biomimetic gradients on cell behaviour (Senior et al., 2019, Xin et al., 2019). Traditional methods of incorporating biochemical or mechanical cues take an 'all or nothing' approach, failing to account for interconnectedness of variables and synergy of cues such as microtopographies and biochemical gradients (Kundu et al., 2013, Mumford et al., 2020). Researchers are beginning to recognise the power of combining various approaches to create multicomponent, versatile and spatiotemporally dynamic culture systems (Fernandes et al., 2021, Liu et al., 2019, Yu et al., 2020). Such advanced systems are capable of recreating some of the compositional and architectural complexity of *in vivo* tissues, whilst also providing insight into the power of interconnected environmental cues on cell behaviour.

1.4.2.7. Hydrogel Mechanics

Homogenous tuning of scaffold stiffness is suggested a means to promote desired phenotypes (Baruffaldi et al., 2021); soft (~1 kPa) hydrogel substrates promote neurogenesis, whereas differentiation of glial cells is favoured on materials with an elastic modulus ~1–10 kPa (Leipzig and Shoichet, 2009, Merryweather and Roach, 2017). Utilising hydrogel materials with tuneable stiffness would also enable recreation of various brain regions and disease states. Modulation of scaffold stiffness is suggested to manipulate the secretome of encapsulated cells, further supporting the concept of mechanical control of cell fates (Nasser, 2018).

Generation of mechanogradients is suggested as an additional means to influence cell behaviour (Xia et al., 2017, Xin et al., 2019). Xin *et al*. employed microfluidics for reliable production of continuous mechanogradients, revealing critical stiffness thresholds for processes such as cell spreading (Xin et al., 2019). Hybrid hydrogels, comprised of blended polymers, enables even greater tailoring, i.e. altered mixing ratios to modulate stiffness, stress-relaxation, or biofunctionality (Liu et al., 2019, Moxon et al., 2019, Palmese et al., 2019, Kapr et al., 2021). Moxon *et al*. demonstrate that inclusion of collagen fibrils within alginate hydrogels acts dually to support neuronal culture by increasing stiffness whilst also improving bioactivity. However, alginate has been shown to lose mechanical integrity in physiological conditions, due to ion exchange reversing the cross-linking process (Cooke et al., 2018). Photopatterning is also suggested as a means of introducing internal structuring or localised mechanical changes within hydrogels, with UV-induced patterning shown to enable greater resolution of geometries (Palmese et al., 2019).

Hybrid hydrogels have become increasingly attractive when considering the limited biocompatibility of conductive polymers (Boni et al., 2018, Lee et al., 2020b, Magaz et al., 2021). Inclusion of conductive elements is important as inhibition of electrical signalling by

biomaterials can impede nervous tissue function (Magaz et al., 2021). Stress-relaxation, whereby internal stress force reduces over time as the material settles under constant strain, is an important feature of a polymer network, with relaxation shown to influence cell spreading independently of stiffness (Chaudhuri et al., 2016). Porosity is also an important consideration when guiding cellular migration and neurite outgrowth; although random interconnectedness does not guide neuronal network formation and the relevance of pore size and shape is still not fully understood (Broguiere et al., 2019, George et al., 2018, Merryweather and Roach, 2017). Modulation of stiffness, porosity, stress relaxation and degradation of the substrate is invaluable when guiding cell behaviour and tissue functionality (Chimene et al., 2020, Eltom et al., 2019).

It is vital to recognise that such features are interconnected and often reliant upon one another; Engler *et al*. sparked debate when first reporting stiffness-mediated differentiation, with literature of the time focusing upon intrinsic differentiation factors (e.g. genetics) or biochemical stimulation (e.g. growth factors) within the stem cell niche . Engler et al. demonstrated that stiffness or elasticity of ECM directly affects stem cell differentiation; specifically, a range of soft, intermediate and rigid matrices were shown to favour differentiation toward adipocyte, muscle and bone, respectively (Engler 2006). Following this discovery, biologists began to acknowledge the underreported importance and interplay of physical properties when guiding stem cell function and fate (Even-Ram et al., 2006, Clause 2010, Engler 2006). Researchers explored how mechanical properties, primarily stiffness and porosity, could influence biological processes such as protein tethering and ultimately cellular differentiation (Trappmann 2012). Protein tethering refers to the process by which proteins are anchored to the ECM (Qu and Ortoleva, 2008, Wu and Sun, 2006). Further research by Wen *et al*. demonstrated that protein tethering and porosity indeed regulate stem cell differentiation, however results implied that substrate stiffness regulates differentiation independently of tethering and porosity (Wen et al., 2014).

While porosity is necessary to facilitate encapsulation of cells via mass transfer of metabolites and waste products, cell processes are implicated to have specific porosity requirements (Loh and Choong, 2013). Porosity and pore interconnectivity allows for cell encapsulation, migration and vascularisation (Annabi et al., 2010, Lien et al., 2009). Surprisingly, pore size has also shown to influence the secretome of encapsulated cells; smaller pores within gelatin hydrogels resulted in a tendency towards cell growth rather than ECM secretion, resulting in over confluence during differentiation protocols (Lien et al., 2009). Tissue engineers could capitalise on this feature, utilising larger pore size to promote ECM deposition and enable a cell-led method of biomaterial functionalisation.

Interplay of mechanical features becomes important when we consider that increasing stiffness can reduce porosity, influencing cell migration and nutrient exchange (Annabi et al., 2010). Conversely, highly porous hydrogels might be less stiff, which could influence cell differentiation and structural support. Therefore, a balance must be struck in order to optimise the biomaterial for desired outcomes. For example, if stem cell differentiation is the primary desired outcome of a biomaterial, porosity may be less important than stiffness, as the latter is found to be more important when inducing differentiation (Pek et al., 2010, Wen et al., 2014).

Researchers now recognise the "sophisticated macromolecular machinery" responsible for converting mechanical stimuli into biochemical signals (Di et al., 2023, Oses et al., 2023, Saraswathibhatla et al., 2023). As such, current theories of stem cell differentiation must acknowledge the complex interplay between mechanical properties of the ECM, genetic and epigenetic factors, biochemical cues (from soluble and bound factors), and interactions within a stem cell niche. This multi-scale (e.g. molecular to cellular to organ-specific) integrated perspective reflects advances in molecular biology, biomechanics, and systems biology, providing a more nuanced understanding of how stem cells make lineage decisions and develop into specialized cell type. Tissue engineers must consider all of these factors when developing advanced biomaterials capable of replicating biological and mechanical signals found within the native CNS.

Development of biomaterials for CNS modelling is hindered by the fact that soft tissues display unusual mechanics; the brain does not behave as a liquid or solid, rather it has viscoelastic properties commonly seen in highly hydrated tissues comprised of heterogeneous polymer networks (Libertiaux and Pascon, 2009). The lack of fibrillary ECM components within the CNS results in a reduced stiffness compared to other tissues within the body (Kim and Choi, 2019). Furthermore, spatiotemporal variation in architecture and composition of the CNS leads to inconsistencies when measuring mechanical stiffness of the tissue; however, there is a broad estimate of ~0.1-10 kPa (Handorf et al., 2015, Kim and Choi, 2019, Pogoda et al., 2014, Sartori et al., 2014). Reductions in stiffness are also observed in grey matter when compared to white matter and in disease states when compared to healthy controls (Budday et al., 2015, Murphy et al., 2011). Interestingly, gender differences are observed when looking at brain tissue stiffness, likely related to differences in neuron/glia ratios and age (Kim and Choi, 2019).

1.4.2.7.1. Rheological properties

One method of characterising the mechanical properties of “soft solid” materials such as hydrogels is rheology. Rheology is the study of deformation or flow, usually of liquids or gasses but also extends to “soft solids”. Eugene Bingham, inspired by the Greek aphorism “everything flows”, coined the term Rheology in the early 1900s (Bingham, 1930). He described that

measure of flow is highly dependent upon timescale, for instance we can readily observe the flow of water, whereas flow of mountains would require thousands of years. The need for this rheological perspective came about following identification of shortfalls in classical laws used to explain liquid and solid behaviour. Newton's law and Hooke's law define characteristics of true liquids and solids respectively; however, such linear approaches fail to explain the behaviour of materials with complex microstructures. Hydrogels display viscoelastic properties in-between that of an ideal Newtonian viscous liquid and a Hookean elastic solid. Here polymeric networks exist alongside the liquid phase, with hydrostatic pressure producing a monolithic structure with increased viscosity and elasticity, causing solid-like behaviour of the viscoelastic material.

In order to understand visco-elasticity, one must understand key definitions and the overlap between viscous and elastic properties. Deformation is defined as the process by which a body of material changes in response to imposed forces (Reid, 1973). Rheological assessment of "soft solid" mechanical properties relies on analysis of stress and strain. Despite the fact that these terms are often synonymous in everyday life, when considering mechanical properties of a material these two terms are distinctly different.

Stress is the amount of applied force per unit area:

$$\sigma = \frac{F}{A}$$

where σ is the stress (Nm^{-2}), F is the applied force (N) and A is the area (m^2).

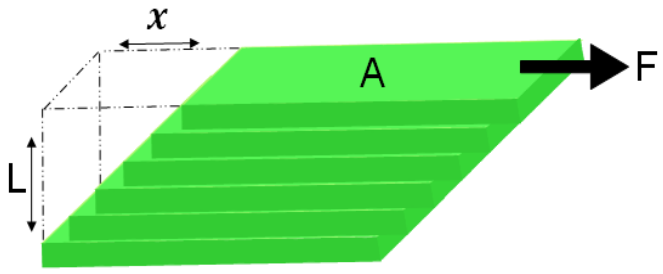

Figure 8. Shear flow occurs within liquid-like materials exposed to forces or pressure. As the uppermost layer of a sample responds to shear force and the bottom layer is unmoved, a displacement gradient forms (γ).

Strain is the degree of deformation of a material due to stress (Kugler et al., 2018). This is shear strain and its equation is given as:

$$\gamma = \frac{x}{L}$$

where γ is the strain, x is the change in length and L is the original length.

Shear rate $(\dot{\gamma})$ is the rate of deformation applied to a material, given as S^{-1}, shown below:

$$\dot{\gamma} = \frac{\mathrm{d}\gamma}{\mathrm{d}t}$$

where $\mathrm{d}\gamma$ is the change in strain and $\mathrm{d}t$ is difference in time (s).

The measure of elasticity for a solid is defined by the ratio of stress to strain, with fluid viscosity defined by the ratio of stress to rate of strain (or flow rate) (Janmey and Schliwa, 2008). It is important to note that the type of force exerted on a material will impact the way stress is measured; while most stresses act perpendicular to a material interface, shear stresses act in a manner parallel to the material surface (Kugler et al., 2018). Viscosity is the propensity of a fluid to resist flow following the addition of force, or put simply a liquids resistance to pouring, with this behaviour defined by Newton's law. Here deformation responds to loss of structure within the material. Newtonian liquids demonstrate constant ratio between shear rate and stress at a given temperature and pressure, however very few liquids display this pure Newtonian behaviour. This constant is defined as shear viscosity or η (Pa.s), where σ shear stress (Nm^{-2}), and $\dot{\gamma}$ is shear rate (S^{-1}):

$$\eta = \frac{\sigma}{\dot{\gamma}}$$

Conversely, elasticity is defined with Hooke's law where deformation corresponds to energy storage within the material. Here *F* is applied force (N), proportional to the amount of stretch or *k* (m) and displacement constant or *x* (N/m):

$$F = kx$$

A truly elastic material will deform with a given strain corresponding to a given stress, returning to its original shape following removal of this stress.

The stiffness of a solid material is described with Young's modulus, defining the relationship between stress and strain of a material undergoing uniaxial deformation. Young's modulus (*E*) can be calculated by subjecting a material to uniaxial stress and measuring elastic deformation (Vila-Parrondo et al., 2020) in the linear region of the stress–strain curve:

$$E = \frac{\sigma}{\gamma} = \frac{F/A}{\Delta L/L} = \frac{FL}{A\Delta L}$$

where σ is uniaxial stress (force over surface), γ is strain, F is force exerted (uniaxial stress), A is the area perpendicular to the applied force, ΔL is change in length (a positive value for material stretching (along the axis of applied force) and a negative value for compression) and L is the original material length.

These equations assume a linear relationship between strain and stress, but in real life this assumption does not hold, as many materials often possess solid and liquid features (Guimarães et al., 2020). Viscous and elastic properties are therefore dependent upon amount and rate of stress; application of low stresses such as gravity enable viewing of stereotypical liquids and solids, however when engaging materials in a range of stresses during rheological testing, it is possible to view some liquid-like behaviour of solids and vice versa. Therefore, we conclude elastic and viscous moduli are interconnected and behave as functions of time and force.

Figure 9. Behaviour of Newtonian vs non-Newtonian (shear-thickening and shear-thinning) fluids. Differential flow behaviour of fluids dependant on the ratio of shear stress to rate. Image available in the public domain, CC0.

The term visco-elasticity is a general term used to describe the interrelated elastic and viscous properties of a material. This is especially relevant for biological materials, as complex biological microstructures display both liquid and solid behaviour, due to coexisting liquid and solid components. To differentiate between elastic and viscous behaviour, a series of dynamic mechanical tests are performed. Here oscillatory shear force is applied to the material and the resulting deformation measured, in order to determine the relationship between stress and strain at various time scales and frequencies. Such oscillatory tests are known as small deformation rheology. The favoured initial test for viscoelastic fluids with high water contents, such as hydrogels, is an amplitude sweep. This test determines the minimum and maximum oscillatory force required to induce flow without total deformation of the material. This analysis of yield behaviour allows for the storage modulus G' and the loss modulus G'' to be plotted against deformation. Following an amplitude sweep, the linear region before deformation is taken forward for a frequency sweep. This linear viscoelastic region (LVR) occurs at low shear, where stress and strain are proportional, until the yield point is reached and the material exhibits non-linear behaviour as it begins to irreversibly deform. Frequency sweeps enable quantification of phase angle and complex modulus G*, which better describes the visco-

elastic properties of a material at rest. When analysing visco-elastic materials, if G' exceeds G" the material is defined as elastic dominant or viscoelastic solid, with the inverse meaning the material is a viscous dominant material or viscoelastic liquid.

Very few materials exhibit Newtonian behaviour, whereby the ratio of shear stress to shear rate is constant. Fluids possessing complex microstructures behave differently, with various other flow behaviours seen in these materials. Power-law fluids, which approximately follow the Ostwald-de Waele power law, are fluids that exhibit a non-linear change in viscosity, with thinning or thickening behaviour reliant upon fluid consistency and degree of non-Newtonian behaviour. The power law can be written as an equation where shear stress (τ) can be calculated from shear rate ($\dot{\varepsilon}$), consistency index (K) and flow behaviour index or viscosity (η):

$$\boldsymbol{\tau} = K\dot{\gamma}^{\eta}$$

Where n<1, fluid presents as shear thinning, with n>1 demonstrating shear thickening (Chen et al., 2017). Shear thinning materials are more common and better understood, with decreased viscosity alongside increased shear rate/shear stress. Degree of thinning is related to amount of microstructure alteration or alignment of polymers; exposing the material to shear forces causes greater alignment of polymers or flocculent breakdown. This alteration of polymer network structure allows for more liquid like behaviour. Thixotropic behaviour refers to time dependency of shear thinning, with decreased viscosity at a given stress over time.

Characterisation of "soft solid" biomaterials via methods such as rheology is invaluable in order to understand the power of biophysical cues in guiding development of engineered tissues. It is also vital to investigate alternative mechanical features such as porosity, viscosity and degradation to better understand behaviour of multicomponent living tissues both *in vivo* and *in vitro.* Identifying and exploiting such environmental cues will allow for creation of model systems with superior biological relevance, alongside improving reliability and reproducibility. The influence of polymer choice and functional modification explored further in chapters 4 & 5.

2. General Aims & Objectives

Current tissue engineering approaches fail to achieve structural complexity seen *in vivo,* despite improved funding into multidisciplinary research, due to a variety of practical and cultural barriers. For example, traditional university infrastructure separates social sciences such as psychology from biology or engineering courses, where students may actually benefit from sharing of different perspectives to an interdisciplinary problem… how to engineer functional neural tissue *in vitro*? Tissue engineers bridge this gap by combining multiple approaches & techniques in order to achieve advanced complexity & functionality of the final construct.

This project aims to develop a hydrogel biomaterial with advanced mechanophysical relevance to the CNS, utilising rheological investigation and statistical analysis to optimise mechanical features whilst promoting biological compatibility & activity.

The aim of developing biomaterials for CNS modelling is broad, so in order to realise this goal, specific and achievable objectives were set:

Chapter 4. Biomaterial Selection

1. **To explore existing hydrogel polymers and assess their suitability for neural tissue engineering, by critical evaluation of the literature & preliminary assessment of biocompatibility via SH-SY5Y cell culture.**

Chapter 5. HAMA Optimisation

2. **To optimise composition of HAMA hydrogels via biocompatibility testing of HAMA components on neural cell (Neural Precursor Cells & astrocytes) culture & rheological analysis of various HAMA hydrogels.**

Chapter 6. Functionalisation and Structuring of HAMA hydrogels

3. **To explore functional proteins for guiding adhesion of Neural Stem Cells in 2D, via immunocytochemistry and fluorescence microscopy.**
4. **To evaluate extrusion bioprinting techniques for structuring of HAMA hydrogel constructs with defined geometries, via 3D cell culture of SH-SY5Ys and rheological analysis.**

3. Materials & Methods

3.1. Cell Culture

Incubation here means humidified incubation at 37°C, 5% CO_2. Cells were monitored daily and confluency assessed by phase contrast microscopy images using the EVOS XL Core Imaging System (Life Technologies).

3.1.1. Cell culture coatings

For typical Neural Precursor Cell (NPC) and Astrocyte culture (Methods 3.1.4-7), plastic 6, 12 or 24-well plates (Corning-Costar, USA) and 13 mm glass coverslips (VWR, UK) were coated with diluted poly-L-ornithine (Sigma-Aldrich, UK, P4957) to give a working concentration of 20 µg/mL in dH_2O. Following 24-hour incubation, vessel surfaces were washed twice with sterile H_2O (Sigma-Aldrich, UK, W3500). Then Engelbreth-Holm-Swarm Laminin (L2020; Sigma-Aldrich, UK) was dissolved in sterile dH_2O to a final concentration of 10 µg/mL before coating and incubation overnight. Surfaces were incubated in PBS without Ca^{2+} or Mg^{2+} (Sigma-Aldrich, UK, D8537) at 37°C for up to 1 week.

For differentiation or co-culture studies, 13 mm round glass coverslips (VWR, UK) were coated with diluted poly-L-ornithine as previously noted. Laminin (Sigma-Aldrich, UK, L2020) was dissolved in sterile dH_2O to a final concentration of 20 µg/mL before coating and incubation at 37°C overnight. All coated surfaces were stored in PBS at 37°C within the incubator for up to 1 week prior to plating.

Alternatively, stock solutions of IKVAV peptides (GGIKVAVG or CCRRIKVAVLC, Neo Biotech, Generon, UK) were generated at 1 mg/mL; the GGIKVAVG peptide was suspended in PBS to aid dissolution whereas the CCRRIKVAVLC peptide or full-form Laminin (Sigma-Aldrich, UK, L2020) readily dissolved in H_2O. Both peptides were then dissolved in sterile H_2O to a final concentration of 20 µg/mL. All coated surfaces were stored in PBS at 37°C within the incubator for up to 1 week prior to plating. For iPSC culture, surfaced were coated with PORN prior to human recombinant vitronectin (ThermoFisher, USA, A14700) diluted 10 µg/mL in PBS without Ca^{2+} or Mg^{2+} for incubation at 37°C overnight. All coated surfaces were stored in PBS at 37°C within the incubator for up to 1 week prior to plating.

3.1.2. SH-SY5Ys

Cryopreserved SH-SY5Y cells were fast thawed in a 37°C water bath, allowing addition of media to the cell suspension in a 9:1 ratio. The suspension was then centrifuged for 5 minutes at 300 x g and the pellet resuspended in complete RPMI 1640 medium (Sigma-Aldrich, UK, R0883) containing 10% FBS (Sigma-Aldrich, UK, F0804) and 1% L-Glutathione (Sigma-

Aldrich, UK, G513), with a sample of the cell suspension taken for counting. Flasks (Corning-Costar, USA) were seeded at 20,000 cells/cm^2.

SH-SY5Y cells were grown in tissue-culture-treated planar T-flasks (Corning-Costar, USA) containing culture medium stored at 4°C and pre-warmed to 37°C before use. At 80% confluency culture media was removed and the flask surface gently washed with PBS without Ca^{2+} or Mg^{2+}, before the addition of 5 mg/mL trypsin (Sigma-Aldrich, UK, T4174) diluted 1:10 in PBS and incubated for 5 minutes. Following detachment of cells, media was added to neutralise the trypsin at a ratio of 3:1. Cell suspensions were then centrifuged for 5 minutes at 300 x g. The supernatant was then discarded and the cell pellet resuspended in pre-warmed complete media for reseeding at the desired density. Cells were monitored daily and confluency assessed by light microscopy.

3.1.3. NPCs

Human Neural Progenitor Cells (NPCs) (Axol Bioscience, UK, ax0013) were obtained via episomal plasmid reprogramming of CD34+ cells from the cord blood of a healthy newborn male here named Donor C. These are referred to as line 13 (L13) NPCs herein. Alternatively, NPCs were differentiated from human iPSCs also derived from the cord blood of a healthy newborn male (Axol Bioscience, UK, ax0015). These cells are referred to as line 5 (L5) NPCs herein.

Cells were fast thawed in a 37°C water bath, allowing addition of media to the cell suspension in a 9:1 ratio. The suspension was then centrifuged for 5 minutes at 200 x *g* and the pellet resuspended in media and a sample taken for counting. Cells were seeded at 50,000 cells/cm^2 onto pre-coated wells/slips (Method 3.1.1). Rock Inhibitor or Y27632 (HelloBio, UK, HB2297) was added prior to plating to a final concentration of 10 µM, and removed after 24-hours. FGF-2 (Axol Bioscience, UK, ax0047) was also added to cultures to a final concentration of 10 ng/mL to support expansion if needed.

NPCs were grown in Neural Maintenance Medium (NMM) and Supplement Kit (Axol Bioscience, UK, Ax0031). Medium was stored at 4°C and pre-warmed to room temperature (RT) before use. At 90%+ confluency culture media was removed and the vessel surface gently washed with PBS without Ca^{2+} or Mg^{2+}, before the addition of Accutase (ThermoFisher Scientific, USA, 11599686) to entirely cover the cell monolayer for 5 minute incubation. Following detachment, media was added to neutralise the Accutase at a ratio of 4:1. The cell suspension was then centrifuged at 200 x *g* for 5 minutes and the supernatant discarded. Resultant cell pellet was resuspended in neural maintenance media for seeding as above. Cells were passaged until passage 6/7.

3.1.4. Astrocytes

Astrocytes were differentiated from human iPSCs and frozen down at an early passage (Gift of Eric Hill, Aston University); Line 5 (line CRMi001-A (RRID:CVCL_1E75)), and Line 13 (HPSI1113i-podx_1) astrocytes are used herein.

Frozen astrocytic cells were fast thawed in a 37°C water bath, for the addition of media to the cell suspension in a 9:1 ratio. The suspension was then centrifuged for 5 minutes at 300 x *g* and the pellet resuspended in media and a sample taken for counting. Cells were seeded at 12,000 cells/cm^2 onto pre-coated wells/slips. Astrocytes were fed every other day with Astrocyte medium, 2% (v/v) foetal bovine serum and 1% (v/v) astrocyte growth supplement (all components from ScienCell Research Laboratories, USA).

3.1.5. Induced Pluripotent Stem Cells

Healthy iPSCs were obtained from (Axol Bioscience, UK, ax0015) following episomal plasmid reprogramming of CD34+ cells from the cord blood of a healthy newborn male. Frozen iPSCs were fast thawed at in a 37°C water bath, for the addition of media to the cell suspension in a 4:1 ratio. The suspension was then centrifuged for 5 minutes at 200 x *g* and the pellet resuspended in completed E8 media (ThermoFisher, USA, A1517001) supplemented with 10 µM Rock-Inhibitor (HelloBio, UK, HB2297), and removed after 24-hours. Care was taken to only triturate the pellet 1-3 times to retain aggregation of cells prior to plating. Cells were then fed daily with additional complete E8 media.

3.1.6. Immunofluorescence staining

3.1.6.1. 2D

2D immunocytochemistry required cell monolayer culture on 13mm round glass coverslips (VWR, UK) to enable handling. Prior to antibody staining planar samples were fixed with 4% (v/v) paraformaldehyde (PFA) in PBS with Ca^{2+} or Mg^{2+}, with samples exposed to equal parts mix PFA and media for 5 minutes RT, then 4% PFA only for a further 5 minutes. Samples were then washed twice with PBS Ca^{2+} or Mg^{2+} for 5 minutes, for immediate staining or storage in wells containing 0.1% sodium azide in PBS. Stored plates were sealed with parafilm and kept at 4°C for up to 1 week. Samples stored in sodium azide were washed twice with PBS before permeabilization.

Samples were permeabilised with 0.2% (v/v) Triton X-100 (Sigma-Aldrich, UK, X100) in PBS with Ca^{2+} or Mg^{2+} for 5 minutes on an orbital rocker at low speed of 5 RPM. Following permeabilization, samples were incubated with blocking buffer; 0.2% Triton and 2% (w/v) bovine serum albumin (Sigma-Aldrich, UK, A9647), for 1 hour on a rocker as previously. Cells

Primary	Expression Marker	Dilution	Source	Secondary
Anti-Nestin (Sigma-Aldrich, UK, 50501001)	Cytoskeletal Protein of Neural Precursor Cells	1:300	Mouse (10C2)	Donkey Anti-Mouse (Jackson ImmunoResearch, UK) Rhodamine Red (715-295-151) FITC green (715-095-151)
Anti βIII-tubulin or Tujj (Invitrogen, USA)	Neuronal Cytoskeletal Tubulin Protein	1:500	Mouse (2G7D4)	
Anti-Sox2 (R&D Systems, UK, MAB2018)	Neural Pluripotency	1:300	Mouse (245610)	
Anti-Oct4 (R&D Systems, UK, MAB1759)	Stem Cell Pluripotency	1:300	Mouse (240408)	
Anti-Pax6 antibody (BioLegend, USA, 901301)	Transcription Factor of Neural Precursor Cells	1:300	Rabbit (Poly19013)	Goat Anti-Rabbit (Jackson ImmunoResearch) FITC green (111-095-144) Rhodamine Red (111-295-144)
Anti-Ki67 (Abcam, UK, ab15580)	Proliferation	1:500	Rabbit	

Table 2. Primary and secondary antibodies for Immunocytochemistry staining.

were stained with up to two primary antibodies from different species, by suspending in blocking buffer at necessary concentrations (Table 2). Primary staining was left to occur for 1hr RT or overnight at 4°C. Samples were then washed for 5 minutes with blocking buffer, a minimum of 3 times, again on the rocker at low speed. From this point onward both antibodies and samples were protected from light. Cells were stained with secondary antibodies complementary to the species of the primary (Table 2), again by suspending in blocking buffer and adding to cells for 1hr RT or overnight at 4°C. Wash steps were again repeated three times, followed by an additional dH_2O rinse, prior to mounting. Coverslips were mounted onto glass slides, via inversion and placing onto a singular drop of Fluoroshield™ mountant containing DAPI (Sigma-Aldrich, UK, F6057). Samples were left to dry overnight before sealing with clear varnish and indefinite storage at 4°C.

3.1.6.2. 3D

Visualisation of cells within 3D hydrogel experiments was facilitated via the use of SH-SY5Ys transfected with fluorescent proteins (George et al., 2018). This approach enabled live imaging without the need for fixing of samples. This was supported via the use of stains such as ActinGreen™ (AlexaFluor™) 488 ReadyProbes™ Reagent (Thermofisher Scientific, USA,

R37110) for cytoskeletal actin, alongside Hoechst 333258 or NucBlue™ Live ReadyProbes™ Reagent (Invitrogen, USA, R37605) to enable visualisation of cell nuclei within hydrogel cytocompatibility experiments.

3.1.7. Quantification of Cell Viability

3.1.7.1. Manual Counting

For cell counting, a sample of cell suspension was mixed in a 1:1 ratio with 0.4% Trypan blue live/dead stain (Sigma-Aldrich, UK, T8154) and visualised using the EVOS microscope.

3.1.7.2. MTT Assay

3-(4,5-dimethyl-2-thiazolyl)-2,5-diphenyl-2H-tetrazolium bromide or MTT (Fisher Scientific, USA, 11312727) stock was created at a concentration of 2.5 mg/mL in sterile PBS and then syringe filtered through a 0.2 um pore sterile filter (Fisher Scientific, USA, 15206869), prior to storage at -20°C. Cells were exposed to stimuli, e.g. Photoinitiator or UV, prior to incubation. Media was then aspirated from wells before addition of MTT at a 0.5 mg/mL working concentration; stock MTT was diluted 1:4 to a final concentration of 0.1 mg/mL with appropriate culture media for the cell type i.e. NMM for NPCs. MTT was then aspirated and 50 µl DMSO dissolve formazan crystals. Plates were incubated at 37°C for 15 minutes to ensure the cells had fully lysed. Absorbance values were measured at 570 nm using (Fluostar Omega).

3.1.8. Statistics

Cell culture data sets were collected in biological triplicate (N=3) with a minimum of three technical repeats (n>3) for each condition within each experiment, unless otherwise stated. Quantitative data was averaged in Microsoft Excel prior to plotting of mean + SEM in GraphPad Prism (v8.1.0). Specific statistical tests are detailed within figure legends.

3.2. Biomaterial Fabrication & Characterisation

3.2.1. Hydrogels

3.2.1.1. Gellan Gum

GG hydrogels were created at 0.2% concentrations (w/v) by adding Gelzan™ powder (Sigma-Aldrich, UK, G1910) to PBS (with Mg^{2+}/Ca^{2+}). Solutions were then autoclaved and left to cool with gelation occurring around 40°C. The resultant solid hydrogel was placed in a 700 Watt microwave for roughly 2 minutes until liquid to enable rapid decanting into well plates. Following plating, hydrogels were left at RT overnight to ensure complete gelation before storage at 4°C for up to 1 week.

Due to rapid gelation of GG hydrogels at physiological temperatures, GG bioinks were formulated with reduced amounts of divalent ions, in order to delay or prevent the gelation process. GG bioinks were created at 0.2% concentrations (w/v) by adding Gelzan™ powder to dH_2O or dH_2O with 10% PBS (with or without Ca^{2+} + Mg^{2+} (1.05 mM + 1.2 mM respectively)) prior to autoclaving for sterility. Cell pellets were gently triturated within bioinks prior to seeding, to ensure homogeneous distribution of cells. Following seeding, RPMI was cautiously added in a slow dropwise manner to the very edge of the well, to induce ionic cross-linking, with care taken not to disturb the GG layer underneath.

3.2.1.2. HyStem™

HyStem™ is an alternative HA-based hydrogel modified with thiol groups, available commercially from Sigma-Aldrich (HYS020). Hydrogels were formulated via manufacturer's instructions whereby HyStem power (Glycosil®) is mixed with a thiol reactive cross-linker (Extralink® PEDGA) to induce gelation.

Encapsulation of cells within HyStem™ hydrogels is enabled by the pre-gelled state being sufficiently viscous for cell mixing and handling, for up to 20 minutes after combining polymer and cross-linker. Protocol for bulk encapsulation follows the manufacturers technical bulletin precisely to generate 2.5 mL 1X HyStem™; 2mL degassed DI water was injected into 2 vials of HyStem™ lyophilized powder (1mL/1 vial) via sterile syringe to produce 2 mL HyStem™ Stock. This mixture was left on a roller for 30 minutes RT to aid dissolution. Addition of 0.5 mL to 1 vial of Extralink PEG-3500 (1.45 mM stock) enabled instant dissolution. Vials were then combined to produce 2.5 mL HyStem™ with a 4:1 ratio of HyStem™ to PEG, final concentration of PEG being 0.29 mM or 20%. Solutions were plated immediately following dissolution, and incubated at 37°C for a minimum of 1 hour prior to addition of media.

3.2.1.3. Hylanuronic Acid (HA)

Hyaluronic acid is a glycosaminogen (linear polysaccharide, non-sulphated, negatively charged) found within the ECM of the brain. The general structure is random coil extended formation, with hydrogen bonding between adjacent saccharides most responsible for stiffness. Functionalisation of HA with methacrylate groups (Hyaluronic Acid MethAcrylate, HAMA) enables photo-polymerisation, with mixing of HAMA and a photo-initiator enabling photo-induced formation via free-radical polymerisation (Bean, 2015). Modulation of the concentration of polymer, photoinitiator and exposure time enables tuning of mechanical properties such as viscoelasticity and stiffness.

3.2.1.3.1. HA modification

Hyaluronic acid methacrylate, or HAMA, was synthesized by first dissolving 1% (w/v) of UV-treated HA sodium salt from Streptococcus equi (Sigma-Aldrich, UK, 53747 (~1.5-1.8 x 10^6 Daltons) in 100 mL of deionised water (DI), for stirring at RT overnight. Following this, trimethylamine (Sigma-Aldrich, UK, 471283), glycidyl methacrylate (Sigma-Aldrich, UK, 779342) and tetrabutyl ammonium bromide (Sigma-Aldrich, UK, 426288) were added sequentially to achieve final concentrations of 2% (v/v), 4.1% (v/v) and 2.1% (w/v) respectively. Addition of the next reagent only occurred after the previous reagent had fully dissolved. The solution was stirred at 300 RPM overnight to ensure homogeneous mixing. The solution was then incubated in an oven for 1hr at 60°C, before precipitation of the HAMA by pouring the solution into approx. 6 times volumes of 100% acetone (Sigma-Aldrich, UK, 179124) with constant stirring at 300 RPM. The precipitated HAMA was retrieved via filtering under vacuum with two grade 1 filter papers (Whatman®, VWR, UK, 512-1001). The result was a singular gelatinous globule that was then dissolved in DI water by heating stirring to 60°C at 900 RPM. The viscous HAMA solution was then filtered twice more, following the same method as above, before collecting into petri dishes for overnight incubation at 60°C. Evaporation of the water results in a clear HAMA film that requires a scalpel blade to carefully remove from the dish.

3.2.1.4. NMR Spectroscopy

Proton NMR spectra were recorded at Loughborough University, under the supervision of Dr Paul Roach, on JEOL ECZ-R (500 MHz NMR) spectrometer (JEOL Ltd., Japan). HA salts and HAMA film were dissolved in DMSO for proton (^{1}H) NMR spectroscopy. Spectra were processed using JEOL's Delta Software (v5.3.3) with DMSO as a reference line. Methacrylate modification was confirmed within samples of HAMA by the addition of two methyl proton peaks at 5.9 and 6.3 ppm (Appendix 8).

3.2.1.5. HAMA Functionalisation

Work was carried out at Loughborough University under the supervision of Dr Paul Roach.

3.2.1.5.1. HAMA – GGIKVAVGG peptide

Adapted from Rowley et al. (1999); peptide conjugation via amide (NH_2) bond formation.

The HAMA film (Method 3.2.1.3.1) was added into 100 mM MES buffer (Sigma-Aldrich, 69889) and 300 mM NaCl, to a final concentration of 1% (w/v) HAMA. The pH was adjusted to 6.5, and then stirred overnight. Following this, EDAC (N-(3-Dimethylaminopropyl)-N′-ethylcarbodiimide hydrochloride, Sigma-Aldrich, UK, E7750) and the GG peptide (Neo Biotech, Generon, UK, CUST-PEP-29042021-A2) were sequentially added to a final concentration of 1 mmol/L and ~130 uM respectively. The solution was again stirred overnight. The solution was then dispensed into dialysis tubing (Fisher Scientific, UK, 10005743) and

crocodile clips were applied to prevent leakage. The solution was then dialysed against 4L ddH_2O for two days with fresh water every 12hrs. Following dialysis, the tubing contents was filtered through a 0.2um filter into an oversized falcon tube e.g. 50 mL. This was to avoid fracturing of the container during subsequent freezing. Once frozen, the sample was freeze dried to produce a fibrous mass of peptide-modified HAMA.

3.2.1.5.2. HAMA – CCRRIKVAVLC peptide

Adapted from Perera et al. (2019); peptide conjugation via thiol (SH) bond formation.

HAMA film was added to ddH_2O to a final concentration of 100 mg/10mL, and the pH adjusted to 10 via the addition of NaOH, with a final addition of ethylene sulphide (Sigma-Aldrich, UK, 12825). The solution was then stirred overnight until fully dissolved and then column filtered through Celite 454 (Sigma-Aldrich, UK, 1026930250), under light vacuum suction. Next, 5 molar excess of DTT (Dithiothreitol, Sigma-Aldrich, UK, 0197777001) was added and pH adjusted to 8.5 with NaOH. The solution was column filtered again, prior to the addition of PBS (Sigma-Aldrich, D8537) to a final volume of ~25 mL. Following the addition of the CC peptide (Neo Biotech, Generon, UK, CUST-PEP-29042021-A1) to a final concentration of 1 mg/25 mL, the solution was left to stir overnight until fully dissolved. This was then dispensed into dialysis tubing (Fisher Scientific, UK, 10005743) and crocodile clips were applied to prevent leakage. The resulting solution was dialysed against 4 Litres ddH_2O for two days with fresh water every 12hrs. Following dialysis, the tubing contents was filtered through a 0.2 um filter into an oversized falcon tube. Once frozen, the sample was freeze dried to produce a fibrous mass of peptide-modified HAMA.

3.2.1.6. HAMA Hydrogels

HAMA hydrogels were formed following dissolution of HAMA film via stirred mixing to produce 1.5-2% solutions (w/v) in PBS containing 10% (v/v) PEG diacrylate (575 or 3500 Daltons (Sigma-Aldrich, UK, 437441, or Extralink® from Mattek, Slovak Republic, GS3007, respectively) and various concentrations of photoinitiator (0.05-1% w/v). Photoinitiators were Irgacure 2959 or 2-Hydroxy-4′- (2-hydroxyethoxy)-2-methylpropiophenone (Sigma-Aldrich, UK, 410896) and LAP or lithium phenyl-2,4,6-trimethylbenzoylphosphinate (Sigma-Aldrich, UK, 900889). Note that following addition of the photoinitiator the solution was kept within containers covered in foil, during stirring and storage at 4°C. The hydrogel precursor was exposed to 365 nm wavelength UV to induce polymerisation.

When optimising HAMA culture conditions, additional components were added to support tissue culture. Due to the viscosity of stock HAMA solutions preventing 0.2 µm sterile filtration, 0.4 µm filtration of HAMA-PBS stock solutions and use of 2% (v/v) penicillin/Streptomycin

(P/S) (Sigma-Aldrich, UK, P4333) ensured sterility. Optimal composition and workflow for generation of bulk HAMA hydrogels for neural tissue culture is highlighted within figure 22.

3.2.2. Fluid gels

3.2.2.1. Fabrication

Fluid gels were fabricated via dissolution of Gellan Gum or DNA-grade Agarose (VWR, UK, 438792U) in PBS with Ca^{2+} + Mg^{2+}, to a final volume of 200 mL. This was done in a 1 Litre glass Duran containing a 70x10 mm magnetic flea (Keeping variables of vessel size, flea size and final volume consistent is vital to ensure shear forces are consistent between batches).

Mixtures were then autoclaved to ensure homogenous mixing and sterility of the hydrogel intermediate. Resultant hydrogels were microwaved for 2 minutes 30 seconds, in 30-second intervals with swirling in-between, to ensure the mixture was homogenous. Mixtures were then placed onto a pre-heated (95°C) rotating magnetic stirrer, for stirring at 250 RPM for 20 minutes. After this time the hot plate was turned off to allow cooling and gelation of the hydrogels, but continual application of shear forces during cooling lead to “pockets” of gelation that enable shear thinning behaviour. Sterile fluid gels were stored at RT for up to 2 weeks.

3.2.2.2. Morphological Analysis

In order to enable visualisation of fluid gel microstructure, gels were diluted 1:10 with dH_2O to aid visualisation via light microscopy.

3.3. Rheology

The viscoelastic properties of hydrogels were assessed using the Kinexus Ultra+ rheometer (Malvern Panalytical) undertaking small oscillatory rheology. Serrated disc geometries were employed to limit slippage at the plate-sample interface and prior to loading of samples geometries were heated to 37°C.

Amplitude sweep testing was performed using serrated disc geometries. This allows identification of linear viscoelastic regions (LVR) of both the storage (G’) and loss (G’’) moduli. Following this, geometries were cleaned, and a fresh piece of the same sample was exposed to a frequency sweep test. This test determines viscoelastic properties as a function of frequency, demonstrating changes in viscoelastic moduli of hydrogels in response to variation in stress frequency. Measurements here occur within the LVR obtained from amplitude testing.

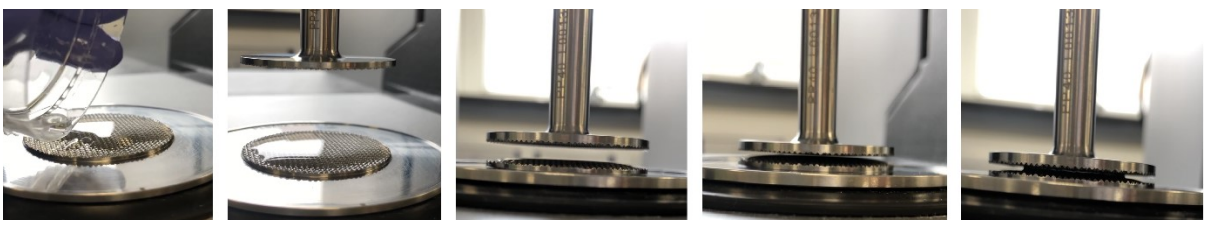

Figure 10. Plating of biomaterials for rheological testing. Chronological order left to right. Sample is places onto serrated disc geometries and compressed, with gap size set to be roughly 10 times the largest particle size, here 1mm. This roughly corresponds to 1mL~ of liquid material. Following this entire set up, the protective cover is returned to establish a consistent temperature prior to testing.

3.3.1. Testing

Stress-controlled sweep testing was carried out with amplitude sweeps ran from a range of 0.1 to 150 Pa, at 1 Hz and 10 decades. Corresponding frequency sweeps ran at 0.1-10 Hz at an unchanging shear stress of 50-80% of the LVR (here 0.1 Pa), 10 samples per decade.

3.3.2. Statistics

All rheological tests were performed in triplicate unless otherwise stated, with data exported from rKinexus software into Microsoft Excel for averaging (Appendix 9). Averages from repeated independent experiments (N=3) were then plotted in GraphPad Prism (v8.1.0) to provide mean ± SEM, unless otherwise stated.

3.3.3. Surface Response Analysis

Contour plots were generated using Minitab Statistical Software (v.21).

Plotting of rheological data required averaging of large continuous datasets to produce singular values for each condition. Amplitude sweep provides n=15 outputs for elastic modulus at 1 Hz, requiring averaging to produce singular values for each N, whereas frequency sweep yields n=1 data point for elastic moduli at 1 Hz.

LAP concentration (% w/v)	**Amplitude**			**Frequency**		
0.5	4586.488	6962.756	2343.67	2984.33	4530.67	5368.27
0.25	3488.667	1998	3032.667	4400	2385.333	909.5
0.1	768.4	1315.447	1376.741	1247.8	720.2	1399.967
0.05	410.16	82.29644	16.814	166.7667	14.90767	274.95
0	1.023133	0.295616	0.362	1.419667	0.3055	0.4384

In order to validate the averaging method for generation of contour plots, two way ANOVA was performed ($P<0.05$), demonstrating no significant differences were observed between averages for each condition.

3.4. Structuring of the Model / Bioprinting

In order to provide an additional level of control over the macroscale architecture of the resultant hydrogel, bioprinting approaches were employed.

3.4.1. Hydrogel Precursors for Printing

In order to promote desirable printing behaviour of bioinks, without modifying the final hydrogel composition, biomaterial formulations here were incubated at 37°C for up to 15 minutes prior to loading into printer cartridges (3 mL UV-shielding cartridges, CELLINK, BICO, USA). This

was to enable partial polymerisation of the material in order to be sufficiently viscous to prevent leakage from the print nozzle during loading/printing. Furthermore, light sensitive materials containing photoinitiators were protected from light during the print process by loading into UV shielded cartridges.

3.4.2. Extrusion of Cell Suspensions

The effect of extrusion processes on cell viability was determined via syringe and needle extrusion of RPMI containing fluorescent SH-SY5Ys. Various extrusion rates, seeding densities (0.5-1x10^6 cells/mL) and needle gauges (25, 27, 30G (Fisnar, UK)) were tested utilising a syringe pump (Harvard PHD 2000) and 5 mL syringes (Fisher Scientific, UK, 15869152) in order to control the rate of extrusion (0.5-3 mL/minute). Cell viability was assessed via manual counting (Method 3.1.9.1). Cell suspensions were plated with additional fresh media at a 1:1 ratio before incubation. Control conditions were held in a syringe for the same holding time as all other conditions before gentle expulsion into wells for counting.

3.4.3. INKREDIBLE+ Bioprinting

Extrusion printing (INKREDIBLE+, CELLINK, BICO, USA) facilitated generation of single layer 3D lattice constructs consisting of a variety of bioinks. A 22G print nozzle was used unless otherwise stated, whereas extrusion pressure was modified dependent upon the viscoelastic properties of the chosen bioink.

Commercial inks from CELLINK (BICO, USA) were utilised for preliminary investigation (N=1) of the extrusion printer set up, namely CELLINK Bioink (IKC200000303) and CELLINK LAMININK+ (IKC205000301). CELLINK Bioink is comprised of an alginate and cellulose composite, whereas LAMININK+ contains this generic formula plus several forms of laminin. Both bioinks were generated via the manufacturers' protocol, with the addition of SHSY-5Y-mCherry or GFP cells at 2 x 10^6/mL. The formulation was mixed thoroughly prior to cartridge loading. Print pressure was kept to ~10 kPa. Constructs were gelated via immersion in $CaCl_2$ for 10 min, followed by a 5min RPMI wash.

HAMA bioink formulation followed the same protocol for generating bulk hydrogels, with pre-gelled states enabling handling/printing for up to 20 minutes after photo-induction of polymersiation. Specific formulation and workflow conditions for bioprinted of HAMA constructs is outlined in Figure 30A. HAMA bioinks were mixed by gentle inversion and incubation for up to 15 mins to promote gelation. Additional components were added to support cell viability (e.g. 10 ug/mL laminin) prior to resuspension of fluorescent SH-SY5Y cells at 1 x 10^6/mL. Print pressure varied depending on bioink and batch due to variables such as temperature, timing and blockages within the print nozzle. Nevertheless, this was kept

within the range of 40-110 kPa to promote extrusion of a smooth filament. Resultant photosensitive printed constructs were photopolymerised via UV, then incubated for 15 minutes prior to first feed.

All constructs were fed with complete RPMI media containing 10% (w/v) P/S. Gentle half media changes were performed every other day. Cells were monitored and imaged via EVOS XL system (Life Technologies, USA).

3.4.3.1. Suspended Layer Additive Manufacture

SLAM bioprinting (Senior et al., 2019) was carried out utilising LAMININK+ bioink and 0.2-0.4% GG (in PBS with Ca^{2+} or Mg^{2+}) fluid gel support beds, both generated via protocols above (Methods 3.4.3 and 3.2.2.1). Fluid gel support beds were created by pipetting 3 mL of fluid gel into 30x15 mm petri dishes and allowing to settle for 1 hour. Height of the print surface was adjusted during the calibration process to ensure printing within the gel phase instead of the petri dish surface. Constructs were fed with complete RPMI 1640 medium (Sigma-Aldrich, UK, R0883) containing 10% FBS (Sigma-Aldrich, UK, F0804) and 1% L-Glutathione (Sigma-Aldrich, UK, G513). Gentle half media changes were performed every other day. Cells were monitored and imaged via EVOS XL system.

3.4.4. Image J analysis

Image J software (Schneider 12) enabled evaluation of printed filament resolution via set scale and measurement tools. Specifically, triplicate measurements of filament width were taken for each image (n=3), for averaging to provide an accurate estimation of CELLINK and LAMININK+ filament resolution.

3.5. UV Radiometry

Power of the both the 'UV Box' (Figure 16) and 'UV Bulb' (Figure 19) systems was measured by a UVX radiometer. The 'UV box' was a purpose built 365 nm UV source loaned from Aston Pharmacy School (Aston University), whereas the 'UV bulb' system encompasses a MacroLED 365 nm light source and separate power/control module (Cairn Research, UK). Both systems were "warmed up" on 5 minutes prior to use to achieve maximum intensity.

Exposure area was divided into 1 cm^2 squares for discrete measurement. The total measured area for the UV Box system was 31x14 cm. For the open UV Bulb system, measurements were taken for a 10x10 cm square surrounding the precise exposure area.

4. Biomaterial Exploration

4.1. Introduction

The tuneable nature of hydrogels makes them ideal candidates for culture scaffolds with the ability to control biochemical features (composition, cellular interactions), as well as physical aspects (porosity, stiffness). The type of polymer, molecular weight and concentration, as well as the degree of polymerisation (influenced by mode of gelation, concentration of (photo)cross-linker, sequential rounds, etc.), influence bulk mechanical properties such as stiffness and porosity. Stiffness and viscoelasticity of cell surroundings regulates cell behaviour, therefore modulation of the water content and polymer concentration can change mechanical properties and provide tissue-specific cues to cells.

4.1.1. Polymers

Gellan gum (GG) is a naturally occurring, negatively charged polysaccharide, produced by S. *elodea* bacterium that exhibits biocompatibility but is relatively inert. GG consists of D-glucose, L-rhamnose and D-glucuronic acid (Figure 11) in a ratio of 2:1:1 (Koivisto et al., 2017). It is widely accepted that gel formation occurs following formation and aggregation of double helices; with addition of cross-linking agent, in this case being monovalent or divalent cations, intermolecular repulsion occurs between helices reduces and junction zones form to produce a translucent matrix (Muthukumar et al., 2019, Picone and Cunha, 2011, Zia et al., 2018). High or low-acyl forms of GG affect hydrogel properties due to limitation of junction zone formation; high-acyl GG yields brittle and rigid gels where the low-acyl form produces soft gels (Mao et al., 2000, Zia et al., 2018). GG is utilised for a wide range of applications, including drug delivery, wound healing, antimicrobial treatments, alongside tissue engineering (Muthukumar et al., 2019).

Polyethylene glycol diacrylate (Barros et al., 2019) is an acrylated form of the polyethylene glycol polymer, favoured due to its water solubility, low immunogenicity and biocompatibility (Choi et al., 2019). Double acrylate bond groups at the end of each PEG monomer are broken, enabling formation of covalent bonds between polymer chains to produce a 3D crosslinked polymeric network. PEG hydrogels are advantageous for tissue engineering applications in that they retain water, porous nature and propensity for chemical modification. Polymerisation of PEG can occur via a multitude of methods (Choi et al., 2019); however, photo-crosslinking holds promise due to its versatility and range of potential biomedical applications (Chapter 5). Unfortunately, PEG crosslinking is sensitive to oxygen inhibition of acrylates, limiting

crosslinking reaction rate (Choi et al., 2019). This may be particularly problematic within cell culture conditions, with oxygen necessary for cell survival.

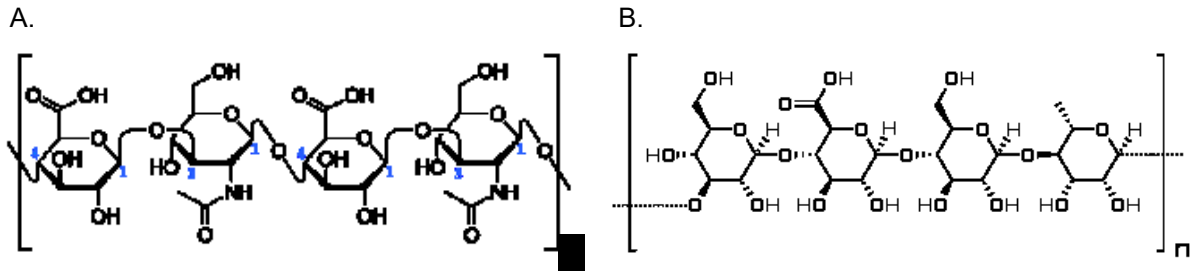

Figure 11. Chemical structure of natural hydrogel building blocks. Polymers are repeated as units of n. 11A) Gellan gum. 11B) Hyaluronic acid. Both display multiple carboxylated side chains, demonstrating capability for chemical modification and/or functionalisation.

Hyaluronic acid (HA) is a negatively charged linear polysaccharide, specifically a glycosaminogen, found within the ECM of the brain. The general structure is random coil extended formation, with hydrogen bonding between adjacent saccharides most responsible for stiffness. HA is known to support structure and function of tissues throughout the body (Khoshakhlagh and Moore, 2015), and is shown to provide similar support *in vitro* (Liu et al., 2019). Whats more, high molecular weight HA (above 1250 kDa) is shown to be immunosuppressive (Lee et al., 2021), potentially combatting inflammatory phenotypes observed *in vitro*. Alternatively, this may be exploited to induce inflammatory conditions within a biomaterial, to model disease states whereby hydrolysis of HA via hyaluronidases reduces its molecular weight and therefore viscosity of ECM fluid (Cowman et al., 2015).

HA is a high molecular weight polymer (over 10^6 Daltons) where D-glucuronic acid and N-acetyl-D-glucosamine groups are linked (Figure 11) via glycosidic bonds (Lam et al., 2014). The structure of HA means various sites are available for modification via crosslinking groups and/or biologically active molecules (Choi et al., 2019). HyStem™ and HAMA hydrogels exploit this, with HyStem™ utilising thiol modification for PEG crosslinking (Sigma-Aldrich, 2012, Zarembinski and Skardal, 2018), where HAMA possesses a methacrylate group that enables photo-polymerisation (Chapter 5).

4.1.2. Cross-linking

Physical properties of hydrogels depend on type of polymer and the method of crosslinking polymer chains i.e. physical and/or chemical bonds between polymers. Physical crosslinks include ionic or electrostatic interaction, hydrogen bonding, crystallization, hydrophobic interaction etc. Whereas chemical crosslinking includes enzyme-induced crosslinking, “click” chemistry such as Diels-Alder and Michael type addition, and photopolymerisation (Chapter 5). Chemical modification of polymers (Section 1.4.2.3) affords even greater control over crosslinking method (Caliari and Burdick, 2016), enabling not only modulation of polymer

network but also inclusion and patterning of additional functional components (Section 1.4.2.5).

Inotropic gelation of GG occurs in the presence of multivalent cations such as Zn^{+2+}, $Al^{3}+$, Ca^{2+}, Mg^{2+}, etc. Use of divalent ions ($^{2+}$) is preferred for production of stronger hydrogels from lower concentrations, when compared to monovalent cations (Zia et al., 2018). This ionic interaction results in a thermally reversible hydrogel. GG hydrogels are resistant to enzymatic or pH degradation (Zia et al., 2018), but not ionic or thermal-induced degradation. Interestingly, amines possessing cationic charge can be utilised for crosslinking of GG, with the added advantage of biological relevance and compatibility (Koivisto et al., 2017). Alternative methods of crosslinking involve methacrylation of free carboxylic or amine groups of GG, enabling photopolymerisation as an alternate cross-linking method (Silva-Correia et al., 2011).

On the other hand, PEG hydrogels rely almost entirely on chemical crosslinking of the synthetic polymer chains. The synthetic and highly modifiable nature of this polymer network enables delicate control over physical properties, with numerous possibilities for biofunctionalisation to make up for limited biological activity. Research into photopolymerisation of PEG established use of LAP as a photoinitiator with reduced cytotoxicity (Fairbanks et al., 2009). PEG may also be utilised as a crosslinking agent for other polymeric systems (Li et al., 2018, Long et al., 2020); Work by Ghosh *et al*. is particularly relevant, demonstrating crosslinking of chemically modified HA via PEG, with a positive correlation observed between stiffness (G') and PEG concentration (Ghosh et al., 2005). In an entirely different approach, Li *et al.* utilised "click" chemistry and a four-armed PEG crosslinker to produce a protein-functionalised hydrogel capable of supporting NSC differentiation (Li et al., 2018). This research went on to show "click" chemistry to be a less toxic mode of ensuring cell encapsulation within hydrogels (Li et al., 2018). The propensity of PEG for modification enables numerous applications (can act as polymer network foundation but also as crosslinker of other chemically modified polymers), making this an even more versatile polymer within the tissue engineering toolkit.

HA hydrogels are typically crosslinked via thermal or ionic methods, with solutions of HA without chemical cross-linking displaying viscous non-newtonian behaviour, due to physical interaction of polymers (Cowman et al., 2015). High viscosity of dilute solutions can be attributed to high molecular weight and flexibility of HA molecules leading to macromolecular crowding (Cowman et al., 2015). Chemical modification of HA also enables greater control over polymerisation and therefore mechanical behaviour; Ma *et al*. demonstrate modification of HA to form aldehyde hyaluronic acid (HA-CHO) enables use of Schiff base formation to produce biocompatible hydrogels for injectable protein delivery (Ma et al., 2018). Alternatively

methacrylation to form HAMA is advantageous for achieving improved mechanical properties via photopolymerisation (Spearman et al., 2020, Ondeck and Engler, 2016), with ionically or thermally crosslinked hydrogels displaying poor mechanical properties such as rapid degradation (Choi et al., 2019). Modulation of methacrylation is also suggested as an additional variable contributing to degree of crosslink formation (Khoshakhlagh and Moore, 2015, Ondeck and Engler, 2016). Use of multiple polymers such as GG methacrylate-HA (Vieira et al., 2020) or HAMA-PEG blends (Ghosh et al., 2005, Shu et al., 2004) alongside dual crosslinking systems (Garrido et al., 2023) and elaborate bio-functionalisation techniques (He et al., 2020) may be the best way of engineering biomaterials capable of mimicking the complexity of polymeric networks observed within ECM of the CNS.

Following critical evaluation of tissue engineering approaches within the literature (Section 1.4), preliminary investigation was carried out, via SH-SY5Y neuroblastoma cells culture and rheological analysis, for exploring biomaterials for neural tissue engineering.

4.2. Results

Exploration of hydrogel polymers for neural tissue engineering (Objective 1) included utilising materials that were readily available within the laboratory. Tissue culture plastic (TCP) is commonplace within 2D cell culture research, however is shown to promote inflammatory responses (Watson et al., 2017). HyStem™ is a semi-synthetic commercially available hydrogel kit favoured by researchers for 3D cell culture due to its cell-friendly nature promoting processes such as adhesion and motility. Such commercially available kits however often come at high monetary cost. Gellan gum (GG) is a natural polymer often utilised as an alternative to agar for microbiological assays.

In order to explore the biocompatibility of HyStem™ and GG hydrogels, SH-SY5Y cells expressing red mCherry protein were encapsulated within polymer solutions (Methods 3.2.1.2 and 3.2.1.1). While the deliberate crosslinking kinetics of HyStem™ enabled mixing of cells prior to complete gelation, GG hydrogels gelate in the presence of divalent ions, therefore solutions containing reduced ionic concentrations (Figure 12A) were employed to enable mixing of cell pellets. Due to the incomplete gelation of GG hydrogel precursors, mixtures were referred to as “bioinks”. To determine biological compatibility, fluorescent cells were encapsulated within GG bioinks or HyStem™ hydrogels, with culture on TCP as a positive control (Figure 12). Following seeding, constructs were fed with complete RPMI media, to support cell viability and provide additional cations for gelation of GG bioinks. Cells were imaged via fluorescent microscopy over two days to assess short-term biocompatibility (Figure 12A). Rheological characterisation (Methods 3.3) of HyStem™ was carried out (Figure 12B) individually as the stiffness of TCP is known (Sigma-Aldrich, 2021) and GG bioinks were all

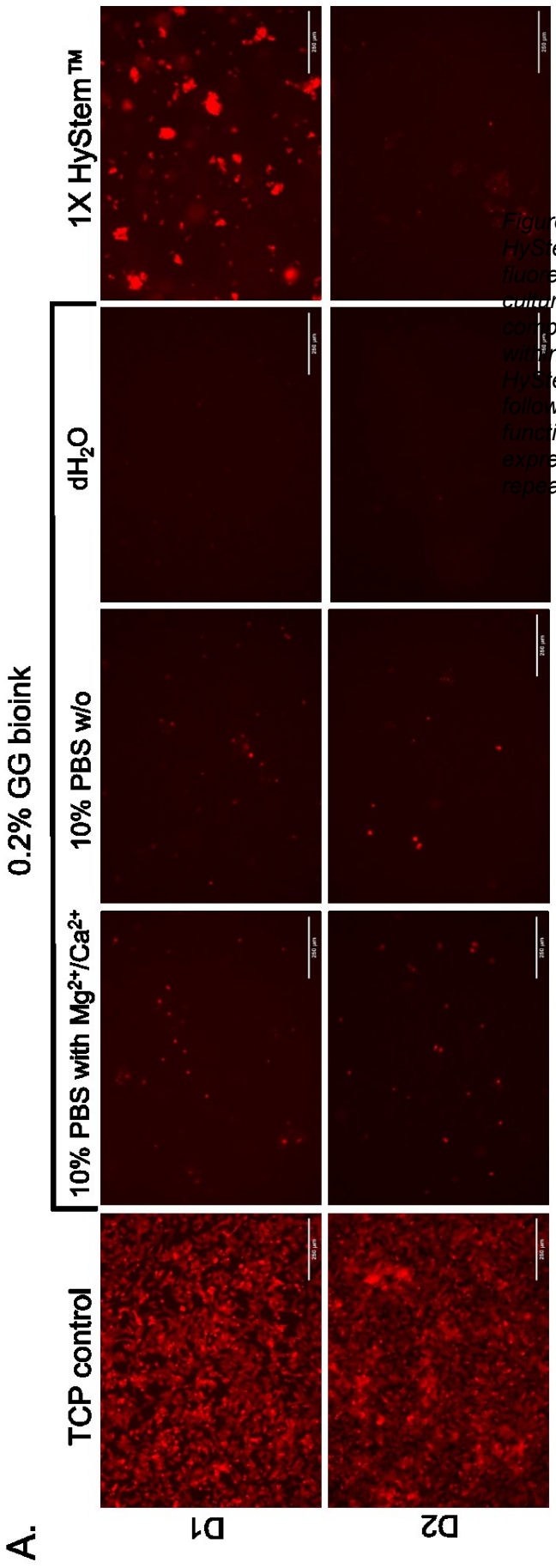

Figure 12. Investigation of Gellan Gum (GG) bioinks and HyStem™ for neural culture. 12A) Representative fluorescence microscopy images of mCherry SH-SY5Ys cultured within GG bioinks with various ionic compositions, compared to culture on Tissue Culture Plastic (TCP) and within HyStem™. 12B) Small oscillatory rheology of HyStem™ hydrogels. Frequency sweeps are performed following amplitude testing to display viscoelastic moduli as a function of frequency ranging from 0.1-10Hz. Results here expressed as mean ± SEM (The average of n=3 biological repeats; with n=3 technical repeats per biological repeat).

extremely viscous; only HyStem™ displayed gelation to the degree necessary for generation of soft-solid biomaterials and evaluation via rheology. Interestingly, all bioinks displayed the same level of viscosity by eye, despite one condition containing 10% PBS with divalent ions. As expected, cells seeded on TCP displayed 2D attachment with an increase in spreading morphologies over two days *in vitro* (Figure 12A). Retention of fluorescence also indicates sustained viability of SH-SY5Ys over the culture period. Morphologically cells were more rounded compared to TCP on both days, as cells were suspended within a fluid-like 3D matrix. However, by day two there was a reduction in fluorescence visible via microscopy, with the majority of fluorescence maintained within clumped areas of cells. Figure 12B shows rheological analysis of HyStem™ (here referred to as 1x HyStem™), with an elastic modulus of 23.7$\pm$1.7 Pa and a viscous modulus of 0.9$\pm$0.3 Pa. With the elastic modulus over twenty times greater than viscous, this demonstrates elastic dominance of the system, resulting in a hydrogel stiff enough to hold its own shape following gelation.

With limited success when encapsulating cells within GG and HyStem™ hydrogels, further work looked to assess biocompatibility of polymers via culture of SH-SY5Y-mCherry cells on top of hydrogel materials (Figure 13). TCP was again utilised as a positive control, beside GG saturated with divalent ions (to ensure complete gelation), however an in-lab hyaluronic acid alternative polymer was utilised instead of HyStem™. Hyaluronic Acid Methacrylate (Method 3.2.1.3.1) was utilised due to reduced cost and availability of the material, with a combination of Polyethylene Glycol or PEG, and light-based photo-polymerisation enabling greater tailoring of the gelation process (Chapter 5). Photoinitiators (Irgacure 2959 and Lithium phenyl-2,4,6-trimethylbenzoylphosphinate or LAP) were chosen based on existing literature (Dai et al., 2021, Fairbanks et al., 2009, Pereira et al., 2023, Xu et al., 2020).

Biocompatibility of SH-SY5Y culture on hydrogel materials was assessed via fluorescent microscopy up to 6 days *in vitro* (Figure 13A). To support this, manual counting (Method 3.1.7.1) of live/dead cells at day six enabled quantification of viability (Figure 13B). To expand on previous rheological work, testing was carried out (Figure 30C) on GG hydrogels (made with 100% PBS with Mg^{2+}/Ca^{2+}), alongside 2% HAMA hydrogels containing 10% PEG (molecular weight; Mn 575) and 0.5% photoinitiator (LAP or Irgacure 2959). All HAMA conditions here were photopolymerised at 365 nm by the UV box system for 60s.

Figure 13 showed TCP control yields high viability and spreading of cells up to day six with increased and sustained fluorescence of SH-SY5Ys, as such was utilised for normalisation of data in Figure 13B. In comparison, culture on GG hydrogels induced rounded morphologies of SH-SY5Ys, with clumping of cells visible at days three and six. By day six, there was visible

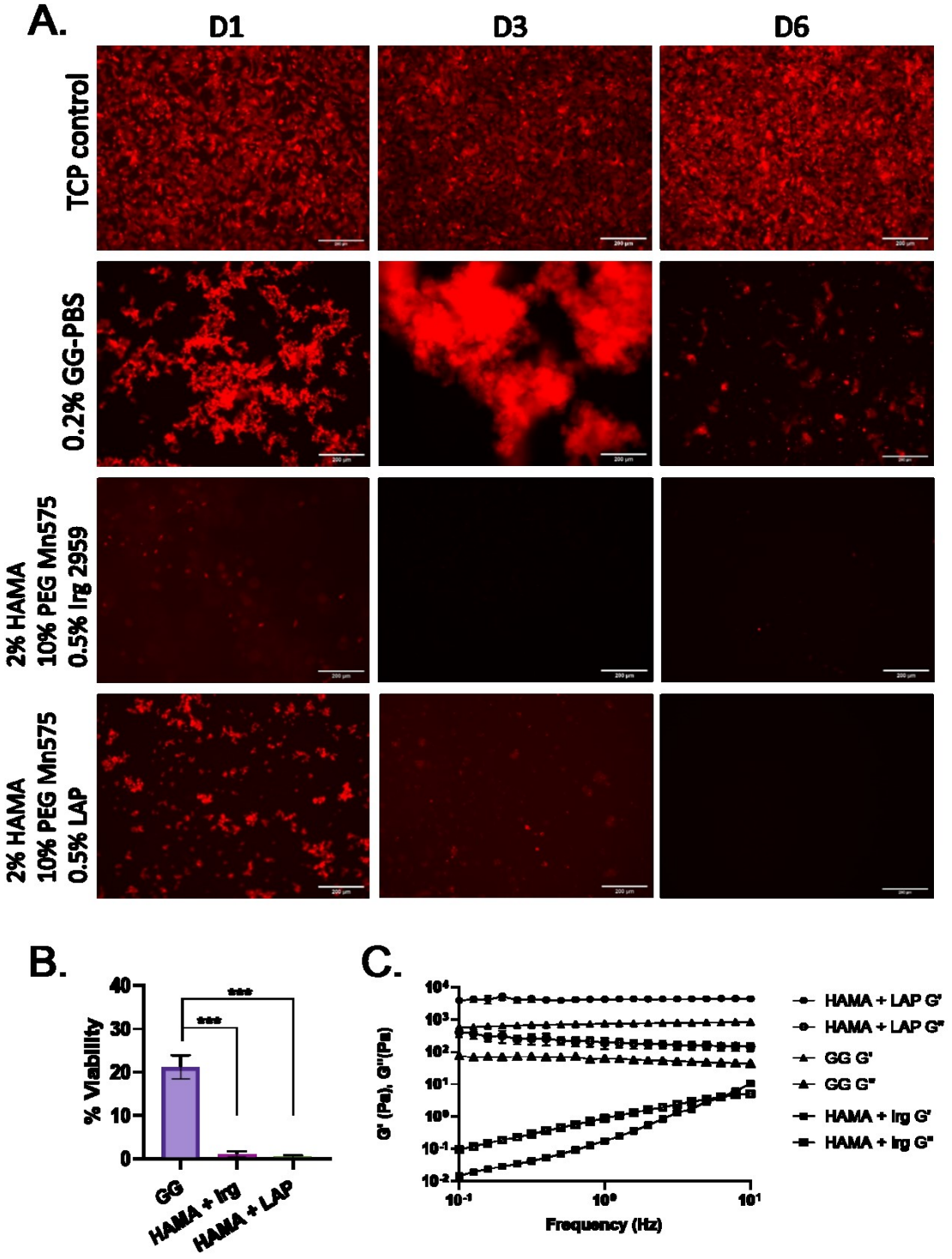

Figure 13. Suitability of various media for neural culture. 13A) Fluorescence microscopy of mCherry SH-SY5Ys cultured on Tissue Culture Plastic (TCP) as a control, alongside Gellan Gum (GG) and Hyaluronic Acid Methacrylate hydrogels. HAMA conditions comprised 0.5% (w/v) of either Irgacure 2959 or Lithium phenyl-2,4,6-trimethylbenzoylphosphinate (LAP) photoinitiator, exposed to 60s of 365 nm UV. 13B) Quantification of cell viability after 6 days via manual live/dead counting. Results expressed as mean ± SEM, P<0.001 (***). 13C) Small oscillatory rheology reveals elastic (G') and viscous (G'') moduli of hydrogels. Frequency sweeps display viscoelastic moduli as a function of frequency ranging from 0.1-10 Hz. Results expressed as mean ± SEM (n=3 biological repeats; average n=3 technical repeats per biological repeat).

reduced fluorescence of cells, with reduced clumping and autofluorescent debris visible. There also appeared to be sparse spreading of SH-SY5Ys in the GG condition. Alternatively, HAMA hydrogels showed a marked reduction in cell fluorescence across all days compared to TCP or GG. Within HAMA conditions, LAP was shown to be more cell compatible than Irgacure 2959 on day one, with visible differences in amount of fluorescence. By day three, HAMA-Irgacure 2959 conditions exhibited near total loss of fluorescence, with negligible visibility of SH-SY5Ys via fluorescence microscopy. A similar result was also observed in HAMA-LAP conditions by day six. These results are supported by manual quantification of viability (Figure 13B), that found all conditions were significantly reduced at day six compared to TCP control (One-way ANOVA with Tukey's post-test, $P<0.001$). With almost 80% cell death (viability of 21.2 $\pm$4.8%) for the GG condition and 98/99% death (1.08 $\pm$1.09% or 0.47 $\pm$0.54%) for HAMA hydrogels made with LAP/Irgacure 2959 respectively. Significant differences (One-way ANOVA with Dunnet's post-test, $P<0.0001$) were observed between GG and both HAMA conditions. No significant difference was observed between cell viability of HAMA-LAP or HAMA-Irgacure 2959 conditions.

Rheological analysis (Figure 13C) shows GG hydrogels displayed elastic dominance with a G' of ~700 Pa (596-850 Pascals) and G'' of 60 Pa (74-43 Pascals), with HAMA-LAP displaying similar elastic dominance where by G' also exceeds G'', at ~4.2 kPa (3947-4456 Pascals) and ~280 Pa (412-147 Pascals) respectively. Conversely, HAMA-Irgacure 2959 hydrogels displayed viscous dominance, with minimal difference between G' and G'', both raising from 0.01 and 0.1 Pa to 10 and 5 Pa respectively. While GG and HAMA-LAP displayed relative stability of viscous and elastic moduli, both moduli for HAMA-Irgacure 2959 hydrogels increased with intensified frequency.

Despite the ability to generate GG hydrogels with physiologically relevant stiffness', HAMA hydrogels were chosen for further investigation, due to their high tuneability. However, HAMA hydrogels required optimisation for improved biological and mechanical properties (Objective 2). HAMA hydrogels in Figure 13 showed near total loss of cell viability, as such further work looked to identify the cause of toxicity. PEG is a large component of the HAMA hydrogels used herein, with up to 10% added to provide additional support to HAMA solutions, alongside additional photopolymerisation. To determine cytotoxicity of PEG components, SH-SY5Ys were exposed to varied concentrations of low (Mn 575) or high (Mn 3500) molecular weight PEG for quantification of cell viability via MTT assay (Methods 3.1.7.2). Repeated experiments utilising matched molar and percentage concentrations were carried out in order to account for differences due to molecular weight e.g. 48 µM of high molecular weight PEG (PEG-3500) corresponds to a 14% (v/v) dilution. Figure 14C depicts PEG as one of the building blocks for generation of HAMA hydrogels, its low position in the hierarchy of variables is indicative of its

degree of tuneability; work here only explores concentration and molecular weight, whereas exploration of light-based polymerisation factors affords greater tuneability.

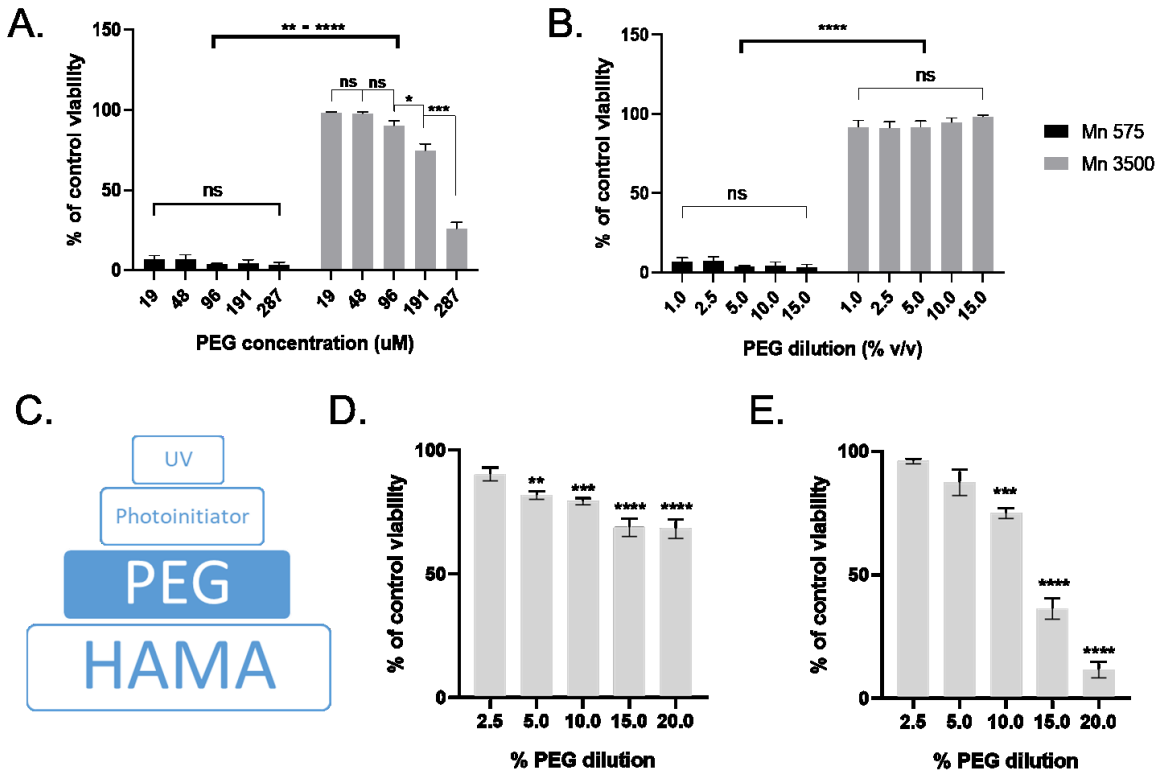

Figure 14. Quantification of Poly(ethylene glycol) diacrylate toxicity on various cell lines via MTT assay. 14A-B) Viability of mCherry SH-SY5Ys exposed to PEG Mn 575 or 3500, matched by molar concentration or percentage dilution (% v/v) in media. 14C) Schematic depicting PEG as a foundational variable for generation of HAMA hydrogels. 14D-E) Viability of L13 Astrocytes and L5 NPCs exposed to PEG Mn 3500. All data normalised against untreated controls. Results expressed as mean ± SEM (n=3 biological repeats; average n=3 technical repeats per biological repeat); Two-Way ANOVA with Dunnet's post-test. P<0.01 (**), P<0.001 (***), P<0.0001 (****).

Figure 14A showed reduction in cell viability of SH-SY5Ys exposed to increasing concentrations of low molecular weight (PEG-575), with no significant differences observed between % viability (7.1 ±2.2% at 19 µM to 3.3 +1.9% at 287 µM) across all molar concentrations (Two-way ANOVA with Tukey's post-test). Every PEG-575 molar concentration resulted in a consistent reduction in viability following exposure (<10% viability), reductions were extremely statistically significant (Two-way ANOVA with Dunnet's post-test, P<0.0001) compared to the 0 µM control condition . Figure 14A also shows a step-wise reduction in cell viability correlated to an increase in molar concentration of high molecular weight (PEG-3500). Whereby slight reductions were observed until 96 µM (90.1 ±3.4%) but no statistically significant decrease from control was observed until reductions in viability to 74.5 ±4.2% and 25.8 ±4.1% at concentrations of 191 µM and 287 µM respectively (Two-way ANOVA with Dunnet's post-test, P<0.0001). This is supported by no significant difference in

SH-SY5Y viability between 19, 48 and 96 µM exposure conditions. However, significant reductions were observed between 96 and 191 µM conditions (Two-way ANOVA with Tukey's post-test, $P<0.05$), with an even greater reduction between 191 and 287 µM conditions in Figure 141A ($P<0.001$). Statistical differences (Appendix 1.1) expand upon this observation, with extremely significant reductions in viability observed from 19/48 µM to both 191/287 µM ($P<0.001$). Statistical analysis demonstrated PEG-575 to cause significant reductions ($P<0.01$) in cell viability when compared to PEG-3500. Note that the majority of differences in cell viability following exposure to PEG-575 or 3500 were shown to be statistically significant ($P<0.0001$), with the most extreme comparisons (i.e. least toxic amount (19 µM) of PEG-575 compared to most toxic amount (287 µM) of PEG-3500) presented as slightly less significant ($P<0.01$).

Figure 14B is an extension of 11A, this time matching different weighted PEGs by percentage dilution. No significant differences were observed within groups (viabilities of 7.1 $\pm$2.2 at 1% to 3.3 $\pm$2% at 15% PEG-575; and 91.8 $\pm$4.1% at 1% to 98.1 $\pm$1.2% at 15% PEG-3500), with extremely significant differences observed between all PEG-575 and all PEG-3500 conditions (Two-way ANOVA with Tukey's post-test, $P<0.0001$). Furthermore, all PEG-575 percentages displayed visible and extremely statistically significant reductions in cell viability (Two-way ANOVA with Dunnet's post-test, $P<0.0001$) whereas no significant loss in viability was observed for all concentrations of PEG-3500. Both Figure 14A and 14B show no significant loss in SH-SY5Y viability upon exposure up to 15% (48 µM) PEG-3500 up.

With high molecular weight PEG well tolerated by cells, this was taken forward for further cytotoxicity testing on L13 Astrocytes and L5 Neural Precursor Cells (NPCs) for increased physiological relevance. To determine the point at which high molecular weight becomes cytotoxic, increasing percentage concentrations were utilised. Both astrocytes (Figure 14D) and NPCs (Figure 14E) displayed increased sensitivity to PEG-3500, with stepwise reduction in cell viability visible from 5% onwards. NPCs display greater reduction in cell viability upon exposure to large concentrations of PEG-3500. Statistical analysis (One-way ANOVA with Dunnet's post-test) reveals statistically significant reductions in cell viability of both astrocytes and NPCs when compared to 0% ($\pm$SEM) controls. Viability of astrocytes reduced significantly to 81.8 $\pm$1.7% when exposed to 5% PEG-3500 (One-way ANOVA with Dunnet's post-test, $P<0.01$), decreasing further to 79.3 $\pm$1.3% at 10% ($P<0.001$), with extremely significant reductions in viability following exposure to 68.8 $\pm$3.6% in 15 and 68.2 $\pm$3.8% in 20% conditions ($P<0.0001$). Further statistical analysis (Appendix 1.2) via Tukey's post-test showed no significant differences between conditions, aside from a slight difference between viability of astrocytes exposed to (81.8 $\pm$1.7% viability) 5% and (68.8 $\pm$3.6% / 68.2 $\pm$3.8% viability)

15/20% PEG-3500 dilutions (P<0.05), and a more significant difference observed between viability of astrocytes exposed 2.5% and 15/20% (P<0.001).

Similar reductions in NPC viability were seen in Figure 14E, with statistically significant reductions occurring at increasing increments of PEG-3500 concentration (viabilities of 74.8 ±2.1% at 10%, 36.3 ±4.2% at 15%, and 11.5 ±3.2% at 20% PEG-3500 exposure), bar the reduction observed at 2.5 % and 5% conditions (96 ±1% and 87.3 ±5.2% respectively). This reduction is not found to be statistically significant when compared to 0% control. As previously, (Appendix 1.3) statistical analysis provides insight into differences between conditions. Significant differences were observed between 2.5% and 10% conditions (One-way ANOVA with Tukey's post-test, P<0.01) but also 2.5% and 15/20% conditions (P<0.0001). Further differences were found between 5% and 15/20% conditions (P<0.0001), 10% and 20% (P<0.0001), but also 15% and 20% conditions (P<0.01). This reduction in viability of the 20% PEG-3500 condition (viability of 11.5 ±3.2%) is found to be significant when compared to every other condition.

Figure 15. Toxicity of photoinitiators on various cell lines. 15A) Schematic depicting photoinitiator as a tertiary variable for generation of HAMA hydrogels. 15B-C) MTT-assessed viability of mCherry SH-SY5Ys exposed to w/v matched concentrations (0.25% – 0.005%) of Irgacure 2959 and LAP. 15D-E) Viability of L13 NPCs and L13 Astrocytes exposed to LAP. Data normalised against untreated controls. Results here expressed as mean ± SEM (the average of n=3 biological repeats; with n=3 technical repeats per biological repeat); P<0.05 (*), P<0.01 (**), P<0.001 (***), P<0.0001 (****).

Following establishment of HAMA and PEG as the foundation blocks of hydrogel composition, the next step was to optimise of photopolymerisation. Photoinitiator type and concentration was therefore the next building block that required investigation in order to optimise the composition of HAMA hydrogels (Figure 15). Seeding of SH-SY5Ys, L5 NPCs and L13 astrocytes within 96 well plates enabled exposure to a variety of photoinitiator (Irgacure 2959 and LAP) with subsequent quantification of cell viability via MTT assay (Method 3.1.7.2).

Figure 15A highlights that modification of photoinitiator variables is a valuable tool for modification of HAMA hydrogels. Work showed both photoinitiators displayed cytotoxic effects (Figures 15B and 15C) on SH-SY5Ys at high concentrations i.e. 10 mM+. Irgacure 2959 was found to exhibit statistically significant (Appendix 2.1) cytotoxic effects beyond 1.2mM when compared to 0 mM control; with a positive correlation observed between increasing concentration and severity of cytotoxic effect (Table 3). Exposure to increasing concentrations of LAP photoinitiator correlated to a steady decline in SH-SY5Y viability, however the only statistically significant (Appendix 2.2) reduction in cell viability compared to control was the 17 mM condition with a percentage cell viability of less than 50% (Table 3).

Next, NPCs and Astrocytes were exposed to a range of LAP concentrations (Figures 15D and 15E, Appendix 2.3 and 2.4, respectively). A general trend of reduced NPC viability was observed with increasing LAP concentration (Table 3), with the highest concentration of 17 mM inducing significant cytotoxicity to ~35% viability. Astrocytes displayed significantly greater reductions in viability following exposure to LAP; viability reduced incrementally from 100% at 0 mM, to approximately 90, 85, 80, 60 then 35% viability. This stepwise reduction in cell viability again correlates to an increasing concentration of LAP. For all neural cell types (Figures 15B, C and D), a trend of reduced viability due to cytotoxicity of LAP photoinitiator was evident, with concentrations above 8.5 mM exhibiting the most severe statistically significant reductions (Table 3).

	Conc (mM)	Viability (%)	SEM	Significance
Fig. 12B	1.2	103.41	14.63	
	2.5	65.49 *	5.84	P<0.05
SH-SY5Y	5.1	64.76 **	8.01	P<0.01
Irgacure 2959	12.75	6.84 ****	4.84	P<0.0001
	25.5	0.62 ****	1.51	P<0.0001
Fig. 12C	0.85	100.48	39.99	
	1.7	101.05	30.31	
SH-SY5Y	3.4	79.79	36.74	
LAP	8.5	83.07	0.87	
	17	36.93 *	14.80	P<0.05
Fig. 12D	0.85	91.99	19.67	
	1.7	93.43	17.41	
NPC	3.4	95.09	10.90	
LAP	8.5	74.90	14.49	
	17	34.95 ***	17.54	P<0.001
Fig. 12E	0.85	90.34	4.69	
	1.7	85.52 *	6.26	P<0.05
Astrocytes	3.4	80.63 **	6.29	P<0.01
LAP	8.5	59.74 ****	5.13	P<0.0001
	17	34.48 ****	7.05	P<0.0001

Table 3. Average percentage viability ±SEM of cell lines (SH-SY5Y, L13 NPC, L13 Astrocytes) following exposure to increasing photoinitiator (Irgacure 2959 or LAP) concentration, corresponding to Figure 15. Statistical significance compared to control calculated via one-way ANOVA with Dunnett's post-test.

Alongside optimisation of photoinitiator concentration, investigation of UV dose was carried out via radiometry (Method

3.5) and biological assessment of cell viability by MTT (Method 3.1.7.2). Here the term UV dose means intensity of light (Watts/cm^2) over the exposure time (seconds) (Diffey, 2002). Figure 16A demonstrates UV dose to be one of the final considerations when generating HAMA hydrogels, with tunability via modification of wavelength, power, distance from light source, exposure time, etc. Figure 16B shows a photograph of the UV box system (Bartlett et al., 2020) alongside a schematic (right) indicating approximate distance of 11-13 cm between the light source and exposure area. To enable quantification of UV intensity across the exposure area, the surface was divided into 1 cm squares for generation of an intensity heat map (Figure 16C). Quantification (Figure 16C and 16D) shows greatest intensity of ~95 μW/cm^2 at the centre of the exposure area, as such plates/dishes were placed here (grey square/circle) for consistency. Intensity reduces incrementally with increasing distance from the centre of the exposure area, with intensities of ~30 μW/cm^2 observed at the outermost edge. Numerical quantification of intensity was carried out via scatter plotting of data points from the central 12x12 cm square, enabling assessment of UV penetrance through various mediums (Figure 16D). Figure 16D shows UV intensity is 94$\pm$7 μW/cm^2 during direct exposure. This reduced to 87$\pm$7 μW/cm^2 through a glass slide, 79$\pm$6 μW/cm^2 through the lid of a 6-well plate, 73$\pm$6 μW/cm^2 through the lid the lid of a petri dish and the greatest reduction to 62$\pm$5 μW/cm2 through a 0.5 cm height construct of 2% HAMA. Statistical testing of means found these reductions (of 7, 15, 21 and 32 μW/cm^2 through a glass slide, 6-well plate lid, petri dish lid and 0.5 cm height HAMA hydrogel respectively) to be statistically significant when compared to direct exposure control (One-way ANOVA with Dunnet's post-test, $P<0.0001$).

Following characterisation of UV intensity, investigation into the effect of UV dose (intensity *and* exposure time) was carried out on viability of SH-SY5Ys, NPCs and astrocytes (Figures 16E-G) 24 hours following exposure. The only significant difference observed across all experiments was the increase in viability seen after 60 seconds UV exposure (112.3 $\pm$2.3%) to SH-SY5Ys compared to the no UV control group (100%) (Unpaired t-test, $P<0.05$).

In order to identify cumulative effects of photoinitiator concentration and UV dose, further MTT assays were performed on SH-SY5Ys following simultaneous exposure to both LAP and 365 nm UV from the UV box system. Optimisation of both variables at once (Figure 16H) enables even greater tunability via exploitation of synergistic effects. SH-SY5Ys were again seeded into central wells of a 96 well plate prior to LAP exposure within media and subsequent

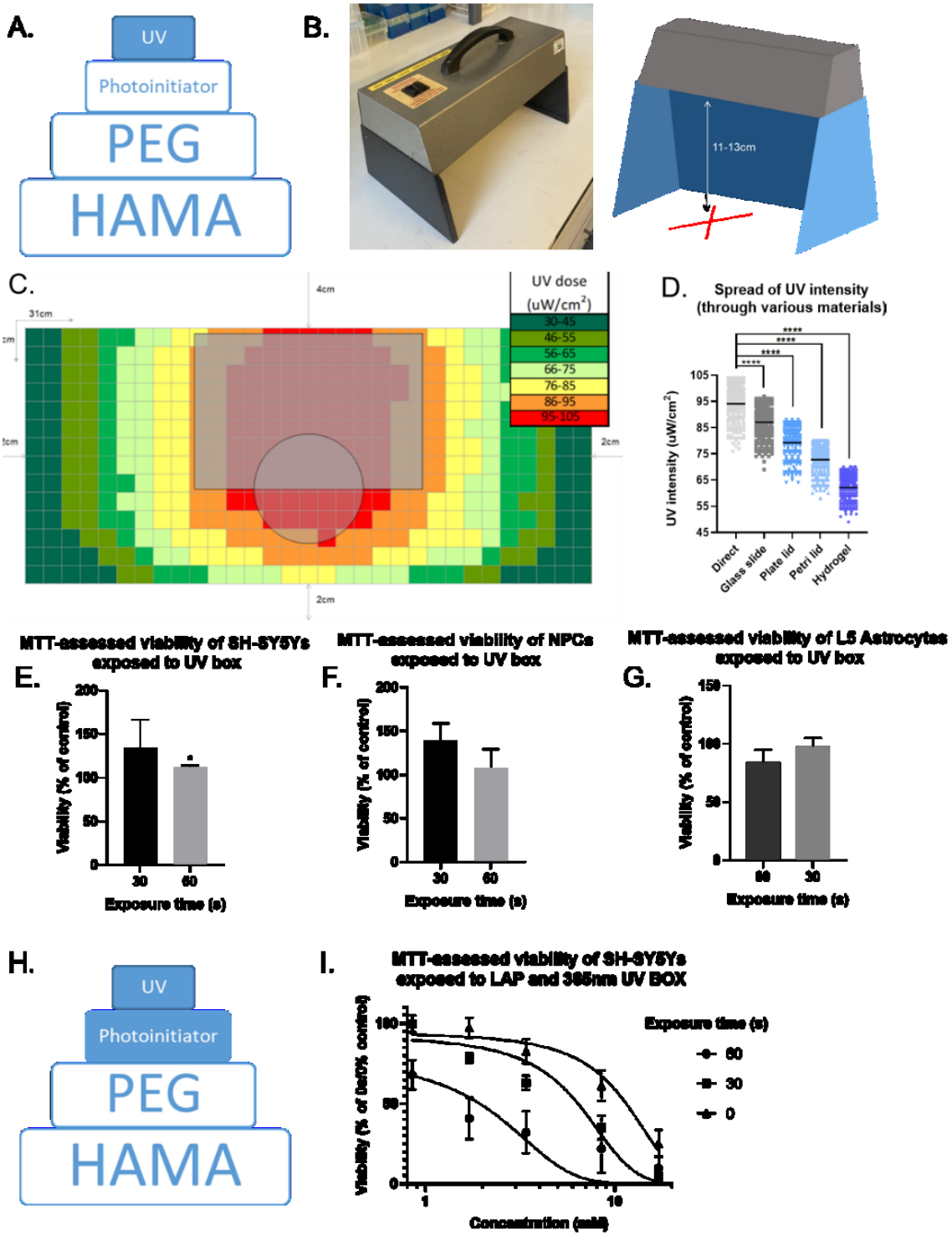

Figure 16. UV box system characterisation and associated toxicity effects on various cell lines. 16A) Schematic visualising UV dose as a highly tuneable variable when generating HAMA hydrogels. 16B) Photograph and schematic of UV box system. 16C) Quantification of UV dose via radiometer, grey box/circle representing the position of culture plates/petri dishes within the wider exposure area. 16D) Scatter plot consolidating spread of UV intensity, through various media, over exposure area. Bars representing mean ± SD (n=1, average n=3 technical repeats). P<0.0001 (****). 16E-G) MTT-assessed viability of SH-SY5Ys, L13 NPCs and L13 Astrocytes exposed to UV. Data normalised against untreated controls. Results expressed as mean ± SEM (n=3 biological repeats; average n=3 technical repeats per biological repeat); Unpaired t-test, P<0.05 (*). 16H) Schematic depicting a combination approach of modulating UV and photoinitiator to tune HAMA hydrogels. 16I) MTT-assessed viability of SH-SY5Ys exposed to LAP then UV. Data normalised against 0% LAP as control. Results expressed as mean ± SEM (n=3 biological repeats; average n=3 technical repeats per biological repeat).

UV treatment. Figure 16I presented viability of SH-SY5Ys following exposure to stimuli, as a dose-response graph with non-linear line of best fit. Statistical analysis (not labelled) shows significant reductions (Two-way ANOVA with Dunnet's post-test, P<0.0001) between 0 mM and 17 mM conditions within all of the time points (0, 30 and 60 s). No other significant differences were seen within 0 second conditions compared to the 0 mM control. Whereas treatment with 8.5 mM showed extremely significant reductions in viability when compared to 0 mM control (64.5 ±11.7%), in both 30 and 60 s conditions (27.1 ±10% and 25.7 ±18.2%, respectively) (P<0.0001).

Having optimised biological effects of LAP photoinitiator and UV dose, further optimisation was carried out to recreate mechanical features of the CNS within HAMA hydrogels. For consistency, PEG-575 was utilised for the following experiments (Figures 17 and 18), alongside the UV box system (as characterisation of the UV bulb system was ongoing). To study mechanical properties of HAMA hydrogels with various concentrations of photoinitiator (0-0.5%) exposed to 0, 30 or 60 s 365 nm UV, at a power of 94±7 μW/cm^2, rheological testing was carried out in the form of stress-controlled amplitude and frequency testing. Rheological analysis here is presented as mean ± SEM.

Figures 17A and 17B show viscous (G'') and elastic (G') moduli of 2% HAMA 10% PEG-575 hydrogels containing either 0.5% Irgacure 2959 or 0.5% LAP, following amplitude and frequency testing (Method 3.3). Following exposure to increasing stress, from 10^{-1} to 10^2 Pascals with frequency maintained at 1 Hz, 0.5% LAP presents with a storage (elastic) moduli of 4256±86.34 Pa and loss (viscous) moduli of 349.7±10.19 Pascals. Data also shows consistent elastic dominance of HAMA hydrogels made with 0.5% LAP; demonstrated by the fact these hydrogels were able to maintain shape following removal from the petri dish container utilised. Conversely, the same concentration of Irgacure 2959 presents with viscous dominance, made clear when handling as the material behaves like a liquid and cannot maintain shape. Elastic and viscous moduli present as 0.15±0.01 Pa and 1.21±0.03 Pa, respectively. Interestingly the elastic modulus decreases at high amplitude, while viscous moduli only slightly decreases. Results are supported by subsequent frequency testing (Figure 17B) shows frequency dependency of hydrogel mechanical features, from 10^{-1} to 10^1 Hz at a consistent stress of 0.1 Pascals. Data shows G' and G'' of 0.5% LAP conditions are 4361±57.84 and 148±16.28 Pa respectively, while 0.5% Irgacure hydrogels present with a G' of 0.01±0.57 Pa and G'' of 1.56±0.35 Pascals. Statistical analysis (Appendix 3.1) shows extremely significant differences (Repeated measures One-way ANOVA with Tukey's post-test, P<0.0001) between all conditions (both moduli/both photoinitiators), except for between G' and G'' of HAMA hydrogels made with 0.5% Irgacure 2959. Interestingly, 12B also shows

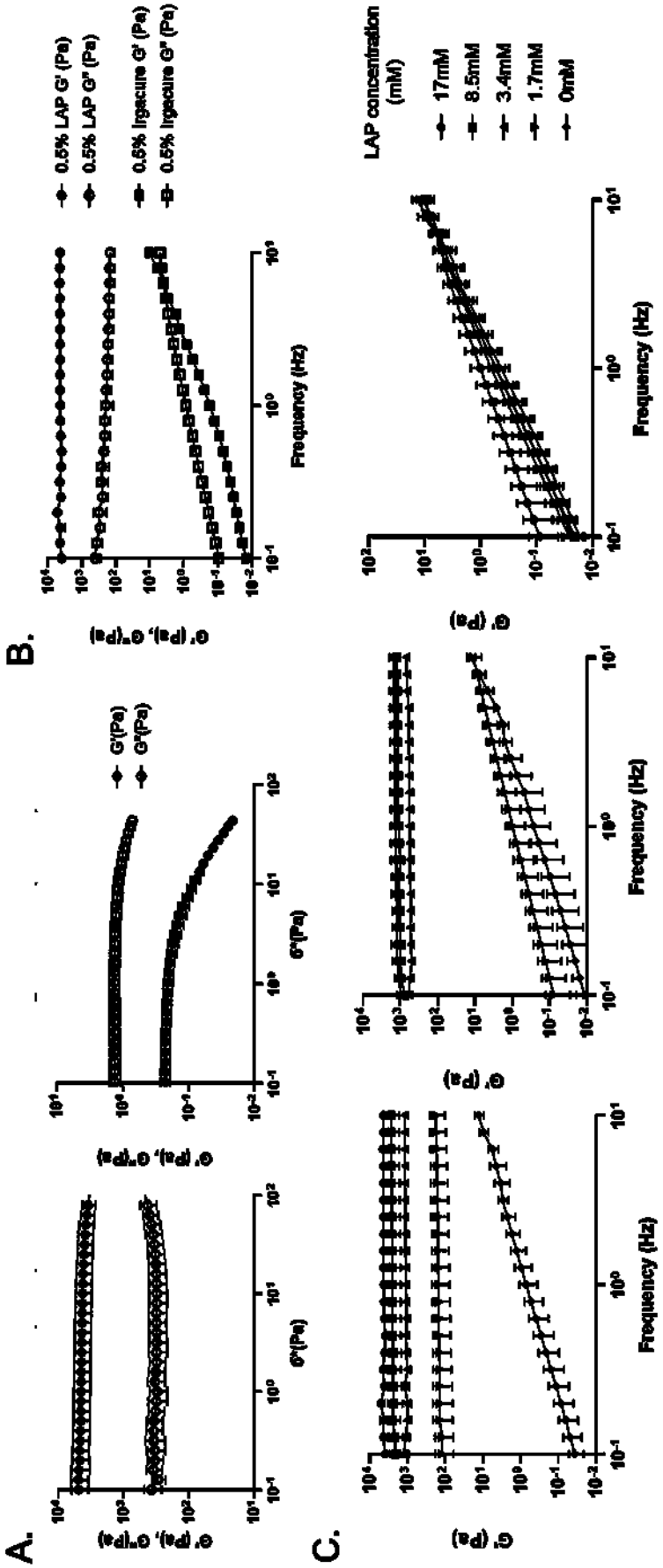

' and viscous G'' moduli of 2% (w/v) HAMA 10% (v
) seconds 365 nm UV from the UV box system.
cy of 1 Hz. Frequency sweep depicts viscoelastic r
drogels containing either 0.5% Irgacure 2959 or LA
only the elastic (G') moduli of HAMA hydrogels con
mean ±SEM (the average of n=3 biological repeats

viscoelastic moduli of 0.5% Irgacure conditions increasing with stress, resulting in eventual elastic dominance at a frequency of 10 Hz. Figures within 17C show frequency testing of 2% HAMA 10% PEG-575 hydrogels made with varied concentrations (0-0.5% or 0-17 mM) of only LAP photoinitiator, however only elastic moduli is shown here. Ungelated HAMA precursor exposed to 60 s UV dose from the box system formed elastically dominant hydrogels in the presence of LAP, displaying stability despite increasing frequency. This is supported by (Appendix 3.2) statistical analysis (Two-way ANOVA), whereby no significant differences in stiffness were observed between frequencies within LAP concentrations. There is a clear increase in G' alongside increasing concentration of LAP; G' increased from 153±3.36 Pa at 1.7 mM, to 1138±13.30 Pa at 3.4 mM, to 2562±39.43 at 8.5 mM, reaching a maximum of 4361±57.84 at 17 mM. Further statistical analysis (Two-way ANOVA) reveals significant variation of mean stiffness' across LAP concentrations ($P<0.0001$). The no LAP condition results in hydrogels that were physically difficult to handle due to liquid behaviour, demonstrated by the low elastic moduli and (not statistically significant) increase in G' with increasing shear rate, seen across all UV dose conditions.

HAMA precursors exposed to 30 seconds UV displayed a similar trend of increasing elastic moduli with increasing concentration of LAP, however numerical values themselves are lower, with a maximum stiffness of 1319±27.75 Pa observed at 17 mM LAP, under half of what is achieved with 17 mM LAP and 60 seconds UV exposure. Elastic moduli after 30 seconds exposure is 1101±26.2 Pa at 8.5 mM LAP, 576.6±11.46 Pa at 3.4 mM, 2.44±0.68 Pa at 1.7 mM, and 1.67±0.7 Pa at 0 mM. Here, both 0 mM and 1.7 mM LAP conditions showed an increase in G' with increasing frequency, where other concentrations showed visually stable values for G'. Interestingly, no statistically significant (Appendix 3.2, Two-way ANOVA) variability was observed between frequencies within LAP concentrations after 30 s UV exposure.

Finally, the 0 second UV exposure conditions presented with consistently low values for G'. Ascending from 0-17 mM: 2.21±0.78 Pa, 1.904±0.64 Pa, 2.36±0.78 Pa, 1.98±0.63 Pa and finally 2.36±0.64 Pa. In contrast to both 60 and 30 seconds UV treatment, no exposure to UV resulted in hydrogels displayed no significant variation (Two-way ANOVA with Tukey's post-test) despite the amount of LAP photoinitiator, bar one significant difference ($P<0.05$) observed between 0 mM and 17 mM conditions at the highest frequency of 10 Hz. Further analysis (Appendix 3.2) revealed no variation ($P<0.0001$) observed between frequencies within LAP concentrations, supported by Tukey's post-test findings where limited statistically significant ($P<0.0001$-0.05) differences were only observed when comparing against uppermost frequencies i.e. 5 Hz onwards. This indicates that there was a significant increase in stiffness as frequency rises.

To further study the complex relationship between photoinitiator concentration and UV exposure time, rheological data established in Figure 17 was averaged alongside amplitude sweep data, for inputting into Minitab statistical software to consider different variables for design of experiments (DOE) (Method 3.3.3). This enabled consolidation of complex datasets to provide greater insight into the synergistic polymerisation effects of photoinitiator and UV dose. Figure 18 demonstrates multiple ways of presenting the complex interplay of LAP concentration and UV dose delivered by the UV box system. In Figure 18A elastic moduli or G' is indicated via darkening shades of red, with darkest red indicative of the highest stiffness.

Figure 18A demonstrates the positive correlation between stiffness and increasing concentration of LAP photoinitiator and increasing UV exposure time, highlighting multiple

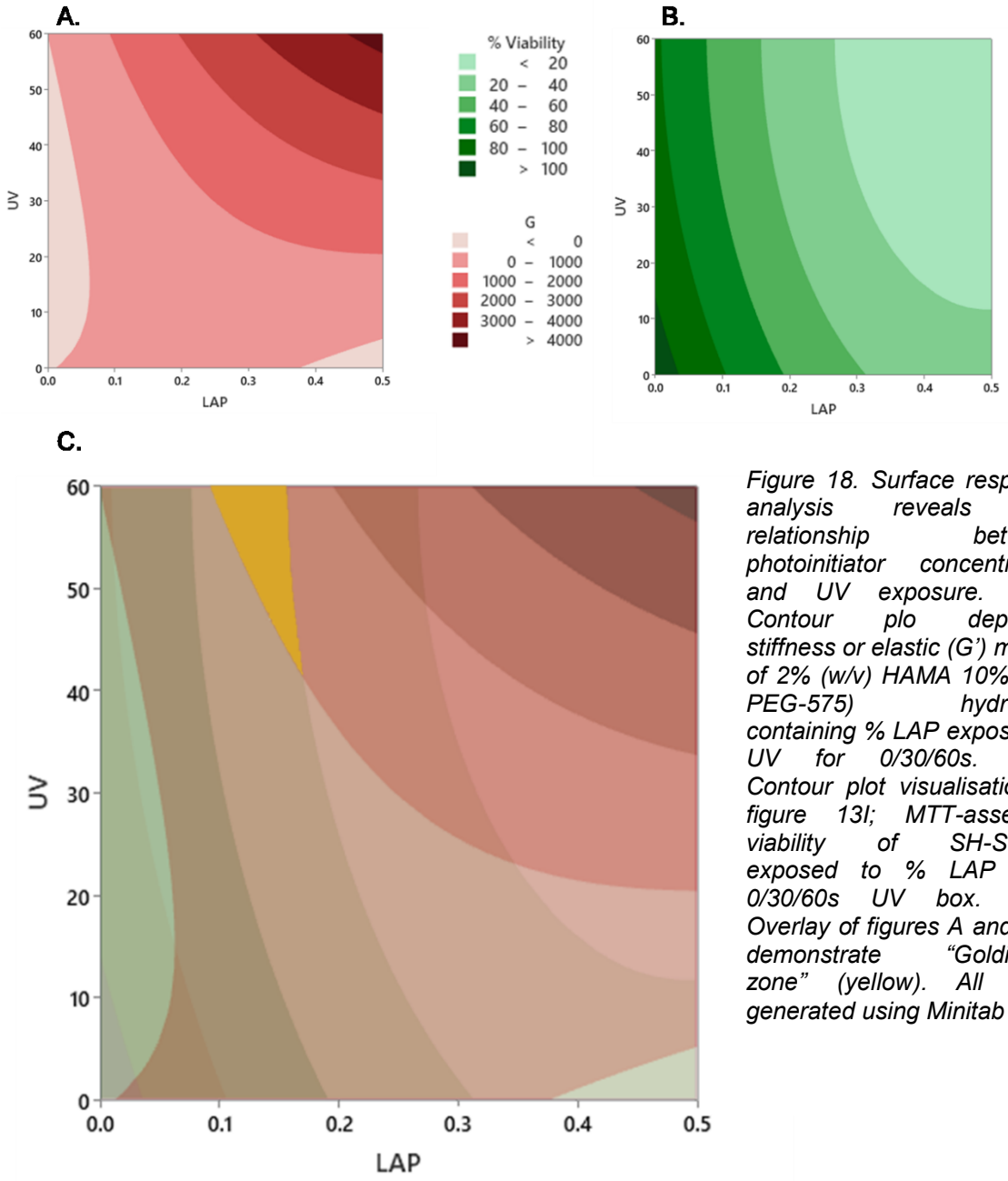

Figure 18. Surface response analysis reveals the relationship between photoinitiator concentration and UV exposure. 18A) Contour plo depicting stiffness or elastic (G') moduli of 2% (w/v) HAMA 10% (v/v) PEG-575) hydrogels containing % LAP exposed to UV for 0/30/60s. 18B) Contour plot visualisation of figure 13I; MTT-assessed viability of SH-SY5Ys exposed to % LAP then 0/30/60s UV box. 18C) Overlay of figures A and B to demonstrate "Goldilocks zone" (yellow). All plots generated using Minitab v.21.

possible combinations of LAP/UV that can produce a specific stiffness. Data shows elastic moduli of 4+ kPa was achieved by utilising 0.5% (or 17 mM) LAP and 60 seconds of UV box exposure. Data also indicates stiffness of 3-4 kPa was reached by utilising ~0.3 to 0.5% LAP alongside ~45 to 60 seconds UV; with reduced concentration of LAP requiring more UV exposure time, and vice versa, to achieve a similar elastic moduli. With decreasing stiffness, shaded areas become larger. Therefore, to achieve elastic moduli of 2-3 kPa, LAP concentrations can fall between a wider range of ~0.22% to 0.5% LAP with UV exposure times of ~35 to 60 seconds. To achieve 1-2 kPa stiffness, an even greater range of conditions may be utilised, from ~0.1% to 0.5% LAP with ~20 to 60 seconds UV exposure. The largest area depicts stiffness of < 1kPa, achieved via the full range processing conditions (up to 0.5% LAP and 60 seconds UV exposure). However balancing is necessary, i.e. greater concentrations of LAP require less exposure time.

Similarly, figure 18B displays the effect of LAP photoinitiator and increasing UV exposure time on MTT-assessed viability of SH-SY5Y cells in 2D culture. Greatest viability is seen at low concentrations of both LAP and UV, with a viable majority (greater than ~50%) only at or below LAP concentrations of 0.2%. Alternatively, when utilising no or low LAP, viability is maintained ~100% despite extreme UV exposure times of 60 seconds. Interestingly, shaded areas are not uniform in size, with larger areas moving from left to right as viability decreases. The curvature of boundaries between areas is suggestive of a non-linear cytotoxic relationship between LAP and UV. The largest area in the top right is indicative of viabilities below 20%, and is irregular in circularity with a heavier leaning towards extremities of LAP (0.5%) vs extremities of UV (60 seconds). Presentation of data via surface response methodology allows for overlaying of contour plots 15A and 15B to produce figure 18C; providing valuable insight into how variables of LAP concentration and UV dose can be optimised to select for biologically relevant stiffness whilst maximising cell viability. Here that optimised zone is referred to as the “Goldilocks zone” whereby LAP concentrations of <0.2% and 40-60 seconds of UV box exposure result in an elastic moduli of 1-2 kPa whilst maximising cell viability ~60%.

4.3. Discussion

The aim of this chapter was to identify, investigate and explore hydrogel biomaterials for neural tissue engineering applications, via biological assessment and rheological characterisation.

Initial investigation revealed readily available materials such as GG and HyStem™ were unsuitable due to handling issues or high cost (Figures 12 and 13). Figure 12 demonstrates rounded morphologies within GG bioinks, as expected from liquid-dominant materials, resulting in suspension culture of SH-SY5Ys. Rheological testing showed that HyStem™ hydrogels display elastic dominance (Figure 12B), with stiffness of around 25 Pascals.

Comparison of HyStem™ G' in Figure 12B and G' of HAMA hydrogels in 13C show different elastic values and behaviours. These differences may be attributes to differing chemical modifications to the HA backbone; HAMA relies on interaction of PEG-575 and photoinitiator with methacrylate groups, whereas HyStem™ is a thiolated form of HA that is crosslinked by PEG-3500 in the presence of additional components such as carboxymethyl hyaluronic acid-thiopropanoyl hydrazide (CMHA-S, CMHA-DTPH, carboxymethyl hyaluronic acid-DTPH) (Sigma-Aldrich, 2012, Zarembinski and Skardal, 2018). The addition of these additional chemical components may be responsible for the unusual viscoelastic behaviour of HyStem™, with a low G' yet still displaying elastic dominance and able to retain its shape during handling. While the G' of HyStem™ falls at the lower end of biologically relevant stiffness (23.7$\pm$1.7 Pa, Figure 12B), and this polymer does indeed display biological compatibility and activity, its use in research is limited by high cost. The HyStem™ system can be utilised to produce constructs up to several hundreds of Pascals in stiffness (Sigma-Aldrich, 2012). However, researchers exploring biomaterials for neural culture typically utilise hydrogels ranging from hundreds to thousands of Pascals (Bartlett et al., 2020, Farrukh et al., 2017, Grifno et al., 2019, Khoshakhlagh and Moore, 2015, Moxon et al., 2019, Sun et al., 2017). Rheology of "soft solid" hydrogels, within the context of neural modelling and HAMA hydrogels, is reviewed further in discussion sections.

From the limited fluorescence observed in Figure 12 we can infer loss of viability, potentially due to failure to attach to the surrounding substrate resulting in death by anoikis. Another explanation may be ionic concentrations of the liquid phase (PBS or dH_2O) inducing cell death via interruption of fundamental cell processes due to osmosis. As expected, relatively high fluorescence of SH-SY5Ys in HyStem™ at day one, as this hydrogel is known to be biocompatible (Zarembinski and Skardal, 2018). Unusually, cells appear to aggregate in HyStem™ conditions, despite an abundance of biologically active proteins to bind to within the polymer network (Zarembinski and Skardal, 2018). Whats more, fluorescence appears to decrease at day two within HyStem™, indicating cell death. One explanation may be that cells have simply settled to the bottom of the construct due to a slow gelation process or relaxation period. While use of fluorescent SH-SY5Ys enables visualisation of cell encapsulation via fluorescence microscopy, quantification is problematic, due to reduced efficiency of staining with co-stains reduced penetrance through gelated materials, difficulty imaging across Z-planes, and difficulties in retrieving cells from within the gel.

In order to overcome this issue, future work utilised culture of cells *on* hydrogel materials (Figure 13), to enable detachment for counting, ease of imaging, and better uptake of dyes/stains by cells. Hyaluronic acid hydrogels were selected following examination of the literature (Section 1.4.2.1) and preliminary assessment of HA-based hydrogel HyStem™,

revealing high biological compatibility (Figure 12). Chemical modification of HA to HAMA was carried out in order to provide better control over photopolymerisation kinetics and ultimate viscoelastic properties. NMR spectra (Method 3.2.1.4) show successful methacrylation of HA to form HAMA, with introduction of dual peaks beyond 5.6 ppm (Appendix 8) confirming methacrylation of the HA backbone (Ondeck and Engler, 2016, Spearman et al., 2020, Tsanaktsidou et al., 2019). Due to time limitations, NMR spectroscopy was not performed on HAMA biofunctionalised with CC or GG peptides. However, literature suggests a reduction in CH2 groups will be seen in biofunctionalised HAMA due to increased binding of peptides (Tsanaktsidou et al., 2019).

Chemical modification is advantageous as hydrogels made from natural polymers may show inconsistent degradation behaviour (He et al., 2020), possibly due to the reversible/physical nature of crosslinking method. Use of HAMA within the literature for neural tissue culture is established (Wu et al., 2017, Lam et al., 2014, Ondeck and Engler, 2016, Pereira et al., 2023, Poldervaart et al., 2017, Spearman et al., 2020). GG hydrogels were utilised as a low-attachment comparison against HAMA hydrogels made with either 0.5% LAP or Irgacure 2959.

Cells were observed to aggregate together on GG and HAMA conditions (Figure 13A); with increased aggregation at day three on GG hydrogels as SH-SY5Ys seek out contact cues to avoid death by anoikis. This is a possible cause of loss of fluorescence visible by day six, as GG is known to be biocompatible (Aref et al., 2018). Controversially, recent work suggests that “inert” materials. previously thought to lack adhesion sites, may indeed possess areas for attachment however sparse configuration limits cell binding (Cooke et al., 2018). This may explain some of the cell attachment and spreading visible by day six. Alternatively, this observation may be due to SH-SY5Y cells migrating around or through the hydrogel and adhering to the plastic well bottom. This migration seems likely with hydrogels made from natural polymers, such as GG, known to lose structural integrity in physiological conditions (e.g. 37°C, highly-hydrated, abundance of divalent ions) (Zia et al., 2018) enabling migration of cells. Research by Hsu *et al*. (2022) could suggest this is advantageous for permitting cell migration and neurite extension (Hsu et al., 2022).

Upon examination of SH-SY5Ys on HAMA hydrogels, we observe immediate reductions in viability, with total loss by day six. This is supported by live/dead staining enabling manual quantification of cell viability. This effect may be attributed to toxicity of LAP and Irgacure 2959 at high concentrations (Xu et al., 2020), however both photoinitiators are widely used for tissue engineering applications due to advantageous characteristics (Choi et al., 2019, Fairbanks et al., 2009, Mironi-Harpaz et al., 2012). In opposition to observations here, use of Irgacure at

0.5% within HA hydrogels has been shown to produce biocompatible gels (Khoshakhlagh and Moore, 2015). However, researchers utilised a UV dose of 181 mW/cm^2 for 55 seconds, compared to the UV box system utilised here that emits ~95 μW/cm^2 (Figure 16) and was utilised for 60 seconds. Reduced intensity of the UV box system employed in Figure 13 may be responsible for this disparity, with insufficient UV exposure leading to leftover Irgacure 2959 within the system, inducing toxicity of cells within the local microenvironment. Alternatively, the cause of the discrepancy may be that Khoshakhlagh and Moore (2015) utilised PEG with a molecular weight of 1000 Mn (Khoshakhlagh and Moore, 2015), whereas research here utilised PEG-575, which is shown to be more cytotoxic (Choi et al., 2019). Most likely, these factors compound one another, resulting in production of 2% HAMA hydrogels with exacerbated toxicity (Figure 13A and 13B).

Irgacure 2959 displays greater toxicity compared to LAP in 2D viability assays (Xu et al., 2020). This is supported by work herein with LAP based HAMA gels showing viability up to day one, whereas Irgacure 2959 does not (Figure 13A). Furthermore, autofluorescent debris can be observed as an increase in background fluorescence or small irregular particles of fluorescence. This may be due to necrotic cell death resulting in release of mCherry protein into the extracellular environment. Quantification of viability in Figure 13B supports these findings, however shows no statistically significant difference between viability of cells exposed to 0.5% LAP or 0.5% Irgacure 2959 hydrogels, this therefore required further investigation (Figure 13).

Rheology shows both GG and HAMA-0.5% LAP hydrogels display biologically relevant stiffness (~700Pa and 4.2 kPa, respectively), with elastic dominance (G'>G'') necessary for creating constructs that do not collapse under their own weight. HAMA hydrogels made with 0.5% Irgacure 2959 display low elastic and viscous moduli that increase with shear rate. Discussion of this shear thickening behaviour is carried out later. Nevertheless, viscoelastic moduli observed within this condition fail to recapitulate tissue stiffness *in vivo*, with lack of crosslinking rendering this biomaterial incapable of recreating the complexity of crosslinked polymeric networks *in vivo*. Literature suggests hydrogels possessing stiffness in the range of 1-3 kPa is most beneficial for promoting differentiation, neurogenesis and neurite outgrowth; however hydrogels varied greatly in polymer type, concentration and mode of crosslinking (Khoshakhlagh and Moore, 2015, Moxon et al., 2017, Sun et al., 2017). Hydrogel biomaterials (both HAMA here and alternative hydrogel biomaterials from the literature) are there useful for recreating mechanical properties of brain tissue, when we consider CNS tissue within humans to display stiffness in the range of ~0.1-10 kPa (Handorf et al., 2015, Kim and Choi, 2019, Pogoda et al., 2014, Sartori et al., 2014). Interestingly, biofunctionalisation of hydrogels with IKVAV motifs led to increased stiffness, as well as improving neural differentiation (Farrukh et

al., 2017). This suggests inclusion of IKVAV motifs within HAMA hydrogels developed here may be an additional method of tailoring stiffness to match native brain tissue. Bartlett et al. demonstrated 1% w/v alginate hydrogels best matched mechanical stiffness of rodent cortex tissue, with an elastic modulus of ~7 kPa, however this was assessed via compressive mechanical analysis (Bartlett et al., 2020). This becomes important when we consider brain tissue has shown to stiffen during compressive testing (as opposed to tensile mechanical analysis), whereas fibrous polymer networks display the inverse (Distler et al., 2020). Nevertheless, work here and supporting literature (Choi et al., 2019, Ondeck and Engler, 2016, Poldervaart et al., 2017, Spearman et al., 2020, Wu et al., 2017) demonstrates suitability of HAMA as a neural biomaterial; but optimisation of photoinitiator type and concentration is needed (Figure 15).

Before further optimisation of light-based polymerisation via photoinitiator and UV systems, molecular weight and concentration of PEG was optimised to ensure ideal biocompatibility within HAMA hydrogel constructs (Figure 14). PEG was utilised alongside HAMA to provide non-specific mechanical support to the low concentration (2% w/v) HAMA polymeric network. This is particularly advantageous when we consider complex viscoelastic behaviour of living tissue is underpinned by composite arrangement and crosslinking of multiple polymeric networks (Libertiaux and Pascon, 2009, Palmese et al., 2019). PEG is highlighted as a minimally-toxic polymer within the literature (Choi et al., 2019), however low molecular weights are found to exhibit greater toxic effects (Biondi et al., 2002).

Figure 14 looked to establish toxicity of low molecular weight (Mn 575) and high molecular weight (Mn 3500), within the context of HAMA hydrogels for neural tissue engineering. PEGs were matched via molar concentration and percentage concentration within media, to account for differences in molecular weight. Work shows PEG-575 to be extremely toxic even at lowest concentrations of 1%, whereas PEG-3500 is well tolerated with no statistically significant reductions in viability at 48 uM (equivalent to 14%) and 15% (Figure 14B and 14C). Figures 14D and 14E expand upon this with neural-specific cell types, with neural cell types/stem cells shown to display increased sensitivity to toxic effects of PEG compared to immortalised SH-SY5Y. This is supported by NPCs experiencing the greatest toxicity (Figure 41E). Both Figures display extremely significant reductions beyond 10%, however both cell types are able to retain at least 75% viability at 10% PEG. While individual differences between conditions vary in significance (Figures 14B-E), there is a clear negative correlation between cell viability and concentration of PEG, with PEG-3500 displaying superior biocompatibility compared to PEG-575. As such further 3D cell work (Figures 21 and 22) would therefore utilise PEG-3500 and a concentration of 10% to minimise toxic effects while still providing mechanical support.

Following determination of polymeric foundations of hydrogel biomaterials, modulation of photopolymerisation via type and concentration of photoinitiator was necessary (Figure 15). Assessment of toxic effects of Irgacure 2959 and LAP via MTT-assay provides quantitative expansion of conclusions drawn from Figure 13, with both photoinitiators showing increasing toxic effects with concentration. While Figure 13 shows similar degrees of toxicity of HAMA hydrogels made with 0.5% Irgacure 2959 or LAP, even at uppermost concentrations utilised in Figures 15B and 15C, Irgacure 2959 is found to produce a far more statistically significant reduction in viability (LAP $P<0.05$, Irgacure 2959 $P<0.0001$). Figure 15 also suggests Irgacure 2959 may exhibit toxic effects at lower concentrations compared to LAP. This is supported by research finding overall viability of cells to be higher in gelatin methacrylate hydrogels with LAP, than those within Irgacure 2959 do (Xu et al., 2020). Research by Fairbanks *et al*. (2009) contradicts this, finding no significant loss or difference in cell viability between LAP and Irgacure 2959 (Fairbanks et al., 2009); however concentrations found to demonstrate significant losses in viability (5.1 mM and 8.4 mM for Irgacure 2959 and LAP respectively) within Figure 15 far exceed that of Fairbanks' work (2.2 mM for both Irgacure 2959 and LAP). Further testing at higher concentrations may be needed in order to observe significant losses and differences in viability. However, Fairbanks *et al.* (2009) assess viability within final 3D hydrogel constructs, whereas work here isolates photoinitiator as a variable for 2D toxicity testing, not accounting for the reduction in photoinitiator immediately following cleavage following UV exposure.

Figures 15D and E enable replication of 15C with increased physiological relevance to the CNS due to utilisation of NPCs and astrocytes. Figure 15D suggests only the highest concentrations of 17 mM to be significantly toxic to NPCs, whereas astrocytes seem to be more sensitive with an almost immediate significant reduction in viability at 3.4 mM. Further work should look to elucidate the mechanism of toxicity for each cell type and repeat experiments to accurately determine toxic effects. Despite such limitations, data shows a clear relationship between increasing photoinitiator concentration and toxic effects. As such, future work looked to minimise photoinitiator concentration whilst promoting generation of hydrogels with desirable stiffness (Figure 17).

Figure 16 looked to characterise the UV box system and investigate cytotoxicity of UV dose provided by this system, alongside cumulative cytotoxicity of LAP and UV. Modulation of UV dose is a powerful tool for controlling photopolymerisation kinetics (Figure 16A) with identification of dose variables important to better understand implications for biological and biomechanical effects. With light wavelength and distance from source established (Figure 16B), radiometry (Method 3.5) was used to evaluate UV intensity (Figures 16C and 16D). This is important as existing research utilising UV-polymerised biomaterials (Table 4) often lack necessary detail.

Author(s)	Year	Cell type	Hydrogel Polymer	Conc	Method of X-linking	Conc	UV dose
Wu et al.	**2017**	hiPSC-NPCs	HAMA	0.75%	Irgacure 2959	0.05%	320 μW/cm^2, 30/60 s
Pan et al.	**2013**	Fibroblast	PEG	10-20%	Irgacure 2959	0.20%	4.96 W/cm^2, 30 s
Poldervaart et al.	**2017**	MSCs	HAMA	1-3%	Irgacure 2959	0.1%,	365 nm, 3 mW/cm^2, 10 mins
Dobre et al.	**2021**	Rat DRGs	PEG	3.50%	Irgacure 2959	0.10%	5 mW/cm^2, 6 mins
Suri et al.	**2011**	Schwann cells	HAMA	1-10%	Irgacure 2959	1%	8 mW/cm^2, 30s per layer
Snyderet al.	**2014**	MSCs	HA-methacyrlic anhyride	1 mg/mL	Irgacure 2959	1%	350 nm, 10 mW/cm^2, 5 mins
Dai et al.	**2021**	Fibroblasts	Elastin-like polypeptide	3-7.8%	LAP	0.025%	365 nm, 76.2 mW/cm^2, 15 s
Periera et al.	**2023**	Mouse NPCs	GelMa + AlgMa + HA	5% + 1% + 1.5%	LAP	0.05%	365 nm, 3 W/cm^2, 5 s
Xu et al.	**2020**	Fibroblasts	Gelatin methacrylate	5%	LAP/Irgacure 2959	0.2-0.9%	365 nm, 10 mw/cm^2, 45 s
Fairbanks et al.	**2009**	Fibroblasts	PEG (Mn 4600)	10%	LAP/Irgacure 2959	2.2 mM	365/405 nm, 10 mw/cm^2
Foster et al.	**2021**	N/A	PEG (Mn 700)	3%	Omirad	0.10%	320-500 nm, 4 mins

Table 4. UV-crosslinking approaches utilising LAP and Irgacure 2959. Researchers often fail to include all necessary variables necessary for replication of UV dose.

UV intensity or irradiance is measured in Watts/cm^2, mW/cm^2, μW/cm^2 (Diffey, 2002), it was therefore convenient and logical to utilise a probe with a 1cm^2 surface area and divide the UV exposure area into a grid comprised of 1x1cm squares. This approach was susceptible to human error with manual manoeuvring of the probe and logging of output data by hand; however, the method was kept consistent for all measurements in Figures 16C, 16D, 20C and 20D, enabling relative comparison despite the imperfect approach. This also enabled assessment of reduction in UV intensity through various media (Figure 16D) necessary when UV curing in sterile environments whereby the culture vessel lid cannot be removed. Interestingly, smallest reductions where observed through plate and petri lid dishes, suggesting only minor adjustments are necessary to translate UV dose from direct exposure within a sterile environment, to exposure through the lid of a culture vessel in a general non-sterile lab environment. This approach may allow researchers to more readily adopt UV polymerisation approaches without the need for expensive sterile UV sources.

Penetrance of UV dose is also an important consideration for curing of thick hydrogels constructs, whereby the dose received at Z-planes closer to the UV source will be higher than that of lower planes, inducing unintended heterogeneity of photopolymerisation (and therefore mechanical properties) within the hydrogel material. Properties of the biomaterial that the UV must pass through must also be considered. Properties of interest that influence UV penetrance through hydrogel biomaterials include volume of the sample and resultant height or thickness, density of polymer network, opacity, liquid fraction, inclusion of chemicals e.g.

antioxidants (which may quench photoinitiator-generated free radicals necessary for photopolymerisation) and additional components that may impede UV light transmission e.g. solid matter such as fibres, particles or even cells. These factors, alongside UV dose variables mentioned previously, will contribute to XYZ specificity of UV dose and localised distribution of free radicals. Within this experiment 2% HAMA, 10% PEG-575 and 0.5% LAP hydrogels photopolymerised for 5 minutes by the UV box system with a height of 0.5 cm were utilised in Figure 16D, due to similarity to HAMA constructs utilised herein. Investigation of UV transmission through a greater variety of hydrogel biomaterials would provide greater insight into causes of mechanical heterogeneity within photo-polymerised HAMA-LAP hydrogels. Further work should also look to investigate penetrance of UV through liquid phases, such as culture media, to understand implications of physiological culture conditions when utilising UV photopolymerisation approaches within tissue engineering.

Investigation into the effect of UV dose on cell viability yielded unclear and largely statistically insignificant results, bar one increase in viability observed in SH-SY5Ys after 60 seconds exposure to the UV box system (Figure 16E). This was unexpected, as UV exposure is known to induce cellular damage via destabilisation of DNA (Ghasemi et al., 2021, He et al., 2022). One explanation for the unusual results seen here may be that the MTT assay fails to provide an accurate measure of cell viability following UV exposure. While the mechanism of MTT reduction to the blue dye formazan is not fully understood, reduction occurs in metabolically active cells to provide an indication of overall cell viability (Ghasemi et al., 2021). However, radiation reduces membrane integrity and increases mitochondrial activity, potentially presenting as a false increase in cell viability (Ghasemi et al., 2021). This may be because mitochondrial DNA is particularly susceptible to UV damage from reactive oxygen species, with lack of histones preventing tight packing and lack of excision repair mechanisms (He et al., 2022). The response of astrocytes to UV exposure was of particular interest as astrocytes are heavily involved in mediating of inflammatory responses that occur following insults to the CNS, via homeostatic maintenance of antioxidants and reactive oxygen species (Chen et al., 2020). However, whether astrocytes display resistance to free radical-induced metabolic dysfunction remains unclear. Inconclusive nature of MTT-assessed viability data here suggests a different methodology should be utilised in order to quantify viability of cells directly exposed to 365nm UV.

Characterisation and optimisation data presented in Figure 16 culminates in investigation into the combinatorial effect of both LAP photoinitiator concentration (mM) and UV exposure time (seconds) from the box system (Shown to be ~95 μW/cm^2 in Figures 16C and 16D). Figures 16E-I show greatest reductions in cell viability were observed at high UV dose (60 seconds) compared to lower doses, and high LAP (17 mM) compared to lower concentrations of LAP,

with the largest reduction observed at 17 mM LAP 60 seconds exposure. Statistically significant differences are observed within exposure times, particularly from 8.5 mM. These results, combined with observations from the dose-response curve, are indicative of a cumulative toxicity effect of LAP photoinitiator and UV exposure time. Utilising a dose-response graph with curved of best fit is advantageous as this enables prediction of biological effects of combinations not specifically explored here. This becomes more apparent upon comparison against Figures 16E to 16G whereby no significant differences were observed with UV alone. Results in Figure 15 also support the cumulative nature of toxic effects seen in 16I, with exposure to only LAP displaying statistically significant decreases to 80.5 ±0.5% and 74.9 ±8.4% at 8.5 mM for SH-SY5Ys and NPCs respectively. Astrocytes also display increased sensitivity to LAP with reductions in viability from 3.4 mM (80.6 ±3.8%). However, such reductions are not as severe as those observed in SH-SY5Y cells exposed to LAP but no UV in 13I, with reductions to 64.6 ±11.7% at 8.5 mM. This is supported by research by that found exposure to photoinitiator *or* UV did not produce the same extend of cytotoxic effects as exposure to photoinitiator *and* UV (Mironi-Harpaz et al., 2012).

Following 2D biological optimisation of photoinitiator concentration, viscoelastic properties of HAMA hydrogels were quantified via rheological testing. Figure 17A-B show amplitude and frequency sweep testing of 2% HAMA 10% PEG-575 hydrogels made with 0.5% LAP or Irgacure 2959 and exposed to 60 seonds UV box. Comparison of amplitude sweeps of HAMA-LAP and HAMA-Irgacure 2959 shows HAMA-LAP produces much stiffer and more stable hydrogels than the latter; with linearity of elastic dominant behaviour even at high stress (100 Pa), compared to viscous dominance of HAMA-Irgacure 2959 and almost immediate deformation of viscoelastic components at low shear (~1 Pa). This stress-dependent deformation is indicative of a loss of internal structuring, whereby the material starts to flow or break down. We can attribute this behaviour to limited photopolymerisation of HAMA-Irgacure 2959 hydrogels, likely due to low reactivityof Irgacure 2959 and less likely due to other variables such as UV dose or handling of the un-gelated precursor, as these factors were controlled for across conditions.

Amplitude sweeps were plotted separately due to variable stress values during averaging, whereas frequency sweep data is presented together, as Hz is consistent across tests (Figure 17B). Figure 17B supports data from 17A, depicting elastic stability of HAMA-LAP hydrogels in a time-dependent manner, with maintenance of ~4000 Pa G' with increasing shear rate. The same cannot be said for HAMA-Irgacure 2959, as increasing viscoelastic moduli with shear rate is indicative of shear-thickening behaviour within the polymeric system. Shear-thickening materials may also be coined "dilatant", due to slight dilation or expansion of the solid-phase presenting as a "loss" of liquid and increased viscosity (Amoo and Layi Fagbenle,

2020). The molecular mechanisms responsible for shear-thickening behaviour are lesser understood than shear-thinning, however can be sorted into two categories: nonlinear tension along stretched chains beyond the Gaussian range, or an increase in the number of elastically active chains (Xu et al., 2010). This may be due to inadequate formation of photo-induced chemical bonds, resulting in deformation of the system even at low shear rates, due to dominance of (reversible) physical bonds. Research into supramolecular polymer networks reveals shear-thickening behaviour of gelated materials may be attributed to reversibility of (supramolecular) bonds (Xu et al., 2010). Dilatant behaviour of HAMA-Irgacure 2959 is not seen in HAMA-LAP hydrogels, possibly due to increased crosslinking of the polymeric network protecting against dilation of the solid-phase network, with such "stronger" hydrogels displaying linear behaviour due to a reduced propensity for network degradation (Figure 17A) or dilation (Figure 17B). Further research into mechanisms underpinning shear-thickening is necessary in order to better understand mechanical behaviours of hydrogel biomaterials and exploit this knowledge for tissue engineering approaches, especially when looking to recreate the unusual viscoelastic properties of the CNS.

Toxicity of Irgacure 2959 (Figure 15), alongside the inability to form stable gels, meant this photoinitiator was not considered for further experiments. Both viscous and elastic moduli are also extremely low for HAMA-Irgacure 2959 hydrogels, even at a high concentration of 0.5%, making this material unsuitable for modelling mechanics of CNS tissue due to lack of mechanophysical relevance. As such only HAMA-LAP hydrogels were taken forward for rheological optimisation of concentration and UV exposure time (Figure 17C). Only elastic moduli (G') are presented in Figure 17C for ease of data interpretation and comparison to literature surrounding stiffness of hydrogels. Results show clear reductions in stiffness (G') when decreasing concentration of LAP within each exposure time, but also when comparing across conditions of reducing exposure time (at the same concentration of LAP). Lack of stable elastic moduli within 0s conditions indicates the need of both a photoinitiator and UV exposure in order to induce photopolymerisation of the polymer network to produce a "solid" or elastically dominant hydrogel. This is supported by similar behaviour of 0mM conditions within 30 and 60 seconds conditions. Interestingly, hydrogels made with 1.7 mM and exposed to 30 seconds UV display similar behaviour but slightly increased elasticity. This may suggest a threshold of UV dose and photoinitiator must be reached in order to generate enough free radicals to catalyse the photopolymerisation process.

Statistical analysis revealed LAP concentration to be a larger source of stiffness variation than frequency within 30 and 60 second conditions (Figure 17C). The inverse is true for 0 second conditions, with all LAP concentrations showing similar values (0.02$\pm$0.01 Pa (0 mM) to 0.09$\pm$0.05 Pa (17 mM) at 0.1 Hz, rising to 14$\pm$3 Pa (0 mM) to 11.2$\pm$1 Pa (at 17 mM) at 10 Hz)

and the same pattern of increasing G' with shear rate. The lack of significant differences between LAP concentrations at 0s provides further evidence to show both LAP and UV are necessary to induce photo-crosslinking. Interestingly, the 17 mM LAP condition presents with a slightly stiffer hydrogel at 0 seconds, despite the total lack of UV exposure. This may be due to visible light sensitivity of LAP at high concentrations (Sharifi et al., 2021). This supports the idea of a polymerisation threshold whereby optimal LAP/UV interactions are needed to generate free radicals for catalysis of the polymerisation chain reaction. For example 1.7 mM LAP exposure for 30 seconds generates similar G' values to that of hydrogels made with 17 mM, but only exposed to visible light during handling. This result also suggests that photoinitiator concentration can be minimised to limit toxicity via compensation of UV dose i.e. reducing LAP concentration would improve biocompatibility of HAMA hydrogels. However, this would require a greater UV dose to achieve the same rheological properties. Having discovered photopolymerisation of HAMA hydrogels is dictated by interaction of LAP and UV exposure time; further statistical analysis looked to investigate this complex relationship underpinning polymerisation kinetics, in order to exploit this polymerisation mechanism for recreation of CNS mechanical properties such as stiffness. Improved control over viscoelastic properties of HAMA biomaterials would also enable tailoring of a model system to mimic inflammatory conditions; increasing viscosity of HA biomaterials could mimic modification via covalent attachment of heavy chains that occurs during inflammation (Cowman et al., 2015).

Figure 18 consolidates data from Figure 17C to produce contour plots that elucidate the relationship between LAP, 365 nm UV exposure time (UV box system) and elastic moduli of hydrogels (G'). While this enables visualisation of large datasets, this approach relies on extensive data processing; averaging of large amounts of continuous rheological data results in loss of outliers, meaning results shown in Figure 18 are therefore approximations and conclusive assumptions cannot be made without further experimental work. Whats more, input data here was categorised discretely (e.g. 0, 30 or 60 seconds), therefore some results displayed here are often predictions of stiffness based upon existing data. Inclusion of more data (e.g. more time points, 5, 10, 15 seconds etc.) would produce contour plots with increased resolution and provide better insight into the complex relationship between photoinitiator and UV that underpins polymerisation of HAMA hydrogels. Another cause for concern when utilising this statistical analysis approach is the presentation of G' as below 0 which is not possible, however this may be resolved by improved resolution following further testing as mentioned above. This demonstrates HAMA-LAP hydrogels not exposed to UV will possess inherent stiffness, due to viscosity of HAMA solutions but also visible light polymerisation (Figure 17C).

Despite the drawbacks mentioned previously, the surface response methodology used here (Figure 18) is advantageous in enabling prediction of hydrogel stiffness and cell viability beyond existing experimental work, with statistical analysis providing insight into the complex relationship between photoinitiator and UV. This approach confirms the cumulative effect of UV and LAP on stiffness of HAMA hydrogels. The non-linear trend observed with increasing LAP concentration and UV exposure time suggests distinctive interactions underpin complex mechanisms driving polymerisation. The reduction in size of stiffness region at the uppermost exposure times and concentrations may suggest saturation of crosslinking sites and ultimately a maximum possible stiffness, further experiments could explore this. Nevertheless, Figure 18A demonstrates the ability to tune viscoelastic properties by controlling photopolymerisation via careful balancing of UV dose and photoinitiator concentration. Within the context of neural tissue engineering, the photopolymerisable HAMA biomaterial developed here could be incredibly useful for generating soft biomaterials, but also recreation of mechanical gradients observed *in vitro* via spatiotemporal modulation of UV dose i.e. increasing intensity of UV along a singular axis, potentially via increased power.

This methodology is also used in figure 18B to visualise data quantified in figure 16I, better displaying the cumulative effect of LAP photoinitiator concentration and UV dose on cell viability. Figure 18B also suggess LAP holds greater responsibility for cytotoxicity than UV. With LAP unable to retain majority viability (~ 50%) above ~0.2%, whereas this is possible even at UV dose of 60 seconds. This is supported by skewing of the <20% viability area towards the LAP axis, indicating optimisation of this variable should be the first step when looking to limit cytotoxic effects during photopolymerisation. The non-linear relationship observed between variables in 18B further supports conclusions drawn from 18A; that complex mechanisms underpin reaction of LAP and UV to generate free radicals responsible for both polymerisation and cytotoxic effects.

Figure 18C demonstrates how contour plots generated via surface response methodology can be overlaid to optimise conditions for multiple desirable outcomes. Identification of the “Goldilocks zone” enables data-driven optimisation of HAMA hydrogel photopolymerisation conditions; with figure 18C indicating limitation of LAP below 0.2% is the best approach to maximising viability whilst still enabling tuning of mechanical properties via UV dose. While the “Goldilocks zone” could be adjusted to maximise viability further (i.e. only consider positions with greater than 80% viability), this would result in a compromise of stiffness below the 1 kPa stiffness already identified as biologically relevant (Section 1.3.2.3). Because of this, further work would therefore limit HAMA hydrogels to 1.7mM or 0.05% LAP, manipulating UV dose as a means to guide formation of hydrogels with biologically relevant stiffness whilst minimising cytotoxic effects (Chapter 5).

To conclude, this approach allows for prediction of response outside current experimental parameters e.g. discrete conditions of 0/30/60 seconds UV were input into DOE software, however resultant contour plots display a continuous response. Whilst this may be advantageous for preliminary testing, further exploration is necessary in order to improve resolution of contour plots and therefore accuracy of predicted responses and "Goldilocks zones". A specific criticism of the overlay approach in figure 18C is that this depicts stiffness values for 3D hydrogel materials (figure 18A) whereas cell viability data was obtained via 2D viability assay (Method 3.1.7.2). This 2D approach was utilised due to ease of use compared to 3D methods, which may require additional optimisation and validation (Bresciani 19, Dominijanni 2021). This discrepancy between dimensions may result in inaccurate conclusions to be drawn from figure 18C. Future work should therefore look to closely match experimental methodologies and processing conditions, even when evaluating different responses or outcomes. Despite limitations, the use of DOE and surface response methodologies is a valuable tool for optimising complex experimental parameters for maximising desirable responses.

5. Biomaterial Optimisation

5.1. Introduction

Chapter 4 determined optimum conditions for producing HAMA hydrogels (Type of PEG (Figure 14), concentration of photoinitiator (Figures 15, 16 and 17), UV exposure time (Figures 16, 17 and 18)) to promote biocompatibility while generating biologically relevant stiffness. Next steps investigated the effect of photoinitiator concentration and UV dose, but focusing upon modulation of UV intensity as a means to guide photopolymerisation of HAMA hydrogels.

5.1.1. Photopolymerisation

Photo-crosslinking is broadly explored within the literature (Choi et al., 2019, Tytgat et al., 2017), with specific reviews highlighting challenges of bioprinting and replicating neural tissue (Billiet et al., 2012, Sokolovski et al., 2018). Methacrylation to form HAMA is advantageous for achieving improved mechanical properties via photopolymerisation (Spearman et al., 2020, Ondeck and Engler, 2016). Photopolymerisation relies on the use of photoinitiators, a light source, and the chosen polymer. Photopolymerisation via free-radical initiated chain polymerisation is used for generating hydrogels from engineered synthetic polymers or natural polymers modified with groups of interest. The exact mechanism for photo-crosslinking may vary, however photoinitiators used herein (type I radical photoinitiators LAP, Irgacure 2959) rely on cleavage following exposure to photons from UV light, producing free radicals. These highly reactive radicals then react to cleave bonds within functional groups of the polymer, promoting formation of chemical crosslinks between polymer chains. While this approach affords spatiotemporal tuning of both physical and biochemical features, it is not without limitations such as cellular toxicity of free radicals, inefficient control over kinetics of the reaction and residual functional groups that have the potential to react negatively with biological molecules (Choi et al., 2019). On the other hand, the latter may actually aid in biological functional modification, whereby unreacted functional groups can be exploited for chemical bonding of additional components e.g. adhesion proteins.

The aim of this chapter was to carry out biological and mechanical optimisation of HAMA biomaterials, utilising immortalised SH-SY5Y alongside healthy neural precursor cells (NPCs) and astrocytes.

5.2. Results

Having established the UV bulb system affords greater tunability of UV dose via modulation of exposure time *and* intensity (Figure 19D); HAMA hydrogels were generated for mechanical testing utilising this system. However from this point only PEG-3500 was used as this was determined to be more biocompatible than PEG-575 (Figure 14). Rheological analysis

(Method 3.3) in figure 19 is referred to as “translational rheology” as focus was given to recreating mechanical features seen in previous work (Figures 17 and 18) with PEG-575 and the UV box system, “translating” the findings for use within a more tuneable (UV bulb system) and biocompatible (PEG-3500) approach.

Figure 19A, similarly to 16A, depicts UV dose as a powerful consideration when generating HAMA hydrogels. However, characterisation of the UV bulb system (Method 3.5) goes further by modifying intensity of the dose, instead of just exposure time. Figure 19B shows a photograph and schematic (left to right) of the UV bulb set up, with an approximate distance of 8.5cm between the LED bulb and exposure area. Exposure area was broken up into 1x1cm squares (as previously, Figure 16C) for quantification via radiometry. Figure 19D shows intensity significantly increased in all conditions compared to 0.5i (Two-way ANOVA with Tukey’s post-test, $P<0.0001$), with (Appendix 4.1) significant differences observed between all conditions ($P<0.0001$). Average irradiance values were reported in mean $\pm$ SD from 1210 ± 86 μW/cm^2 at 0.5i, to 2553 ± 194 μW/cm^2 at 1i, to 3887 ± 269 μW/cm^2 and 5344 ± 350 μW/cm^2. No significant differences were observed across readings of intensity within conditions i.e. all readings (3x3 cm area shown in Figure 19C) of intensity were consistent within 0.5i, 1i, 1.5i and 2i.

Rheological analysis (Method 3.3) of HAMA hydrogels made with 0.5% LAP and 10% PEG-3500 exposed to UV from the bulb system was carried out via amplitude sweep testing (Figure 19E), demonstrating viscous dominance of all conditions. Specific values for G’ (elastic) and G’’ (viscous) components (Table 5) show a trend of reduction in all conditions with increasing amplitude of oscillatory force. Elastic moduli, or G’, display the largest reductions following increased amplitude, however this was not found to be statistically significant until the most extreme stresses of 5 Pa (Appendix 4.2). Within each condition, differences between G’ and G’’ were found to be statistically significant (Table 5). Interestingly, significant differences (Appendix 4.2) were found between all conditions besides G’ of 30s 1.5i vs. G’ of 30 seconds 2i, G’ of 60 seconds 1.5i vs. G’ of 30 seconds 2i, and G’’ of 60 seconds 1.5i vs. G’’ of 30 seconds 2i. Ensuing frequency sweep testing (Figure 19F) shows similarly low values for G’ and G’’ (Table 5). Interestingly, no significant differences (Appendix 4.3) were observed between G’ and G’’ within each condition

.

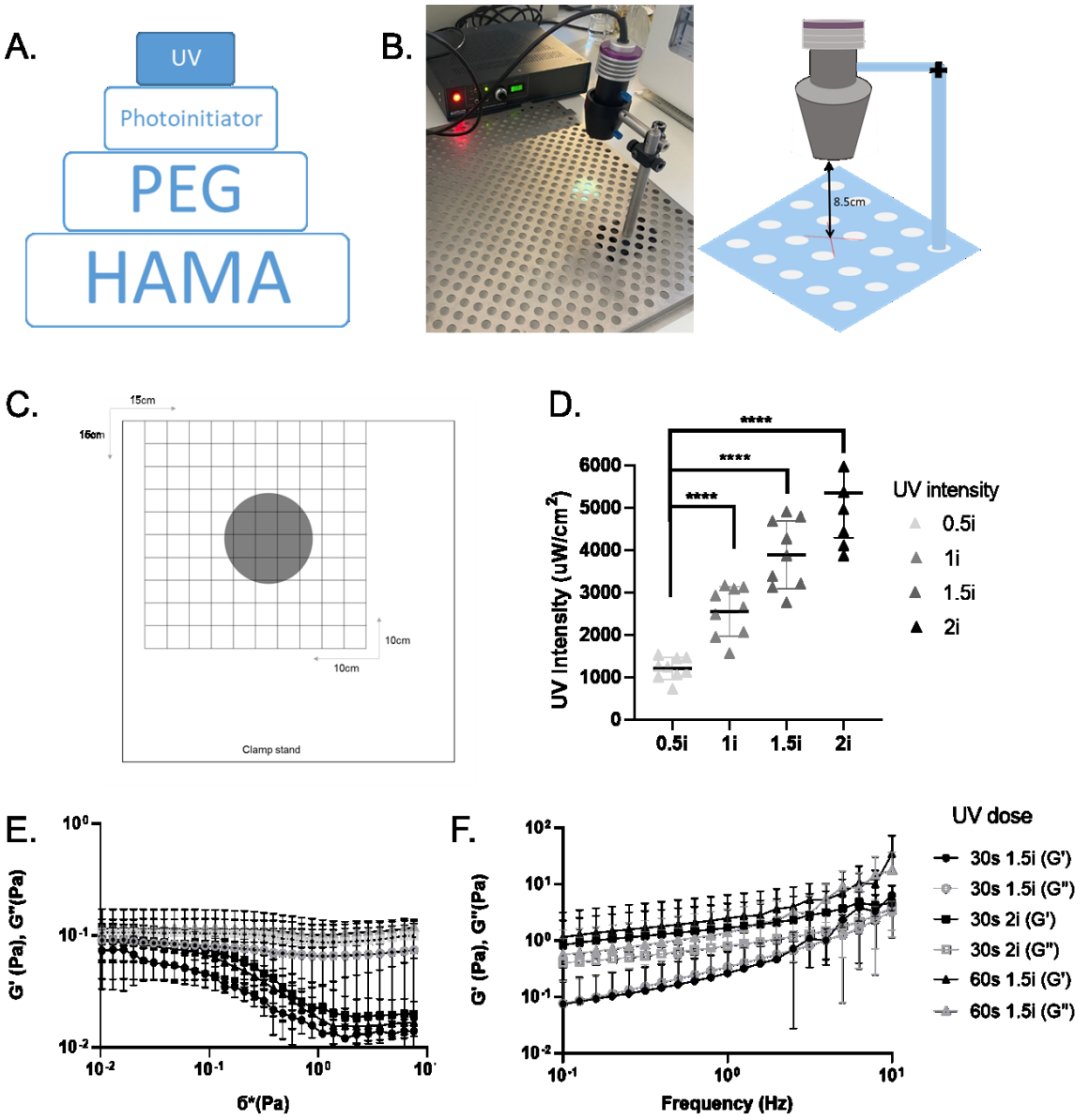

Figure 19. UV bulb system characterisation and translational rheology. 19A) Schematic visualising UV dose as a highly tuneable variable when generating HAMA hydrogels. 19B) Photograph and schematic of UV bulb system. 19C) Schematic of UV exposure area, grey circle representing position of petri dishes within the wider 15x15 cm area. Position of well plates not shown, as plates are moved to expose specific wells i.e. exposure area (3x3 cm) fits a singular 6 well, or up to 4 96 wells. 9D) Scatter plot comparing spread of UV intensity of 9 measurement points within the UV bulb system exposure area; 9 squares over central 3x3 cm exposure area utilised for crosslinking. Bars represent mean + SD (9 measurement points, average of n=3 technical repeats per measurement point)19E-F) Small Oscillatory rheology reveals elastic (G') and viscous (G") moduli of 2% (w/v) HAMA, 10% (v/v) PEG-3500, 0.05% (w/v) LAP hydrogels made in PBS exposed to 1.5i or 2i UV for 30 or 60 seconds. Amplitude sweep testing occurred over increasing stress (0.1-150 Pa) at a constant frequency of 1 Hz. Frequency sweep depicts viscoelastic moduli as a function of frequency ranging from 0.1-10 Hz. Data here is expressed as mean + SD (average of n=3 biological repeats; with n=3 technical repeats per biological repeat).

Condition	Amplitude Sweep		Frequency Sweep	
	G' (Pascals)	G'' (Pascals)	G' (Pascals)	G'' (Pascals)
30s 1.5i	0.04±0.02	0.08±0.01	1±1.64	0.68±0.83
60s 1.5i	0.06±0.03	0.1±0.01	4.99±7.24	3.67±4.8
30s 2i	0.05±0.03	0.11±0.01	2.15±1.25	1.12±0.88

Table 5. Average elastic (G') and viscous (G'') moduli values for 2% (w/v) HAMA, 10% (v/v) PEG-3500, 0.05% (w/v) LAP hydrogels made in PBS exposed to 1.5i or 2i UV for 30 or 60 seconds, corresponding to figures 19E and F.

While previous work examined the mechanical features of HAMA hydrogels exposed to UV from the bulb system (Figure 19), biological assessment of this UV source (Method 3.1.7.2) was necessary (Figure 20), as done previously for the UV box system (Figure 16). Figure 20A depicts UV dose as the final variable that can be tuned for modulating photopolymerisation of HAMA hydrogels, therefore various intensities of the UV bulb system (exact UV intensity characterised in Figure 19D) were evaluated for effects on cell viability. Figures B-D show the effect of intensities 0.5-3 in increments of 0.5 on MTT-assessed viability of SH-SY5Ys, NPCs and astrocytes. SH-SY5Ys presented with viability of ~80% (82±7.5% at 0.5i to 90.1±3.1% at 3i) across all conditions, however no statistically significant reductions were observed (Two-way ANOVA with Tukey's post-test). Both NPCs and astrocytes presented with variable changes in viability compared to 100% viability of the control, but again no statistically significant differences were observed.

Figures 20F-H expand upon this, via investigating synergistic toxic effects of LAP and UV bulb dose via MTT-assessed viability of SH-SY5Ys, NPCs and astrocytes following exposure. Here graphs are presented as dose-response graph with non-linear line of best fit. Optimisation of both variables together enables for even greater tuning of HAMA hydrogel polymerisation (Figure 20E). SH-SY5Ys showed reductions in MTT-assessed viability following exposure to LAP and UV, with significant reductions in cell viability observed between control (0 mM LAP) and 3.4/8.5 mM conditions for the 60 seconds exposure group (Two-way ANOVA with Dunnet's post-test, $P<0.0001$). Furthermore, within the 30 seconds exposure group, statistically significant reductions were observed between control and (82. 6±4%) 1.7mM ($P<0.01$), (42.3 ±12.5%) 3.4 mM and (30.6 ±12.4%) 8.5 mM (both $P<0.0001$). 60, 30 and 0-second groups displayed relatively consistent reduction to 92.5 ±2.4%, 94 ±1.8% and 89.8 ±3.8% respectively at 0.17 mM. At 0.85 mM, these values reduced further to 75.7 ±1.9%, 89 ±2+0.7% and 83 ±3.8%. At 1.7 mM, values of 69.4 ±1.4%, 82.6 ±4% and 80 ±11.2% were observed. By 3.4 mM, values of 43 ±1.9%, 42.3 ±12.6% and 72.8 ±7.6% were seen.

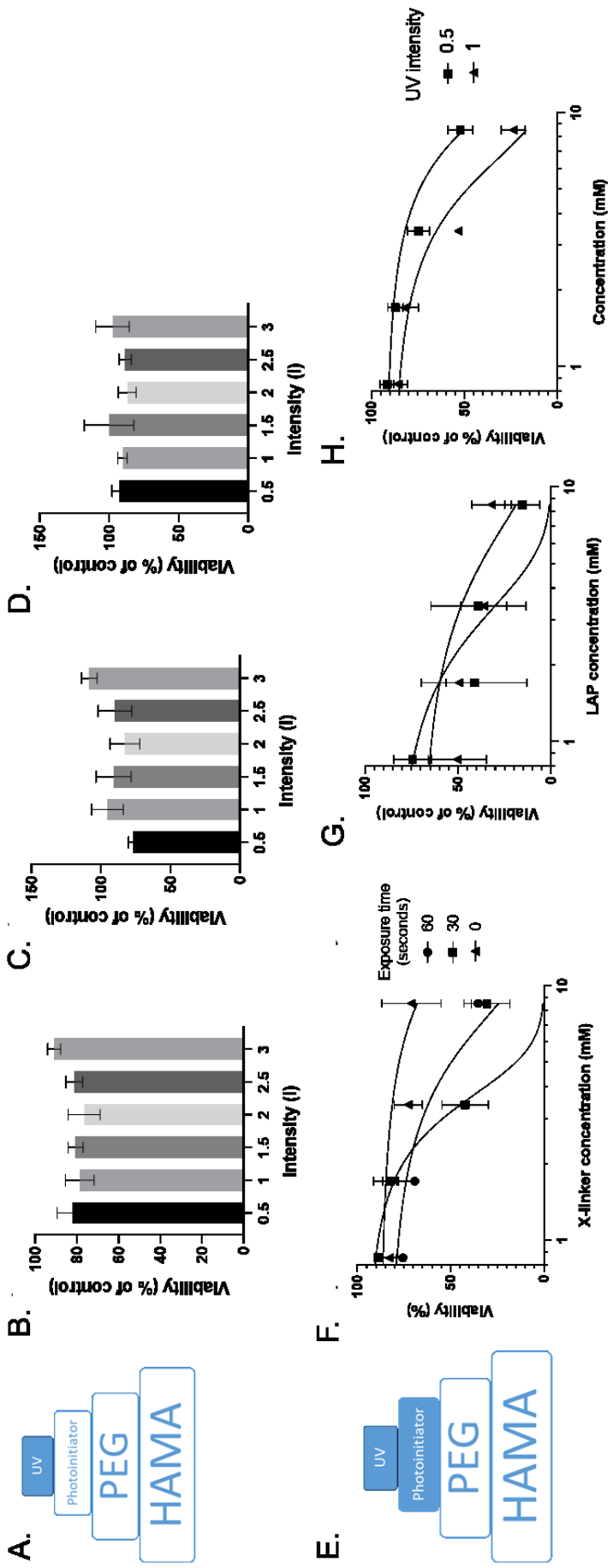

NPCs and L13 astrocytes exposed to UV from the bulb s variable when generating HAMA hydrogels. 20B-D) Viab approach of modifying UV dose and photoinitiator. 20F) ata normalised against 0 mM LAP control. 20G-H) L5 N ds. Data normalised against 0mM LAP at 0s exposure a ere is expressed as mean + SD (average of n=3 biologica

Finally, at 8.5 mM LAP, SH-SY5Y viability reduced to 35.3 ±3.7%, 30.6 ±12.4% and 71 ±15.9% for 60/30/0 second conditions respectively. The consistency of reductions across exposure time groups is supported by statistical analysis (Appendix 5.1, Two-way ANOVA with Tukey's post-test), showing no significant differences within exposure times for each LAP concentration.

In an alternative approach, NPCs and astrocytes were exposed to either 0.5 or 1 intensity for the same amount of time (30 seconds). Figure 20G shows reductions in cell viability with increasing LAP concentration and UV intensity. Statistically significant (Appendix 5.2) reductions were observed at 1.7 mM (Two-way ANOVA with Dunnet's post-test, $P<0.001$), 3.4 mM ($P<0.001$) and 8.5 mM ($P<0.0001$) compared to control within the 0.5i group. Similar reductions are seen in the 1i group, whereby 0.85 mM and 1.7 mM ($P<0.01$), alongside 3.4 mM and 8.5 mM ($P<0.0001$) concentrations displayed significantly reduced viability compared to control. Within the 0.5i group, average percentage viability values decreased as LAP increased; 85.2 ±4.3% at 0.17 mM, then significant reductions to 74.5 ±5.8%, 41.4 ±16.4%, 39.2 ±14.8%, and 15.5 ±5.5%. The same trend was observed in the 1i group, with viability decreasing from 72.6 ±8.3% at 0.17 mM, to 50.4 ±9%, with significant reductions to 49.4 ±4.2%, 36.3 ±7.1%, and 32.2 ±6%. No significant differences were observed between 0.5 and 1i conditions within each concentration.

Figure 20H repeats this work with astrocytes. Average percentage viability values for conditions exposed to 30 seconds 0.5i UV were (in ascending LAP concentration, 0.17-8.5 mM) 94.3±0.9%, 91.8 ±2.1%, 87.2 ±2.4%, 74.8 ±3.4% and 52.3 ±4%. Statistically significant (Appendix 5.3) reductions were observed for the last three highest LAP concentrations (1.7, 3.4 and 8.5 mM) when compared to control (Two-way ANOVA with Dunnet's post-test, $P<0.05$, $P<0.0001$, $P<0.0001$ respectively). Within the 1i group, no significant reductions were observed at 0.17 mM with viability of 90.6 ±3%. On the other hand, significant reductions were observed with reductions to 85.9 ±2.9% at 0.85 mM ($P<0.01$), 82 ±4.1% at 1.7 mM ($P<0.001$), finally 53.3 ±0.7% and 24 ±3.7% at 3.4 and 8.5 mM ($P<0.0001$), respectively. No statistically significant differences were seen between 0.5 and 1i conditions within each concentration, aside from at 3.4 mM (Two-way ANOVA with Tukey's post-test, $P<0.001$) and 8.5 mM ($P<0.0001$).

Previous work carried out 2D optimisation of HAMA hydrogel variables; PEG molecular weight (Figures 14), photoinitiator concentration (Figures 15, 16, 17 and 20) and UV intensity and exposure time (Figure 16, 17 and 20). This was done by MTT assay (Method 3.1.7.2) (Figures 14, 15 and 20), alongside 3D investigation via cell culture studies (Figures12 and 13) and rheological testing (Figure 13 and 17). Having carried out biological optimisation of variables

via 2D cell culture and mechanical investigation of 3D hydrogels, additional work looked to translate these findings into a singular 3D experiment encompassing both biological and mechanical assessment (Figure 21). Figures 21A and B depict the rationale and workflow of generating 2% HAMA hydrogels, with six conditions enabling exploration into the combined effect of PEG (no PEG, PEG-575, PEG-3500) and the use of LAP (0%/0 mM or 0.5%/17 mM) alongside the UV bulb system (1.5i for 60 seconds). Figure 21C shows conditions A-E appeared visually similar in terms of transparency and viscoelastic behaviour, with hydrogel materials in these conditions displaying similar fluid behaviour during handling i.e. materials spread and move within the wells during rotation of the culture plate. This is true excepting for condition F made with PEG-575 and 0.05%/17 mM LAP that appeared more opaque by eye when compared to other conditions and was not observed to move as fluidly within the plate during handling. Quantification of viscoelastic behaviour via rheological testing (Method 3.3) (Figure 21D) showed differing elastic (G') behaviour of conditions A-F. Conditions A-E all displayed an increase in viscoelastic moduli with increased shear rate, whereas condition F comprised of PEG-575 and LAP displays stable elastic moduli at 458.2$\pm$18.73 Pa. This increase is extremely significant (Appendix 6, Two-way ANOVA with Tukey's post-test, $P<0.0001$) compared to all other conditions. Whats more no significant differences were observed within elastic moduli of F as frequency increases, bar between stiffness at 0.1Hz and the highest five frequencies 4, 5, 6, 7.9 and 10 Hz ($P<0.05$, $P<0.05$, $P<0.05$, $P<0.01$ and $P<0.01$ respectively). Condition D presented with highest stiffness of conditions A-E, however still low at 10.36$\pm$7.05 Pa. The stiffness of hydrogels in condition E fell centrally with an average G' of 3.17$\pm$3.03 Pa. Conditions A and C were shown to display overlapping elastic moduli, with averages of 1.8$\pm$0.67 Pa and 1.1$\pm$0.29 Pa. The moduli of condition B with PEG-3500 and no LAP averages at 1.36$\pm$0.58 Pa. Statistical analysis revealed no significant differences in elastic moduli between frequencies (within and across conditions) or between conditions (within and across frequencies), aside from when comparing against condition D at frequencies of above 6 Hz ($P<0.05$ to 0.0001).

Alongside mechanical assessment of HAMA conditions, hydrogel biocompatibility was evaluated via seeding of fluorescent SH-SY5Ys onto the gel surface (Figure 21E). Live fluorescent microscopy was carried out for seven days, with the addition of DAPI stain at day seven enabling additional indication of cell viability. HAMA hydrogels made without LAP (conditions A-C) presented with rounded cells dispersed throughout the Z-plane, with no attachment seen and visible debris at all time points. Limited fluorescence was seen within conditions A and B at day one, however total loss of fluorescence by day seven. Condition C presented with minimal fluorescence initially, and again loss of fluorescence by day seven.

Within conditions D to F in Figure 21, cells displayed rounded morphologies at day one; however, fluorescent monolayers indicated settling of viable cells *on* the hydrogel surface. Interestingly, greater fluorescence was observed in condition F, whereby HAMA hydrogels are made with both PEG-575 and LAP. By day five visible clumping of cells can be seen in conditions D and E, slightly more so in D with formation of dense "tubes" containing fluorescent cells. Both D and E exhibited sustained fluorescence and aggregation of cells until day seven, whereas condition F showed total loss of fluorescence beyond day one, where cells maintained rounded monolayer morphology across the entire gel surface.

Previous work in this chapter established optimal composition of HAMA hydrogels for biocompatibility; condition E (2% HAMA 10% PEG-3500, 0.05% LAP) was taken forward for further investigation (Figure 22). However, UV dose was increased to 60 seconds at 2i from 60 seconds 1.5i, as this was shown to produce hydrogels with low elastic modulus (Figure 21C). The tissue culture protocol was expanded (Figure 22A) to include addition of laminin peptides to promote adhesion and BDNF to promote survivability of SH-SY5Ys.

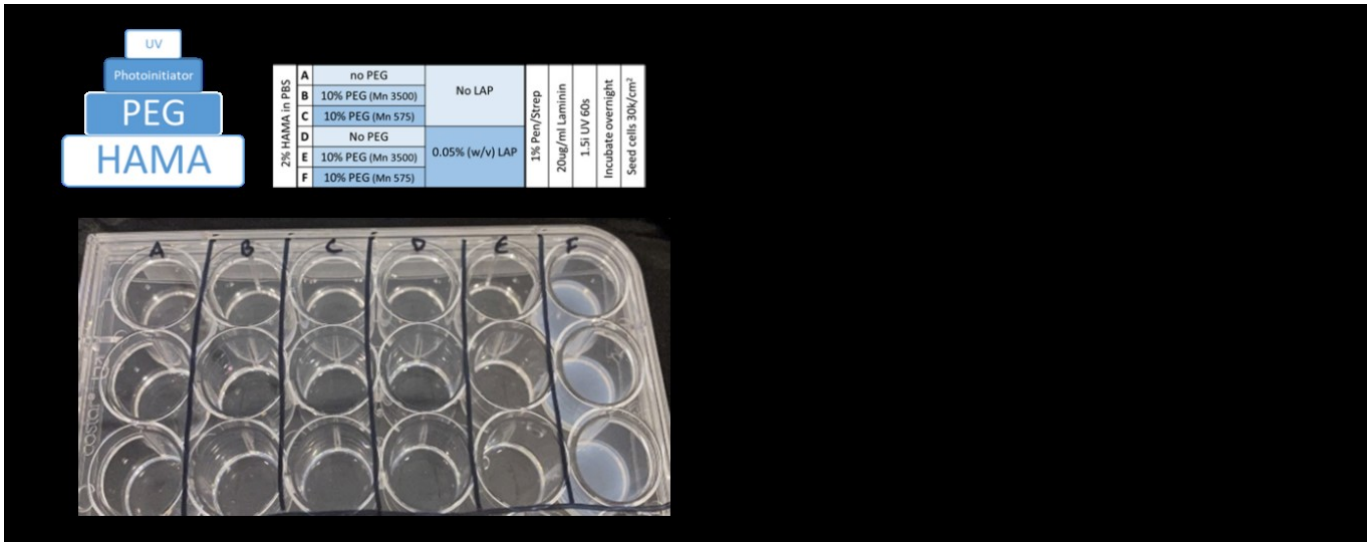

Figure 21. Optimisation of 2% HAMA hydrogels for neural culture. 21A) Schematic indicating modulation of PEG and photoinitiator to be foundational for determining properties of HAMA hydrogels. 21B) Composition & workflow of different HAMA conditions labelled A-F. 21C) Representative photograph of conditions A-F. 21D) Small oscillatory rheology reveals elastic (G') moduli of conditions A-F. Frequency sweeps were performed following amplitude testing to display elastic moduli as a function of frequency from 0.1-10 Hz. Results here expressed as mean ± SD (average n=3 biological repeats; with n=3 technical repeats per biological repeat).

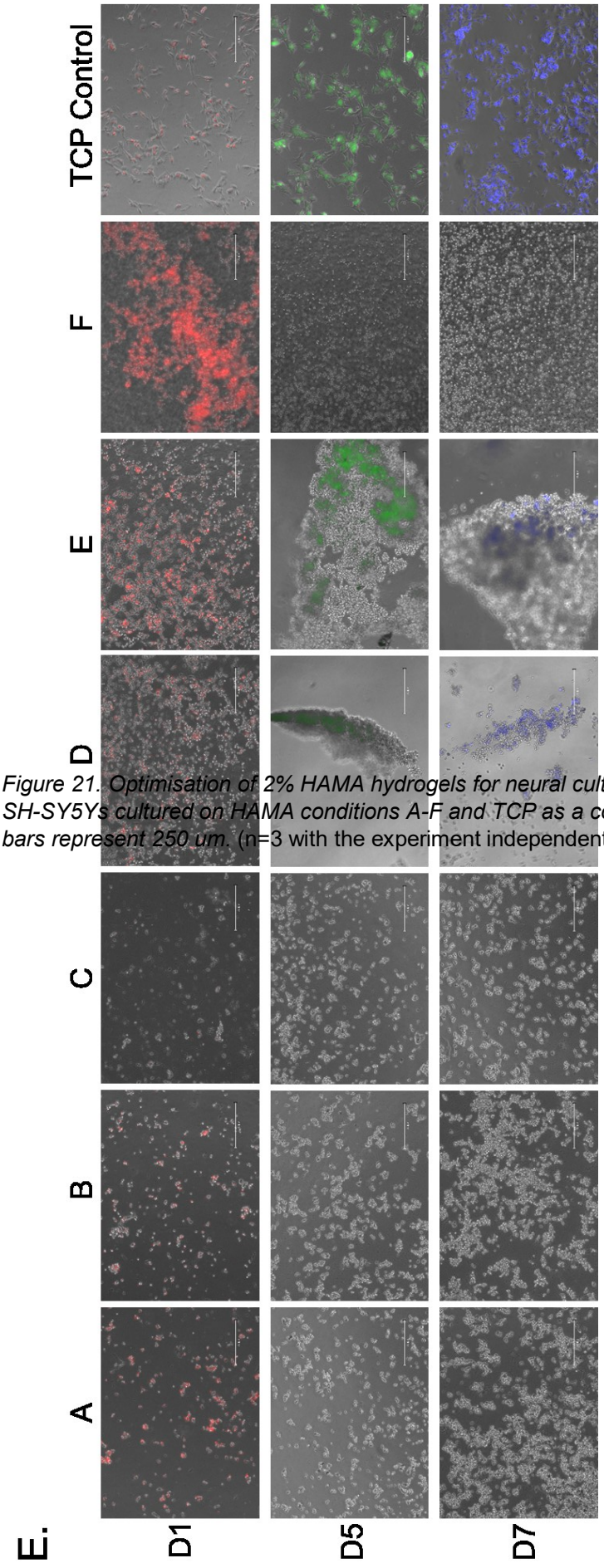

Figure 21. Optimisation of 2% HAMA hydrogels for neural culture.218E) Representative fluorescence microscop
SH-SY5Ys cultured on HAMA conditions A-F and TCP as a control. Hoechst 333258 enables visualisation of cel
bars represent 250 um. (n=3 with the experiment independently repeated 3 times, with 3 technical repeats per pl

Figure 22A depicts the workflow of generating optimal HAMA hydrogels, enabling encapsulation of GFP-fluorescent SH-SY5Ys within (Method 3.1.6.2) (Figure 22C). Dissolution of HAMA film within PBS produces a smooth transparent viscous mixture; introduction of air bubbles at this stage prevented successful addition of further components due to large air bubbles limiting thorough mixing. The optimization process for creating optimal HAMA precursors revealed that mixing via slow roller was preferred over vortexing or inverting, due to the introduction of air bubbles. Prolonged mixing with PEGDA led to stiffening of the mixture. The next stage of adding LAP was carried out in the dark, to prevent premature photopolymerisation. Exposure of the mixture to visible light at this stage prevented mixing of additional components or handling for plating, as such containers were covered with tinfoil during mixing to limit light exposure. Incorporation of final components such as antibiotics and growth factors made no observable difference to the mechanical properties of the mixture due to the small volumes added. Mixing of the cell pellet into the hydrogel precursor was carried out gently, to limit stresses exerted on cells and introduction of air bubbles. Presence of air bubbles within this final mixture led to constructs containing large gaps where air bubbles occupied space during polymerisation. Extrusion of the hydrogel precursor into a tight square led to spreading of the material to produce a flatter spread out square seen (Figure 22B). At this stage, excessive movement or tilting of the culture vessel led to excessive spreading and loss of shape. As such, constructs were carefully placed underneath the UV source for photopolymerisation. HAMA hydrogels here displayed viscous shear thickening behaviour; with elastic dominance of the hydrogel, ensuring constructs maintained their shape following polymerisation. Nevertheless, gentle addition of media was necessary, due to sensitivity of the hydrogel structure despite polymerisation. With careful handling and feeding, constructs maintained their shape up to day seven *in vitro* (Figure 22B).

Across all days tested, a rounded cellular morphology was observed via microscopy, with dispersion throughout the hydrogel exemplified by cell bodies seen across the Z-plane of the hydrogel. Viability was maintained until day seven as shown by maintained fluorescence. This was confirmed via NucBlue™ stain of live cells. After seven days *in vitro,* hydrogels underwent rheological testing (Method 3.3). Figure 22D shows rheological analysis of optimal HAMA hydrogels, specifically frequency sweep testing. Slight pink colour observed upon removal of media indicates HAMA hydrogels swelled to retain phenol and other factors found within media. Average values for G' and G'' were observed to be 4.12$\pm$0.6 and 0.68$\pm$0.15 Pascals. Statistical analysis (Appendix 7.1) revealed no significant differences within G' and G'' values across frequencies, except for when looking at elastic behaviour (G') at high frequencies; at 10 Hz elastic moduli of 13.5$\pm$7.3 Pa was found to be significantly greater than elastic moduli of all lower frequencies (Two-way ANOVA with Tukey's post-test, $P<0.0001$).

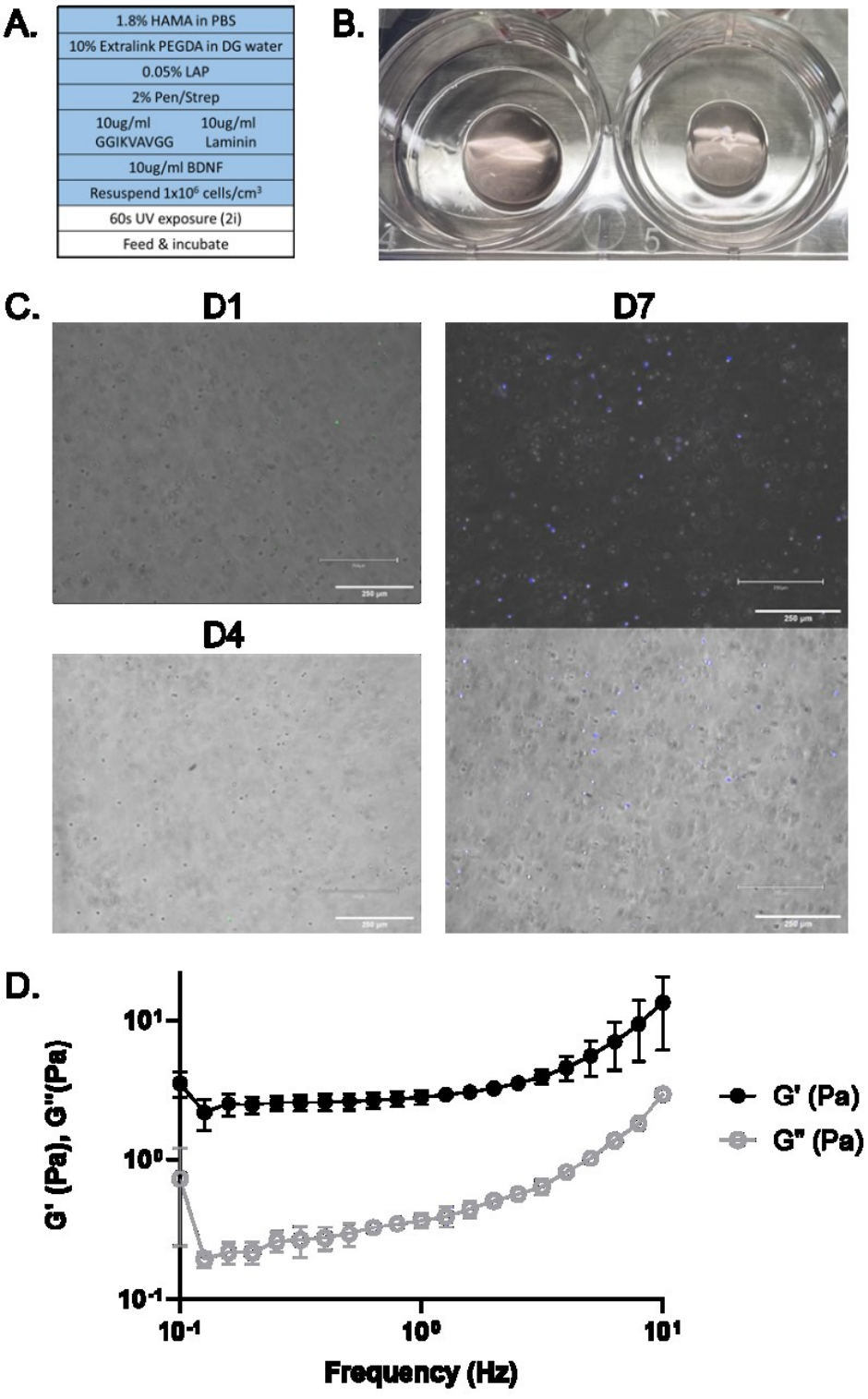

Figure 22. Characterising optimal HAMA hydrogels for neural culture. 22A) Workflow for generation of optimal HAMA hydrogels. 22B) Photograph of HAMA hydrogel constructs within 6-well plates, at day seven. 22C) Fluorescence microscopy of GFP SH-SY5Ys within HAMA hydrogels. NucBlue™ stain enables visualisation of live cells at day 7. Error bars represent 250 µm. N=3. 22D) Small oscillatory rheology reveals elastic (G') moduli of final optimal HAMA hydrogel after 7 days in vitro. Frequency sweeps were performed to display elastic moduli as a function of frequency from 0.1-10 Hz. Results expressed as mean ± SD. N=1 (three technical repeats of each condition per experiment allow averaging, but the experiment was only carried out once).

Further analysis showed significant differences were observed when comparing between G' at frequencies up to <5.5 Pa at 4 Hz and 9.5±4.4 Pa at 8 Hz (P<0.05-0.001). This was also observed when comparing between G' at frequencies between G' of 1.6-3.1 Pa at 0.13-0.8 Hz and 7.1±2.7 Pa at 6 Hz (all P<0.05). Additional testing (Appendix 7.2) revealed no statistically significant differences between G' and G'' at low frequencies, however beyond 3.6 Hz this changed. Differences in G' and G'' were observed at 4 Hz (G' 4.6±0.9 Pa and G'' 0.83±0.08 Pa, P<0.05), 5 Hz (G' 5.6±1.6 Pa and G'' 1±0.1 Pa, P<0.01), 6.3 Hz (G' 7.1±2.7Pa and G'' 1.4±0.12 Pa, P<0.001), 8 Hz (G' 9.5±4.4 Pa and G'' 1.8±0.14 Pa) and 10 Hz (G' 13.5±7.3 Pa and G'' 3±0.11 Pa) (both P<0.0001).

5.3. Discussion

Having determined that UV exposure time and LAP act synergistically to drive polymerisation of HAMA, further work looked to modulate UV intensity as a means to control stiffness of HAMA hydrogels (Figure 19A). To do this, the UV bulb system (19B) was utilised, due to the ability to change light intensity as well as exposure time. Note that hydrogels herein utilise 10% PEG-3500 as this is significantly less cytotoxic than PEG-575 used previously (Figure 14).

Prior to experimental use, the UV bulb system was characterised (Methods 3.5) as with the UV box system (Figure 16). However, 16C is not displayed as a heat map as in 16C, due to the wide range of available intensities (0-10i in increments of 0.1). Figures 19B and 19C are included to show the experimental set up and position of petri dishes/well of a 6-well plate in order to ensure consistent UV dose. Figure 19D shows quantification of UV intensity at the lowest settings (0.5i, 1i, 1.5i, 2i), however only focusing on the central 3x3 cm^2 as the exposure area is far more condensed than the UV box system (Figures 16B and C). Significant differences are seen between intensities, but not within intensities of each condition, supporting the conclusion that the UV bulb system supplies intense consistent dosage of UV radiation. This system was utilised herein due to its superior reliability and dose tuning ability.

In order to translate previous findings utilising the UV box system and PEG-575 to the new approach using the tuneable UV bulb and PEG-3500, "translational" or "transition" rheology was carried out utilising the lowest UV bulb intensities for 30 or 60 seconds (Figures 19E and F). Concentration of LAP was kept to 1.7 mM of 0.05% as this concentration presented with tolerable reductions in cell viability during 2D cytotoxicity testing (Figure 15). This was in the hopes of recreating similar viscoelastic properties to those seen previously (Figure 17). Figure 19E shows viscous dominance of all conditions, indicating low LAP conditions combined with low UV intensity is not enough to induce sufficient polymerisation for elastic dominance, with deformation even at low shear. This is supported by shear-thickening behaviour of viscous

moduli seen in Figure 19F. Statistical analysis reveals no significant difference between 30s 1.5i to 2i, but a statistically significant difference between 60 seconds 1.5i to 30 secons 2i and an even more significant difference between 30 seconds 1.5i and 60 seconds 1.5i. Latter results suggest that modulation of exposure time may be a more powerful approach for significantly altering the mechanical properties of HAMA hydrogels, compared to modulation of intensity alone.

As previously described (Figures 16E to I), the cytotoxic effect of UV dose was investigated (Figure 200), however for the UV bulb system. Work here expands upon work in Figure 16, with exploration of various UV intensities (Figure 20B-D) and various cell types following exposure to UV and LAP. Figure 20F investigated the effect of 0-8.5 mM LAP and 0.5i UV for 0, 30 or 60 seconds on SH-SY5Ys, whereas Figures G and H explored 0-8.5 mM LAP and 0.5 or 1i for 30 seconds on astrocytes and NPCs. As discussed previously (Figures 14E-G), exposure of cells to just UV has an inconclusive effect on cell viability when assessed via MTT assay (Figures 20B-D).

Sequential assessment into the effect of UV and LAP on the same cell lines did yield significant results; SH-SY5Ys exposed to LAP then UV showed consistent grouping within concentrations despite different exposure times. This was ture until 8.5 mM where toxic effects of UV are exacerbated by high LAP concentration, with a reduction in viability observed even in the 8.5 mM 0 seconds condition (Figure 20F). Thus supporting previous findings (Figure 15) of LAP toxicity even without UV exposure. Due to toxicity effects of LAP even in 0 seconds conditions, 0 mM LAP 0 seconds UV exposure was selected as the control for astrocyte/NPC experiments (Figures 20G and H). This new control established a precise baseline for measuring combined toxic effects of LAP and UV intensity. As expected, lowest viability is seen in highest LAP and greatest UV intensity in both NPCs and astrocytes, supporting the hypothesis of cumulative cytotoxic effects of LAP and UV combined. This is unsurprising, with generation of free radicals from LAP known to occur with UV exposure, however the power of this cumulative effect is lesser understood. Work here aims to elucidate this complex relationship. Utilisation of multiple neural cell types enables investigation of the toxic effect of photopolymerisation methods, within the context of neural tissue engineering. Specifically, NPCs (Figure 20G) present with highly variable reductions in cell viability following exposure to LAP and UV, with no statistical significance between intensities, but a general trend of reduction with increasing exposure to stimuli. Conversely, astrocyte data displays minimal variation and a steeper line of fit, potentially suggesting reduced sensitivity to free radical-induced toxicity. Comparison of data from SH-SY5Ys and astrocytes suggests limiting LAP to 1.7 mM (or 0.05%) limits reductions in viability (~80% or more viable cells), despite increasing UV exposure time or intensity. Variability of NPC viability data hinders extraction of

biocompatible ranges of LAP/UV dose; further work should look to repeat this. Further work should also explore cytotoxic effects on cocultures of astrocytes and NPCs to provide elevated biological relevance, as the CNS is multicellular in nature with glial cells providing crucial support to NPCs (Bayraktar et al., 2020, Chen et al., 2020, Molyneaux et al., 2007).

Previous experimental work looked to optimise HAMA hydrogel composition for neural tissue engineering via 2D cell culture of SH-SY5Ys, NPCs, Astros (MTT-assay) and 3D culture of SH-SY5Ys, alongside analysing viscoelastic properties of 3D hydrogels via rheological testing. While this work enabled stepwise investigation of HAMA components, a clear gap exists whereby biological compatibility and activity of 3D hydrogels was not assessed. In order to address this, experiments carried out in Figure 21 investigated tissue culture of SH-SY5Ys within six compositions of HAMA hydrogel (Figure 21B), to evaluate 3D biological compatibility *alongside* mechanical properties. Having established that UV dose from the bulb system is highly tuneable (Figure 19), and that exposure of various cell types to combined UV and LAP is well tolerated at low concentrations (Figure 20F-H), combinatorial effects of LAP and PEG when generating 3D HAMA hydrogels were investigated (Figure 21). With HA known to possess limited sites for adhesion (Rauti et al., 2020), the addition of laminin promotes attachment and provides additional tissue specificity, with laminin a key constituent of CNS ECM and therefore commonly utilised for neural tissue engineering (Section 1.3.2.2). Whats more, inclusion of laminin is shown not to effect mechanical properties of hydrogels (Koivisto et al., 2017).

Initial comparison of hydrogels by eye (Figure 21D) yields no visual differences in conditions A-E, excepting condition F whereby the hydrogel becomes opaque following UV exposure. This opacity may be due to phase segregation where PEG an HAMA become immiscible and form an emulsion, resulting in visually and mechanically different hydrogels. Figure 18C shows condition F to possess dramatically increased elastic moduli' compared to all other conditions, however toxicity of PEG-575 (Figure 14) is likely the cause of near total loss of viability following seeding (Figure 21E). Conversely, conditions A-E display significantly reduced G' (Figure 21C) indicative of limited polymerisation, possibly explaining visualisation of cells across Z-planes with mixing/dispersion of cells within surface layers of softer hydrogels (A-E) following seeding (Figure 21E). This is supported by rounded morphologies of cells. Conditions B, C and D present with overlapping elastic moduli of extremely low values, as such were not considered for further use due to their lack of biological relevance and difficulty when handling. Interestingly, the no PEG and no LAP condition (A) presents with similar elastic moduli to the PEG-3500 and 0.05% LAP condition (E), presenting as stable elastic moduli with consistent stiffness around tens of pascals. Condition E presents as slightly stiffer, likely due to the interaction of PEG-3500. Both A and E were identified as potential compositions for

generation of optimal HAMA following rheology (Figure 21C), however biological compatibility must also be considered (Figure 21E).

Rounded morphologies of SH-SY5Ys seeded on top of HAMA hydrogels within conditions A-C suggests limited attachment (Figure 21E), and dispersion throughout the 3D hydrogel indicative of limited polymerisation and some viscous behaviour of the hydrogel. Conditions A and B display limited fluorescence at day one followed by total loss from day five, whereas C presents with an instant loss of fluorescence, indicating immediate cell death. This could be attributed to cell death via anoikis; however, this process would not explain the immediate death of almost all cells within the sample. Previous work (Figure 14) supports the hypothesis that the inclusion of PEG-575 results in toxicity of C HAMA hydrogels, whereas inclusion within condition F results in less immediate toxicity as PEG-575 is trapped within the hydrogel structure (Figure 21C) following photopolymerisation of the HAMA network. This entrapment of PEG-575 may be responsible for opacity of HAMA hydrogels within this condition (Figure 21D). Nevertheless, cells seeded onto HAMA hydrogels made with PEG-575 and LAP display toxicity from day five onwards, possibly due to leaching of toxic PEG-575 from the hydrogel into surrounding media. As such, conditions A-C were excluded entirely in further work due to lack of biocompatibility and unsuitable mechanics (G' of <1 Pa).

Conditions D to E also display rounded morphologies compared to spreading seen in TCP controls (Figure 21E). Condition F presents with some spreading of cells and increased fluorescence, compared to D and E. This may be due to increased stiffness of F (Figure 19C), with tighter grouping of viable cells within a singular Z-plane presenting as heightened fluorescence (Figure 21E). Whereas D and E may be viscous enough to allow some movement of cells within surface layers of the viscous hydrogel biomaterial i.e. the surface of D and E hydrogels is softer than F enabling some sinking of cells. Figures D and E both display sustained fluorescence, however clumping of cell bodies is visible (Figure 21E). The manner in which cells aggregate appears to be slightly different, with tube-like aggregation possibly alluding to "rolling up" of gelated material i.e. surface layers of hydrogel receive the highest dose of UV, resulting in sheets of polymerised material that roll up to form tubes following addition of media. This is supported by Figure 16, demonstrating that penetrance of UV light through 0.5cm height hydrogels is significantly reduced, possibly explaining heterogeneity of polymerisation within layers of HAMA. Previous studies suggest attenuation of light by photoinitiators also limits curing depth (Xu et al., 2018). This may be overcome by ensuring opacity of hydrogels precursors to allow UV penetrance, optimisation of polymerisation kinetics to allow for more diffuse free-radical movement or use of multiple UV sources.

Cells cultured on conditions D and E maintained fluorescence until day seven *in vitro* (Figure 21E). Whereas F presents with suitable mechanics (Figure 21C) but increased toxicity compared to D and E conditions (Figure 21E). Loss of viability is observed in in all conditions bar D and E that display similar biocompatibility, however rheological analysis reveals slight differences; condition D presents as slightly less stiff hydrogels, with increased variability (indicated by outlier results at high frequencies causing statistically significant differences) compared to HAMA hydrogels from condition E. These hydrogels display consistent elastic moduli even at high shear rate, indicating PEG-3500 provides additional mechanical support to hydrogels following LAP-induced photopolymerisation. While conditions A and E present with ideal mechanical properties (Figure 21C), conditions D and E display superior biocompatibility (Figure 21E). Work here therefore suggests condition E to be the optimal composition for reliable generation of HAMA hydrogels with desirable mechanical properties (easy to handle, low batch variability, biologically relevant stiffness) alongside biological compatibility. The use of LAP/UV photopolymerisation alongside mechanical support from PEG polymers enables greater tuning of mechanical features within HAMA hydrogels; this is a fundamental advantage to single polymer hydrogels, with greater potential for tuneability of the system. This is supported by research that found inclusion of synthetic PEG within a natural hydrogel enables modulation of stiffness without compromising biofunctional domains of the natural polymer network (Almany and Seliktar, 2005).

Previous work in this chapter looked to optimise composition and processing conditions of HAMA hydrogels via compartmentalisation of variables that effect biocompatibility and mechanical properties. Investigation into biocompatibility of PEG (Figure 14), photoinitiators (Figure 15) and UV dose (Figures 16 and 20), provided a foundation for exploration of compounding effects of photoinitiator and UV on 2D cell viability (Figures 16 and 20) and 3D mechanical properties (Figures 17, 18 and 19). Figure 21 finalises this investigation by investigating biological and mechanical properties of various combinations of PEG and LAP photoinitiator. Stepwise optimisation of singular and compounding variables provides insight into how variables interact, enabling exploitation of these interactions to produce optimal HAMA hydrogels (i.e. high compatibility, physiologically relevant stiffness) for neural tissue engineering.

Exploratory investigation of GG and HyStem™ polymers (Figures 12 and 13) found advantageous characteristics such as low cost (GG) and high biological relevance (HyStem™ is a HA-based hydrogel). However, limitations such as unstable polymerisation (GG) and high cost (HyStem™) prevent widespread use by tissue engineers. Work in this chapter therefore looked to develop a hydrogel biomaterial possessing desirable traits. HA was identified as a polymer of interest due to its biological relevance within the CNS, however required chemical modification in order to enable photopolymerisation. As such, HAMA was selected as the foundational polymer (Figure 23). Further chemical modification of the polymer network is suggested as a means to instil greater functionality within resultant hydrogels, however additional modification of the HA backbone increases risk for steric hindrance and inhibition of polymer network formation (Perera et al., 2019). An alternative approach employed here involved modification of viscoelasticity to favour specific cell behaviours, with modifications to hydrogel mechanics shown to promotion neurite proliferation and extension (Khoshakhlagh and Moore, 2015).

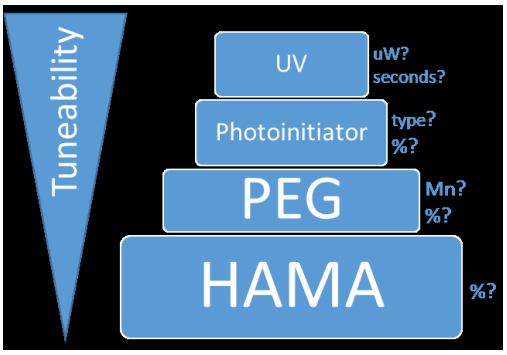

Figure 23. Variables explored herein when producing HAMA hydrogels, increasing in potential tuneability.

Figure 23 highlights variables explored within this research when producing HAMA hydrogels, correlating to schematics (Figures 14-21A). Tuning of hydrogel properties is possible via modulation of variables: changing the molecular weight and concentration of PEG enables some tuneability, whereas modulation of photoinitiator (type and concentration) alongside UV dose (by source, intensity and exposure time) enables greater tailoring of HAMA hydrogel properties (Figure 23). Tuneability of the system is invaluable when developing biomaterials for tissue engineers, increasing the range of potential applications beyond CNS modelling.

Having optimised variables for production of HAMA hydrogels in previous work (Figures 11-21), the last experimental figure within this chapter (Figure 22) looked to consolidate findings and characterise this optimal HAMA hydrogel. Optimal composition was found to be 2% HAMA, 10% PEG-3500, 0.05% (or 1.7 mM) LAP, with the inclusion of BDNF and laminin to promote viability and biocompatibility, respectively. Figure 22 expands upon previous work with inclusion of IKVAV peptides alongside full form laminin, with such short sequences shown to improve biological properties of hydrogels within the literature without significant changes to mechanical properties (Perera et al., 2019).

The UV bulb system was utilised to induce polymerisation, having shown superior consistency within UV intensity across exposure area compared to the box system (Figures 16 and 20). Based on results observed in Figure 21C, UV exposure was increased from 60 seconds 1.5i to 60 seconds 2i, in the hopes of producing HAMA hydrogels with increased elastic moduli without increasing concentration of LAP. This rationale underpins workflow seen in 22A.

Optimal HAMA hydrogels here made with 10% PEG-3500 and 0.05% LAP display superior mechanical properties (Figure 22D), with maintenance and stability of hydrogel structure until day seven (Figure 22B) and increased viscoelastic moduli compared to Figure 21C ($4.12 \pm 0.6 > 3.17 \pm 3.03$ Pa, respectively). Optimal HAMA hydrogels also display reduced shear-thickening behaviour at low shear when compared to previous formulations (Figures 17 and 19), indicative of increased polymerisation and resistance of the polymeric network to deformation. This improvement in mechanical properties was observed during manual handling, as well as stability of constructs throughout culture (Figure 22B). However, rheological analysis of samples was carried out at the end of day seven *in vitro*, whereas previous rheological samples were not incubated with cells. This may mean samples utilised here (Figure 22D) display swelling due to exposure to culture media, with HA and PEG known to display water-absorbing properties (Choi et al., 2019, Khoshakhlagh and Moore, 2015). Cells are known to deposit and remodel CNS ECM *in vivo* (Simsa et al., 2021), as such, we would expect the same to occur within 3D matrices *in vitro*, however it is unlikely that significant remodelling would have occurred within such short timescale.

Following optimisation of the workflow based on quantitative observations during the preparation process, the workflow and exact formulation utilised to create bulk HAMA hydrogels (Figure 22) was modified for creation of a HAMA bioink for bioprinting (Figure 30). Optimisation of the HAMA preparation process led to a carefully developed mixing protocol, to favour thorough incorporation without the addition of air bubbles or premature polymerisation. Indeed premature stiffening of the material was found to occur with excessive mixing or exposure to light (be that visible or UV), indicating a time-sensitive balance is essential for achieving the desired consistency for cell encapsulation. The necessity of carrying out LAP addition in the dark to prevent premature photopolymerization illustrates the importance of controlling environmental factors during hydrogel preparation. This precautionary measure emphasizes the delicate balance between maintaining mixture integrity and ensuring effective crosslinking. The extrusion of the hydrogel precursor into a tight square and its subsequent spreading upon placement emphasizes the importance of controlling the geometry of the constructs during initial setup. The ability of this hydrogel formulation to be extruded via a pipette, yet retain its shape, was a fundamental consideration when developing a HAMA formulation suitable for bioprinting. These versatile viscoelastic

properties, alongside the ability to withstand culture conditions (immersed in media at 37ºC, with gentle agitation during feeding) made this HAMA formulation attractive for further exploration.

Optimal HAMA hydrogels (Figure 22) also possess superior biocompatibility to previous experiments (Figures 11, 13 and 21) with maintained fluorescence indicating sustained viability until day seven *in vitro* (Figure 22C). Fluorescence microscopy shows rounded morphology of cells, indicating limited cell attachment despite inclusion of additional laminin components. This may be due to loss of small molecules from the hydrogel during culture and feeding, with no chemical bonding of attachment proteins to ensure retention within the hydrogel structure. Viability of encapsulated cells at day seven is confirmed via NucBlue™ staining of live cells, indicating optimised HAMA hydrogels display vastly improved biocompatibility compared to un-optimised HAMA hydrogels (Figure 13). The HAMA biomaterial utilised here (Figure 22) display superior mechanical and biological properties when compared to previous formulations. As such, the formulation process was carried forward for incorporation into the INKREDIBLE+ bioprinter (Figure 30).

6. Functionalisation and Structuring of HAMA hydrogels

6.1. Introduction

While the power of soluble small molecules is an established tool utilised by researchers to guide neural cell fates (Sections 1.2.3 and 1.4), the power of environmental signalling via biomaterials is gaining interest (Leipzig and Shoichet, 2009). Physical or chemical modification (Sections 1.4.2.2 and 1.4.2.3) can instil hydrogel biomaterials with specific physiomechanical features. Chemical modification allows tailored tuning of hydrogel mechanical features, by enabling photocrosslinking of natural polymers (Chapter 4) and photo-patterning (Biggs et al., 2017, Knight et al., 2018), but also stimuli-responsive behaviour (Fonseca et al., 2020, Palmese et al., 2019). Modulation of mechanical cues of hydrogels within the context of neural engineering is explored in chapter 4.

Assimilation of physiomechanical and biochemical cues holds the most hope for recreating complexity seen in the CNS ECM *in vivo* (Figure 6). With conditioning of cells via biochemical and mechanical stimuli shown to induce changes in protein/small molecules secretion (Daneshmandi et al., 2020). This demonstrates potential for exploiting compounding effects as cells become more committed to specific fates i.e. cells exposed to “soft” biomaterials favour CNS fates (Merryweather and Roach, 2017, Pek et al., 2010), resulting in increased expression of CNS-associated factors (Leipzig and Shoichet, 2009, Moxon et al., 2019). A review by Handorf *et al.* (2015) highlights effect of ECM stiffness on cellular expression within other “stiff” tissues and disease states (Handorf et al., 2015). The inverse is also true, with biochemical induction of neuronal differentiation shown to result in global changes in gene expression and increased secretion of CNS-associated proteins (Frese et al., 2017), known to contribute to ECM mechanical features. However, existing research often fails to account for the integrative nature of biological and physical features within naturally occurring tissues and biomaterials for tissue culture. Further investigation into interconnectedness of physical features (stiffness, viscosity, porosity, degradation etc.) would enable accurate determination into the cause and effect of modulating singular characteristics such as stiffness.

Exploiting cumulative effects of environmental signals would result in CNS biomaterials that display advanced functionality, compared to approaches whereby only mechanical or biochemical cues are employed to guide cell fates. As such additional structuring to hydrogel biomaterials is suggested as a means to provide an added level control over macroscale architecture of the final tissue engineered system. Figure 1 highlights common methods of guiding macroscale architecture of tissue-engineered constructs. Microfluidics holds great promise (Sections 1.2.4 and 1.4), particularly for patterning of hydrogel matrices (Section 1.4.2.6). Alternatively, 3D bioprinting is developing technology within tissue engineering,

capable of recreating complex multi-scale architectures seen in tissues *in vivo*. However, further investigation into the complex spatial arrangements found in neuronal tissue would allow for production of models with increased validity by providing a better “map” to follow when bioprinting.

Amalgamation of intrinsic and environmental cues drives cell fates and ultimately wider tissue structuring. Cells interact with components of ECM via receptor binding, resulting in translation of environmental signals into the electrochemical language necessary for evoking cellular responses (Section 1.3.2). This interaction of biological processes and physical features is responsible for the dynamic nature of the extracellular matrix (ECM) (Figure 6); however, regulatory mechanisms of mechanical features are poorly understood (Di et al., 2023, Petzold and Gentleman, 2021). Replication of environmental signals, via biomaterial functionalisation and structuring, enables tissue engineers to guide cell fates and ultimately influence *in vitro* tissue architecture and function (Section 1.2.4).

Having established the biocompatible and mechanically tuneable suitability of HAMA hydrogels (Chapter 4), further work looked to investigate biofunctionalisation and extrusion bioprinting approaches. Biofunctionalisation of HAMA-PEG hydrogels utilised within research here is especially important when we consider the limited binding sites within HA and PEG hydrogel scaffolds (Choi et al., 2019, Rauti et al., 2020, Almany and Seliktar, 2005). Extrusion bioprinting, particularly SLAM methodologies, are of interest due to their compatibility with “soft solid” hydrogel materials and potential for modification to suit polymerisation needs. These methods provide additional support to encapsulated cells via promotion of cell-matrix adhesion, and equip tissue engineered constructs with additional macroscale level of structuring. For neural tissue, this is particularly important, with the CNS shown to display distinct morphological layering *in vivo* (Section 1.3.2).

6.2. Results

6.2.1. Functionalisation

Having optimised HAMA composition and processing conditions for generation of hydrogel biomaterials for neural tissue engineering, work looked to explore functional proteins to improve cell attachment and cell-matrix interaction (Objective 3). Traditional 2D methods of neural precursor cell (NPC) culture rely on coating of culture vessels with poly-L-ornithine and laminin (Methods 3.1.1). This is replicated in Figure 24 to show morphology and protein expression of NPCs.

Protein expression visualisation via immunocytochemistry staining (Method 3.1.6.1) provided an indication of differentiation status of NPCs; Pax (Pax6 transcription factor), Nestin (neuroepithelial cytoskeletal intermediate filament protein), Ki67 (proliferation-associated protein) and Tujj (neuron-specific cytoskeletal β-tubulin protein), alongside DAPI staining of cell nuclei.

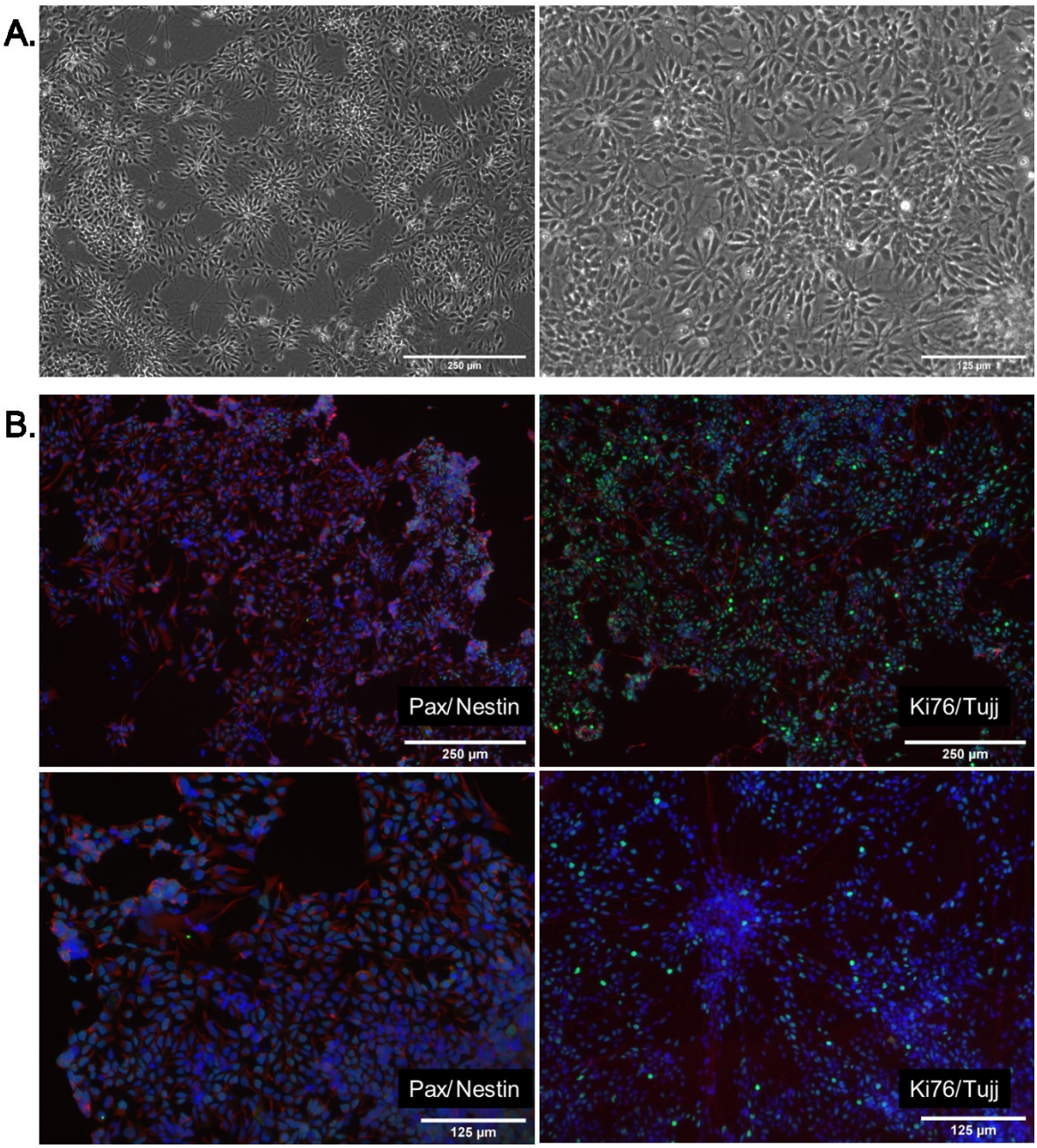

Figure 24. Representative fluorescent images of 2D morphology of L13 NPCs on mouse laminin coating. 24A) Phase microscopy of NPCs after two days in vitro. 24B) ICC staining of NPCs after five days in vitro. Nucleus staining by DAPI in blue, Pax stained in green and Nestin in red, Ki67 in green and Tujj in red. (Images representative of n=3 biological repeats; average n=3 technical repeats per biological repeat).

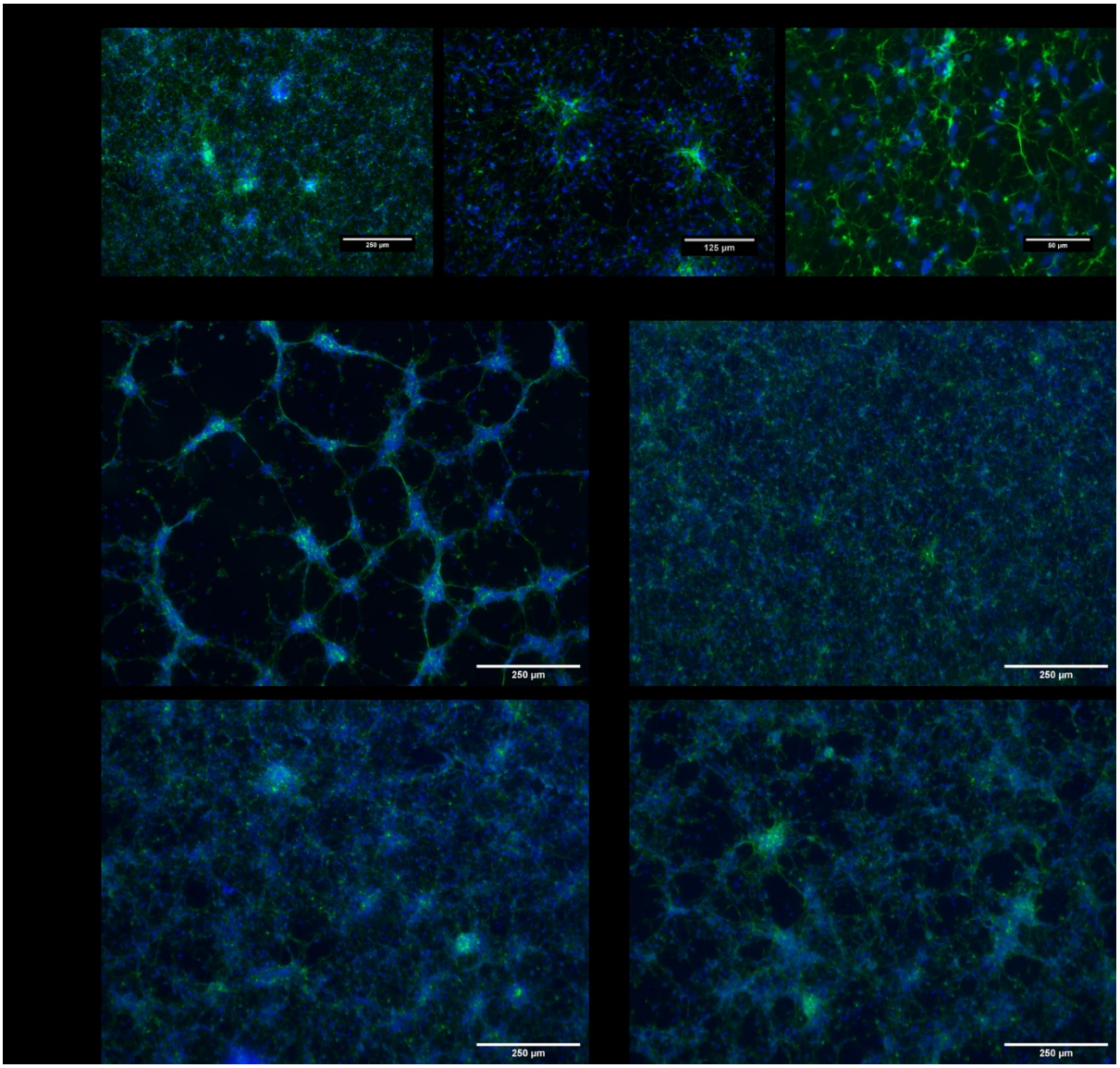

Figure 25. Representative images of L5 NPC culture on various substrates, stained with ActinGreen™ and DAPI in blue. 21A) Representative images NPC culture on (poly-l-ornithine) PORN-Laminin after two days in culture, at various magnification. 21B) Representative images of NPC culture on PORN, PORN-Laminin, PORN-CCRRIKVAVC or PORN-GGIKVAVGG coated surfaces after four days. (Images representative of n=2 biological repeats; average n=3 technical repeats per biological repeat).

IPSC-derived cortical NPCs presented as neural rosettes (Figure 24A), a unique morphological arrangement specific to this cell type that potentially represents neural tube formation during development (Townshend et al., 2020). Staining via ICC revealed expression of Pax protein via localisation of green staining within cell nuclei (Figure 24B). Unfortunately, blue DAPI staining limited visualisation, as this too localised to the nucleus. Figure 24B also displayed nestin staining of NPCs in red, restriction of staining to cell periphery indicated localisation of nestin within the cytoskeleton. Green staining of Ki67 revealed high expression levels within cell nuclei of NPCs, whereas Tujj staining (in red) was sparse, limited to expression at outer edges of neural rosettes (Figure 24B).

Following establishment of typical NPC culture on mouse laminin (Figure 24), further work looked to compare mouse laminin to IKVAV-peptides GGIKVAVGG and CCRRIKVAVLC (Figure 25). Glass coverslips were coated following methods 3.1.1 prior to NPC seeding and evaluation of cell morphology via fluorescence microscopy following staining. Figure 25A showed monolayer culture of NPCs on PORN-Laminin with increasing magnification, with formation of elaborate networks of cytoskeletal proteins (green) encircling DAPI stained cell nuclei (blue). Co-localisation of DAPI and ActinGreen™ indicated areas of increased cellular density, with similar morphology to rosettes seen in Figure 25; however, ActinGreen™ staining enabled increased visualisation of cytoskeletal proteins extending outward from rosettes (Figure 25A). Increased magnification enabled visualisation of thicker actin filaments in areas with reduced cell nuclei, indicative of actin aggregation at the cell body periphery.

Figure 25B expands on work in Figures 24 and 25A, investigating suitability of IKVAV peptides for promoting NPC attachment. Fluorescence microscopy (Method 3.1.6.1) of NPCs on PORN-Laminin at day four showed similar morphology to the same coating after two days *in vitro* (Figure 24A); with maintained monolayer culture, however reduced visibility of rosette structures. Coating of substrates with only PORN resulted in clumping of NPCs, exemplified by aggregate blue DAPI nuclei staining (~50 µm diameter spheres, with some aggregates longer and thinner) with increased intensity of actin filaments surrounding these aggregates. Some DAPI staining of individual NPC nuclei was observed within gaps that exist between large aggregates. Large areas of no staining show network of cells on PORN was less diffuse compared to PORN-LAM or PORN-CC or PORN-GG conditions. Both IKVAV conditions displayed similar morphology (Figure 25B), where diffuse actin staining indicated fine meshwork of cytoskeletal proteins, with intensity of actin filaments greatest at periphery of rosette structures. PORN-CC conditions displayed some gaps within this meshwork, while PORN-GG conditions displayed similar gaps but more aggregation of NPCs resulting in larger gaps. Despite this observation, both conditions did not display the level of NPC aggregation seen when culturing on PORN alone. Results showed functionalisation of NPC substrates promotes cell and adhesion in 2D (Figures 24 and 25); demonstrating IKVAV functional motifs display similar bioactivity to full form laminin.

Following exploration of NPCs on various coatings, focus turned towards iPSC culture, with the eventual aim of optimising the coating protocol for both cell types. Figure 26 shows iPSC culture on PORN-Vitronectin coated surface. Cells here display colony formation indicative of PSC lines; however, colonies are typically expected to show smooth edges (personal communication from Dr Eric Hill, Aston University). Nevertheless, cells here show heightened Oct4 expression, which is characteristic of iPSC cells. Unfortunately, iPSC cells beyond this

point began to differentiate, with this process observed in the far left of Figure 26 whereby an abnormally shaped cell displays reduced Oct4 expression.

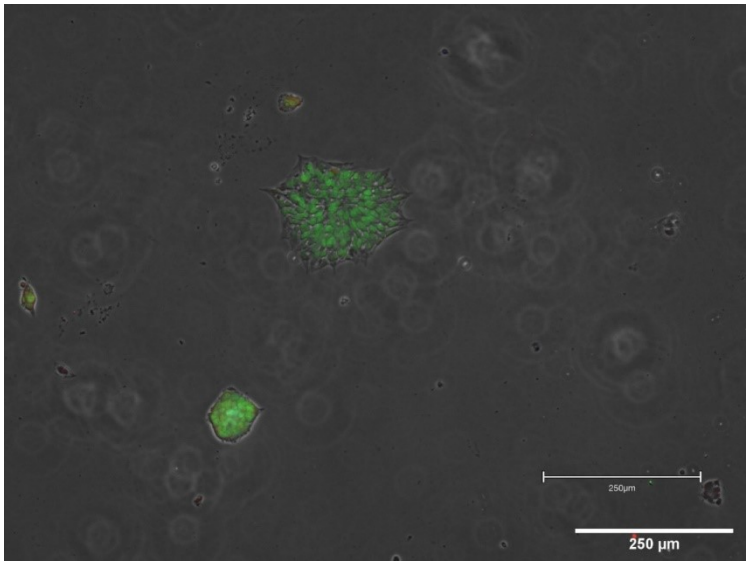

.

Figure 26. Representative image of L5 iPSCs one day after plating onto PORN-Vitronectin. IPSCs stained with Anti-Oct4 (Green) antibody. N=1 (images representative of three technical repeats per experiment, but the experiment only carried out once).

6.2.2. Structuring via Bioprinting

Evaluation of extrusion bioprinting, including the SLAM method, for optimised printing of HAMA constructs with defined macroscale geometries was carried out (Objective 4). Printing of low viscosity bioinks (such as hydrogel precursors for neural tissue engineering) is limited due to spreading during printing and ultimately loss of macroscale architecture and reduced resolution (Senior et al., 2019).The SLAM method was therefore considered for printing of HAMA hydrogels as a means to provide support to printed constructs.

Prior to inclusion of HAMA biomaterials within the bioprinting system or adoption of SLAM, characterisation of fluid gels was carried out (Figure 27). Fluid gels are physically modified hydrogels (Section 1.4.2.2) that display shear thinning behaviour, enabling use as support bath material for extrusion bioprinting of viscous bioinks. Figure 27 shows fluid gel particles present with differing morphological properties depending on type of polymer (gellan gum or agarose) and concentration (0.2/0.4% or 0.5/0.75% respectively) (Method 3.2.2). Light microscopy (Method 3.2.2.2) revealed gellan gum (GG) and agarose (Ag) hydrogels sheared during gelation display inhomogeneous polymerisation (Figure 27), where particles of gelated material form with a liquid phase existing between them (Figure 7).

GG materials undergo gelation via physical crosslinking of polymers in the presence of divalent ions when cooled, whereas agarose undergoes gelation during cooling. The physically reversible nature of this crosslinking readily enables production of fluid gel materials via removal of heat during application of shear (Methods 3.2.2). Gelation of GG materials was seen to occur around ~46°C in the presence of divalent ions, whereas Ag gelation began at a

slightly lower temperature of ~37°C. Additionally, all fluid gel formulations here displayed self-healing ability. Visualisation of particles is enabled by dilution of the fluid gel material (Figure 27). Particles overlap and intermingle in all conditions, with interaction of “hairy” filamentous protrusions generated during controlled shear responsible for particle fusion and self-healing properties (Norton et al., 1999).

GG fluid gels displayed truncated or blunt particles, ranging in size from 125 μm however difficult to observe due to overlapping interaction of particles even when diluted. Increasing the concentration of GG from 0.2 to 0.4% led to increased contrast of phase images, with denser particles shown to be less translucent (Figure 27). Increased concentration also appeared to lead to less filamentous protrusions and increased heterogeneity, with a wider range of visible particle sizes. In contrast Ag fluid gels were easier to visualise via phase and presented with dense rounded particles of a smaller size $\leq$125 μm that packed together tightly, seen via intermingling of particles and “hairy” protrusions. At higher concentrations (0.75%) Ag particles appeared more “hairy” (than 0.5% Ag), with increased interaction of these protrusions (Figure 27).

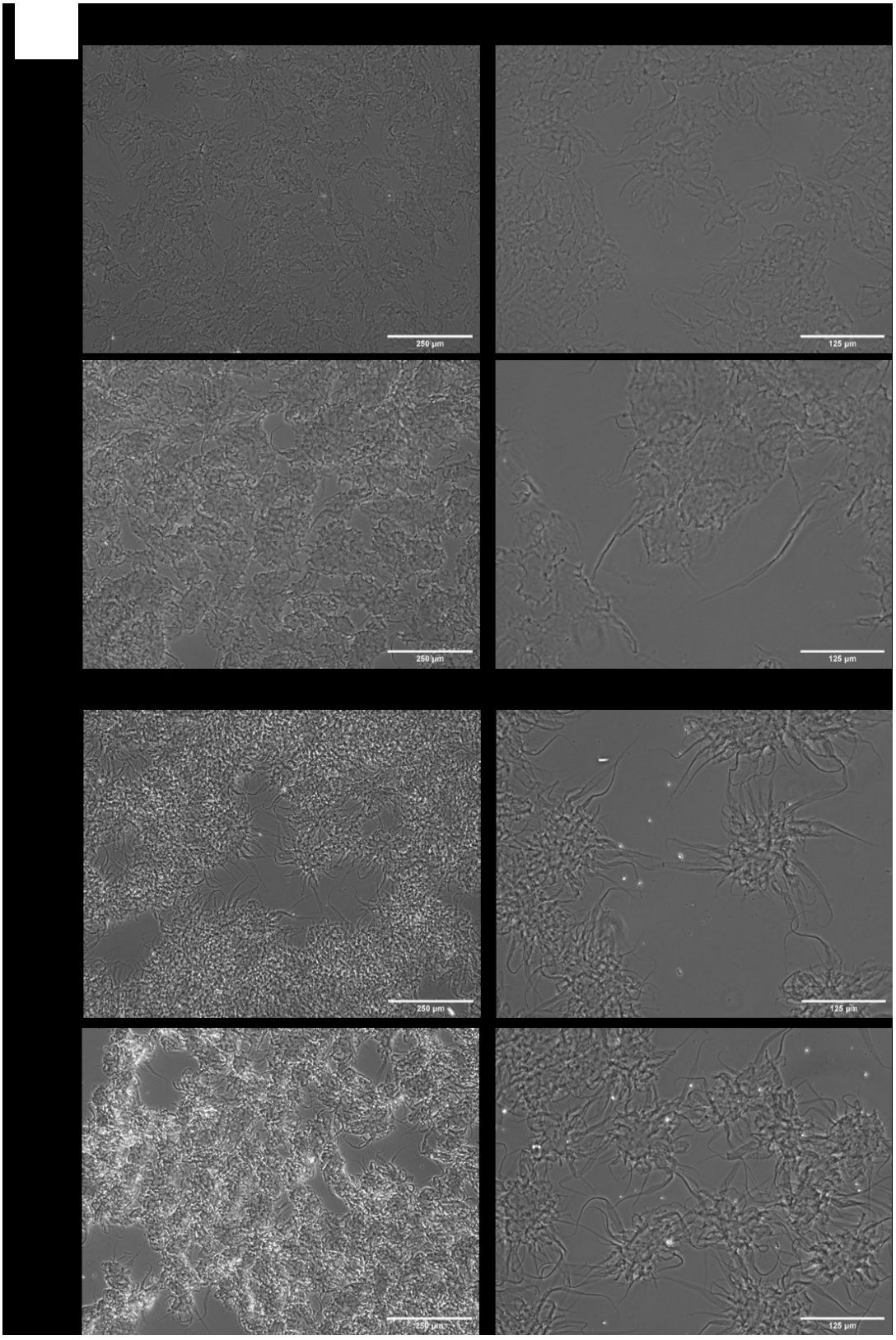

Figure 27. Representative light microscopy images for visualisation of fluid gel particulate morphology. Undiluted and 10% diluted (in PBS) gellan gum (GG; 0.2 or 0.4%) or agarose (Ag; 0.5 or 0.75%) fluid gels. (Images representative of n=3 biological repeats; with n=3 technical repeats per biological repeat).

Another consideration for extrusion bioprinting is the effect of extrusion forces on cell viability (Method 3.4.2). As such, Figure 28 quantified the effect of speed, cell density, and needle gauge on cell viability of SH-SY5Ys within culture media (Methods 3.4.2). Statistical analysis (Two-way ANOVA with Dunnet's post-test) revealed no statistically significant changes in any condition after 0 and 24 hours, indicating extrusion pressures experiences by cells at low speeds/low cell density (Figure 28), as well as those at high speed/high cell density (Figure 28), were not severe enough to induce cell death.

In order to explore suitability of the INKREDIBLE+ extrusion bioprinter and optimise print conditions, initial investigation was carried out utilising commercially available bioinks, namely CELLINK Bioink and LAMININK+ (Method 3.4.3). Figures 29B and D depict extrusion bioprinting of CELLINK Bioink into generic lattice structures (Figure 2). Figure 29B demonstrates extrusion printing of CELLINK Bioink enabled generation of lattice structures that retain printed macro-architecture and display spreading of filaments necessary for layer-layer integration, resulting in a 3D printed structure. Repeated printing yielded visually near-identical constructs with high consistency. Fluorescence microscopy enabled visualisation of SH-SY5Ys within printed structures (Figures 29D and E). Figure 29D shows resolution of CELLINK Bioink printed filaments ranges from ~400-800 µm. This bioink also displayed autofluorescence, somewhat limiting visualisation of cells at lower magnification (Figure 29D), whereas increased magnification revealed high viability of cells within CELLINK Bioink constructs to day five. High magnification microscopy revealed that as days in culture increase, encapsulated SH-SY5Ys were seen to migrate through the hydrogel to attach and spread on the glass substrate underneath (Figure 29D).

Figure 28. Manual quantification of SH-SY5Y viability 0 and 24 hours post-extrusion of within RPMI culture media. Cell suspensions held in 1mL syringes ran through various needle gauges (25, 27, 30G) at low density/low speeds and high density/high speed. 28A) 0.5 mL/min at 0.5 x10^6 cells/mL. 28B) 3 mL/min at 1 x10^6 cells/mL. Data here shown as mean ±SD. (average of n=3 biological repeats; with n=3 technical repeats per biological repeat).

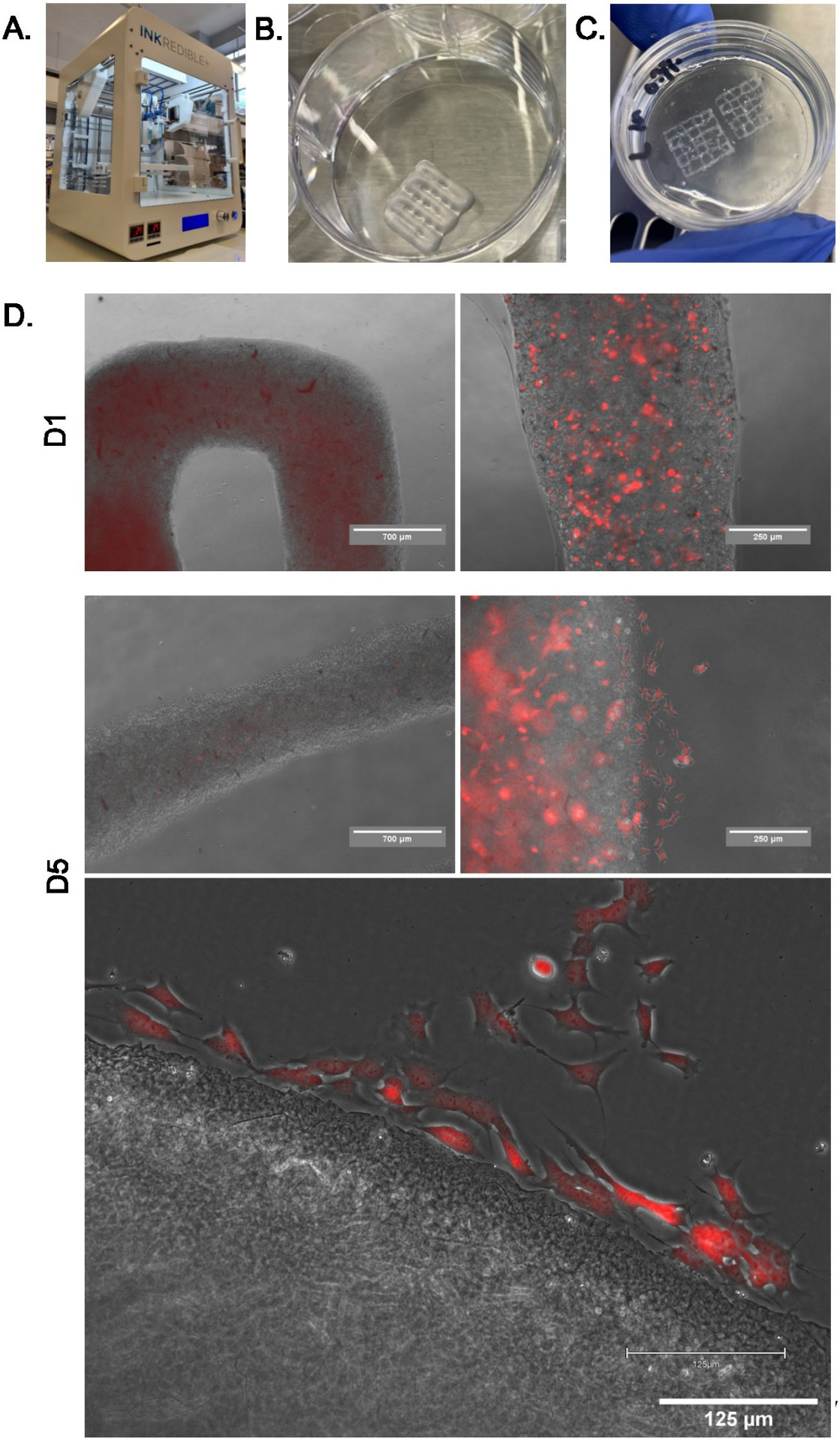
A.
INKREDIBLE+
B.
C.
D.
D1
700 µm
250 µm
D5
700 µm
250 µm
125µm
125 µm

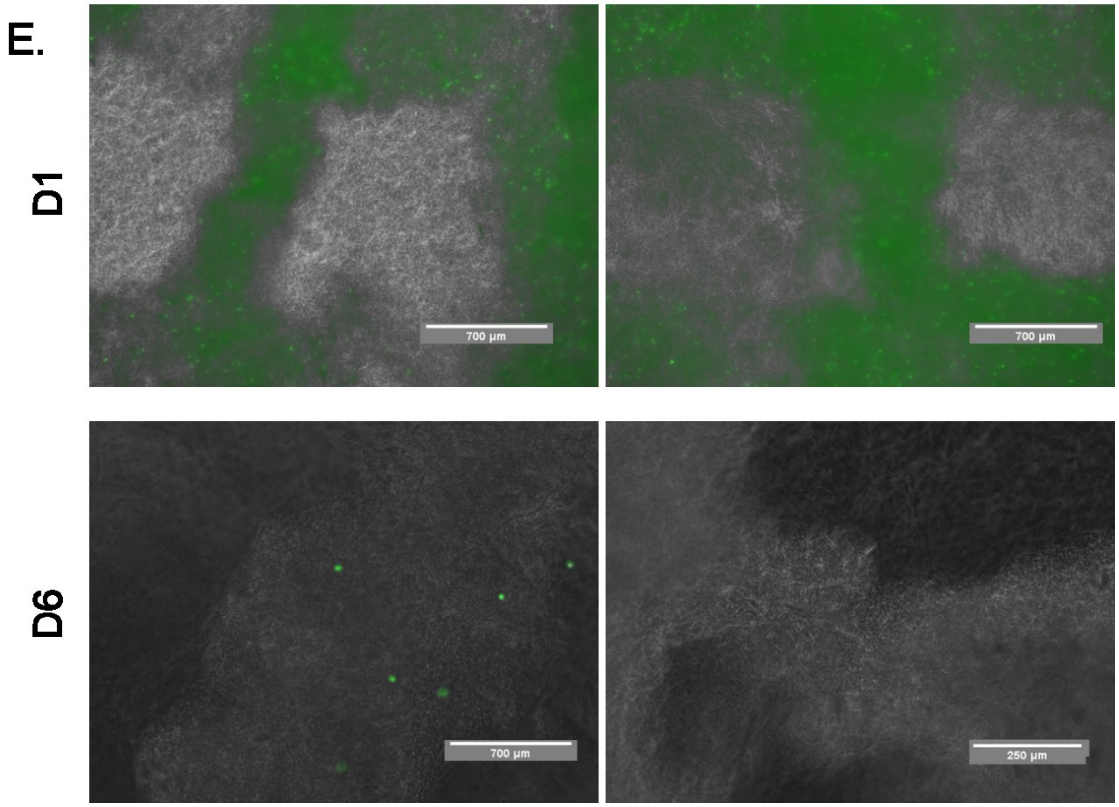

Figure 29. Preliminary investigation of extrusion bioprinting by the INKREDIBLE+. 29A) Photograph of the INKREDIBLE+ Bioprinter (CELLINK). 29B) Photograph of freestanding 1x1 cm^2 lattice of CELLINK Bioink. 29C) Photograph of SLAM printed construct; LAMININK+ within 0.3% GG fluid gel support bed. 29D) Representative fluorescence microscopy images of mCherry SH-SY5Ys encapsulated within CELLINK Bioink, at days one and five. 29E) Representative fluorescence microscopy images of SH-SY5Y-GFP within LAMININK+ SLAM printed constructs, at days one and six. N=1 (Images are representative of up to 6 technical repeats of each condition per experiment, with the experiment only carried out once).

Following assessment of fluid gel properties (Figure 27), GG fluid gels were selected for further use during SLAM bioprinting. This was done via printing of LAMININK+ bioink into a GG support bed (Method 3.4.3.10 (Figures 29E). Figure 29C shows the SLAM method is successful in generating lattice structures from the LAMININK+ bioink, with comparatively greater resolution i.e. finer printed filaments, when compared to freestanding printing of CELLINK Bioink (Figure 29B). Print resolution was measured via Image J analysis (Method 3.4.4), revealing average filament width for CELLINK lattices to be 986$\pm$88.8 µm, while LAMININK+ constructs SLAM printed into the support bath displayed an average width of 714$\pm$180 µm. Similarly to CELLINK Bioink, LAMININK+ also displayed autofluorescence (Figure 29E), that also reduced with increasing magnification. At day one, viable SH-SY5Y-GFP cells were dispersed throughout the printed structure, with gaps between autofluorescent LAMININK+ filaments shown to be filled with GG fluid gel particles as seen in Figure 27. By day six, while bioink structure and presence of GG was maintained, little to no viable cells were observed when compared to day one (Figure 29E).Having established suitability of the INKREDIBLE+ printer for extrusion of cell-laden hydrogel bioinks (Figure

29), work looked to incorporate optimised HAMA biomaterials (Chapter 4). Formulation of HAMA bioinks followed previously established protocols (Figure 19A), with additional mixing and incubation time prior to printer cartridge loading to imbue homogeny of viscoelastic properties to printing (Methods 3.4.1). Figure 30A presents workflow for generating bioprinted HAMA constructs. HAMA bioprinted lattices displayed good resolution and discrete arrangement of thin filaments (Figure 30B), with overlapping filaments fusing and occasionally over spilling to fill gaps within the lattice structure. Constructs maintained stability up to 19 days *in vitro*, with retention of phenol red from RPMI culture media indicative of liquid retention and swelling (image not shown). Fluorescence microscopy of printed HAMA constructs revealed encapsulated SH-SY5Y-GFP cells displayed rounded morphologies indicative of suspension culture in all time points (Figure 30C). GFP fluorescence of individual cells was observed until day nineteen in vitro. Figure 30C shows visualisation of individual cell fluorescence was difficult due to autofluorescence of HAMA material and diffuse distribution of GFP-expressing cells throughout the Z-axis. As such, overexposure of green fluorescence was occasionally necessary in order to aid visualisation of GFP protein. Nevertheless, sustained fluorescence is indicative of maintained viability of SH-SY5Ys until day nineteen. Hoechst staining at day nineteen supports this (Method 3.1.6.2), with blue staining of SH-SY5Ys throughout bioprinted HAMA constructs. Results here show that optimised HAMA hydrogel formulation (Chapter 4; Figure 22) translates well as a bioink for use within extrusion based bioprinting systems (such as the INKREDIBLE+), for production of biologically compatible hydrogel constructs.

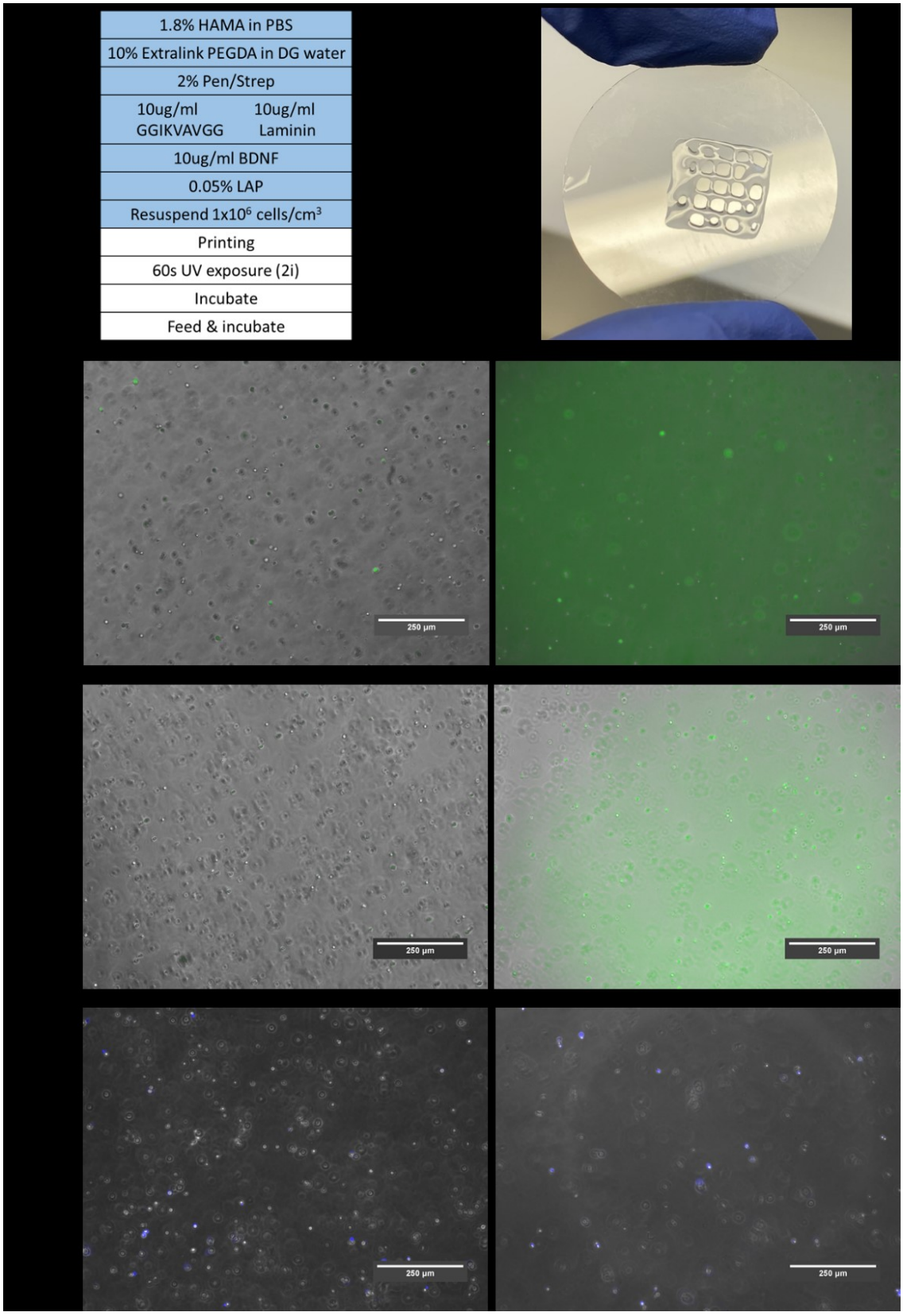

Figure 30. Representative images of bioprinted HAMA materials for neural culture. 30A) Composition & workflow for generation of bioprinted HAMA hydrogels. 30B) Photograph of printed constructs post UV-curing.30C) Representative images of GFP SH-SY5Ys within printed hydrogel lattices, stained with Hoechst 333258 at day nineteen. (Images representative of n=3 biological repeats; with n=3 technical repeats per biological repeat).

6.3. Discussion

This chapter looked to explore biofunctionality of the IKVAV sequence for application within tissue-engineered biomaterials such as HAMA hydrogels. Alongside this, extrusion printing and the SLAM method were evaluated for suitability when structuring HAMA hydrogels for neural tissue engineering applications.

6.3.1. Biofunctionalisation

Characterisation of NPC cells within traditional 2D culture conditions (Figure 24) yielded positive results, with morphology and expression indicative of homogeneous NPC culture. Expression of Nestin and Pax is expected, as the latter is heavily implicated in neurogenesis (Manuel et al., 2015); with widespread expression by *in vivo* human NPCs and *in vitro* iPSC derived NPCs (Zhang et al., 2010). Ki67 expression within Figure 24B is indicative of proliferative ability seen within almost all precursor cells (Sun and Kaufman, 2018), with expression lost in post-mitotic cells such as differentiated neurons (Kim et al., 2012). Low Tujj expression is expected, as this is a mature cytoskeletal protein specific to neuronal populations, however red staining of Tujj proteins is visible. This indicates partial differentiation of NPCs to neuronal cells. Highest red fluorescence is visible at the periphery of neural rosette structures, potentially indicating differentiation. While this is not ideal when looking to utilise NPCs within models of neural development, some degree of differentiation is inevitable due to limitations within existing culture practices (Aref et al., 2018).

Figures 25 compares various substrates for promotion of NPC adhesion in 2D. Figure 25A expands upon observations within Figure 24, both displaying NPC culture on PORN-Laminin coated substrates. This coating is commonly utilised for NPC culture (Calvo-Garrido et al., 2021), as such was used a positive control for comparison of IKVAV-functionalised substrates. Substrates coated with only poly-l-ornithine (PORN) display undesirable clumping compared to monolayers observed in other conditions (Figure 25B). This is supported by the observation that absence of laminin following PORN treatment will impede uniform NSC attachment to the substrate (Calvo-Garrido et al., 2021). It is likely that utilising laminin or laminin-derived sequences for cell-substrate interaction better mimics cell-ECM interaction seen *in vivo*. All other conditions (PORN-Laminin, PORN-GG and PORN-CC) present with a fine meshwork of NPCs, with small gaps visible between cells. Empty space visible between NPCs grown on PORN-GG and PORN-CC substrates is indicative of a lack of cell adhesion within those areas, with larger gaps visible in the GG condition. This could suggest irregular distribution of IKVAV peptides (both GG and CC) resulting in irregular formation of cell-substrate adhesion sites. Alternatively, the issue may lie within the coating method, with further optimisation necessary in order to understand the chemical bonding occurring to join functional peptides to the

substrate surface (Havins et al., 2022). Utilisation of stronger binding regime may present with improved retention of proteins for surface coating, via amine or thiol bond formation to the substrate surface.

Figures 24 and 25 display undifferentiated NPCs that are passaged to maintain their potency and prevent spontaneous differentiation. This careful management ensures that the NPCs remain in a pluripotent state, preventing their commitment to a terminal cell fate. Given additional time, this experiment would have been repeated to investigate the attachment of NPCs to various surface coatings during the differentiation process, as they transition into neurons. Preliminary investigation of NPC differentiation on PORN-Laminin is presented within the appendix (See Appendix 10). While differentiation was unsuccessful (evidenced via off-target differentiation), a loss of Sox2 expression (Appendix 10B) demonstrates a deviation from pluripotency, while increased expression of Tujj (Appendix 10A) indicates development of neuronal cells. Optimisation of the differentiation process on PORN-Laminin will provide a control for further exploration of alternative coatings, such as IKVAV peptides explored within this chapter.

Use of ActinGreen™ (phalloidin conjugated to a green fluorescent probe) enables visualisation of filamentous actin or F-actin, the polymerised form of actin found within the cytoskeleton of all human cells. F-actin contributes to cytoskeletal processes such as maintaining internal cell structure and driving motility, often mediating cell behaviour via interaction with adhesion proteins found in the cell membrane. Meshwork of F-actin marks the forward edge of cell movement, forming lamellipodia that “reach out” to substrates to form focal adhesions. These focal adhesions comprise of multiple structural proteins and provide mechanical linkage of the internal cytoskeleton, to proteins found within the cell membrane such as integrins, to external factors. These external factors include proteins and receptors found on nearby cells or ECM, with cell-cell and cell-matrix adhesion driving tissue formation via relaying of environmental and biochemical signals.

Figure 25B supports this, with staining of F-actin throughout cell bodies but highest intensities are observed at the cell periphery away from nuclei. Spreading of cells and localisation of F-actin to the cell periphery (Figure 25) indicates NPCs here are actively looking for adhesion sites, such as those found on full form laminin and IKVAV motifs. This is supported by increased intensity of ActinGreen™ staining of NPCs on PORN substrates (Figure 25B), with cells undergoing substantial cytoskeletal rearrangement into large actin-rich filaments, generating large protrusions for seeking out adhesion sites within the ECM but also on nearby cells. With interaction of cell “clumps” leading to the formation of the gap-filled meshwork of NPCs on PORN substrates. Conversely, diffuse distribution of F-actin throughout meshwork

of NPCs cultured on full form laminin and IKVAV substrates may be indicative of an abundance of attachment sites. This is supported by literature showing IKVAV promotes fundamental neural processes such as adhesion and neurite outgrown.

Use of IKVAV to provide additional biofunctionality to synthetic biomaterials is increasing; however, RGD remains the most studied integrin-binding peptide (Ligorio and Mata, 2023). Alternative proteins for biofunctionalisation may include glycan-mimetic peptides, with these proteins known to bind soluble and immobilised factors such as growth factors (Ligorio and Mata, 2023). Biofunctionalisation of hydrogels with glycan peptides could therefore lead to improved biological relevance of CNS biomaterials, with sequestering of additional tissue-specific factors such as BDNF. Better understanding of region-specific components of the ECM will allow for creation of improved bioinks with increased specificity for CNS regions or disease states. Increasing amount and variety of biofunctional components would emulate compositional and structural complexity of native ECM, however consideration of biomechanical and biochemical (Hui Chong et al., 2021) effects is necessary.

Limitations of experiments herein include the lack of quantitative data, however this currently limited by an N=2 for Figure 25. Further work should look to repeat this experiment to enable statistical analysis, alongside replication for differentiation of NPCs, allowing quantification of neurite extension alongside qualitative staining. Quantification of fluorescence intensities as a means to assess reorganisation of cytoskeletal F-actin over time would also be a useful measure of cell-matrix interaction, alongside further staining to identify co-localisation of focal adhesions and adhesion sites (IKVAV) found on the substrate. Whats more, cell culture here is carried out on 2D coated substrates, shown to not recapitulate complex 3D cell-matrix interaction seen *in vivo* (Garrido et al., 2023).

Figure 26 demonstrates that iPSCs did indeed express pluripotency-associated marker Oct4, confirmed via ICC. This cell line and maintenance protocol was utilised as this established method was shown to be successful in maintaining pluripotency (personal communication, Dr Eric Hill, Aston University).The Oct4 marker was chosen as previous research utilising PCR gene analysis revealed this was highly expressed in iPSCs compared to other cell types (Bharathan et al., 2017). While iPSC cultures here were shown to display pluripotency, cultures also displayed premature differentiation (Figure 26). Further research should focus on optimizing the maintenance protocol for iPSCs to enhance maintain pluripotency, while minimising differentiation. By refining these protocols, methods of biomaterial biofunctionalisation can be adapted for iPSC culture, similar to those explored for NPCs (Figure 25). This adaptation would enable the development of tailored culture environments that promote iPSC maintenance while facilitating their differentiation into specific cell types.

Ultimately, such advancements could improve the integration of iPSCs into tissue engineering applications, as their ability to differentiate into various cell types will be invaluable for recreating heterogeneity of cells seen *in vivo*.

While Figures 24 and 25 assesses NPC attachment in 2D, translation to 3D biofunctionalisation of HAMA hydrogels holds great promise; with previous research showing IKVAV-functionalised hydrogel biomaterials promote neural cell-matrix interaction *in vitro* (Aydeger et al., 2023, Farrukh et al., 2017, Long et al., 2020, Perera et al., 2019, Sun et al., 2017). Further work should look to utilise methods of chemically modifying HAMA with covalently bound IKVAV peptide sequences (Methods 3.2.1.4) in order to optimise hydrogel biofunctionality via assessment of 3D cell-matrix interactions. Nevertheless research within this chapter demonstrates potential of functional motifs such as IKVAV for biofunctionalisation of hydrogel biomaterials

6.3.2. Structuring via Bioprinting

Prior to investigation of bioprinting approaches, gellan gum (GG) and agarose (Ag) fluid gels were characterised to determine suitability as support phases within SLAM. All conditions presented with particulate gelation and interaction of filamentous protrusions (Figure 27). This morphology is induced via early termination of the polymerisation process during gelation by exposure to shear forces, resulting in particles of gelation instead of a single continuous network.

Both GG and Ag readily lend to use as fluid gels, with the physical and reversible nature of their gelation processes enabling ease of fabrication, compared to other (synthetic) polymers incurring a higher monetary cost and requiring advanced polymerisation modalities. Both polymers form hydrogel matrices following physical bonding of randomly distributed coil chains to form helices, and aggregation to form a 3D polymeric network (Compaan et al., 2019, Ghebremedhin et al., 2021). Differences within fluid gel morphology of GG and Ag (Figure 27) may however be due to GG's reliance upon ionic interaction, alongside hydrogen bond formation during cooling (as seen in Ag hydrogels), resulting in differential aggregate ordering between the two polymers. Alternatively, differences observed here may be due to fundamental differences in chemical structure of polymers, the difference in percentage concentration, or even due to human error. Further work should look to precisely match percentage compositions and production processes, to provide additional insight into the differences between GG and Ag fluid gels.

Fluid gels present as visually transparent due to dispersal of crosslinked particles within a wider liquid phase. However, visualisation of gelated particles via phase microscopy is difficult (Figure 27), with low particle density and high liquid phase resulting in reduced contrast. This

is supported by increasing contrast of images as concentration of fluid gel increases, with morphology of 0.75% Ag fluid gels displaying sharper definition of particles than 0.2% GG fluid gels. Use of dyes would enable better visualisation of particles, enabling precise quantification of particle size and length of protrusions. Interaction of “hairy” particles driving self-healing ability of fluid gels is considered (Norton et al., 1999), measuring features of “hairy” protrusions would enable inference of the relationship between size/length/distribution of “hairy” protrusions and self-healing properties (Fernández Farrés et al., 2014).

Figure 27 presents with decreasing particle size with increasing concentration in both GG (0.2 to 0.4%) and Ag (0.5 to 0.75%) conditions, this is supported by the literature (Ghebremedhin et al., 2021). This means the inverse is true whereby particle size increases with decreasing concentration. This is thought to be due to lower concentration of gelated polymer i.e. lower volume fraction of particles within the hydrogel, resulting in less shear stresses and particular collisions during processing and ultimately larger particle formation (Norton et al., 1999). This logic extends to explaining the heterogeneity of particle size seen with increasing concentration (Ghebremedhin et al., 2021). While shear rate here is kept consistent (Methods 3.2.2), modulation of this variable is another mode of controlling fluid gel particle morphology, future work could look to explore cumulative effects of polymer concentration and shear rate.

Fluid gels are highly versatile hydrogel materials, with physical properties dictated by both formulation (polymer, concentration) and processing (mode of crosslinking, shear force, shear rate) parameters (Fernández Farrés et al., 2014). Quantification of fluid gel properties via rheology enables assessment of mechanical behaviours such as viscoelasticity, stress-relaxation and shear thinning behaviour (Ghebremedhin et al., 2021). Alternatively, quantification of particle size and protrusion length could provide additional insight into the relationship between morphology of fluid gel type and concentration, and self-healing ability. Improved understanding of these unique materials would enable increased utilisation within fields such as neural tissue engineering, for use as primary biomaterials but also as support phases for bioprinting of low viscosity bioinks such as HAMA.

Work here also looked to quantify the cytotoxic effects of extrusion pressures on SH-SY5Ys, however no significant reductions were observed in all conditions. This suggests work should be repeated with increased cell densities and higher print speeds (i.e. increased extrusion pressure and therefore shear stresses), as prolonged shear stresses during extrusion bioprinting are known to negatively impact cell viability (Boularaoui et al., 2020, Xu et al., 2022). Assessment of viability within Figure 28 also utilises extrusion speed (mL/min) as a measure of shear force, and while this indeed allows relative comparison between conditions, further work should look to measure viability in response to standard measures of shear stress

i.e. extrusion forces within the INKREDIBLE+ are in units of Pascals. Figure 28 should also be expanded to investigate additional needle gauges, specifically when we consider that 22G needles are utilised within the bioprinting process here (Methods 3.4.3). Needle gauges explored in Figure 28 (25, 27 and 30G) are smaller in diameter than those used within the INKREDIBLE+ printing process used here, which could potentially suggest that the 22G needle will also not exert cytotoxic levels of shear stress on cells, if it were not for differences in the liquid phase of extruded material. Assessment of multiple needle gauges is imperative when investigating cytotoxic effects of shear stresses; with increased cell viability directly related to increased nozzle diameter, however such increase would likely reduce print resolution (Boularaoui et al., 2020, Chand et al., 2022).

Whats more, figure 28 only explores SH-SY5Ys within liquid culture media, whereas bioprinting employs the use of viscous bioinks. The difference in liquid phase properties prevents translation of findings from figure 28 to bioprinting of viscoelastic materials. Investigation into the effects of extrusion forces on cells is necessary in order to develop extrusion bioprinting systems and bioink materials capable of minimising/preventing cell death i.e. shear thinning materials protect cells from shear stress during extrusion (Boularaoui et al., 2020). Development of bioinks with cell-protective mechanical properties could be one method of preventing stressed or inflammatory phenotypes during extrusion bioprinting. Exploration of further neural cell types would also prove invaluable in determining ideal print parameters for tissue engineering applications; with cell types known to differ in their response to shear stress, i.e. stem cells are more sensitive to shear-induced death (Xu et al., 2022).

Prior to inclusion of HAMA materials developed previously (Chapter 4) within the INKREDIBLE+ bioprinter (Figure 30), preliminary investigation and optimisation of the system was carried out via utilisation of commercially available bioinks (Figure 29). Use of the INKREDIBLE range of bioprinters from CELLINK is established for neural tissue engineering; Hirano *et al.* (201) formed a novel scaffold for neural network formation via printing of gelatin-based bioink containing Irgacure 2959 within a sacrificial gelatin methacrylate bath (Hirano et al., 2021). Bordoni *et al.* (2018) praise the INKREDIBLE+ system for its ease of use and standardised prints (Bordoni et al., 2018), yet further work looked to investigate the extrusion system via utilisation of commercial inks (Figure 29). Consistency of printed structures (Figure 29B) supports this, however may also indicate robustness of preparation protocol and homogeny of CELLINK and LAMININK+ bioinks. Unfortunately, work here is representative of only one batch of each bioink due to high cost (£125-269/3 mL, plus shipping costs), thus limiting reliability of results seen in Figure 29. Nevertheless, use of these commercial materials enabled establishment of the INKREDIBLE+ extrusion system for bioprinting of hydrogels.

Interestingly, SH-SY5Ys were observed to migrate out of the CELLINK Bioink over time, with the generic alginate and cellulose formulae not providing sufficient biofunctional activity to promote cell attachment and retention (Figure 29D). On the other hand, use of this natural polymer bioink enabled physical polymerisation via exposure to $CaCl_2$ solution, which did not appear to be detrimental to viability of encapsulated cells. Conversely, SLAM bioprinting appears to produce constructs of greater resolution (Figure 29D), due to physical confinement of printed filaments. This is supported by microscopic visualisation of SLAM printed constructs (Figure 29E), whereby particles of the GG fluid gel support phase are visible between printed filaments of LAMININK+. Quantification of filament size via Image J (Method 3.4.4) supports this further, with SLAM printed LAMININK+ filaments displaying a smaller resolution (714±180 µm) compared to direct printing of CELLINK Bioink (956±98.8 µm). Side-by-side comparison of print resolution following direct printing (28B) and slam printing (28D) is not entirely accurate, due to difficulty optimising standard microscopy approaches for 3D analysis. Furthermore,printed filaments are comprised of different bioinks (CELLINK Bioink/LAMININK+) with different mechanical properties i.e. bioinks with increased viscosity will display reduced spreading, without the need for a support phase. The use of different bioinks, and the potential for various support materials, brings the additional challenge of optimising imaging via microscopy. Type of polymer, concentration, processing conditions (e.g. fluid gels), refractive indices' etc. will heavily influence the type of microscopy imaging possible, thereby limiting evaluation of print resolution via conventional image analysis. Nevertheless, these results do support the suggestion that SLAM printing provides greater resolution of printed constructs compared to freestanding alternative methods. Unfortunately, SLAM methods requiring a support phase require additional optimisation in order to ensure suitability of the support material to provide biological and physical support to printed bioinks. Budharaju et al. highlight transparency of the support bath is necessary to facilitate visualisation of the printed construct, and also to enable penetration of UV for crosslinking of photoreactive bioinks (Budharaju et al., 2024). The authors go on to note that any supportive medium should provide a compatible environment for printed constructs, providing both biological and mechanical support (Budharaju et al., 2024).

Unfortunately, SLAM printed constructs here present with a total loss of viability by day six, potentially due to osmotic dysregulation of encapsulated cells; with prolonged exposure to Ca^{2+}/Mg^{2+} ions present within the 99% PBS-GG fluid gel support. Quantification of viability would provide better indication of cellular responses to specific bioinks and support phases. Loss of viability within SLAM conditions (Figure 29E) suggests careful modulation of support phase is necessary, in order to provide not only mechanical support but also biochemical compatibility to printed constructs within. In fact, biofunctionalisation of secondary support

phases is suggested as a means of imbuing increased biological relevance and biochemical support to bioprinted tissues (Fernández Farrés et al., 2014).

Figure 30 incorporates all of the findings found in chapters 4 and 5 to bioprint cell-laden HAMA constructs capable of maintaining long-term (19 days *in vitro*) viability of SH-SY5Ys. HAMA bioink composition is the same as the optimised formulation shown in chapter 4 (Figure 17A), with inclusion of GGIKVAVG peptide supported by further work within this chapter demonstrating the power biofunctionalisation for neural culture. Whats more, preliminary optimisation of printing parameters accelerated the optimisation process for HAMA extrusion bioprinting; i.e. extrusion pressures were kept within the range of 40-110 kPa to prevent leakage or premature expulsion of bioinks and HAMA bioinks were incubated to undergo partial gelation in order to increase viscosity for reduced spreading following printing.

Figure 30B demonstrates printing of HAMA materials via the INKREDIBLE+ to produce lattice structures comprising of thin printed filaments, with optimal viscoelastic properties limiting spreading of filaments whilst also enabling merging of overlapping filaments to produce a singular meshwork. However, some spreading is visible, which is not desirable when looking to print high resolution constructs necessary for precise placement of CNS-specific bioinks for generation of defined neuronal architectures. Biocompatibility of printed HAMA constructs is shown in Figure 30C by sustained fluorescence of SH-SY5Y cells up to day nineteen *in vitro*. Rounded morphologies are visible throughout culture may indicate lack of adhesion to the HAMA matrix, however IKVAV and laminin are known to provide support to cells *in vitro* and lack of cell death may indicate some cell-matrix interaction but insufficient amounts/distribution/immobilisation to evoke cell spreading. Without chemical binding of IKVAV or laminin to the HAMA backbone, it is likely that such biofunctional proteins are providing support to encapsulated cells via soluble binding prior to leaching out from hydrogels.

Rheology of printed HAMA constructs was not carried out due to time limitations and practical barriers such as transportation of printed constructs. However, rheology of optimal bulk HAMA hydrogels (Figure 22D) provides an approximation of viscoelastic properties of bioprinted HAMA hydrogels, as composition was kept the same. While structuring via bioprinting of complex architectures may influence viscoelastic properties of the HAMA construct, any differences between rheological properties of bulk vs bioprinted HAMA hydrogels could be attributed to processing conditions. We can therefore infer that bioprinted HAMA hydrogels display stiffness of approximately 4.12$\pm$0.6 Pascals. While this value falls at the softest end of biologically relevant stiffness for neural tissue engineering, tuneability of the HAMA system described herein leaves room for modulation of mechanical properties.

This chapter demonstrates that mechanical properties of low-viscosity HAMA hydrogel precursors can be incorporated into extrusion printing systems, such as the INKREDIBLE+ extrusion bioprinter from CELLINK, in order to generate defined architectures. The photopolymerisable nature of HAMA hydrogels also lends to use within light-based printing systems. Laser-based approaches such as 2PP are a cutting-edge 3D bioprinting approach enabling high resolution on a nm-μm scale (Cadena et al., 2021, de la Vega et al., 2019). Laser-based bioprinting approaches would therefore be invaluable in recreating complex patterning seen within the CNS *in vivo* within hydrogel biomaterials; with recent research indicating a laser-based hydrogel droplet-deposition approach shown to have no detrimental effects on viability of astrocytes or NSCs (Koch et al., 2023). Stereolithography or vat polymerisation utilises a light source to preferentially polymerise hydrogel biomaterials to create elaborate 3D geometries and structures (Anandakrishnan et al., 2020). Digital light processing is an emerging stereolithographic technology that utilises a projected light source to selectively cure layers of photopolymerisable material, an advantage over time-consuming laser based approaches (Paone et al., 2023). Use of stereolithographic methods alongside advanced functionalisation techniques is invaluable for spatiotemporally controlled photopatterning of proteins (Yu et al., 2020). The BIONOVA X (CELLINK, BICO) is marketed as the most accurate DLP, with rapid generation of 10 μm resolution features, with the potential for generation of stiffness gradients from multi-material cell-laden bioinks.

7. Conclusions and Future Perspectives

Development of biomaterials for *in vitro* tissue engineering applications relies upon replication and recreation of hallmarks of natural tissues *in vivo*. Ensuring tissue-specificity of environmental features within biomaterials is imperative for guiding of cell fates and generation of biomimetic tissues for modelling *in vitro*. This advanced biomimicry via exploitation of biochemical and mechanical factors is fundamental in development of cutting-edge model systems. Production of such model systems is invaluable in understanding (patho)physiology and accelerating the search for therapeutics, specifically for complex tissues such as the CNS and clinically challenging disease states like AD.

Unfortunately, recreating the insurmountable complexity of the CNS is near impossible, with innumerable biochemical and physiomechanical features of the ECM interconnecting to supporting countless cellular interactions. Neural tissue engineering is therefore an imperfect science, limited by incomplete understanding of CNS ECM development and tissue homeostasis *in vivo,* and slow progress within the field of material science to develop "soft solid" materials capable of mimicking mechanical properties of elaborate polymeric networks such as the ECM. Research into the power of mechanical signals within ECM is gaining interest; however, utilisation of such signals is hindered by limited understanding of mechanisms of action and difficulty separating physiomechanical and biochemical components of the ECM. This project therefore looked to investigate biomaterials for neural tissue engineering applications with specific focus on mechanical features, such as stiffness. As such, a fundamental recommendation for tissue engineers is to employ a similar multidisciplinary approach when developing biomaterials such as hydrogels. This approach will empower improved understanding of physiomechanical and biochemical features of native ECM, enabling better recreation of structural and functional heterogeneity within *in vitro* culture systems. In order to do this, researchers must carefully consider compounding effects when integrating multiple biochemical and mechanical features, exploiting advantageous synergistic effects whilst minimising unwanted outcomes i.e. cytotoxicity. This is particularly important when attempting to recapitulate tissues with intricate hierarchical ordering and compound cell-ECM interactions, such as the CNS.

This project aimed to develop a hydrogel biomaterial to possess mechanical and biochemical properties necessary for mimicry of CNS ECM; this began via exploration of polymers in chapter 4. Indeed research here presents HAMA as a superior polymer when generating hydrogels for neural tissue engineering, due to potential for tuning of mechanical properties to produce biologically relevant stiffness (0.5-10 kPa). Unfortunately, the optimal HAMA composition utilised for bioprinting presents with reduced stiffness <0.5 kPa, suggesting

further research should expand upon investigative work into photopolymerisation of HAMA hydrogels here, via exploration UV intensity and exposure time as a means of guiding hydrogel mechanics without modification to hydrogel composition.

HAMA itself is not a novel proposal as this polymer has been utilised previously (Section 1.4.2) to produce biomaterials for neural tissue engineering applications, with chemical modification lending the polymer to photopolymerisation (Chapter 5 and table 4). Novelty of this project therefore lies within the methodical approach to the optimisation process; isolation of variables (polymer, photoinitiator, additional factors) enabled progressive investigation into singular and compounding effects when modifying biomaterial formulation and processing conditions (Figure 23). This carefully considered approach to optimisation in chapters 4 and 5 elucidates complex relationships that underpin photopolymerisation of polymeric networks to produce HAMA hydrogels, providing valuable insight into bulk mechanical properties, but also biochemical signals encapsulated cells are exposed to during polymerisation and into cell culture. Chapter 4 takes an innovative approach to biomaterial optimisation with data-driven statistical modelling enabling prediction of hydrogel properties; such approaches are currently underutilised for deliberate engineering of biomaterials. This improved understanding of relationships between variables that underpin hydrogel formation (polymers, crosslinking, modifications), alongside continuous mechanical and biological characterisation, enables generation of a mechanically tuneable hydrogel biomaterial; stiffness of HAMA hydrogels can be tuned via modulation of UV dose to guide the photopolymerisation reaction without increasing concentration of cytotoxic photoinitiators. Given further time this project would have looked to investigate degree of methacrylation as a variable for consideration when generating HAMA hydrogels.

Chapter 5 aimed to optimise hydrogel properties via photocrosslinking, shown to be attractive avenue for spatiotemporal control of biomaterial polymerisation (Section 1.4.2). However, research within this area often fails to report much of the information necessary for replication of UV dose, as such this project ensured to characterise all UV systems fully. Chapter 5 succeeds in optimising HAMA materials for neural engineering, going on to demonstrate tuneability of the optimal HAMA hydrogel formulation via modulation of photopolymerisation via UV dose. This unique approach of isolation, characterisation and translation of UV dose elements will lead the way for future tissue engineers; demonstrating the usefulness of UV photopolymerisation, but also necessity for definitive characterisation of UV dose. Utilisation of multiple cell types for biological investigation is a novel advantage to this project, where tissue engineers commonly utilise singular cell types and fail to account for sensitivity of stem cells and neural cells. Indeed biomaterial investigation and optimisation within chapters 4 and 5 enables fine-tuning of biomaterial properties via sequential modulation of individual factors.

This tuneability is desirable when tissue engineering specific microenvironments *in vitro*, with potential for tweaking of properties such as stiffness to increase biological relevance to specific (disease) states *in vivo*. Due to time limitations this project was unable to modulate stiffness for modelling neurodegenerative diseases like AD.

Findings throughout research here corroborate the lack of cell-matrix adhesion reported in HA-based hydrogels, demonstrating necessity of biofunctionalisation techniques. Use of functional motifs instead of full form proteins is gaining interest, specifically IKVAV sequence for neural tissue engineering. Chapter 6 aimed to explore such functional proteins for NPC adhesion in 2D and indeed this was achieved. Unfortunately, incorporation of biofunctional IKVAV sequences within HAMA hydrogels was not explored within this project due to time limitations. Nevertheless, 2D investigation here lays foundations for future researchers to translate these findings into 3D biofunctionalisation of hydrogels. Certainly, biofunctionalisation is a powerful tool for displaying biochemical signals to cells within hydrogels, to guide cell processes and ultimately tissue development. Future work should therefore look to utilise advanced methods of biofunctionalisation whereby exploitation of unique binding regimes (click reactions, photopolymerisation) enables elaborate patterning, i.e. gradient, orthogonal gradients etc. of bioactive components within hydrogels, in order to reproduce the dynamic spatiotemporal patterning indicative of *in vivo* tissue. In fact, forward-thinking methods of photopolymerisation will enable production of next-generation hydrogel biomaterials containing multiple cohesive patterns.

Unfortunately, this project was unable to incorporate iPSC-derived neural cells into HAMA hydrogels for generation of 3D neuronal networks; due to toxicity of the hydrogel during early development leading to extended optimisation times and ultimately reduced time for encapsulation of neural cells within the optimal HAMA formulation. This is a fundamental limitation of the project, with ability to support neuronal network formation and maintenance an imperative part of any model of neural tissue. Given further time, this project would have optimised properties of HAMA hydrogels to support NPC or neuronal culture, via 3D biofunctionalisation of HAMA polymers, inclusion of additional biological factors, structuring via 3D bioprinting etc.

Despite underexplored biofunctionalisation, this project demonstrates combination of calculated functionalisation techniques and photopolymerisation enables fine-tuning of polymerisation to produce hydrogels with a range of stiffness. This mechanical malleability of photopolymerised biomaterials (such as HAMA) enables use within bioprinting systems, as a means to equip the model with additional structuring. Extrusion bioprinting is uncommon within neural tissue engineering, due to incompatibility of low-viscosity or “soft” biomaterials resulting

in loss of resolution following printing. The final aim of this research was to explore bioprinting techniques for structuring of HAMA hydrogels, and indeed research here establishes HAMA as an extrusion bioink; this is highly significant for neural tissue engineers, demonstrating it is possible to engineer a biologically and mechanically compatible “soft solid” hydrogel with potential for additional structuring via extrusion printing. Further work should look to investigate the impact of extrusion bioprinting on not only encapsulated cells but also physiomechanical features. With printing of defined structures with overhangs or empty spaces undoubtedly altering bulk mechanical behaviour of hydrogel constructs compared to monolithic structures.

Future research should look to combine mechanically optimised bioinks, such as HAMA, with novel printing approaches, such as the fluid-gel support phase in SLAM, to produce bioprinted hydrogel constructs with CNS-specific composition (HA polymer, IKVAV motif), mechanics (0.5-10 kPa) and intricate macroscale structuring (layering, gyrus). Incorporation of HAMA hydrogels within the INKREDIBLE+ bioprinter demonstrates suitability of HAMA within extrusion printing systems, but also the versatility of HAMA for use within alternative structuring systems i.e. other printing systems, microfluidics etc. Given more time this project would have explored alternative printing modalities for generation of HAMA constructs with improved properties compared to extrusion based approaches utilised here. Next-generation neural models will likely embrace hydrogel biomaterials containing a myriad of unified biochemical and physical signals. Introduction of such signals may be carried out via; layering of materials/techniques, multiscale/gradient patterning, biofunctionalisation, inclusion of conductive carbon-based materials, novel mechanical behaviours, macroscale structuring or even a combination of all of the above (Farrukh et al., 2017, Tiwari et al., 2020, Yang et al., 2016, Ligorio and Mata, 2023, Kajtez et al., 2022, Paone et al., 2023). This project indeed highlights the necessity of combined biological, materials science and engineering approaches in order to develop a biomaterial with the necessary complexity to model human ECM and functional tissue.

Work here highlights versatility of photopolymerised HAMA hydrogels (tuneable stiffness, potential for biofunctionalisation, malleability for use within bioprinting systems), with such versatility highly advantageous for tissue engineers as a means to modify material properties depending on the application. Within the context of neural tissue engineering, the optimisation, functionalisation and structuring of hydrogels here presents HAMA as an ideal polymer for inclusion within engineered neural tissue. Moreover, conclusions drawn here extend beyond tissue engineering, demonstrating the power of deliberate and considered engineering approaches to instil desirable properties within polymeric biomaterials for limitless applications.

Bibliography

AARONS, T., BRADBURN, S., ROBINSON, A., PAYTON, A., PENDLETON, N. & MURGATROYD, C. 2019. Dysregulation of BDNF in Prefrontal Cortex in Alzheimer's Disease. *J Alzheimers Dis,* 69**,** 1089-1097.

ABDEEN, A. A., LEE, J. & KILIAN, K. A. 2016. Capturing extracellular matrix properties in vitro: Microengineering materials to decipher cell and tissue level processes. *Experimental Biology and Medicine,* 241**,** 930-938.

ABELSETH, E., ABELSETH, L., DE LA VEGA, L., BEYER, S. T., WADSWORTH, S. J. & WILLERTH, S. M. 2019. 3D Printing of Neural Tissues Derived from Human Induced Pluripotent Stem Cells Using a Fibrin-Based Bioink. *ACS Biomaterials Science & Engineering,* 5**,** 234-243.

AHMAD, M. A., KAREEM, O., KHUSHTAR, M., AKBAR, M., HAQUE, M. R., IQUBAL, A., HAIDER, M. F., POTTOO, F. H., ABDULLA, F. S., AL-HAIDAR, M. B. & ALHAJRI, N. 2022. Neuroinflammation: A Potential Risk for Dementia. *Int J Mol Sci,* 23.

AILI, Y., MAIMAITIMING, N., WANG, Z. & WANG, Y. 2024. Brain organoids: A new tool for modelling of neurodevelopmental disorders. *J Cell Mol Med,* 28**,** e18560.

AISENBREY, E. A. & MURPHY, W. L. 2020. Synthetic alternatives to Matrigel. *Nature Reviews Materials,* 5**,** 539-551.

ALAYLIOĞLU, M., DURSUN, E., YILMAZER, S. & AK, D. G. 2020. A Bridge Between in vitro and in vivo Studies in Neuroscience: Organotypic Brain Slice Cultures. *Noro Psikiyatr Ars,* 57**,** 333-337.

ALLEN, J. L., COOKE, M. E. & ALLISTON, T. 2012. ECM stiffness primes the TGFβ pathway to promote chondrocyte differentiation. *Molecular Biology of the Cell,* 23**,** 3731-3742.

ALMANY, L. & SELIKTAR, D. 2005. Biosynthetic hydrogel scaffolds made from fibrinogen and polyethylene glycol for 3D cell cultures. *Biomaterials,* 26**,** 2467-2477.

AMADIO, S., DE NINNO, A., MONTILLI, C., BUSINARO, L., GERARDINO, A. & VOLONTÉ, C. 2013. Plasticity of primary microglia on micropatterned geometries and spontaneous long-distance migration in microfluidic channels. *BMC Neuroscience,* 14.

AMIRIFAR, L., SHAMLOO, A., NASIRI, R., DE BARROS, N. R., WANG, Z. Z., UNLUTURK, B. D., LIBANORI, A., IEVGLEVSKYI, O., DILTEMIZ, S. E., SANCES, S., BALASINGHAM, I., SEIDLITS, S. K. & ASHAMMAKHI, N. 2022. Brain-on-a-chip: Recent advances in design and techniques for microfluidic models of the brain in health and disease. *Biomaterials,* 285**,** 121531.

AMOO, L. M. & LAYI FAGBENLE, R. 2020. 14 - Overview of non-Newtonian boundary layer flows and heat transfer. *In:* FAGBENLE, R. O., AMOO, O. M., ALIU, S. & FALANA, A. (eds.) *Applications of Heat, Mass and Fluid Boundary Layers.* Woodhead Publishing.

ANANDAKRISHNAN, N., YE, H., GUO, Z., CHEN, Z., MENTKOWSKI, K. I., LANG, J. K., RAJABIAN, N., ANDREADIS, S. T., MA, Z., SPERNYAK, J. A., LOVELL, J. F., WANG, D., XIA, J., ZHOU, C. & ZHAO, R. 2020. Fast 3D printing of large-scale biocompatible hydrogel models. *bioRxiv***,** 2020.10.22.345660.

ANNABI, N., NICHOL, J. W., ZHONG, X., JI, C., KOSHY, S., KHADEMHOSSEINI, A. & DEHGHANI, F. 2010. Controlling the porosity and microarchitecture of hydrogels for tissue engineering. *Tissue Eng Part B Rev,* 16**,** 371-83.

ANNECCHINO, L. A. & SCHULTZ, S. R. 2018. Progress in automating patch clamp cellular physiology. *Brain Neurosci Adv,* 2**,** 2398212818776561.

APPLEGATE, M. B., COBURN, J., PARTLOW, B. P., MOREAU, J. E., MONDIA, J. P., MARELLI, B., KAPLAN, D. L. & OMENETTO, F. G. 2015. Laser-based three-dimensional multiscale micropatterning of biocompatible hydrogels for customized

tissue engineering scaffolds. *Proceedings of the National Academy of Sciences,* 112**,** 12052.
AREF, A. R., CAMPISI, M., IVANOVA, E., PORTELL, A., LARIOS, D., PIEL, B. P., MATHUR, N., ZHOU, C., COAKLEY, R. V., BARTELS, A., BOWDEN, M., HERBERT, Z., HILL, S., GILHOOLEY, S., CARTER, J., CAÑADAS, I., THAI, T. C., KITAJIMA, S., CHIONO, V., PAWELETZ, C. P., BARBIE, D. A., KAMM, R. D. & JENKINS, R. W. 2018. 3D microfluidic ex vivo culture of organotypic tumor spheroids to model immune checkpoint blockade. *Lab on a Chip,* 18**,** 3129-3143.
ASEYEV, N., IVANOVA, V., BALABAN, P. & NIKITIN, E. 2023. Current Practice in Using Voltage Imaging to Record Fast Neuronal Activity: Successful Examples from Invertebrate to Mammalian Studies. *Biosensors,* 13**,** 648.
AYDEGER, A., AYSIT, N., BAYDAS, G., CAKICI, C., ERIM, U. C., ARPA, M. D. & OZCICEK, I. 2023. Design of IKVAV peptide/gold nanoparticle decorated, micro/nano-channeled PCL/PLGA film scaffolds for neuronal differentiation and neurite outgrowth. *Biomaterials Advances,* 152**,** 213472.
BANG, S., JEONG, S., CHOI, N. & KIM, H. N. 2019. Brain-on-a-chip: A history of development and future perspective. *Biomicrofluidics,* 13**,** 051301.
BARDY, C., VAN DEN HURK, M., EAMES, T., MARCHAND, C., HERNANDEZ, R. V., KELLOGG, M., GORRIS, M., GALET, B., PALOMARES, V., BROWN, J., BANG, A. G., MERTENS, J., BÖHNKE, L., BOYER, L., SIMON, S. & GAGE, F. H. 2015. Neuronal medium that supports basic synaptic functions and activity of human neurons in vitro. *Proceedings of the National Academy of Sciences,* 112**,** E2725.
BARROS, D., CONDE-SOUSA, E., GONÇALVES, A. M., HAN, W. M., GARCÍA, A. J., AMARAL, I. F. & PÊGO, A. P. 2019. Engineering hydrogels with affinity-bound laminin as 3D neural stem cell culture systems. *Biomaterials Science,* 7**,** 5338-5349.
BARTLETT, R. D., ELEFTHERIADOU, D., EVANS, R., CHOI, D. & PHILLIPS, J. B. 2020. Mechanical properties of the spinal cord and brain: Comparison with clinical-grade biomaterials for tissue engineering and regenerative medicine. *Biomaterials,* 258**,** 120303.
BARUFFALDI, D., PALMARA, G., PIRRI, C. & FRASCELLA, F. 2021. 3D Cell Culture: Recent Development in Materials with Tunable Stiffness. *ACS Applied Bio Materials,* 4**,** 2233-2250.
BAYRAKTAR, O. A., BARTELS, T., HOLMQVIST, S., KLESHCHEVNIKOV, V., MARTIROSYAN, A., POLIOUDAKIS, D., BEN HAIM, L., YOUNG, A. M. H., BATIUK, M. Y., PRAKASH, K., BROWN, A., ROBERTS, K., PAREDES, M. F., KAWAGUCHI, R., STOCKLEY, J. H., SABEUR, K., CHANG, S. M., HUANG, E., HUTCHINSON, P., ULLIAN, E. M., HEMBERG, M., COPPOLA, G., HOLT, M. G., GESCHWIND, D. H. & ROWITCH, D. H. 2020. Astrocyte layers in the mammalian cerebral cortex revealed by a single-cell in situ transcriptomic map. *Nature Neuroscience,* 23**,** 500-509.
BEAN, J. 2015. *Hydrogel Systems for Triggered Release of Bacteriophage K and Directed Cell Growth.* Doctor of Philosophy, Bath University.
BEDIR, T., ULAG, S., USTUNDAG, C. B. & GUNDUZ, O. 2020. 3D bioprinting applications in neural tissue engineering for spinal cord injury repair. *Materials Science and Engineering: C,* 110**,** 110741.
BERTRAM, L. & TANZI, R. E. 2009. Genome-wide association studies in Alzheimer's disease. *Human molecular genetics,* 18**,** R137-R145.
BESPALOV, A., STECKLER, T., ALTEVOGT, B., KOUSTOVA, E., SKOLNICK, P., DEAVER, D., MILLAN, M. J., BASTLUND, J. F., DOLLER, D., WITKIN, J., MOSER, P., O'DONNELL, P., EBERT, U., GEYER, M. A., PRINSSEN, E., BALLARD, T. & MACLEOD, M. 2016. Failed trials for central nervous system disorders do not necessarily invalidate preclinical models and drug targets. *Nature Reviews Drug Discovery,* 15**,** 516-516.
BHARATHAN, S. P., MANIAN, K. V., AALAM, S. M., PALANI, D., DESHPANDE, P. A., PRATHEESH, M. D., SRIVASTAVA, A. & VELAYUDHAN, S. R. 2017. Systematic

evaluation of markers used for the identification of human induced pluripotent stem cells. *Biol Open,* 6**,** 100-108.
BIGGS, M. J. P., FERNANDEZ, M., THOMAS, D., COOPER, R., PALMA, M., LIAO, J., FAZIO, T., DAHLBERG, C., WHEADON, H., PALLIPURATH, A., PANDIT, A., KYSAR, J. & WIND, S. J. 2017. The Functional Response of Mesenchymal Stem Cells to Electron-Beam Patterned Elastomeric Surfaces Presenting Micrometer to Nanoscale Heterogeneous Rigidity. *Advanced Materials,* 29.
BILLIET, T., VANDENHAUTE, M., SCHELFHOUT, J., VAN VLIERBERGHE, S. & DUBRUEL, P. 2012. A review of trends and limitations in hydrogel-rapid prototyping for tissue engineering. *Biomaterials,* 33**,** 6020-6041.
BINDER, D. K. & SCHARFMAN, H. E. 2004. Brain-derived neurotrophic factor. *Growth Factors,* 22**,** 123-31.
BINGHAM, E. C. 1930. Some Fundamental Definitions of Rheology. *Journal of Rheology,* 1**,** 507-516.
BIONDI, O., MOTTA, S. & MOSESSO, P. 2002. Low molecular weight polyethylene glycol induces chromosome aberrations in Chinese hamster cells cultured in vitro. *Mutagenesis,* 17**,** 261-264.
BIRD, T. D. 2008. Genetic aspects of Alzheimer disease. *Genetics in medicine : official journal of the American College of Medical Genetics,* 10**,** 231-239.
BLAIKIE, L., KAY, G., MACIEL, P. & KONG THOO LIN, P. 2022. Experimental modelling of Alzheimer's disease for therapeutic screening. *European Journal of Medicinal Chemistry Reports,* 5**,** 100044.
BONI, R., ALI, A., SHAVANDI, A. & CLARKSON, A. N. 2018. Current and novel polymeric biomaterials for neural tissue engineering. *Journal of biomedical science,* 25**,** 90.
BORDONI, M., REY, F., FANTINI, V., PANSARASA, O., DI GIULIO, A. M., CARELLI, S. & CEREDA, C. 2018. From Neuronal Differentiation of iPSCs to 3D Neuro-Organoids: Modelling and Therapy of Neurodegenerative Diseases. *Int J Mol Sci,* 19.
BOULARAOUI, S., AL HUSSEIN, G., KHAN, K. A., CHRISTOFOROU, N. & STEFANINI, C. 2020. An overview of extrusion-based bioprinting with a focus on induced shear stress and its effect on cell viability. *Bioprinting,* 20**,** e00093.
BROGUIERE, N., HUSCH, A., PALAZZOLO, G., BRADKE, F., MADDURI, S. & ZENOBI-WONG, M. 2019. Macroporous hydrogels derived from aqueous dynamic phase separation. *Biomaterials,* 200**,** 56-65.
BRUCE, A. J., MALFROY, B. & BAUDRY, M. 1996. beta-Amyloid toxicity in organotypic hippocampal cultures: protection by EUK-8, a synthetic catalytic free radical scavenger. *Proc Natl Acad Sci U S A,* 93**,** 2312-6.
BRUNEL, L. G., HULL, S. M. & HEILSHORN, S. C. 2022. Engineered assistive materials for 3D bioprinting: support baths and sacrificial inks. *Biofabrication,* 14.
BUDDAY, S., NAY, R., DE ROOIJ, R., STEINMANN, P., WYROBEK, T., OVAERT, T. C. & KUHL, E. 2015. Mechanical properties of gray and white matter brain tissue by indentation. *Journal of the mechanical behavior of biomedical materials,* 46**,** 318-330.
BUDHARAJU, H., SUNDARAMURTHI, D. & SETHURAMAN, S. 2024. Embedded 3D bioprinting – An emerging strategy to fabricate biomimetic & large vascularized tissue constructs. *Bioactive Materials,* 32**,** 356-384.
CADENA, M., NING, L., KING, A., HWANG, B., JIN, L., SERPOOSHAN, V. & SLOAN, S. A. 2021. 3D Bioprinting of Neural Tissues. *Adv Healthc Mater,* 10**,** e2001600.
CALIARI, S. R. & BURDICK, J. A. 2016. A practical guide to hydrogels for cell culture. *Nature Methods,* 13**,** 405-414.
CALÓ, E. & KHUTORYANSKIY, V. V. 2015. Biomedical applications of hydrogels: A review of patents and commercial products. *European Polymer Journal,* 65**,** 252-267.
CALVO-GARRIDO, J., WINN, D., MAFFEZZINI, C., WEDELL, A., FREYER, C., FALK, A. & WREDENBERG, A. 2021. Protocol for the derivation, culturing, and differentiation of human iPS-cell-derived neuroepithelial stem cells to study neural differentiation in vitro. *STAR Protoc,* 2**,** 100528.

CAPITANIO, J. P. & EMBORG, M. E. 2008. Contributions of non-human primates to neuroscience research. *The Lancet,* 371**,** 1126-1135.
CASTIAUX, A. D., SPENCE, D. M. & MARTIN, R. S. 2019. Review of 3D cell culture with analysis in microfluidic systems. *Analytical Methods,* 11**,** 4220-4232.
CAVINESS, V. S., JR., NOWAKOWSKI, R. S. & BHIDE, P. G. 2009. Neocortical neurogenesis: morphogenetic gradients and beyond. *Trends in neurosciences,* 32**,** 443-450.
CHAMBERS, S. M., FASANO, C. A., PAPAPETROU, E. P., TOMISHIMA, M., SADELAIN, M. & STUDER, L. 2009. Highly efficient neural conversion of human ES and iPS cells by dual inhibition of SMAD signaling. *Nature Biotechnology,* 27**,** 275-280.
CHAND, R., MUHIRE, B. S. & VIJAYAVENKATARAMAN, S. 2022. Computational Fluid Dynamics Assessment of the Effect of Bioprinting Parameters in Extrusion Bioprinting. *Int J Bioprint,* 8**,** 545.
CHANSORIA, P. & SHIRWAIKER, R. 2019. Characterizing the Process Physics of Ultrasound-Assisted Bioprinting. *Scientific Reports,* 9**,** 13889.
CHAUDHURI, O., GU, L., KLUMPERS, D., DARNELL, M., BENCHERIF, S. A., WEAVER, J. C., HUEBSCH, N., LEE, H.-P., LIPPENS, E., DUDA, G. N. & MOONEY, D. J. 2016. Hydrogels with tunable stress relaxation regulate stem cell fate and activity. *Nature Materials,* 15**,** 326-34.
CHEN, M. H., WANG, L. L., CHUNG, J. J., KIM, Y.-H., ATLURI, P. & BURDICK, J. A. 2017. Methods To Assess Shear-Thinning Hydrogels for Application As Injectable Biomaterials. *ACS Biomaterials Science & Engineering,* 3**,** 3146-3160.
CHEN, Y., QIN, C., HUANG, J., TANG, X., LIU, C., HUANG, K., XU, J., GUO, G., TONG, A. & ZHOU, L. 2020. The role of astrocytes in oxidative stress of central nervous system: A mixed blessing. *Cell Prolif,* 53**,** e12781.
CHIMENE, D., KAUNAS, R. & GAHARWAR, A. K. 2020. Hydrogel Bioink Reinforcement for Additive Manufacturing: A Focused Review of Emerging Strategies. *Advanced Materials,* 32**,** 1902026.
CHIMENE, D., LENNOX, K. K., KAUNAS, R. R. & GAHARWAR, A. K. 2016. Advanced Bioinks for 3D Printing: A Materials Science Perspective. *Annals of Biomedical Engineering,* 44**,** 2090-2102.
CHO, S., WOOD, A. & BOWLBY, M. R. 2007. Brain slices as models for neurodegenerative disease and screening platforms to identify novel therapeutics. *Curr Neuropharmacol,* 5**,** 19-33.
CHOI, J. R., YONG, K. W., CHOI, J. Y. & COWIE, A. C. 2019. Recent advances in photo-crosslinkable hydrogels for biomedical applications. *BioTechniques,* 66**,** 40-53.
CHRIST, A. & LATZ, E. 2019. The Western lifestyle has lasting effects on metaflammation. *Nature Reviews Immunology,* 19**,** 267-268.
COLOMBE DROMEL, P., SINGH, D., ALEXANDER-KATZ, A., KURISAWA, M., SPECTOR, M. & YOUNG, M. 2020. Injectable gelatin hydroxyphenyl propionic acid hydrogel protects human retinal progenitor cells (hRPCs) from shear stress applied during small-bore needle injection. *Applied Materials Today,* 19**,** 100602.
COMPAAN, A. M., SONG, K. & HUANG, Y. 2019. Gellan Fluid Gel as a Versatile Support Bath Material for Fluid Extrusion Bioprinting. *ACS Applied Materials & Interfaces,* 11**,** 5714-26.
COOKE, M. E., JONES, S. W., TER HORST, B., MOIEMEN, N., SNOW, M., CHOUHAN, G., HILL, L. J., ESMAELI, M., MOAKES, R. J. A., HOLTON, J., NANDRA, R., WILLIAMS, R. L., SMITH, A. M. & GROVER, L. M. 2018. Structuring of Hydrogels across Multiple Length Scales for Biomedical Applications. *Advanced Materials,* 30**,** 1705013.
COPPARI, S., RAMAKRISHNA, S., TEODORI, L. & ALBERTINI, M. C. 2021. Cell signalling and biomaterials have a symbiotic relationship as demonstrated by a bioinformatics study: The role of surface topography. *Current Opinion in Biomedical Engineering,* 17**,** 100246.

CORNING. 2020. *Matrigel Matrix* [Online]. Available: https://www.corning.com/worldwide/en/products/life-sciences/products/surfaces/matrigel-matrix.html#:~:text=%20Use%20the%20online%20Corning%20Matrigel%20Lot%20Selection,to%20the%20previously%20requested%20lot%20number.%20More%20 [Accessed 05/08/2020].
COSSON, S., KOBEL, S. A. & LUTOLF, M. P. 2009. Capturing Complex Protein Gradients on Biomimetic Hydrogels for Cell-Based Assays. *Advanced Functional Materials,* 19**,** 3411-3419.
COULTHARD, E. J. & LOVE, S. 2018. A broader view of dementia: multiple co-pathologies are the norm. *Brain,* 141**,** 1894-1897.
COWMAN, M., SCHMIDT, T., RAGHAVAN, P. & STECCO, A. 2015. Viscoelastic Properties of Hyaluronan in Physiological Conditions [version 1; peer review: 2 approved]. *F1000Research,* 4.
CROFT, C. L. & NOBLE, W. 2018. Preparation of organotypic brain slice cultures for the study of Alzheimer's disease. *F1000Res,* 7**,** 592.
CUADRADO-TEJEDOR, M. & GARCÍA-OSTA, A. 2014. Current animal models of Alzheimer's disease: challenges in translational research. *Frontiers in neurology,* 5**,** 182-182.
CUKIERMAN, E., PANKOV, R., STEVENS, D. R. & YAMADA, K. M. 2001. Taking Cell-Matrix Adhesions to the Third Dimension. *Science,* 294**,** 1708.
CUMMINGS, J. L., MORSTORF, T. & ZHONG, K. 2014. Alzheimer's disease drug-development pipeline: few candidates, frequent failures. *Alzheimer's Research & Therapy,* 6**,** 37.
CUMMINGS, J. L., TONG, G. & BALLARD, C. 2019. Treatment Combinations for Alzheimer's Disease: Current and Future Pharmacotherapy Options. *Journal of Alzheimer's disease : JAD,* 67**,** 779-794.
CUOMO, A. S. E., SEATON, D. D., MCCARTHY, D. J., MARTINEZ, I., BONDER, M. J., GARCIA-BERNARDO, J., AMATYA, S., MADRIGAL, P., ISAACSON, A., BUETTNER, F., KNIGHTS, A., NATARAJAN, K. N., AGU, C. A., ALDERTON, A., DANECEK, P., DENTON, R., DURBIN, R., GAFFNEY, D. J., GONCALVES, A., HALAI, R., HARPER, S., KIRTON, C. M., KOLB-KOKOCINSKI, A., LEHA, A., MCCARTHY, S. A., MEMARI, Y., PATEL, M., BIRNEY, E., CASALE, F. P., CLARKE, L., HARRISON, P. W., KILPINEN, H., STREETER, I., DENOVI, D., MELECKYTE, R., MOENS, N., WATT, F. M., OUWEHAND, W. H., LAMOND, A. I., BENSADDEK, D., BEALES, P., VALLIER, L., MARIONI, J. C., CHHATRIWALA, M., STEGLE, O. & HIPSCI, C. 2020. Single-cell RNA-sequencing of differentiating iPS cells reveals dynamic genetic effects on gene expression. *Nature Communications,* 11**,** 810.
DANESHMANDI, L., SHAH, S., JAFARI, T., BHATTACHARJEE, M., MOMAH, D., SAVEH-SHEMSHAKI, N., LO, K. W. H. & LAURENCIN, C. T. 2020. Emergence of the Stem Cell Secretome in Regenerative Engineering. *Trends in Biotechnology*.
DAWSON, T. M., GOLDE, T. E. & LAGIER-TOURENNE, C. 2018. Animal models of neurodegenerative diseases. *Nat Neurosci,* 21**,** 1370-1379.
DE LA VEGA, L., LEE, C., SHARMA, R., AMEREH, M. & WILLERTH, S. M. 2019. 3D bioprinting models of neural tissues: The current state of the field and future directions. *Brain Research Bulletin,* 150**,** 240-249.
DE RUIJTER, M., RIBEIRO, A., DOKTER, I., CASTILHO, M. & MALDA, J. 2019. Simultaneous Micropatterning of Fibrous Meshes and Bioinks for the Fabrication of Living Tissue Constructs. *Advanced Healthcare Materials,* 8**,** 1800418.
DE STROOPER, B. & KARRAN, E. 2016. The Cellular Phase of Alzheimer’s Disease. *Cell,* 164**,** 603-615.
DEFOREST, C. A. & ANSETH, K. S. 2012. Advances in Bioactive Hydrogels to Probe and Direct Cell Fate. *Annual Review of Chemical and Biomolecular Engineering,* 3**,** 421-444.

DESHMUKH, L. D., D. 2022. Organ-on-Chip Market Size, Share, Competitive Landscape and Trend Analysis Report by Type (Heart on chip, Human on chip, Intestine on chip, Kidney on chip, Liver on chip, Lung on chip): Global Opportunity Analysis and Industry Forecast, 2020-2030.
DHIR, N., MEDHI, B., PRAKASH, A., GOYAL, M. K., MODI, M. & MOHINDRA, S. 2020. Pre-clinical to Clinical Translational Failures and Current Status of Clinical Trials in Stroke Therapy: A Brief Review. *Curr Neuropharmacol,* 18**,** 596-612.
DI, X., GAO, X., PENG, L., AI, J., JIN, X., QI, S., LI, H., WANG, K. & LUO, D. 2023. Cellular mechanotransduction in health and diseases: from molecular mechanism to therapeutic targets. *Signal Transduction and Targeted Therapy,* 8**,** 282.
DIFFEY, B. L. 2002. Sources and measurement of ultraviolet radiation. *Methods,* 28**,** 4-13.
DISTLER, T., SCHALLER, E., STEINMANN, P., BOCCACCINI, A. R. & BUDDAY, S. 2020. Alginate-based hydrogels show the same complex mechanical behavior as brain tissue. *Journal of the Mechanical Behavior of Biomedical Materials,* 111**,** 103979.
DOBRE, O., AZEVEDO GONZALEZ OLIVA, M., CICCONE, G., TRUJILLO, S., RODRIGO-NAVARRO, A., VENTERS, D., LLOPIS HERNÁNDEZ, V., VASSALLI, M., GONZALEZ-GARCIA, C., DALBY, M. & SALMERÓN-SÁNCHEZ, M. 2021. A Hydrogel Platform that Incorporates Laminin Isoforms for Efficient Presentation of Growth Factors – Neural Growth and Osteogenesis. *Advanced Functional Materials***,** 2010225.
DRAGUNOW, M. 2020. Human Brain Neuropharmacology: A Platform for Translational Neuroscience. *Trends in Pharmacological Sciences,* 41**,** 777-792.
DRAGUNOW, M., XU, R., WALTON, M., WOODGATE, A., LAWLOR, P., MACGIBBON, G. A., YOUNG, D., GIBBONS, H., LIPSKI, J., MURAVLEV, A., PEARSON, A. & DURING, M. 2000. c-Jun promotes neurite outgrowth and survival in PC12 cells. *Brain Res Mol Brain Res,* 83**,** 20-33.
ELTOM, A., ZHONG, G. & MUHAMMAD, A. 2019. Scaffold Techniques and Designs in Tissue Engineering Functions and Purposes: A Review. *Advances in Materials Science and Engineering,* 2019**,** 3429527.
ENGLE, S. J., BLAHA, L. & KLEIMAN, R. J. 2018. Best Practices for Translational Disease Modeling Using Human iPSC-Derived Neurons. *Neuron,* 100**,** 783-797.
EVERETT, D. H. 1972. Manual of Symbols and Terminology for Physicochemical Quantities and Units, Appendix II: Definitions, Terminology and Symbols in Colloid and Surface Chemistry. *Pure and Applied Chemistry.*
FAGERLUND, I., DOUGALIS, A., SHAKIRZYANOVA, A., GÓMEZ-BUDIA, M., KONTTINEN, H., OHTONEN, S., FEROZE, F., KOSKUVI, M., KUUSISTO, J., HERNÁNDEZ, D., PEBAY, A., KOISTINAHO, J., LEHTONEN, S., KORHONEN, P. & MALM, T. 2020. Microglia orchestrate neuronal activity in brain organoids. *bioRxiv***,** 2020.12.08.416388.
FAIRBANKS, B. D., SCHWARTZ, M. P., BOWMAN, C. N. & ANSETH, K. S. 2009. Photoinitiated polymerization of PEG-diacrylate with lithium phenyl-2,4,6-trimethylbenzoylphosphinate: polymerization rate and cytocompatibility. *Biomaterials,* 30**,** 6702-6707.
FARRUKH, A., ORTEGA, F., FAN, W., MARICHAL, N., PAEZ, J. I., BERNINGER, B., CAMPO, A. D. & SALIERNO, M. J. 2017. Bifunctional Hydrogels Containing the Laminin Motif IKVAV Promote Neurogenesis. *Stem Cell Reports,* 9**,** 1432-1440.
FATEHULLAH, A., TAN, S. H. & BARKER, N. 2016. Organoids as an in vitro model of human development and disease. *Nature Cell Biology,* 18**,** 246-254.
FEDORCHAK, N. J., IYER, N. & ASHTON, R. S. 2021. Bioengineering tissue morphogenesis and function in human neural organoids. *Seminars in Cell & Developmental Biology,* 111**,** 52-59.
FERNANDES, D. C., REIS, R. L. & OLIVEIRA, J. M. 2021. Advances in 3D neural, vascular and neurovascular models for drug testing and regenerative medicine. *Drug Discovery Today,* 26**,** 754-768.

FERNÁNDEZ FARRÉS, I., MOAKES, R. J. A. & NORTON, I. T. 2014. Designing biopolymer fluid gels: A microstructural approach. *Food Hydrocolloids,* 42**,** 362-372.
FLIGOR, C. M., LANGER, K. B., SRIDHAR, A., REN, Y., SHIELDS, P. K., EDLER, M. C., OHLEMACHER, S. K., SLUCH, V. M., ZACK, D. J., ZHANG, C., SUTER, D. M. & MEYER, J. S. 2018. Three-Dimensional Retinal Organoids Facilitate the Investigation of Retinal Ganglion Cell Development, Organization and Neurite Outgrowth from Human Pluripotent Stem Cells. *Scientific Reports,* 8**,** 14520.
FONSECA, A. C., MELCHELS, F. P. W., FERREIRA, M. J. S., MOXON, S. R., POTJEWYD, G., DARGAVILLE, T. R., KIMBER, S. J. & DOMINGOS, M. 2020. Emulating Human Tissues and Organs: A Bioprinting Perspective Toward Personalized Medicine. *Chemical Reviews,* 120**,** 11093-11139.
FRATTINI, A., FABBRI, M., VALLI, R., DE PAOLI, E., MONTALBANO, G., GRIBALDO, L., PASQUALI, F. & MASERATI, E. 2015. High variability of genomic instability and gene expression profiling in different HeLa clones. *Sci Rep,* 5**,** 15377.
FRESE, C. K., MIKHAYLOVA, M., STUCCHI, R., GAUTIER, V., LIU, Q., MOHAMMED, S., HECK, A. J. R., ALTELAAR, A. F. M. & HOOGENRAAD, C. C. 2017. Quantitative Map of Proteome Dynamics during Neuronal Differentiation. *Cell Rep,* 18**,** 1527-1542.
FROTSCHER, M. 2010. Role for Reelin in stabilizing cortical architecture. *Trends in Neurosciences,* 33**,** 407-414.
GALIAKBEROVA, A. A. & DASHINIMAEV, E. B. 2020. Neural Stem Cells and Methods for Their Generation From Induced Pluripotent Stem Cells in vitro. *Front Cell Dev Biol,* 8**,** 815.
GARRIDO, C. A., GARSKE, D. S., THIELE, M., AMINI, S., REAL, S., DUDA, G. N., SCHMIDT-BLEEK, K. & CIPITRIA, A. 2023. Hydrogels with stiffness-degradation spatial patterns control anisotropic 3D cell response. *Biomaterials Advances,* 151**,** 213423.
GEORGE, J., HSU, C.-C., NGUYEN, L. T. B., YE, H. & CUI, Z. 2019. Neural tissue engineering with structured hydrogels in CNS models and therapies. *Biotechnology Advances*.
GEORGE, J. H., NAGEL, D., WALLER, S., HILL, E., PARRI, H. R., COLEMAN, M. D., CUI, Z. & YE, H. 2018. A closer look at neuron interaction with track-etched microporous membranes. *Scientific Reports,* 8**,** 15552.
GHASEMI, M., TURNBULL, T., SEBASTIAN, S. & KEMPSON, I. 2021. The MTT Assay: Utility, Limitations, Pitfalls, and Interpretation in Bulk and Single-Cell Analysis. *Int J Mol Sci,* 22.
GHEBREMEDHIN, M., SEIFFERT, S. & VILGIS, T. A. 2021. Physics of agarose fluid gels: Rheological properties and microstructure. *Current Research in Food Science,* 4**,** 436-448.
GHOSH, K., SHU, X. Z., MOU, R., LOMBARDI, J., PRESTWICH, G. D., RAFAILOVICH, M. H. & CLARK, R. A. F. 2005. Rheological Characterization of in Situ Cross-Linkable Hyaluronan Hydrogels. *Biomacromolecules,* 6**,** 2857-2865.
GILMOUR, A., POOLE-WARREN, L. & GREEN, R. A. 2019. An Improved in vitro Model of Cortical Tissue. *Frontiers in neuroscience,* 13**,** 1349-1349.
GLADKOV, A., PIGAREVA, Y., KUTYINA, D., KOLPAKOV, V., BUKATIN, A., MUKHINA, I., KAZANTSEV, V. & PIMASHKIN, A. 2017. Design of Cultured Neuron Networks in vitro with Predefined Connectivity Using Asymmetric Microfluidic Channels. *Scientific Reports,* 7**,** 15625.
GONZALEZ, C., ARMIJO, E., BRAVO-ALEGRIA, J., BECERRA-CALIXTO, A., MAYS, C. E. & SOTO, C. 2018. Modeling amyloid beta and tau pathology in human cerebral organoids. *Molecular psychiatry,* 23**,** 2363-2374.
GRAINGER, A. I., KING, M. C., NAGEL, D. A., PARRI, H. R., COLEMAN, M. D. & HILL, E. J. 2018. In vitro Models for Seizure-Liability Testing Using Induced Pluripotent Stem Cells. *Frontiers in Neuroscience,* 12**,** 590.

GRAY, H. 1858. *Anatomy of the Human Body*.
GRIFNO, G. N., FARRELL, A. M., LINVILLE, R. M., AREVALO, D., KIM, J. H., GU, L. & SEARSON, P. C. 2019. Tissue-engineered blood-brain barrier models via directed differentiation of human induced pluripotent stem cells. *Scientific Reports,* 9**,** 13957.
GU, Q., TOMASKOVIC-CROOK, E., LOZANO, R., CHEN, Y., KAPSA, R. M., ZHOU, Q., WALLACE, G. G. & CROOK, J. M. 2016. Functional 3D Neural Mini-Tissues from Printed Gel-Based Bioink and Human Neural Stem Cells. *Advanced Healthcare Materials,* 5**,** 1429-1438.
GU, Q., TOMASKOVIC-CROOK, E., WALLACE, G. G. & CROOK, J. M. 2017. 3D Bioprinting Human Induced Pluripotent Stem Cell Constructs for In Situ Cell Proliferation and Successive Multilineage Differentiation. *Advanced Healthcare Materials,* 6**,** 1700175.
GUIMARÃES, C. F., GASPERINI, L., MARQUES, A. P. & REIS, R. L. 2020. The stiffness of living tissues and its implications for tissue engineering. *Nature Reviews Materials*.
GULREZ, S., AL-ASSAF, S. & PHILLIPS, G. 2011. Hydrogels: Methods of Preparation, Characterisation and Applications. *Progress in Molecular and Environmental Bioengineering - From Analysis and Modeling to Technology Applications.*
HANDORF, A., ZHOU, Y., HALANSKI, M. & LI, W.-J. 2015. Tissue Stiffness Dictates Development, Homeostasis, and Disease Progression. *Organogenesis,* 11**,** 1-15.
HARTMANN, J., LAURIA, I., BENDT, F., RÜTTEN, S., KOCH, K., BLAESER, A. & FRITSCHE, E. 2023. Alginate-Laminin Hydrogel Supports Long-Term Neuronal Activity in 3D Human Induced Pluripotent Stem Cell-Derived Neuronal Networks. *Advanced Materials Interfaces,* 10**,** 2200580.
HAVINS, L., CAPEL, A., CHRISTIE, S., LEWIS, M. & ROACH, P. 2022. Gradient biomimetic platforms for neurogenesis studies. *Journal of Neural Engineering,* 19**,** 011001.
HE, H., XIONG, L., JIAN, L., LI, L., WU, Y. & QIAO, S. 2022. Role of mitochondria on UV-induced skin damage and molecular mechanisms of active chemical compounds targeting mitochondria. *Journal of Photochemistry and Photobiology B: Biology,* 232**,** 112464.
HE, W., REAUME, M., HENNENFENT, M., LEE, B. P. & RAJACHAR, R. 2020. Biomimetic hydrogels with spatial- and temporal-controlled chemical cues for tissue engineering. *Biomater. Sci.,* 8**,** 3248-3269.
HENDEL, T., MANK, M., SCHNELL, B., GRIESBECK, O., BORST, A. & REIFF, D. F. 2008. Fluorescence Changes of Genetic Calcium Indicators and OGB-1 Correlated with Neural Activity and Calcium In Vivo and In Vitro. *The Journal of Neuroscience,* 28**,** 7399-7411.
HILL, L. J., MOAKES, R. J. A., VAREECHON, C., BUTT, G., NG, A., BROCK, K., CHOUHAN, G., VINCENT, R. C., ABBONDANTE, S., WILLIAMS, R. L., BARNES, N. M., PEARLMAN, E., WALLACE, G. R., RAUZ, S., LOGAN, A. & GROVER, L. M. 2018. Sustained release of decorin to the surface of the eye enables scarless corneal regeneration. *npj Regenerative Medicine,* 3**,** 23.
HINTON, T. J., JALLERAT, Q., PALCHESKO, R. N., PARK, J. H., GRODZICKI, M. S., SHUE, H.-J., RAMADAN, M. H., HUDSON, A. R. & FEINBERG, A. W. 2015. Three-dimensional printing of complex biological structures by freeform reversible embedding of suspended hydrogels. *Science Advances,* 1**,** e1500758.
HIRANO, M., HUANG, Y., VELA JARQUIN, D., DE LA GARZA HERNÁNDEZ, R. L., JODAT, Y. A., LUNA CERÓN, E., GARCÍA-RIVERA, L. E. & SHIN, S. R. 2021. 3D bioprinted human iPSC-derived somatosensory constructs with functional and highly purified sensory neuron networks. *Biofabrication,* 13**,** 035046.
HODGE, R. D., BAKKEN, T. E., MILLER, J. A., SMITH, K. A., BARKAN, E. R., GRAYBUCK, L. T., CLOSE, J. L., LONG, B., JOHANSEN, N., PENN, O., YAO, Z., EGGERMONT, J., HÖLLT, T., LEVI, B. P., SHEHATA, S. I., AEVERMANN, B., BELLER, A., BERTAGNOLLI, D., BROUNER, K., CASPER, T., COBBS, C., DALLEY, R., DEE, N., DING, S.-L., ELLENBOGEN, R. G., FONG, O., GARREN, E., GOLDY, J., GWINN, R.

P., HIRSCHSTEIN, D., KEENE, C. D., KESHK, M., KO, A. L., LATHIA, K., MAHFOUZ, A., MALTZER, Z., MCGRAW, M., NGUYEN, T. N., NYHUS, J., OJEMANN, J. G., OLDRE, A., PARRY, S., REYNOLDS, S., RIMORIN, C., SHAPOVALOVA, N. V., SOMASUNDARAM, S., SZAFER, A., THOMSEN, E. R., TIEU, M., QUON, G., SCHEUERMANN, R. H., YUSTE, R., SUNKIN, S. M., LELIEVELDT, B., FENG, D., NG, L., BERNARD, A., HAWRYLYCZ, M., PHILLIPS, J. W., TASIC, B., ZENG, H., JONES, A. R., KOCH, C. & LEIN, E. S. 2019. Conserved cell types with divergent features in human versus mouse cortex. *Nature,* 573**,** 61-68.

HOSPODIUK, M., DEY, M., SOSNOSKI, D. & OZBOLAT, I. T. 2017. The bioink: A comprehensive review on bioprintable materials. *Biotechnol Adv,* 35**,** 217-239.

HROMADKOVA, L., BEZDEKOVA, D., PALA, J., SCHEDIN-WEISS, S., TJERNBERG, L. O., HOSCHL, C. & OVSEPIAN, S. V. 2020. Brain-derived neurotrophic factor (BDNF) promotes molecular polarization and differentiation of immature neuroblastoma cells into definitive neurons. *Biochimica et Biophysica Acta (BBA) - Molecular Cell Research,* 1867**,** 118737.

HSU, C. C., GEORGE, J. H., WALLER, S., BESNARD, C., NAGEL, D. A., HILL, E. J., COLEMAN, M. D., KORSUNSKY, A. M., CUI, Z. & YE, H. 2022. Increased connectivity of hiPSC-derived neural networks in multiphase granular hydrogel scaffolds. *Bioact Mater,* 9**,** 358-372.

HUI CHONG, L. S., ZHANG, J., BHAT, K. S., YONG, D. & SONG, J. 2021. Bioinspired cell-in-shell systems in biomedical engineering and beyond: Comparative overview and prospects. *Biomaterials,* 266**,** 120473.

HUTSLER, J. & GALUSKE, R. A. W. 2003. Hemispheric asymmetries in cerebral cortical networks. *Trends in Neurosciences,* 26**,** 429-435.

HYYSALO, A., RISTOLA, M., MÄKINEN, M. E. L., HÄYRYNEN, S., NYKTER, M. & NARKILAHTI, S. 2017. Laminin α5 substrates promote survival, network formation and functional development of human pluripotent stem cell-derived neurons in vitro. *Stem Cell Research,* 24**,** 118-127.

JANG, K.-J., OTIENO, M. A., RONXHI, J., LIM, H.-K., EWART, L., KODELLA, K. R., PETROPOLIS, D. B., KULKARNI, G., RUBINS, J. E., CONEGLIANO, D., NAWROTH, J., SIMIC, D., LAM, W., SINGER, M., BARALE, E., SINGH, B., SONEE, M., STREETER, A. J., MANTHEY, C., JONES, B., SRIVASTAVA, A., ANDERSSON, L. C., WILLIAMS, D., PARK, H., BARRILE, R., SLIZ, J., HERLAND, A., HANEY, S., KARALIS, K., INGBER, D. E. & HAMILTON, G. A. 2019. Reproducing human and cross-species drug toxicities using a Liver-Chip. *Science Translational Medicine,* 11**,** eaax5516.

JANMEY, P. A. & MCCULLOCH, C. A. 2007. Cell Mechanics: Integrating Cell Responses to Mechanical Stimuli. *Annual Review of Biomedical Engineering,* 9**,** 1-34.

JANMEY, P. A. & SCHLIWA, M. 2008. Rheology. *Current biology : CB,* 18**,** R639-R641.

JAYAKUMAR, A., JOSE, V. & LEE, J. M. 2020. Hydrogels for Medical and Environmental Applications. *Small Methods***,** 1900735.

JENSEN, G., MORRILL, C. & HUANG, Y. 2018. 3D tissue engineering, an emerging technique for pharmaceutical research. *Acta Pharmaceutica Sinica B,* 8**,** 756-766.

JIA, X. & KIICK, K. L. 2009. Hybrid Multicomponent Hydrogels for Tissue Engineering. *Macromolecular Bioscience,* 9**,** 140-156.

JIAO, S. S., SHEN, L. L., ZHU, C., BU, X. L., LIU, Y. H., LIU, C. H., YAO, X. Q., ZHANG, L. L., ZHOU, H. D., WALKER, D. G., TAN, J., GÖTZ, J., ZHOU, X. F. & WANG, Y. J. 2016. Brain-derived neurotrophic factor protects against tau-related neurodegeneration of Alzheimer's disease. *Translational Psychiatry,* 6**,** e907-e907.

JIN, H., LI, M., JEONG, E., CASTRO-MARTINEZ, F. & ZUKER, C. S. 2024. A body–brain circuit that regulates body inflammatory responses. *Nature,* 630**,** 695-703.

KAJTEZ, J., WESSELER, M. F., BIRTELE, M., KHORASGANI, F. R., OTTOSSON, D. R., HEISKANEN, A., KAMPERMAN, T., LEIJTEN, J., MARTÍNEZ-SERRANO, A., LARSEN, N. B., ANGELINI, T. E., PARMAR, M., LIND, J. U. & EMNÉUS, J. 2022.

Embedded 3D printing in self-healing annealable composites for precise patterning of functionally mature human neural constructs. *bioRxiv*, 2021.08.04.455135.
KAMUDZANDU, M., KÖSE-DUNN, M., EVANS, M. G., FRICKER, R. A. & ROACH, P. 2019. A micro-fabricated in vitro complex neuronal circuit platform. *Biomedical Physics & Engineering Express,* 5**,** 045016.
KANDRATAVICIUS, L., BALISTA, P. A., LOPES-AGUIAR, C., RUGGIERO, R. N., UMEOKA, E. H., GARCIA-CAIRASCO, N., BUENO-JUNIOR, L. S. & LEITE, J. P. 2014. Animal models of epilepsy: use and limitations. *Neuropsychiatr Dis Treat,* 10**,** 1693-705.
KANE, K. I. W., MORENO, E. L., HACHI, S., WALTER, M., JARAZO, J., OLIVEIRA, M. A. P., HANKEMEIER, T., VULTO, P., SCHWAMBORN, J. C., THOMA, M. & FLEMING, R. M. T. 2019. Automated microfluidic cell culture of stem cell derived dopaminergic neurons. *Scientific reports,* 9**,** 1796-1796.
KAPLAN, B., MERDLER, U., SZKLANNY, A. A., REDENSKI, I., GUO, S., BAR-MUCHA, Z., MICHAEL, N. & LEVENBERG, S. 2020. Rapid prototyping fabrication of soft and oriented polyester scaffolds for axonal guidance. *Biomaterials,* 251**,** 120062.
KAPR, J., PETERSILIE, L., DISTLER, T., LAURIA, I., BENDT, F., SAUTER, C. M., BOCCACCINI, A. R., ROSE, C. R. & FRITSCHE, E. 2021. Human Induced Pluripotent Stem Cell-Derived Neural Progenitor Cells Produce Distinct Neural 3D In Vitro Models Depending on Alginate/Gellan Gum/Laminin Hydrogel Blend Properties. *Advanced Healthcare Materials,* 10**,** 2100131.
KASTELIK-HRYNIEWIECKA, A., JEWULA, P., BAKALORZ, K., KRAMER-MAREK, G. & KUŹNIK, N. 2021. Targeted PET/MRI Imaging Super Probes: A Critical Review of Opportunities and Challenges. *Int J Nanomedicine,* 16**,** 8465-8483.
KAUL, H. & VENTIKOS, Y. 2015. On the genealogy of tissue engineering and regenerative medicine. *Tissue Eng Part B Rev,* 21**,** 203-17.
KELAVA, I. & LANCASTER, MADELINE A. 2016. Stem Cell Models of Human Brain Development. *Cell Stem Cell,* 18**,** 736-748.
KERR, J. N. D. & DENK, W. 2008. Imaging in vivo: watching the brain in action. *Nature Reviews Neuroscience,* 9**,** 195-205.
KHOSHAKHLAGH, P. & MOORE, M. J. 2015. Photoreactive interpenetrating network of hyaluronic acid and Puramatrix as a selectively tunable scaffold for neurite growth. *Acta Biomaterialia,* 16**,** 23-34.
KIM, C. K., LEE, Y. R., ONG, L., GOLD, M., KALALI, A. & SARKAR, J. 2022. Alzheimer's Disease: Key Insights from Two Decades of Clinical Trial Failures. *J Alzheimers Dis,* 87**,** 83-100.
KIM, D. S., LEE, D. R., KIM, H. S., YOO, J. E., JUNG, S. J., LIM, B. Y., JANG, J., KANG, H. C., YOU, S., HWANG, D. Y., LEEM, J. W., NAM, T. S., CHO, S. R. & KIM, D. W. 2012. Highly pure and expandable PSA-NCAM-positive neural precursors from human ESC and iPSC-derived neural rosettes. *PLoS One,* 7**,** e39715.
KIM, H. J. & INGBER, D. E. 2013. Gut-on-a-Chip microenvironment induces human intestinal cells to undergo villus differentiation. *Integrative Biology,* 5**,** 1130-1140.
KIM, H. N. & CHOI, N. 2019. Consideration of the Mechanical Properties of Hydrogels for Brain Tissue Engineering and Brain-on-a-chip. *BioChip Journal,* 13**,** 8-19.
KIM, J., SULLIVAN, G. J. & PARK, I.-H. 2021. How well do brain organoids capture your brain? *iScience,* 24**,** 102063-102063.
KIM, J. B., GREBER, B., ARAÚZO-BRAVO, M. J., MEYER, J., PARK, K. I., ZAEHRES, H. & SCHÖLER, H. R. 2009. Direct reprogramming of human neural stem cells by OCT4. *Nature,* 461**,** 649-3.
KIM, J. H. 2014. Brain-derived neurotrophic factor exerts neuroprotective actions against amyloid β-induced apoptosis in neuroblastoma cells. *Exp Ther Med,* 8**,** 1891-1895.
KIPP, M., NYAMOYA, S., HOCHSTRASSER, T. & AMOR, S. 2017. Multiple sclerosis animal models: a clinical and histopathological perspective. *Brain Pathol,* 27**,** 123-137.

KNIGHT, G. T., LUNDIN, B. F., IYER, N., ASHTON, L. M., SETHARES, W. A., WILLETT, R. M. & ASHTON, R. S. 2018. Engineering induction of singular neural rosette emergence within hPSC-derived tissues. *Elife,* 7.
KOCH, L., DEIWICK, A., SORIANO, J. & CHICHKOV, B. 2023. Laser bioprinting of human iPSC-derived neural stem cells and neurons: Effect on cell survival, multipotency, differentiation, and neuronal activity. *2023,* 9.
KOIVISTO, J. T., JOKI, T., PARRAGA, J. E., PÄÄKKÖNEN, R., YLÄ-OUTINEN, L., SALONEN, L., JÖNKKÄRI, I., PELTOLA, M., IHALAINEN, T. O., NARKILAHTI, S. & KELLOMÄKI, M. 2017. Bioamine-crosslinked gellan gum hydrogel for neural tissue engineering. *Biomedical Materials,* 12**,** 025014.
KOVALEVICH, J. & LANGFORD, D. 2013. Considerations for the use of SH-SY5Y neuroblastoma cells in neurobiology. *Methods Mol Biol,* 1078**,** 9-21.
KUGLER, E. M., MICHEL, K., KIRCHENBÜCHLER, D., DREISSEN, G., CSISZÁR, A., MERKEL, R., SCHEMANN, M. & MAZZUOLI-WEBER, G. 2018. Sensitivity to Strain and Shear Stress of Isolated Mechanosensitive Enteric Neurons. *Neuroscience,* 372**,** 213-224.
KUMAR, S. V., ER, P. X., LAWLOR, K. T., MOTAZEDIAN, A., SCURR, M., GHOBRIAL, I., COMBES, A. N., ZAPPIA, L., OSHLACK, A., STANLEY, E. G. & LITTLE, M. H. 2019. Kidney micro-organoids in suspension culture as a scalable source of human pluripotent stem cell-derived kidney cells. *Development,* 146**,** dev172361.
KUNDU, A., MICHOLT, L., FRIEDRICH, S., RAND, D. R., BARTIC, C., BRAEKEN, D. & LEVCHENKO, A. 2013. Superimposed topographic and chemical cues synergistically guide neurite outgrowth. *Lab on a Chip,* 13**,** 3070-3081.
LAFERLA, F. M. & GREEN, K. N. 2012. Animal models of Alzheimer disease. *Cold Spring Harbor perspectives in medicine,* 2**,** a006320.
LAM, D., ENRIGHT, H. A., CADENA, J., PETERS, S. K. G., SALES, A. P., OSBURN, J. J., SOSCIA, D. A., KULP, K. S., WHEELER, E. K. & FISCHER, N. O. 2019. Tissue-specific extracellular matrix accelerates the formation of neural networks and communities in a neuron-glia co-culture on a multi-electrode array. *Scientific Reports,* 9**,** 4159.
LAM, J., TRUONG, N. F. & SEGURA, T. 2014. Design of cell-matrix interactions in hyaluronic acid hydrogel scaffolds. *Acta biomaterialia,* 10**,** 1571-1580.
LANCASTER, M. A., CORSINI, N. S., WOLFINGER, S., GUSTAFSON, E. H., PHILLIPS, A. W., BURKARD, T. R., OTANI, T., LIVESEY, F. J. & KNOBLICH, J. A. 2017. Guided self-organization and cortical plate formation in human brain organoids. *Nature biotechnology,* 35**,** 659-666.
LANCASTER, M. A., RENNER, M., MARTIN, C.-A., WENZEL, D., BICKNELL, L. S., HURLES, M. E., HOMFRAY, T., PENNINGER, J. M., JACKSON, A. P. & KNOBLICH, J. A. 2013. Cerebral organoids model human brain development and microcephaly. *Nature,* 501**,** 373-379.
LANJEWAR, S. N. & SLOAN, S. A. 2021. Growing Glia: Cultivating Human Stem Cell Models of Gliogenesis in Health and Disease. *Front Cell Dev Biol,* 9**,** 649538.
LEE, B., KIM, S., KO, J., LEE, S.-R., KIM, Y., PARK, S., KIM, J., HYUNG, S., KIM, H.-Y. & JEON, N. L. 2022. 3D micromesh-based hybrid bioprinting: multidimensional liquid patterning for 3D microtissue engineering. *NPG Asia Materials,* 14**,** 6.
LEE, B. M., PARK, S. J., NOH, I. & KIM, C.-H. 2021. The effects of the molecular weights of hyaluronic acid on the immune responses. *Biomaterials Research,* 25**,** 27.
LEE, E. J., KIM, D. E., AZELOGLU, E. U. & COSTA, K. D. 2008. Engineered Cardiac Organoid Chambers: Toward a Functional Biological Model Ventricle. *Tissue Engineering Part A,* 14**,** 215-225.
LEE, K. M., HAWI, Z. H., PARKINGTON, H. C., PARISH, C. L., KUMAR, P. V., POLO, J. M., BELLGROVE, M. A. & TONG, J. 2020a. The application of human pluripotent stem cells to model the neuronal and glial components of neurodevelopmental disorders. *Molecular Psychiatry,* 25**,** 368-378.

LEE, S., OZLU, B., EOM, T., MARTIN, D. C. & SHIM, B. S. 2020b. Electrically conducting polymers for bio-interfacing electronics: From neural and cardiac interfaces to bone and artificial tissue biomaterials. *Biosens Bioelectron,* 170**,** 112620.
LEE, Y.-B., POLIO, S., LEE, W., DAI, G., MENON, L., CARROLL, R. S. & YOO, S.-S. 2010. Bio-printing of collagen and VEGF-releasing fibrin gel scaffolds for neural stem cell culture. *Experimental Neurology,* 223**,** 645-652.
LEIPZIG, N. D. & SHOICHET, M. S. 2009. The effect of substrate stiffness on adult neural stem cell behavior. *Biomaterials,* 30**,** 6867-78.
LEUNG, C. M., DE HAAN, P., RONALDSON-BOUCHARD, K., KIM, G.-A., KO, J., RHO, H. S., CHEN, Z., HABIBOVIC, P., JEON, N. L., TAKAYAMA, S., SHULER, M. L., VUNJAK-NOVAKOVIC, G., FREY, O., VERPOORTE, E. & TOH, Y.-C. 2022. A guide to the organ-on-a-chip. *Nature Reviews Methods Primers,* 2**,** 33.
LEWIS, F., KARLSBERG SCHAFFER, S., SUSSEX, J., O'NEILL, P. AND COCKCROFT, L. 2014. The Trajectory of Dementia in the UK - Making a Difference. *In:* UK, O. O. H. E. F. A. S. R. (ed.).
LI, H., ZHENG, J., WANG, H., BECKER, M. L. & LEIPZIG, N. D. 2018. Neural stem cell encapsulation and differentiation in strain promoted crosslinked polyethylene glycol-based hydrogels. *Journal of Biomaterials Applications,* 32**,** 1222-1230.
LI, Y., MUFFAT, J., OMER, A., BOSCH, I., LANCASTER, M. A., SUR, M., GEHRKE, L., KNOBLICH, J. A. & JAENISCH, R. 2017. Induction of Expansion and Folding in Human Cerebral Organoids. *Cell Stem Cell,* 20**,** 385-396.e3.
LIAO, C., WUETHRICH, A. & TRAU, M. 2020. A material odyssey for 3D nano/microstructures: two photon polymerization based nanolithography in bioapplications. *Applied Materials Today,* 19**,** 100635.
LIBERTIAUX, V. & PASCON, F. 2009. Viscoelastic Modeling of Brain Tissue: A Fractional Calculus-Based Approach. *In:* GANGHOFFER, J. F. & PASTRONE, F. (eds.) *Mechanics of Microstructured Solids: Cellular Materials, Fibre Reinforced Solids and Soft Tissues.* Berlin, Heidelberg: Springer Berlin Heidelberg.
LIEN, S. M., KO, L. Y. & HUANG, T. J. 2009. Effect of pore size on ECM secretion and cell growth in gelatin scaffold for articular cartilage tissue engineering. *Acta Biomater,* 5**,** 670-9.
LIGORIO, C. & MATA, A. 2023. Synthetic extracellular matrices with function-encoding peptides. *Nature Reviews Bioengineering,* 1**,** 518-536.
LIN, M. Z. & SCHNITZER, M. J. 2016. Genetically encoded indicators of neuronal activity. *Nature Neuroscience,* 19**,** 1142-1153.
LIU, C.-C., LIU, C.-C., KANEKIYO, T., XU, H. & BU, G. 2013. Apolipoprotein E and Alzheimer disease: risk, mechanisms and therapy. *Nature reviews. Neurology,* 9**,** 106-118.
LIU, H., WANG, Y., CUI, K., GUO, Y., ZHANG, X. & QIN, J. 2019. Advances in Hydrogels in Organoids and Organs-on-a-Chip. *Adv Mater,* 31**,** e1902042.
LIU, J. 2018. Three-Dimensional Macroporous Nanoelectronics Scaffold Innervated Synthetic Tissue. *In:* LIU, J. (ed.) *Biomimetics Through Nanoelectronics: Development of Three Dimensional Macroporous Nanoelectronics for Building Smart Materials, Cyborg Tissues and Injectable Biomedical Electronics.* Cham: Springer International Publishing.
LOAI, S., KINGSTON, B. R., WANG, Z., PHILPOTT, D. N., TAO, M. & CHENG, H.-L. M. 2019. Clinical Perspectives on 3D Bioprinting Paradigms for Regenerative Medicine. *Regenerative Medicine Frontiers,* 1**,** e190004.
LOH, Q. L. & CHOONG, C. 2013. Three-dimensional scaffolds for tissue engineering applications: role of porosity and pore size. *Tissue engineering. Part B, Reviews,* 19**,** 485-502.
LONG, J. M. & HOLTZMAN, D. M. 2019. Alzheimer Disease: An Update on Pathobiology and Treatment Strategies. *Cell,* 179**,** 312-339.

LONG, Y., YAN, L., DAI, H., YANG, D., WU, X., DONG, X., LIU, K., WEI, W. & CHEN, Y. 2020. Enhanced proliferation and differentiation of neural stem cells by peptide-containing temperature-sensitive hydrogel scaffold. *Materials Science and Engineering: C,* 116**,** 111258.

LOSI, G., MARCON, I., MARIOTTI, L., SESSOLO, M., CHIAVEGATO, A. & CARMIGNOTO, G. 2016. A brain slice experimental model to study the generation and the propagation of focally-induced epileptiform activity. *J Neurosci Methods,* 260**,** 125-31.

LOZANO, R., STEVENS, L., THOMPSON, B. C., GILMORE, K. J., GORKIN, R., STEWART, E. M., IN HET PANHUIS, M., ROMERO-ORTEGA, M. & WALLACE, G. G. 2015. 3D printing of layered brain-like structures using peptide modified gellan gum substrates. *Biomaterials,* 67**,** 264-273.

LUO, G., YU, Y., YUAN, Y., CHEN, X., LIU, Z. & KONG, T. 2019. Freeform, Reconfigurable Embedded Printing of All-Aqueous 3D Architectures. *Advanced Materials,* 31**,** 1904631.

MA, X., WU, Y., SHE, J., ZHAO, A., YANG, S., YANG, X., XIAO, F. & SUN, Y. 2022. On-chip electrochemical sensing of neurotransmitter in nerve cells by functionalized graphene fiber microelectrode. *Sensors and Actuators B: Chemical,* 365**,** 131874.

MA, X., XU, T., CHEN, W., QIN, H., CHI, B. & YE, Z. 2018. Injectable hydrogels based on the hyaluronic acid and poly (γ-glutamic acid) for controlled protein delivery. *Carbohydrate Polymers,* 179**,** 100-109.

MADHUSUDANAN, P., RAJU, G. & SHANKARAPPA, S. 2020. Hydrogel systems and their role in neural tissue engineering. *Journal of The Royal Society Interface,* 17**,** 20190505.

MAGAZ, A., LI, X., GOUGH, J. E. & BLAKER, J. J. 2021. Graphene oxide and electroactive reduced graphene oxide-based composite fibrous scaffolds for engineering excitable nerve tissue. *Materials Science and Engineering: C,* 119**,** 111632.

MANTHA, S., PILLAI, S., KHAYAMBASHI, P., UPADHYAY, A., ZHANG, Y., TAO, O., PHAM, H. M. & TRAN, S. D. 2019. Smart Hydrogels in Tissue Engineering and Regenerative Medicine. *Materials (Basel, Switzerland),* 12**,** 3323.

MANUEL, M. N., MI, D., MASON, J. O. & PRICE, D. J. 2015. Regulation of cerebral cortical neurogenesis by the Pax6 transcription factor. *Front Cell Neurosci,* 9**,** 70.

MAO, R., TANG, J. & SWANSON, B. G. 2000. Texture properties of high and low acyl mixed gellan gels. *Carbohydrate Polymers,* 41**,** 331-338.

MARSHALL, L. J., BAILEY, J., CASSOTTA, M., HERRMANN, K. & PISTOLLATO, F. 2023. Poor Translatability of Biomedical Research Using Animals — A Narrative Review. *Alternatives to Laboratory Animals,* 51**,** 102-135.

MATERNE, E.-M., RAMME, A. P., TERRASSO, A. P., SERRA, M., ALVES, P. M., BRITO, C., SAKHAROV, D. A., TONEVITSKY, A. G., LAUSTER, R. & MARX, U. 2015. A multi-organ chip co-culture of neurospheres and liver equivalents for long-term substance testing. *Journal of Biotechnology,* 205**,** 36-46.

MATHUR, J., SHENOY, V. B. & PATHAK, A. 2020. Mechanical memory in cells emerges from mechanotransduction with transcriptional feedback and epigenetic plasticity. *bioRxiv***,** 2020.03.20.000802.

MATSUNAGA, S., KISHI, T. & IWATA, N. 2015. Memantine monotherapy for Alzheimer's disease: a systematic review and meta-analysis. *PloS one,* 10**,** e0123289-e0123289.

MAURI, E., SACCHETTI, A. & ROSSI, F. 2016. The Synthesis of RGD-functionalized Hydrogels as a Tool for Therapeutic Applications. *Journal of visualized experiments : JoVE***,** 54445.

MCGLEENON, B. M., DYNAN, K. B. & PASSMORE, A. P. 1999. Acetylcholinesterase inhibitors in Alzheimer's disease. *British journal of clinical pharmacology,* 48**,** 471-480.

MERKER, S. R., WEITZ, J. & STANGE, D. E. 2016. Gastrointestinal organoids: How they gut it out. *Developmental Biology,* 420**,** 239-250.

MERRYWEATHER, D. & ROACH, P. 2017. The need for advanced three-dimensional neural models and developing enabling technologies. *MRS Communications,* 7**,** 309-319.
MERTENS, J., REID, D., LAU, S., KIM, Y. & GAGE, F. H. 2018. Aging in a Dish: iPSC-Derived and Directly Induced Neurons for Studying Brain Aging and Age-Related Neurodegenerative Diseases. *Annual review of genetics,* 52**,** 271-293.
MILLER, D. J., BHADURI, A., SESTAN, N. & KRIEGSTEIN, A. 2019. Shared and derived features of cellular diversity in the human cerebral cortex. *Curr Opin Neurobiol,* 56**,** 117-124.
MIREK, A., BELAID, H., BARTKOWIAK, A., BARRANGER, F., SALMERON, F., KAJDAN, M., GRZECZKOWICZ, M., CAVAILLÈS, V., LEWIŃSKA, D. & BECHELANY, M. 2023. Gelatin methacrylate hydrogel with drug-loaded polymer microspheres as a new bioink for 3D bioprinting. *Biomaterials Advances,* 150**,** 213436.
MIRONI-HARPAZ, I., WANG, D. Y., VENKATRAMAN, S. & SELIKTAR, D. 2012. Photopolymerization of cell-encapsulating hydrogels: Crosslinking efficiency versus cytotoxicity. *Acta Biomaterialia,* 8**,** 1838-1848.
MIRONOV, V., VISCONTI, R. P., KASYANOV, V., FORGACS, G., DRAKE, C. J. & MARKWALD, R. R. 2009. Organ printing: tissue spheroids as building blocks. *Biomaterials,* 30**,** 2164-2174.
MIYATA, S. & KITAGAWA, H. 2017. Formation and remodeling of the brain extracellular matrix in neural plasticity: Roles of chondroitin sulfate and hyaluronan. *Biochimica et Biophysica Acta (BBA) - General Subjects,* 1861**,** 2420-2434.
MOLYNEAUX, B. J., ARLOTTA, P., MENEZES, J. R. L. & MACKLIS, J. D. 2007. Neuronal subtype specification in the cerebral cortex. *Nature Reviews Neuroscience,* 8**,** 427-437.
MONTEIRO, R. & AZEVEDO, I. 2010. Chronic inflammation in obesity and the metabolic syndrome. *Mediators Inflamm,* 2010.
MORIZANE, A., DOI, D., KIKUCHI, T., NISHIMURA, K. & TAKAHASHI, J. 2011. Small-molecule inhibitors of bone morphogenic protein and activin/nodal signals promote highly efficient neural induction from human pluripotent stem cells. *J Neurosci Res,* 89**,** 117-26.
MOXON, S. R., COOKE, M. E., COX, S. C., SNOW, M., JEYS, L., JONES, S. W., SMITH, A. M. & GROVER, L. M. 2017. Suspended Manufacture of Biological Structures. *Advanced Materials,* 29**,** 1605594.
MOXON, S. R., CORBETT, N. J., FISHER, K., POTJEWYD, G., DOMINGOS, M. & HOOPER, N. M. 2019. Blended alginate/collagen hydrogels promote neurogenesis and neuronal maturation. *Materials Science and Engineering: C,* 104**,** 109904.
MUIR, V. G., QAZI, T. H., SHAN, J., GROLL, J. & BURDICK, J. A. 2021. Influence of Microgel Fabrication Technique on Granular Hydrogel Properties. *ACS Biomaterials Science & Engineering*.
MUMFORD, T. R., ROTH, L. & BUGAJ, L. J. 2020. Reverse and Forward Engineering Multicellular Structures with Optogenetics. *Current Opinion in Biomedical Engineering***,** 100250.
MUNDULA, T., RUSSO, E., CURINI, L., GIUDICI, F., PICCIONI, A., FRANCESCHI, F. & AMEDEI, A. 2022. Chronic Systemic Low-Grade Inflammation and Modern Lifestyle: The Dark Role of Gut Microbiota on Related Diseases with a Focus on COVID-19 Pandemic. *Curr Med Chem,* 29**,** 5370-5396.
MURPHY, M. C., HUSTON, J., 3RD & EHMAN, R. L. 2019. MR elastography of the brain and its application in neurological diseases. *Neuroimage,* 187**,** 176-183.
MURPHY, M. C., HUSTON, J., 3RD, JACK, C. R., JR., GLASER, K. J., MANDUCA, A., FELMLEE, J. P. & EHMAN, R. L. 2011. Decreased brain stiffness in Alzheimer's disease determined by magnetic resonance elastography. *Journal of magnetic resonance imaging : JMRI,* 34**,** 494-498.

MUTHUKUMAR, T., SONG, J. E. & KHANG, G. 2019. Biological Role of Gellan Gum in Improving Scaffold Drug Delivery, Cell Adhesion Properties for Tissue Engineering Applications. *Molecules (Basel, Switzerland),* 24**,** 4514.
NASSER, M., GHOSH, G. 2018. Engineering Microenvironments to Regulate Mesenchymal Stem Cell Secretome. *American Institute of Chemical Engineers Annual Meeting.*
NASSOR, F., JARRAY, R., BIARD, D. S. F., MAÏZA, A., PAPY-GARCIA, D., PAVONI, S., DESLYS, J.-P. & YATES, F. 2020. Long Term Gene Expression in Human Induced Pluripotent Stem Cells and Cerebral Organoids to Model a Neurodegenerative Disease. *Frontiers in Cellular Neuroscience,* 14**,** 14.
NAVABPOUR, S., KWAPIS, J. L. & JAROME, T. J. 2020. A neuroscientist's guide to transgenic mice and other genetic tools. *Neurosci Biobehav Rev,* 108**,** 732-748.
NC3RS. 2023. *The 3 R's* [Online]. Available: https://www.nc3rs.org.uk/who-we-are/3rs [Accessed 2023].
NHS. 2020. *NHS England. Dementia* [Online]. Available: www.england.nhs.uk/mental-health/dementia/ [Accessed 03/08/2020].
NICHOL, J. W., KOSHY, S. T., BAE, H., HWANG, C. M., YAMANLAR, S. & KHADEMHOSSEINI, A. 2010. Cell-laden microengineered gelatin methacrylate hydrogels. *Biomaterials,* 31**,** 5536-5544.
NORTON, I. T., JARVIS, D. A. & FOSTER, T. J. 1999. A molecular model for the formation and properties of fluid gels. *International Journal of Biological Macromolecules,* 26**,** 255-261.
OBERHEIM, N. A., TAKANO, T., HAN, X., HE, W., LIN, J. H. C., WANG, F., XU, Q., WYATT, J. D., PILCHER, W., OJEMANN, J. G., RANSOM, B. R., GOLDMAN, S. A. & NEDERGAARD, M. 2009. Uniquely hominid features of adult human astrocytes. *The Journal of neuroscience : the official journal of the Society for Neuroscience,* 29**,** 3276-3287.
OBERHEIM, N. A., WANG, X., GOLDMAN, S. & NEDERGAARD, M. 2006. Astrocytic complexity distinguishes the human brain. *Trends in Neurosciences,* 29**,** 547-553.
OBIEN, M. E., DELIGKARIS, K., BULLMANN, T., BAKKUM, D. J. & FREY, U. 2014. Revealing neuronal function through microelectrode array recordings. *Front Neurosci,* 8**,** 423.
OFFICE, U. H. 2023. Annual Statistics of Scientific Procedures on Living Animals, Great Britain 2022.
OGAWA, J., PAO, G. M., SHOKHIREV, M. N. & VERMA, I. M. 2018. Glioblastoma Model Using Human Cerebral Organoids. *Cell Rep,* 23**,** 1220-1229.
ONDECK, M. G. & ENGLER, A. J. 2016. Mechanical Characterization of a Dynamic and Tunable Methacrylated Hyaluronic Acid Hydrogel. *Journal of biomechanical engineering,* 138**,** 021003-021003.
OSES, C., DE ROSSI, M. C., BRUNO, L., VERNERI, P., DIAZ, M. C., BENÍTEZ, B., GUBERMAN, A. & LEVI, V. 2023. From the membrane to the nucleus: mechanical signals and transcription regulation. *Biophys Rev,* 15**,** 671-683.
OSÓRIO, L. A., SILVA, E. & MACKAY, R. E. 2021. A Review of Biomaterials and Scaffold Fabrication for Organ-on-a-Chip (OOAC) Systems. *Bioengineering (Basel),* 8.
OUYANG, L., ARMSTRONG, J. P. K., SALMERON-SANCHEZ, M. & STEVENS, M. M. 2020. Assembling Living Building Blocks to Engineer Complex Tissues. *Advanced Functional Materials,* n/a**,** 1909009.
OZBOLAT, I. T. & HOSPODIUK, M. 2016. Current advances and future perspectives in extrusion-based bioprinting. *Biomaterials,* 76**,** 321-43.
PALMESE, L. L., THAPA, R. K., SULLIVAN, M. O. & KIICK, K. L. 2019. Hybrid hydrogels for biomedical applications. *Current Opinion in Chemical Engineering,* 24**,** 143-157.
PANKEVICH, D. E., ALTEVOGT, B. M., DUNLOP, J., GAGE, F. H. & HYMAN, S. E. 2014. Improving and accelerating drug development for nervous system disorders. *Neuron,* 84**,** 546-553.

PANZA, F., LOZUPONE, M., LOGROSCINO, G. & IMBIMBO, B. P. 2019. A critical appraisal of amyloid-β-targeting therapies for Alzheimer disease. *Nature Reviews Neurology,* 15**,** 73-88.
PAONE, L. S., BENMASSAOUD, M. M., CURRAN, A., VEGA, S. L. & GALIE, P. A. 2023. A 3D-printed blood-brain barrier model with tunable topology and cell-matrix interactions. *Biofabrication,* 16.
PARK, J., LEE, B. K., JEONG, G. S., HYUN, J. K., LEE, C. J. & LEE, S.-H. 2015. Three-dimensional brain-on-a-chip with an interstitial level of flow and its application as an in vitro model of Alzheimer's disease. *Lab on a Chip,* 15**,** 141-150.
PAŞCA, A. M., SLOAN, S. A., CLARKE, L. E., TIAN, Y., MAKINSON, C. D., HUBER, N., KIM, C. H., PARK, J.-Y., O'ROURKE, N. A., NGUYEN, K. D., SMITH, S. J., HUGUENARD, J. R., GESCHWIND, D. H., BARRES, B. A. & PAŞCA, S. P. 2015. Functional cortical neurons and astrocytes from human pluripotent stem cells in 3D culture. *Nature methods,* 12**,** 671-678.
PAŞCA, S. P. 2019. Assembling human brain organoids. *Science,* 363**,** 126.
PASTOR, D. M., PORITZ, L. S., OLSON, T. L., KLINE, C. L., HARRIS, L. R., KOLTUN, W. A., CHINCHILLI, V. M. & IRBY, R. B. 2010. Primary cell lines: false representation or model system? a comparison of four human colorectal tumors and their coordinately established cell lines. *Int J Clin Exp Med,* 3**,** 69-83.
PEARCE, O. M. T., DELAINE-SMITH, R., MANIATI, E., NICHOLS, S., WANG, J., BÖHM, S., RAJEEVE, V., ULLAH, D., CHAKRAVARTY, P., JONES, R. R., MONTFORT, A., DOWE, T., GRIBBEN, J., JONES, J. L., KOCHER, H. M., SERODY, J. S., VINCENT, B. G., CONNELLY, J., BRENTON, J. D., CHELALA, C., CUTILLAS, P. R., LOCKLEY, M., BESSANT, C., KNIGHT, M. & BALKWILL, F. R. 2017. Deconstruction of a metastatic tumor microenvironment reveals a common matrix response in human cancers. *Cancer Discovery***,** CD-17-0284.
PEK, Y. S., WAN, A. C. A. & YING, J. Y. 2010. The effect of matrix stiffness on mesenchymal stem cell differentiation in a 3D thixotropic gel. *Biomaterials,* 31**,** 385-391.
PEREIRA, I., LOPEZ-MARTINEZ, M. J., VILLASANTE, A., INTRONA, C., TORNERO, D., CANALS, J. M. & SAMITIER, J. 2023. Hyaluronic acid-based bioink improves the differentiation and network formation of neural progenitor cells. *Front Bioeng Biotechnol,* 11**,** 1110547.
PERERA, T. H., HOWELL, S. M. & SMITH CALLAHAN, L. A. 2019. Manipulation of Extracellular Matrix Remodeling and Neurite Extension by Mouse Embryonic Stem Cells Using IKVAV and LRE Peptide Tethering in Hyaluronic Acid Matrices. *Biomacromolecules,* 20**,** 3009-3020.
PETERKA, D. S., TAKAHASHI, H. & YUSTE, R. 2011. Imaging Voltage in Neurons. *Neuron,* 69**,** 9-21.
PETZOLD, J. & GENTLEMAN, E. 2021. Intrinsic Mechanical Cues and Their Impact on Stem Cells and Embryogenesis. *Front Cell Dev Biol,* 9**,** 761871.
PEYRIN, J.-M., DELEGLISE, B., SAIAS, L., VIGNES, M., GOUGIS, P., MAGNIFICO, S., BETUING, S., PIETRI, M., CABOCHE, J., VANHOUTTE, P., VIOVY, J.-L. & BRUGG, B. 2011. Axon diodes for the reconstruction of oriented neuronal networks in microfluidic chambers. *Lab on a Chip,* 11**,** 3663-3673.
PICONE, C. S. F. & CUNHA, R. L. 2011. Influence of pH on formation and properties of gellan gels. *Carbohydrate Polymers,* 84**,** 662-668.
POGODA, K., CHIN, L., GEORGES, P. C., BYFIELD, F. J., BUCKI, R., KIM, R., WEAVER, M., WELLS, R. G., MARCINKIEWICZ, C. & JANMEY, P. A. 2014. Compression stiffening of brain and its effect on mechanosensing by glioma cells. *New journal of physics,* 16**,** 075002-075002.
POLDERVAART, M. T., GOVERSEN, B., DE RUIJTER, M., ABBADESSA, A., MELCHELS, F. P. W., ÖNER, F. C., DHERT, W. J. A., VERMONDEN, T. & ALBLAS, J. 2017. 3D

bioprinting of methacrylated hyaluronic acid (MeHA) hydrogel with intrinsic osteogenicity. *PLOS ONE,* 12**,** e0177628.
POTJEWYD, G., MOXON, S., WANG, T., DOMINGOS, M. & HOOPER, N. M. 2018. Tissue Engineering 3D Neurovascular Units: A Biomaterials and Bioprinting Perspective. *Trends in Biotechnology,* 36**,** 457-472.
POTTER, S. M., EL HADY, A. & FETZ, E. E. 2014. Closed-loop neuroscience and neuroengineering. *Frontiers in neural circuits,* 8**,** 115-115.
PRIMO, G. A. & MATA, A. 2021. 3D Patterning within Hydrogels for the Recreation of Functional Biological Environments. *Advanced Functional Materials***,** 2009574.
PRIOR, N., INACIO, P. & HUCH, M. 2019. Liver organoids: from basic research to therapeutic applications. *Gut,* 68**,** 2228.
QI, Y., ZHANG, X.-J., RENIER, N., WU, Z., ATKIN, T., SUN, Z., OZAIR, M. Z., TCHIEU, J., ZIMMER, B., FATTAHI, F., GANAT, Y., AZEVEDO, R., ZELTNER, N., BRIVANLOU, A. H., KARAYIORGOU, M., GOGOS, J., TOMISHIMA, M., TESSIER-LAVIGNE, M., SHI, S.-H. & STUDER, L. 2017. Combined small-molecule inhibition accelerates the derivation of functional cortical neurons from human pluripotent stem cells. *Nature Biotechnology,* 35**,** 154-163.
QIAN, X., NGUYEN, HA N., SONG, MINGXI M., HADIONO, C., OGDEN, SARAH C., HAMMACK, C., YAO, B., HAMERSKY, GREGORY R., JACOB, F., ZHONG, C., YOON, K.-J., JEANG, W., LIN, L., LI, Y., THAKOR, J., BERG, DANIEL A., ZHANG, C., KANG, E., CHICKERING, M., NAUEN, D., HO, C.-Y., WEN, Z., CHRISTIAN, KIMBERLY M., SHI, P.-Y., MAHER, BRADY J., WU, H., JIN, P., TANG, H., SONG, H. & MING, G.-L. 2016. Brain-Region-Specific Organoids Using Mini-bioreactors for Modeling ZIKV Exposure. *Cell,* 165**,** 1238-1254.
QIAN, X., SU, Y., ADAM, C. D., DEUTSCHMANN, A. U., PATHER, S. R., GOLDBERG, E. M., SU, K., LI, S., LU, L., JACOB, F., NGUYEN, P. T. T., HUH, S., HOKE, A., SWINFORD-JACKSON, S. E., WEN, Z., GU, X., PIERCE, R. C., WU, H., BRIAND, L. A., CHEN, H. I., WOLF, J. A., SONG, H. & MING, G. L. 2020. Sliced Human Cortical Organoids for Modeling Distinct Cortical Layer Formation. *Cell Stem Cell,* 26**,** 766-781.e9.
QIU, B., BESSLER, N., FIGLER, K., BUCHHOLZ, M.-B., RIOS, A. C., MALDA, J., LEVATO, R. & CAIAZZO, M. 2020. Bioprinting Neural Systems to Model Central Nervous System Diseases. *Advanced Functional Materials,* 30**,** 1910250.
QU, K. & ORTOLEVA, P. 2008. Understanding stem cell differentiation through self-organization theory. *Journal of Theoretical Biology,* 250**,** 606-620.
RANJAN, V. D., QIU, L., TAN, E. K., ZENG, L. & ZHANG, Y. 2018. Modelling Alzheimer's disease: Insights from in vivo to in vitro three-dimensional culture platforms. *Journal of Tissue Engineering and Regenerative Medicine,* 12**,** 1944-1958.
RAUTI, R., RENOUS, N. & MAOZ, B. M. 2020. Mimicking the Brain Extracellular Matrix in Vitro: A Review of Current Methodologies and Challenges. *Israel Journal of Chemistry,* 60**,** 1141-1151.
REID, C. N. 1973. Chapter 1 - The Concepts of Stress and Strain. *In:* REID, C. N. (ed.) *Deformation Geometry for Materials Scientists.* Pergamon.
REINHARDT, P., GLATZA, M., HEMMER, K., TSYTSYURA, Y., THIEL, C. S., HÖING, S., MORITZ, S., PARGA, J. A., WAGNER, L., BRUDER, J. M., WU, G., SCHMID, B., RÖPKE, A., KLINGAUF, J., SCHWAMBORN, J. C., GASSER, T., SCHÖLER, H. R. & STERNECKERT, J. 2013. Derivation and Expansion Using Only Small Molecules of Human Neural Progenitors for Neurodegenerative Disease Modeling. *PLOS ONE,* 8**,** e59252.
RICOULT, S. G., KENNEDY, T. E. & JUNCKER, D. 2015. Substrate-Bound Protein Gradients to Study Haptotaxis. *Frontiers in Bioengineering and Biotechnology,* 3.
ROACH, P., PARKER, T., GADEGAARD, N. & ALEXANDER, M. R. 2013. A bio-inspired neural environment to control neurons comprising radial glia, substrate chemistry and topography. *Biomaterials Science,* 1**,** 83-93.

ROBERTSON, J. M. 2014. Astrocytes and the evolution of the human brain. *Medical Hypotheses,* 82**,** 236-239.
ROWLEY, J. A., MADLAMBAYAN, G. & MOONEY, D. J. 1999. Alginate hydrogels as synthetic extracellular matrix materials. *Biomaterials,* 20**,** 45-53.
RUBENSTEIN, J. L. R. 2011. Annual Research Review: Development of the cerebral cortex: implications for neurodevelopmental disorders. *Journal of child psychology and psychiatry, and allied disciplines,* 52**,** 339-355.
RUOSLAHTI, E. 1996. Brain extracellular matrix. *Glycobiology,* 6**,** 489-92.
RUZHA, Y., NI, J., QUAN, Z., LI, H. & QING, H. 2022. Role of Vitronectin and Its Receptors in Neuronal Function and Neurodegenerative Diseases. *Int J Mol Sci,* 23.
SÁEZ, P., DUÑÓ, C., SUN, L. Y., ANTONOVAITE, N., MALVÈ, M., TOST, D. & GORIELY, A. 2020. Topological features dictate the mechanics of the mammalian brains. *International Journal of Mechanical Sciences,* 187**,** 105914.
SAFINSHA, S. & MUBARAK ALI, M. 2020. Composite scaffolds in tissue engineering. *Materials Today: Proceedings,* 24**,** 2318-2329.
SAMANTA, S., YLÄ-OUTINEN, L., RANGASAMI, V. K., NARKILAHTI, S. & OOMMEN, O. P. 2022. Bidirectional cell-matrix interaction dictates neuronal network formation in a brain-mimetic 3D scaffold. *Acta Biomaterialia,* 140**,** 314-323.
SARASWATHIBHATLA, A., INDANA, D. & CHAUDHURI, O. 2023. Cell–extracellular matrix mechanotransduction in 3D. *Nature Reviews Molecular Cell Biology*.
SARTORI, S., CHIONO, V., TONDA-TURO, C., MATTU, C. & GIANLUCA, C. 2014. Biomimetic polyurethanes in nano and regenerative medicine. *Journal of Materials Chemistry B,* 2**,** 5128-5144.
SCHMIDT, R., STRÄHLE, U. & SCHOLPP, S. 2013. Neurogenesis in zebrafish – from embryo to adult. *Neural Development,* 8**,** 3.
SENIOR, J. J., COOKE, M. E., GROVER, L. M. & SMITH, A. M. 2019. Fabrication of Complex Hydrogel Structures Using Suspended Layer Additive Manufacturing (SLAM). *Advanced Functional Materials,* 29**,** 1904845.
SERVAIS, B., MAHMOUDI, N., GAUTAM, V., TONG, W., IBBOTSON, M. R., NISBET, D. R. & COLLINS, D. 2024. Engineering brain-on-a-chip platforms. *Nature Reviews Bioengineering,* 2**,** 691-709.
SHAHIN-SHAMSABADI, A. & SELVAGANAPATHY, P. R. 2020. Tissue-in-a-Tube: three-dimensional in vitro tissue constructs with integrated multimodal environmental stimulation. *Materials Today Bio,* 7**,** 100070.
SHARIFI, S., SHARIFI, H., AKBARI, A. & CHODOSH, J. 2021. Systematic optimization of visible light-induced crosslinking conditions of gelatin methacryloyl (GelMA). *Scientific Reports,* 11**,** 23276.
SHI, Y., KIRWAN, P., SMITH, J., ROBINSON, H. P. & LIVESEY, F. J. 2012. Human cerebral cortex development from pluripotent stem cells to functional excitatory synapses. *Nat Neurosci,* 15**,** 477-86, s1.
SHI, Y., YAMADA, K., LIDDELOW, S. A., SMITH, S. T., ZHAO, L., LUO, W., TSAI, R. M., SPINA, S., GRINBERG, L. T., ROJAS, J. C., GALLARDO, G., WANG, K., ROH, J., ROBINSON, G., FINN, M. B., JIANG, H., SULLIVAN, P. M., BAUFELD, C., WOOD, M. W., SUTPHEN, C., MCCUE, L., XIONG, C., DEL-AGUILA, J. L., MORRIS, J. C., CRUCHAGA, C., FAGAN, A. M., MILLER, B. L., BOXER, A. L., SEELEY, W. W., BUTOVSKY, O., BARRES, B. A., PAUL, S. M. & HOLTZMAN, D. M. 2017. ApoE4 markedly exacerbates tau-mediated neurodegeneration in a mouse model of tauopathy. *Nature,* 549**,** 523-527.
SHIMIZU, A., GOH, W. H., ITAI, S., HASHIMOTO, M., MIURA, S. & ONOE, H. 2020. ECM-based microchannel for culturing in vitro vascular tissues with simultaneous perfusion and stretch. *Lab on a Chip,* 20**,** 1917-1927.
SHU, X. Z., GHOSH, K., LIU, Y., PALUMBO, F. S., LUO, Y., CLARK, R. A. & PRESTWICH, G. D. 2004. Attachment and spreading of fibroblasts on an RGD peptide–modified

injectable hyaluronan hydrogel. *Journal of Biomedical Materials Research Part A,* 68A**,** 365-375.
SIGMA-ALDRICH 2012. HyStem Cell Culture Scaffold Kit

for 7.5 ml of hydrogel scaffold - Technical Bulletin.
SIGMA-ALDRICH. 2021. *CytoSoft® Elastic Modulus Plates: An Innovative Tool to Analyze the Effect of Matrix Stiffness/Rigidity on Regulating Cellular Behavior* [Online]. Available: https://www.sigmaaldrich.com/technical-documents/articles/biology/cell-culture/cytosoft-elastic-modulus-plates.html [Accessed 4/1/2021].
SILVA-CORREIA, J., OLIVEIRA, J. M., CARIDADE, S. G., OLIVEIRA, J. T., SOUSA, R. A., MANO, J. F. & REIS, R. L. 2011. Gellan gum-based hydrogels for intervertebral disc tissue-engineering applications. *Journal of Tissue Engineering and Regenerative Medicine,* 5**,** e97-e107.
SIMSA, R., ROTHENBÜCHER, T., GÜRBÜZ, H., GHOSHEH, N., EMNEUS, J., JENNDAHL, L., KAPLAN, D. L., BERGH, N., SERRANO, A. M. & FOGELSTRAND, P. 2021. Brain organoid formation on decellularized porcine brain ECM hydrogels. *PLoS One,* 16**,** e0245685.
SOKOLOVSKI, S. G., CROWE, J. A., NAGEL, D., HILL, E. J., EL-TAMER, A., KOROLEVA, A. V., PARRI, R., CHICHKOV, B. N. & RAFAILOV, E. U. Printing brain in vitro at 3D scaffolds: materials and patterns. 2018 International Conference Laser Optics (ICLO), 4-8 June 2018 2018. 504-504.
SONG, L., YUAN, X., JONES, Z., GRIFFIN, K., ZHOU, Y., MA, T. & LI, Y. 2019. Assembly of Human Stem Cell-Derived Cortical Spheroids and Vascular Spheroids to Model 3-D Brain-like Tissues. *Scientific Reports,* 9**,** 5977.
SONTHEIMER-PHELPS, A., HASSELL, B. A. & INGBER, D. E. 2019. Modelling cancer in microfluidic human organs-on-chips. *Nature Reviews Cancer,* 19**,** 65-81.
SOOD, D., CAIRNS, D. M., DABBI, J. M., RAMAKRISHNAN, C., DEISSEROTH, K., BLACK, L. D., SANTANIELLO, S. & KAPLAN, D. L. 2019. Functional maturation of human neural stem cells in a 3D bioengineered brain model enriched with fetal brain-derived matrix. *Scientific Reports,* 9**,** 17874.
SPEARMAN, B. S., AGRAWAL, N. K., RUBIANO, A., SIMMONS, C. S., MOBINI, S. & SCHMIDT, C. E. 2020. Tunable methacrylated hyaluronic acid-based hydrogels as scaffolds for soft tissue engineering applications. *J Biomed Mater Res A,* 108**,** 279-291.
SUMMERS, R. A., FAGIANI, F., ROWITCH, D. H., ABSINTA, M. & REICH, D. S. 2024. Novel human iPSC models of neuroinflammation in neurodegenerative disease and regenerative medicine. *Trends in Immunology*.
SUN, W., INCITTI, T., MIGLIARESI, C., QUATTRONE, A., CASAROSA, S. & MOTTA, A. 2017. Viability and neuronal differentiation of neural stem cells encapsulated in silk fibroin hydrogel functionalized with an IKVAV peptide. *Journal of Tissue Engineering and Regenerative Medicine,* 11**,** 1532-1541.
SUN, X. & KAUFMAN, P. D. 2018. Ki-67: more than a proliferation marker. *Chromosoma,* 127**,** 175-186.
TAKAHASHI, K. & YAMANAKA, S. 2006. Induction of pluripotent stem cells from mouse embryonic and adult fibroblast cultures by defined factors. *Cell,* 126**,** 663-76.
TAKASATO, M., ER, P. X., CHIU, H. S., MAIER, B., BAILLIE, G. J., FERGUSON, C., PARTON, R. G., WOLVETANG, E. J., ROOST, M. S., CHUVA DE SOUSA LOPES, S. M. & LITTLE, M. H. 2015. Kidney organoids from human iPS cells contain multiple lineages and model human nephrogenesis. *Nature,* 526**,** 564-568.
TAN, H.-Y. & TOH, Y.-C. 2020. What can microfluidics do for human microbiome research? *Biomicrofluidics,* 14.
TANG, L. 2019. Investigating heterogeneity in HeLa cells. *Nature Methods,* 16**,** 281-281.
TASHIRO, K., SEPHEL, G. C., WEEKS, B., SASAKI, M., MARTIN, G. R., KLEINMAN, H. K. & YAMADA, Y. 1989. A Synthetic Peptide Containing the IKVAV Sequence from the

A Chain of Laminin Mediates Cell Attachment, Migration, and Neurite Outgrowth. *Journal of Biological Chemistry,* 264**,** 16174-16182.
TAYLOR, K. & ALVAREZ, L. R. 2019. An Estimate of the Number of Animals Used for Scientific Purposes Worldwide in 2015. *Alternatives to Laboratory Animals,* 47**,** 196-213.
TIBBITT, M. W. & ANSETH, K. S. 2009. Hydrogels as extracellular matrix mimics for 3D cell culture. *Biotechnology and Bioengineering,* 103**,** 655-663.
TIWARI, S., PATIL, R., DUBEY, S. K. & BAHADUR, P. 2020. Graphene nanosheets as reinforcement and cell-instructive material in soft tissue scaffolds. *Advances in Colloid and Interface Science***,** 102167.
TOMASZEWSKI, C. E., DILILLO, K. M., BAKER, B. M., ARNOLD, K. B. & SHIKANOV, A. 2021. Sequestered cell-secreted extracellular matrix proteins improve murine folliculogenesis and oocyte maturation for fertility preservation. *Acta Biomater*.
TOWNSHEND, R. F., SHAO, Y., WANG, S., CORTEZ, C. L., ESFAHANI, S. N., SPENCE, J. R., O'SHEA, K. S., FU, J., GUMUCIO, D. L. & TANIGUCHI, K. 2020. Effect of Cell Spreading on Rosette Formation by Human Pluripotent Stem Cell-Derived Neural Progenitor Cells. *Frontiers in Cell and Developmental Biology,* 8.
TRUJILLO, C. A., GAO, R., NEGRAES, P. D., GU, J., BUCHANAN, J., PREISSL, S., WANG, A., WU, W., HADDAD, G. G., CHAIM, I. A., DOMISSY, A., VANDENBERGHE, M., DEVOR, A., YEO, G. W., VOYTEK, B. & MUOTRI, A. R. 2019. Complex Oscillatory Waves Emerging from Cortical Organoids Model Early Human Brain Network Development. *Cell stem cell,* 25**,** 558-569.e7.
TSANAKTSIDOU, E., KAMMONA, O. & KIPARISSIDES, C. 2019. On the synthesis and characterization of biofunctional hyaluronic acid based injectable hydrogels for the repair of cartilage lesions. *European Polymer Journal,* 114**,** 47-56.
TYTGAT, L., BAUDIS, S., OTTEVAERE, H., LISKA, R., THIENPONT, H., DUBRUEL, P. & VAN VLIERBERGHE, S. 2017. Photopolymerizable Materials for Cell Encapsulation. *In:* OVSIANIKOV, A., YOO, J. & MIRONOV, V. (eds.) *3D Printing and Biofabrication.* Cham: Springer International Publishing.
UENO, H., SUEMITSU, S., MURAKAMI, S., KITAMURA, N., WANI, K., MATSUMOTO, Y., OKAMOTO, M. & ISHIHARA, T. 2019. Layer-specific expression of extracellular matrix molecules in the mouse somatosensory and piriform cortices. *IBRO Rep,* 6**,** 1-17.
VACANTI, C. A. 2006. The history of tissue engineering. *Journal of Cellular and Molecular Medicine,* 10**,** 569-576.
VAN DEN BERG, A., MUMMERY, C. L., PASSIER, R. & VAN DER MEER, A. D. 2019. Personalised organs-on-chips: functional testing for precision medicine. *Lab on a Chip,* 19**,** 198-205.
VAN DYCK, C. H. 2018. Anti-Amyloid-β Monoclonal Antibodies for Alzheimer's Disease: Pitfalls and Promise. *Biological Psychiatry,* 83**,** 311-319.
VAN NORMAN, G. A. 2019. Limitations of Animal Studies for Predicting Toxicity in Clinical Trials: Is it Time to Rethink Our Current Approach? *JACC: Basic to Translational Science,* 4**,** 845-854.
VAN PRAAG, H. 2018. Lifestyle Factors and Alzheimer's Disease. *Brain plasticity (Amsterdam, Netherlands),* 4**,** 1-2.
VANDERHAEGHEN, P. & POLLEUX, F. 2023. Developmental mechanisms underlying the evolution of human cortical circuits. *Nature Reviews Neuroscience,* 24**,** 213-232.
VELASCO, S., KEDAIGLE, A. J., SIMMONS, S. K., NASH, A., ROCHA, M., QUADRATO, G., PAULSEN, B., NGUYEN, L., ADICONIS, X., REGEV, A., LEVIN, J. Z. & ARLOTTA, P. 2019. Individual brain organoids reproducibly form cell diversity of the human cerebral cortex. *Nature,* 570**,** 523-527.
VIEIRA, S., STRYMECKA, P., STANASZEK, L., SILVA-CORREIA, J., DRELA, K., FIEDOROWICZ, M., MALYSZ-CYMBORSKA, I., ROGUJSKI, P., JANOWSKI, M., REIS, R. L., LUKOMSKA, B., WALCZAK, P. & OLIVEIRA, J. M. 2020. Methacrylated

gellan gum and hyaluronic acid hydrogel blends for image-guided neurointerventions. *Journal of Materials Chemistry B*.
VILA-PARRONDO, C., GARCÍA-ASTRAIN, C. & LIZ-MARZÁN, L. M. 2020. Colloidal systems toward 3D cell culture scaffolds. *Advances in Colloid and Interface Science,* 283**,** 102237.
VIOLA, J., LAL, B., & GRAD, O. 2003. The Emergence of Tissue Engineering as a Research Field. Arlington, VA 22230: The National Science Foundation.
WALUS, K., BEYER, S. & WILLERTH, S. M. 2020. 3D bioprinting healthy and disease models of brain tissue using stem cells. *Current Opinion in Biomedical Engineering*.
WANG, L. L., HIGHLEY, C. B., YEH, Y.-C., GALARRAGA, J. H., UMAN, S. & BURDICK, J. A. 2018. Three-dimensional extrusion bioprinting of single- and double-network hydrogels containing dynamic covalent crosslinks. *Journal of Biomedical Materials Research Part A,* 106**,** 865-875.
WANG, Z., NUMADA, A., WAGAI, F., ODA, Y., OHGUSHI, M., MAKI, K., ADACHI, T. & EIRAKU, M. 2024. Spatial cell fate manipulation of human pluripotent stem cells by controlling the microenvironment using photocurable hydrogel. *Development,* 151.
WATSON, P. M. D., KAVANAGH, E., ALLENBY, G. & VASSEY, M. 2017. Bioengineered 3D Glial Cell Culture Systems and Applications for Neurodegeneration and Neuroinflammation. *SLAS DISCOVERY: Advancing the Science of Drug Discovery,* 22**,** 583-601.
WEI, Z., VOLKOVA, E., BLATCHLEY, M. R. & GERECHT, S. 2019. Hydrogel vehicles for sequential delivery of protein drugs to promote vascular regeneration. *Advanced Drug Delivery Reviews,* 149-150**,** 95-106.
WEN, J. H., VINCENT, L. G., FUHRMANN, A., CHOI, Y. S., HRIBAR, K. C., TAYLOR-WEINER, H., CHEN, S. & ENGLER, A. J. 2014. Interplay of matrix stiffness and protein tethering in stem cell differentiation. *Nature Materials,* 13**,** 979-987.
WESTON, C. A., ANOVA, L., RIALAS, C., PRIVES, J. M. & WEEKS, B. S. 2000. Laminin-1 Activates Cdc42 in the Mechanism of Laminin-1-Mediated Neurite Outgrowth. *Experimental Cell Research,* 260**,** 374-378.
WILLERTH, S. M. 2017. Biomimetic strategies for replicating the neural stem cell niche. *Current Opinion in Chemical Engineering,* 15**,** 8-14.
WU, H. & SUN, Y. E. 2006. Epigenetic Regulation of Stem Cell Differentiation. *Pediatric Research,* 59**,** 21-25.
WU, Q., LIU, J., WANG, X., FENG, L., WU, J., ZHU, X., WEN, W. & GONG, X. 2020. Organ-on-a-chip: recent breakthroughs and future prospects. *Biomed Eng Online,* 19**,** 9.
WU, S., XU, R., DUAN, B. & JIANG, P. 2017. Three-dimensional hyaluronic acid hydrogel-based models for in vitro human iPSC-derived NPC culture and differentiation. *Journal of Materials Chemistry B,* 5**,** 3870-3878.
WYSMOLEK, P. M., KIESSLER, F. D., SALBAUM, K. A., SHELTON, E. R., SONNTAG, S. M. & SERWANE, F. 2022. A minimal-complexity light-sheet microscope maps network activity in 3D neuronal systems. *Scientific Reports,* 12**,** 20420.
XIA, T., LIU, W. & YANG, L. 2017. A review of gradient stiffness hydrogels used in tissue engineering and regenerative medicine. *Journal of Biomedical Materials Research Part A,* 105**,** 1799-1812.
XIN, S., DAI, J., GREGORY, C. A., HAN, A. & ALGE, D. L. 2019. Creating Physicochemical Gradients in Modular Microporous Annealed Particle Hydrogels via a Microfluidic Method. *Advanced Functional Materials,* n/a**,** 1907102.
XIONG, Y., MAHMOOD, A. & CHOPP, M. 2013. Animal models of traumatic brain injury. *Nat Rev Neurosci,* 14**,** 128-42.
XU, C., NEDERGAARD, M., FOWELL, D. J., FRIEDL, P. & JI, N. 2024. Multiphoton fluorescence microscopy for in vivo imaging. *Cell,* 187**,** 4458-4487.
XU, D., HAWK, J. L., LOVELESS, D. M., JEON, S. L. & CRAIG, S. L. 2010. Mechanism of Shear Thickening in Reversibly Cross-linked Supramolecular Polymer Networks. *Macromolecules,* 43**,** 3556-3565.

XU, H., CASILLAS, J., KRISHNAMOORTHY, S. & XU, C. 2020. Effects of Irgacure 2959 and lithium phenyl-2,4,6-trimethylbenzoylphosphinate on cell viability, physical properties, and microstructure in 3D bioprinting of vascular-like constructs. *Biomed Mater,* 15**,** 055021.
XU, H. Q., LIU, J. C., ZHANG, Z. Y. & XU, C. X. 2022. A review on cell damage, viability, and functionality during 3D bioprinting. *Mil Med Res,* 9**,** 70.
XU, Z., LI, Z., JIANG, S. & BRATLIE, K. M. 2018. Chemically Modified Gellan Gum Hydrogels with Tunable Properties for Use as Tissue Engineering Scaffolds. *ACS omega,* 3**,** 6998-7007.
YADAV, N. & PUROW, B. W. 2024. Understanding current experimental models of glioblastoma-brain microenvironment interactions. *Journal of Neuro-Oncology,* 166**,** 213-229.
YAGI, T., ITO, D., OKADA, Y., AKAMATSU, W., NIHEI, Y., YOSHIZAKI, T., YAMANAKA, S., OKANO, H. & SUZUKI, N. 2011. Modeling familial Alzheimer's disease with induced pluripotent stem cells. *Human Molecular Genetics,* 20**,** 4530-4539.
YAN, Y., LI, X., GAO, Y., MATHIVANAN, S., KONG, L., TAO, Y., DONG, Y., LI, X., BHATTACHARYYA, A., ZHAO, X. & ZHANG, S.-C. 2024. 3D bioprinting of human neural tissues with functional connectivity. *Cell Stem Cell,* 31**,** 260-274.e7.
YANG, G., LIN, H., ROTHRAUFF, B. B., YU, S. & TUAN, R. S. 2016. Multilayered polycaprolactone/gelatin fiber-hydrogel composite for tendon tissue engineering. *Acta Biomaterialia,* 35**,** 68-76.
YIGIT, S., SANYAL, R. & SANYAL, A. 2011. Fabrication and Functionalization of Hydrogels through “Click” Chemistry. *Chemistry – An Asian Journal,* 6**,** 2648-2659.
YOKOYAMA, M., KOBAYASHI, H., TATSUMI, L. & TOMITA, T. 2022. Mouse Models of Alzheimer's Disease. *Front Mol Neurosci,* 15**,** 912995.
YOON, S.-J., ELAHI, L. S., PAȘCA, A. M., MARTON, R. M., GORDON, A., REVAH, O., MIURA, Y., WALCZAK, E. M., HOLDGATE, G. M., FAN, H. C., HUGUENARD, J. R., GESCHWIND, D. H. & PAȘCA, S. P. 2019. Reliability of human cortical organoid generation. *Nature methods,* 16**,** 75-78.
YOU, S., LI, J., ZHU, W., YU, C., MEI, D. & CHEN, S. 2018. Nanoscale 3D printing of hydrogels for cellular tissue engineering. *Journal of Materials Chemistry B,* 6**,** 2187-2197.
YU, C., MILLER, K. L., SCHIMELMAN, J., WANG, P., ZHU, W., MA, X., TANG, M., YOU, S., LAKSHMIPATHY, D., HE, F. & CHEN, S. 2020. A sequential 3D bioprinting and orthogonal bioconjugation approach for precision tissue engineering. *Biomaterials,* 258**,** 120294.
ZAREMBINSKI, T. I. & SKARDAL, A. 2018. HyStem®: A Unique Clinical Grade Hydrogel for Present and Future Medical Applications. *Hydrogels - Smart Materials for Biomedical Applications*.
ZHANG, X., HUANG, C. T., CHEN, J., PANKRATZ, M. T., XI, J., LI, J., YANG, Y., LAVAUTE, T. M., LI, X. J., AYALA, M., BONDARENKO, G. I., DU, Z. W., JIN, Y., GOLOS, T. G. & ZHANG, S. C. 2010. Pax6 is a human neuroectoderm cell fate determinant. *Cell Stem Cell,* 7**,** 90-100.
ZHU, J. & MARCHANT, R. E. 2011. Design properties of hydrogel tissue-engineering scaffolds. *Expert review of medical devices,* 8**,** 607-626.
ZHU, M. H., JANG, J., MILOSEVIC, M. M. & ANTIC, S. D. 2021. Population imaging discrepancies between a genetically-encoded calcium indicator (GECI) versus a genetically-encoded voltage indicator (GEVI). *Scientific Reports,* 11**,** 5295.
ZIA, K. M., TABASUM, S., KHAN, M. F., AKRAM, N., AKHTER, N., NOREEN, A. & ZUBER, M. 2018. Recent trends on gellan gum blends with natural and synthetic polymers: A review. *International Journal of Biological Macromolecules,* 109**,** 1068-1087.
ZOTOVA, E., NICOLL, J. A., KALARIA, R., HOLMES, C. & BOCHE, D. 2010. Inflammation in Alzheimer's disease: relevance to pathogenesis and therapy. *Alzheimer's research & therapy,* 2**,** 1-1.

Appendix

1.1. Figure 14A.

Tukey's multiple comparisons test	Mean Diff.	95.00% CI of diff.	Significant?	Summary	Adjusted P Value
19:Mn 575 vs. 19:Mn 3500	-91.5	-104.9 to -78.13	Yes	****	<0.0001
19:Mn 575 vs. 48:Mn 575	-0.05586	-13.43 to 13.31	No	ns	>0.9999
19:Mn 575 vs. 48:Mn 3500	-90.58	-104.0 to -77.21	Yes	****	<0.0001
19:Mn 575 vs. 96:Mn 575	3.08	-10.29 to 16.45	No	ns	0.9974
19:Mn 575 vs. 96:Mn 3500	-83.02	-96.39 to -69.65	Yes	****	<0.0001
19:Mn 575 vs. 191:Mn 575	2.645	-10.73 to 16.02	No	ns	0.9992
19:Mn 575 vs. 191:Mn 3500	-67.44	-80.81 to -54.07	Yes	****	<0.0001
19:Mn 575 vs. 287:Mn 575	3.783	-9.588 to 17.15	No	ns	0.9887
19:Mn 575 vs. 287:Mn 3500	-18.75	-32.12 to -5.374	Yes	**	0.0024
19:Mn 3500 vs. 48:Mn 575	91.44	78.07 to 104.8	Yes	****	<0.0001
19:Mn 3500 vs. 48:Mn 3500	0.917	-12.45 to 14.29	No	ns	>0.9999
19:Mn 3500 vs. 96:Mn 575	94.58	81.21 to 107.9	Yes	****	<0.0001
19:Mn 3500 vs. 96:Mn 3500	8.476	-4.894 to 21.85	No	ns	0.4609
19:Mn 3500 vs. 191:Mn 575	94.14	80.77 to 107.5	Yes	****	<0.0001
19:Mn 3500 vs. 191:Mn 3500	24.06	10.69 to 37.43	Yes	***	0.0001
19:Mn 3500 vs. 287:Mn 575	95.28	81.91 to 108.7	Yes	****	<0.0001
19:Mn 3500 vs. 287:Mn 3500	72.75	59.38 to 86.12	Yes	****	<0.0001
48:Mn 575 vs. 48:Mn 3500	-90.52	-103.9 to -77.15	Yes	****	<0.0001
48:Mn 575 vs. 96:Mn 575	3.136	-10.23 to 16.51	No	ns	0.997
48:Mn 575 vs. 96:Mn 3500	-82.97	-96.34 to -69.59	Yes	****	<0.0001
48:Mn 575 vs. 191:Mn 575	2.701	-10.67 to 16.07	No	ns	0.999
48:Mn 575 vs. 191:Mn 3500	-67.38	-80.75 to -54.01	Yes	****	<0.0001
48:Mn 575 vs. 287:Mn 575	3.839	-9.532 to 17.21	No	ns	0.9875
48:Mn 575 vs. 287:Mn 3500	-18.69	-32.06 to -5.319	Yes	**	0.0024
48:Mn 3500 vs. 96:Mn 575	93.66	80.29 to 107.0	Yes	****	<0.0001
48:Mn 3500 vs. 96:Mn 3500	7.559	-5.811 to 20.93	No	ns	0.6072
48:Mn 3500 vs. 191:Mn 575	93.23	79.85 to 106.6	Yes	****	<0.0001
48:Mn 3500 vs. 191:Mn 3500	23.14	9.770 to 36.51	Yes	***	0.0002
48:Mn 3500 vs. 287:Mn 575	94.36	80.99 to 107.7	Yes	****	<0.0001
48:Mn 3500 vs. 287:Mn 3500	71.84	58.46 to 85.21	Yes	****	<0.0001
96:Mn 575 vs. 96:Mn 3500	-86.1	-99.47 to -72.73	Yes	****	<0.0001
96:Mn 575 vs. 191:Mn 575	-0.4354	-13.81 to 12.94	No	ns	>0.9999
96:Mn 575 vs. 191:Mn 3500	-70.52	-83.89 to -57.15	Yes	****	<0.0001
96:Mn 575 vs. 287:Mn 575	0.7029	-12.67 to 14.07	No	ns	>0.9999
96:Mn 575 vs. 287:Mn 3500	-21.83	-35.20 to -8.455	Yes	***	0.0004
96:Mn 3500 vs. 191:Mn 575	85.67	72.30 to 99.04	Yes	****	<0.0001
96:Mn 3500 vs. 191:Mn 3500	15.58	2.211 to 28.95	Yes	*	0.0147
96:Mn 3500 vs. 287:Mn 575	86.8	73.43 to 100.2	Yes	****	<0.0001
96:Mn 3500 vs. 287:Mn 3500	64.28	50.91 to 77.65	Yes	****	<0.0001
191:Mn 575 vs. 191:Mn 3500	-70.08	-83.45 to -56.71	Yes	****	<0.0001
191:Mn 575 vs. 287:Mn 575	1.138	-12.23 to 14.51	No	ns	>0.9999
191:Mn 575 vs. 287:Mn 3500	-21.39	-34.76 to -8.019	Yes	***	0.0005
191:Mn 3500 vs. 287:Mn 575	71.22	57.85 to 84.59	Yes	****	<0.0001
191:Mn 3500 vs. 287:Mn 3500	48.69	35.32 to 62.06	Yes	****	<0.0001
287:Mn 575 vs. 287:Mn 3500	-22.53	-35.90 to -9.157	Yes	***	0.0003

1.1. Figure 14A.

PEG-3500 - “Statistical differences expand upon this observation, with extremely significant reductions in viability observed from 19/48 μM to both 191/287 μM (P<0.001).” PEG-575 vs PEG-3500 - “Note that the majority of differences in cell viability following exposure to PEG-575 or 3500 were shown to be statistically significant (P<0.0001), with the most extreme comparisons (i.e. least toxic amount (19 μM) of PEG-575 compared to most toxic amount (287 μM) of PEG-3500) presented as slightly less significant (P<0.01).”

1.2. Figure 14D.

Tukey's multiple comparisons test		Mean Diff.	95.00% CI of diff.	Significant?	Summary	Adjusted P Value
B-C	2.5% vs. 5%	8.537	-3.653 to 20.73	No	ns	0.2464
B-D	2.5% vs. 10%	11.06	-1.130 to 23.25	No	ns	0.0838
B-E	2.5% vs. 15%	21.55	9.357 to 33.74	Yes	***	0.0007
B-F	2.5% vs. 20%	22.14	9.947 to 34.33	Yes	***	0.0006
C-D	5% vs. 10%	2.523	-9.667 to 14.71	No	ns	0.979
C-E	5% vs. 15%	13.01	0.8200 to 25.20	Yes	*	0.0342
C-F	5% vs. 20%	13.6	1.410 to 25.79	Yes	*	0.026
D-E	10% vs. 15%	10.49	-1.703 to 22.68	No	ns	0.1083
D-F	10% vs. 20%	11.08	-1.113 to 23.27	No	ns	0.0832
E-F	15% vs. 20%	0.59	-11.60 to 12.78	No	ns	>0.9999

Astrocytes - “…aside from a slight difference between viability of astrocytes exposed to (81.8 ±1.7% viability) 5% and (68.8 ±3.6% / 68.2 ±3.8% viability) 15/20% PEG-3500 dilutions (P<0.05), and a more significant difference observed between viability of astrocytes exposed 2.5% and 15/20% (P<0.001).”

1.3. Figure 14E.

Tukey's multiple comparisons test		Mean Diff.	95.00% CI of diff.	Significant?	Summary	Adjusted P Value
B-C	2.5% vs. 5%	8.65	-6.437 to 23.74	No	ns	0.4329
B-D	2.5% vs. 10%	21.12	6.033 to 36.21	Yes	**	0.0053
B-E	2.5% vs. 15%	59.67	44.59 to 74.76	Yes	****	<0.0001
B-F	2.5% vs. 20%	84.48	69.39 to 99.57	Yes	****	<0.0001
C-D	5% vs. 10%	12.47	-2.617 to 27.56	No	ns	0.1297
C-E	5% vs. 15%	51.02	35.94 to 66.11	Yes	****	<0.0001
C-F	5% vs. 20%	75.83	60.74 to 90.91	Yes	****	<0.0001
D-E	10% vs. 15%	38.55	23.47 to 53.64	Yes	****	<0.0001
D-F	10% vs. 20%	63.36	48.27 to 78.44	Yes	****	<0.0001
E-F	15% vs. 20%	24.8	9.715 to 39.89	Yes	**	0.0014

NPCs - “Significant differences were observed between 2.5% and 10% conditions (One-way ANOVA with Tukey’s post-test, P<0.01) but also 2.5% and 15/20% conditions (P<0.0001). Further differences were found between 5/10% and 15/20% conditions (P<0.0001), but also 15% and 20% conditions (P<0.01). This reduction in viability of the 20% PEG-3500 condition (viability of 11.5 ±3.2%) is found to be significant when compared to every other condition.”

2.1. Figure 15B.

Tukey's multiple comparisons test		Mean Diff.	95.00% CI of diff.	Significant?	Summary	Adjusted P Value
B-C	01.2mM vs. 2.5mM	31.92	4.856 to 58.99	Yes	*	0.02
B-D	01.2mM vs. 5.1mM	38.66	11.59 to 65.72	Yes	**	0.0059
B-E	01.2mM vs. 12.76mM	96.58	69.51 to 123.6	Yes	****	<0.0001
B-F	01.2mM vs. 25.5mM	102.8	75.73 to 129.9	Yes	****	<0.0001
C-D	2.5mM vs. 5.1mM	6.731	-20.34 to 33.80	No	ns	0.919
C-E	2.5mM vs. 12.76mM	64.65	37.58 to 91.72	Yes	***	0.0001
C-F	2.5mM vs. 25mM	70.87	43.81 to 97.94	Yes	****	<0.0001
D-E	5.1mM vs. 12.76mM	57.92	30.85 to 84.99	Yes	***	0.0003
D-F	5.1mM vs. 25mM	64.14	37.07 to 91.21	Yes	***	0.0001
E-F	12.76mM vs. 25mM	6.221	-20.85 to 33.29	No	ns	0.9375

SH-SY5Ys + Irgacure 2959 - “Statistical differences (Appendix 2.1) were observed between 1.2 mM and 2.5 mM conditions (One-way ANOVA with Tukey’s post-test, P<0.05), as well as 1.2 mM and 5.1 mM (P<0.01). Significant differences were observed between all conditions (One-way ANOVA with Tukey’s post-test, P<0.001), bar between 2.5 mM and 5.1 mM, also 12.75 mM and 25.5 mM, that displayed no significant statistical difference.”

2.2. Figure 15C.

Tukey's multiple comparisons test		Mean Diff.	95.00% CI of diff.	Significant?	Summary	Adjusted P Value
B-C	0.8mM vs. 1.7mM	10.83	-61.08 to 82.75	No	ns	0.9949
B-D	0.8mM vs. 3.4mM	21.2	-50.72 to 93.11	No	ns	0.9125
B-E	0.8mM vs. 8.5mM	49.81	-22.10 to 121.7	No	ns	0.2556
B-F	0.8mM vs. 17mM	94.13	22.21 to 166.0	Yes	**	0.0087
C-D	1.7mM vs. 3.4mM	10.36	-61.55 to 82.28	No	ns	0.9959
C-E	1.7mM vs. 8.5mM	38.98	-32.94 to 110.9	No	ns	0.4889
C-F	1.7mM vs. 17mM	83.29	11.38 to 155.2	Yes	*	0.0204
D-E	3.4mM vs. 8.5mM	28.61	-43.30 to 100.5	No	ns	0.761
D-F	3.4mM vs. 17mM	72.93	1.013 to 144.8	Yes	*	0.0462
E-F	8.5mM vs. 17mM	44.31	-27.60 to 116.2	No	ns	0.3621

SH-SY5Ys + LAP - “… except for when comparing against the highest concentration of 17mM; significant reductions in cell viability are observed between 0.8 mM and 17 mM (One-way ANOVA with Tukey’s post-test, P<0.01), as well as 1.7/3.4 mM and 17 mM (P<0.05).”

2.3. Figure 15D.

Tukey's multiple comparisons test		Mean Diff.	95.00% CI of diff.	Significant?	Summary	Adjusted P Value
B-C	0.8mM vs. 1.7mM	-1.453	-42.24 to 39.33	No	ns	>0.9999
B-D	0.8mM vs. 3.4mM	-3.101	-43.88 to 37.68	No	ns	0.9998
B-E	0.8mM vs. 8.5mM	17.09	-23.70 to 57.87	No	ns	0.7228
B-F	0.8mM vs. 17mM	58.04	17.26 to 98.82	Yes	**	0.0046
C-D	1.7mM vs. 3.4mM	-1.648	-42.43 to 39.13	No	ns	>0.9999
C-E	1.7mM vs. 8.5mM	18.54	-22.24 to 59.32	No	ns	0.6554
C-F	1.7mM vs. 17mM	59.5	18.71 to 100.3	Yes	**	0.0038
D-E	3.4mM vs. 8.5mM	20.19	-20.60 to 60.97	No	ns	0.5775
D-F	3.4mM vs. 17mM	61.14	20.36 to 101.9	Yes	**	0.0031
E-F	8.5mM vs. 17mM	40.96	0.1750 to 81.74	Yes	*	0.0488

NPCs + LAP - "… again except for comparison against the 17 mM condition. Comparison of 0.8, 1.7 and 3.4 mM against 17 mM conditions identified significant differences (P<0.01), with a slightly less significant reduction observed between 8.5 mM and 17 mM (P<0.05)."

2.4. Figure 15E.

Tukey's multiple comparisons test		Mean Diff.	95.00% CI of diff.	Significant?	Summary	Adjusted P Value
B-C	0.85mM vs. 0.17mM	4.817	-11.36 to 20.99	No	ns	0.8583
B-D	0.85mM vs. 3.4mM	9.706	-6.471 to 25.88	No	ns	0.3425
B-E	0.85mM vs. 8.5mM	30.59	14.42 to 46.77	Yes	***	0.0007
B-F	0.85mM vs. 17mM	55.85	39.67 to 72.03	Yes	****	<0.0001
C-D	0.17mM vs. 3.4mM	4.888	-11.29 to 21.07	No	ns	0.852
C-E	0.17mM vs. 8.5mM	25.77	9.598 to 41.95	Yes	**	0.0027
C-F	0.17mM vs. 17mM	51.03	34.85 to 67.21	Yes	****	<0.0001
D-E	3.4mM vs. 8.5mM	20.89	4.709 to 37.06	Yes	*	0.0114
D-F	3.4mM vs. 17mM	46.14	29.97 to 62.32	Yes	****	<0.0001
E-F	8.5mM vs. 17mM	25.26	9.080 to 41.43	Yes	**	0.0031

Astrocytes + LAP. "Specifically, reductions in viability when comparing between 0.85 and 8.5mM (P<0.001), alongside 0.17 and 8.5 mM (P<0.01). As previously, the highest concentration of LAP (17mM) presented with the most significant differences when compared to 0.85/0.17/3.4 mM conditions (P<0.0001). The difference between 8.5 and 17 mM is significant, but slightly less so (P<0.01)."

3.1. Figure 17B.

Tukey's multiple comparisons test	Mean Diff.	95.00% CI of diff.	Significant?	Summary	Adjusted P Value
LAP G' vs. LAP G"	4137	3964 to 4310	Yes	****	<0.0001
LAP G' vs. Irgacure G'	4360	4198 to 4521	Yes	****	<0.0001
LAP G' vs. 0.5% Irgacure G"	4359	4198 to 4521	Yes	****	<0.0001
LAP G" vs. 0.5% Irgacure G'	222.5	176.2 to 268.9	Yes	****	<0.0001
LAP G" vs. Irgacure G"	222.4	176.1 to 268.7	Yes	****	<0.0001
Irgacure G' vs. Irgacure G"	-0.1617	-1.039 to 0.7157	No	ns	0.9543

Frequency sweep testing - "…significant differences (Repeated measures One-way ANOVA with Tukey's post-test, P<0.0001) between all conditions (both moduli/both photoinitators), except for between G' and G'' of HAMA hydrogels made with 0.5% Irgacure 2959."

3.2. Figure 17C.

Source of Variation	% of total variation	P value	P value summary	Significant?
Interaction	0.4559	>0.9999	ns	No
Row Factor	0.1465	>0.9999	ns	No
Column Factor	79.31	<0.0001	****	Yes

Frequency sweep 60s UV - "This is supported by (Appendix 3.2) statistical analysis (Two-way ANOVA), whereby no significant variation in stiffness was observed between frequencies within LAP concentrations."

Source of Variation	% of total variation	P value	P value summary	Significant?
Interaction	0.8559	>0.9999	ns	No
Row Factor	0.7805	0.9941	ns	No
Column Factor	76.35	<0.0001	****	Yes

Frequency sweep 30s UV - "Interestingly, no statistically significant (Appendix 3.2, Two-way ANOVA) variability was observed between frequencies within LAP concentrations after 30s UV exposure."

Source of Variation	% of total variation	P value	P value summary	Significant?
Interaction	2.134	>0.9999	ns	No
Frequency	80.97	<0.0001	****	Yes
LAP conc.	0.3079	0.4224	ns	No

Frequency sweep 0s UV - "Further analysis (Appendix 3.2) revealed significant variation (P<0.0001) observed between frequencies within LAP concentrations, supported by Tukey's post-test findings where statistically significant (P<0.0001-0.05)* differences were observed when comparing against uppermost frequencies i.e. 5 Hz onwards."

*large dataset available upon request.

4.1. Figure 19D.

Tukey's multiple comparisons test	Mean Diff.	95.00% CI of diff.	Significant?	Summary	Adjusted P Value
0.5i vs. 1i	-1343	-1921 to -765.9	Yes	****	<0.0001
0.5i vs. 1.5i	-2677	-3254 to -2099	Yes	****	<0.0001
0.5i vs. 2i	-4134	-4712 to -3557	Yes	****	<0.0001
1i vs. 1.5i	-1333	-1911 to -755.9	Yes	****	<0.0001
1i vs. 2i	-2791	-3369 to -2214	Yes	****	<0.0001
1.5i vs. 2i	-1458	-2035 to -880.3	Yes	****	<0.0001

UV bulb radiometry - comparison between intensities "…with (Appendix 4.1) significant differences observed between all conditions (P<0.0001)."

4.2. Figure 19E.

Tukey's multiple comparisons test	Mean Diff.	95.00% CI of diff.	Significant?	Summary	Adjusted P Value
30s 1.5i (G') vs. 30s 1.5i (G")	-0.04026	-0.05413 to -0.02639	Yes	****	<0.0001
30s 1.5i (G') vs. 60s 1.5i (G')	-0.01856	-0.03243 to -0.004689	Yes	**	0.002
30s 1.5i (G') vs. 60s 1.5i (G")	-0.06237	-0.07624 to -0.04851	Yes	****	<0.0001
30s 1.5i (G') vs. 30s 2i (G')	-0.01264	-0.02651 to 0.001226	No	ns	0.097
30s 1.5i (G') vs. 30s 2i (G")	-0.07477	-0.08864 to -0.06090	Yes	****	<0.0001
30s 1.5i (G") vs. 60s 1.5i (G')	0.02217	0.007836 to 0.03557	Yes	****	<0.0001
30s 1.5i (G") vs. 60s 1.5i (G")	-0.02211	-0.03598 to -0.008244	Yes	****	<0.0001
30s 1.5i (G") vs. 30s 2i (G')	0.02762	0.01375 to 0.04149	Yes	****	<0.0001
30s 1.5i (G") vs. 30s 2i (G")	-0.03451	-0.04838 to -0.02064	Yes	****	<0.0001
60s 1.5i (G') vs. 60s 1.5i (G")	-0.04382	-0.05768 to -0.02995	Yes	****	<0.0001
60s 1.5i (G') vs. 30s 2i (G')	0.005915	-0.007954 to 0.01978	No	ns	0.8263
60s 1.5i (G') vs. 30s 2i (G")	-0.05621	-0.07008 to -0.04235	Yes	****	<0.0001
60s 1.5i (G") vs. 30s 2i (G')	0.04973	0.03586 to 0.06360	Yes	****	<0.0001
60s 1.5i (G") vs. 30s 2i (G")	-0.0124	-0.02627 to 0.001471	No	ns	0.1098
30s 2i (G') vs. 30s 2i (G")	-0.06213	-0.07600 to -0.04826	Yes	****	<0.0001

Amplitude testing - comparison between UV dose "…differences were observed (Appendix 4.2) between almost all conditions (Two-way ANOVA with Tukey's post-test, P<0.0001), with a slightly less significant difference between G' of 30s 1.5i vs. G' of 60s 1.5i (P<0.01)."

4.3. Figure 19F.

Tukey's multiple comparisons test	Mean Diff.	95.00% CI of diff.	Significant?	Summary	Adjusted P Value
30s 1.5i (G') vs. 60s 1.5i (G')	-3.965	-6.440 to -1.490	Yes	****	<0.0001
30s 1.5i (G') vs. 30s 2i (G')	-1.127	-3.602 to 1.348	No	ns	0.7805
30s 1.5i (G") vs. 60s 1.5i (G")	-2.98	-5.455 to -0.5053	Yes	**	0.0083
30s 1.5i (G") vs. 30s 2i (G")	-0.4393	-2.914 to 2.036	No	ns	0.9958
60s 1.5i (G') vs. 30s 2i (G')	2.837	0.3625 to 5.312	Yes	*	0.0143
60s 1.5i (G") vs. 30s 2i (G")	2.541	0.06597 to 5.016	Yes	*	0.0404

Frequency testing - "Slight significant differences (Appendix 4.3) were seen in G' of 60s 1.5i (4.99±7.24 Pa) and 30s 2i (2.15±1.23 Pa) conditions (P<0.05). The greatest significant difference was observed between G' of 30s 1.5i (1±1.64 Pa) and 60s 1.5i (4.99±7.24 Pa) hydrogels (P<0.0001), while G'' of the same hydrogels (0.68±0.83 Pa and 3.67±4.8 Pa, for 1.5i 30s and 60s respectively) presented with a slightly less significant difference (P<0.01)."

5.1. Figure 20F.

Tukey's multiple comparisons test		Mean Diff.	95.00% CI of diff.	Significant?	Summary	Adjusted P Value
17mM LAP	60s vs. 30s	-0.09341	-32.33 to 32.14	No	ns	>0.9999
	60s vs. 0s	-5.717	-37.95 to 26.51	No	ns	0.9019
	30s vs. 0s	-5.624	-37.86 to 26.61	No	ns	0.9049
8.5mM LAP	60 vs. 30	-5.74	-37.97 to 26.49	No	ns	0.9011
	60 vs. 0	-45.09	-77.32 to -12.86	Yes	**	0.0044
	30 vs. 0	-39.35	-71.58 to -7.119	Yes	*	0.0137
3.4mM LAP	60 vs. 30	-9.346	-41.58 to 22.89	No	ns	0.7599
	60 vs. 0	-30.9	-63.13 to 1.330	No	ns	0.0625
	30 vs. 0	-21.56	-53.79 to 10.68	No	ns	0.2444
1.7mM LAP	60 vs. 30	-13.23	-45.46 to 19.00	No	ns	0.5797
	60 vs. 0	-43.97	-76.20 to -11.74	Yes	**	0.0055
	30 vs. 0	-30.74	-62.98 to 1.487	No	ns	0.0641
0.85mM LAP	60 vs. 30	-23.65	-55.88 to 8.584	No	ns	0.1862
	60 vs. 0	-43.28	-75.52 to -11.05	Yes	**	0.0063
	30 vs. 0	-19.64	-51.87 to 12.60	No	ns	0.308
No LAP	60 vs. 30	9.695	-22.54 to 41.93	No	ns	0.7444
	60 vs. 0	4.848	-27.38 to 37.08	No	ns	0.9284
	30 vs. 0	-4.848	-37.08 to 27.38	No	ns	0.9284

SH-SY5Ys + LAP + UV - "…supported by statistical analysis (Appendix 5.1) Two-way ANOVA with Tukey's post-test), showing no significant differences* within 60 and 30 seconds exposure time for each LAP concentration."

*large dataset available upon request.

5.2. Figure 20G.

Dunnett's multiple comparisons test		Mean Diff.	95.00% CI of diff.	Significant?	Summary	Adjusted P Value
0.5i	0mM vs 0.17mM	14.81	-16.78 to 46.40	No	ns	0.5959
	0mM vs 0.85mM	25.49	-6.097 to 57.08	No	ns	0.1435
	0mM vs 1.7mM	58.63	27.04 to 90.22	Yes	***	0.0002
	0mM vs 3.4mM	60.77	29.18 to 92.36	Yes	***	0.0001
	0mM vs 8.5mM	84.5	52.91 to 116.1	Yes	****	<0.0001
1i	0mM vs 0.17mM	27.37	-4.225 to 58.96	No	ns	0.1054
	0mM vs 0.85mM	49.57	17.98 to 81.16	Yes	**	0.0013
	0mM vs 1.7mM	50.61	19.02 to 82.20	Yes	**	0.0011
	0mM vs 3.4mM	63.66	32.07 to 95.25	Yes	****	<0.0001
	0mM vs 8.5mM	67.85	36.26 to 99.44	Yes	****	<0.0001

NPCs + LAP + UV - "Statistically significant (Appendix 5.2) reductions were observed at 1.7mM (Two-way ANOVA with Dunnet's post-test, P<0.001), 3.4 mM (P<0.001) and 8.5 mM (P<0.0001) compared to control within the 0.5i group. Similar reductions are seen in the 1i group, whereby 0.85 mM and 1.7 mM (P<0.01), alongside 3.4 mM and 8.5 mM (P<0.0001) concentrations displayed significantly reduced viability compared to control."

5.3. Figure 20H.

Dunnett's multiple comparisons test		Mean Diff.	95.00% CI of diff.	Significant?	Summary	Adjusted P Value
0.5i	0mM vs 0.17mM	5.723	-4.492 to 15.94	No	ns	0.4343
	0mM vs 0.85mM	8.261	-1.954 to 18.48	No	ns	0.1423
	0mM vs 1.7mM	12.78	2.566 to 23.00	Yes	*	0.0108
	0mM vs 3.4mM	25.24	15.02 to 35.45	Yes	****	<0.0001
	0mM vs 8.5mM	47.66	37.45 to 57.88	Yes	****	<0.0001
1i	0mM vs 0.17mM	9.392	-0.8230 to 19.61	No	ns	0.0789
	0mM vs 0.85mM	14.09	3.876 to 24.31	Yes	**	0.0047
	0mM vs 1.7mM	17.97	7.751 to 28.18	Yes	***	0.0004
	0mM vs 3.4mM	46.65	36.44 to 56.87	Yes	****	<0.0001
	0mM vs 8.5mM	76.05	65.83 to 86.26	Yes	****	<0.0001

Astrocytes + LAP + UV - “Statistically significant (Appendix 5.3) reductions were observed for the last three highest LAP concentrations (1.7, 3.4 and 8.5 mM) when compared to control (Two-way ANOVA with Dunnet’s post-test, P<0.05, P<0.0001, P<0.0001 respectively). Within the 1i group, no significant reductions were observed at 0.17 mM with viability of 90.6±3%. On the other hand, significant reductions were observed with reductions to 85.9 ±2.9% at 0.85 mM (P<0.01), 82±4.1% at 1.7 mM (P<0.001), finally 53.3±0.7% and 24±3.7% at 3.4 and 8.5 mM (P<0.0001), respectively. No statistically significant differences (See appendix*) were seen between 0.5 and 1i conditions within each concentration, aside from at 3.4 mM (Two-way ANOVA with Tukey’s post-test, P<0.001) and 8.5 mM (P<0.0001).”

*large dataset available upon request.

6. Figure 21C.

Frequency testing optimal HAMA conditions A-E - “This increase is extremely significant (Appendix 6*, Two-way ANOVA with Tukey’s post-test, P<0.0001) compared to all other conditions. Whats more no significant differences* were observed within elastic moduli of F as frequency increases, bar between stiffness at 0.1 Hz and the highest five frequencies 4, 5, 6, 7.9 and 10 Hz (P<0.05, P<0.05, P<0.05, P<0.01 and P<0.01 respectively.”

“Statistical analysis revealed no significant differences* in elastic moduli between frequencies (within and across conditions) or between conditions (within and across frequencies), aside from when comparing against condition D at frequencies of above 6 Hz (P<0.05- to 0.0001).”

*large dataset available upon request.

7.1 Figure 22D.

Frequency testing, comparison of all means - “Statistical analysis (Appendix 7.1*) revealed no significant differences within G’ and G’’ values across frequencies, except for when looking at elastic behaviour (G’) at high frequencies; at 10 Hz elastic moduli of 13.5±7.3 Pa was found to be significantly greater than elastic moduli of all lower frequencies (Two-way ANOVA with Sidak’s post-test, P<0.0001). Further analysis showed significant differences* were observed when comparing between G’ at frequencies up to <5.5 Pa at 4 Hz and 9.5±4.4 Pa at 8 Hz (P<0.05-0.001). This was also observed when comparing between G’ at frequencies between G’ of 1.6-3.1 Pa at 0.13-0.8 Hz and 7.1±2.7 Pa at 6 Hz (all P<0.05).”

*large dataset available on request.

7.2 Figure 22D.

Dunnett's multiple comparisons test		Mean Diff.	95.00% CI of diff.	Significant?	Summary	Adjusted P Value
G' - G"	0.1Hz	2.832	-0.8278 to 6.493	No	ns	0.3135
	0.1259Hz	1.988	-1.672 to 5.649	No	ns	0.872
	0.1585Hz	2.317	-1.344 to 5.977	No	ns	0.6684
	0.1995Hz	2.277	-1.384 to 5.937	No	ns	0.697
	0.2512Hz	2.322	-1.338 to 5.982	No	ns	0.6644
	0.3162Hz	2.314	-1.346 to 5.974	No	ns	0.6702
	0.3981Hz	2.327	-1.333 to 5.988	No	ns	0.6607
	0.5012Hz	2.343	-1.318 to 6.003	No	ns	0.6496
	0.631Hz	2.365	-1.295 to 6.026	No	ns	0.6329
	0.7943Hz	2.41	-1.251 to 6.070	No	ns	0.6005
	1Hz	2.465	-1.195 to 6.126	No	ns	0.5594
	1.259Hz	2.555	-1.105 to 6.215	No	ns	0.494
	1.585Hz	2.643	-1.017 to 6.303	No	ns	0.4327
	1.995Hz	2.768	-0.8919 to 6.428	No	ns	0.3514
	2.512Hz	2.996	-0.6645 to 6.656	No	ns	0.2293
	3.162Hz	3.315	-0.3450 to 6.975	No	ns	0.1152
	3.981Hz	3.771	0.1106 to 7.431	Yes	*	0.0376
	5.012Hz	4.534	0.8737 to 8.194	Yes	**	0.0045
	6.31Hz	5.689	2.029 to 9.350	Yes	***	0.0001
	7.943Hz	7.649	3.989 to 11.31	Yes	****	<0.0001
	10Hz	10.49	6.830 to 14.15	Yes	****	<0.0001

Frequency testing comparison between G and G” - “Additional testing (Appendix 7.2) revealed no statistically significant differences between G’ and G’ at low frequencies, however beyond 3.6 Hz this changed. Differences in G’ and G’’ were observed at 4 Hz (G’ 4.6±0.9 Pa and G’’ 0.83±0.08 Pa, P<0.05), 5 Hz (G’ 5.6±1.6 Pa and G’’ 1±0.1 Pa, P<0.01), 6.3 Hz (G’ 7.1±2.7 Pa and G’’ 1.4±0.12 Pa, P<0.001), 8 Hz (G’ 9.5±4.4 Pa and G’’ 1.8±0.14 Pa) and 10 Hz (G’ 13.5±7.3 Pa and G’’ 3±0.11 Pa) (both P<0.0001).”

8. NMR Spectroscopy.

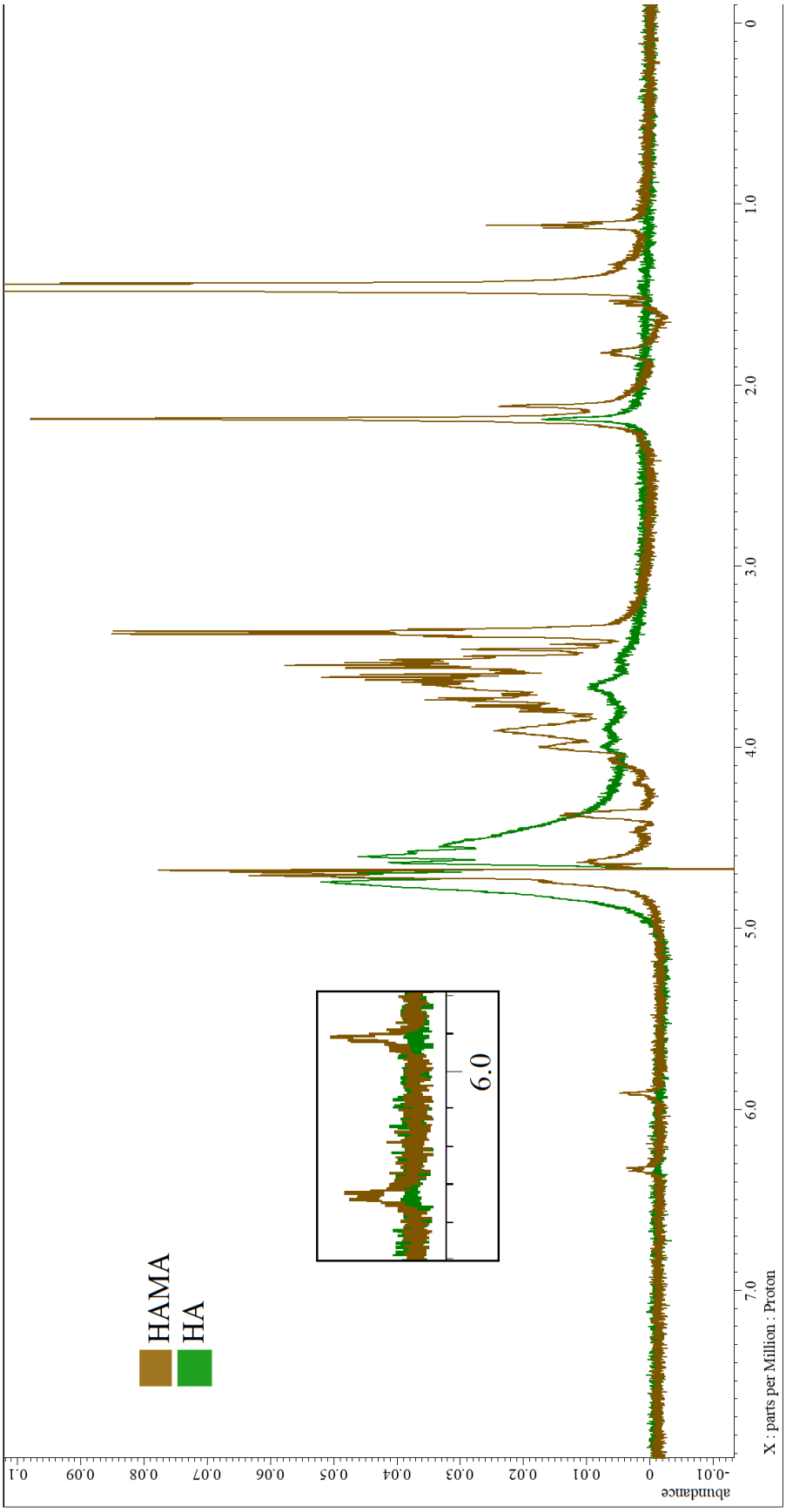

[1]H Proton NMR spectra (JEOL ECZ-R 500 MHz NMR) - “Methacrylation was confirmed within samples of HAMA by the addition of two methyl proton peaks at 5.9 and 6.3 ppm”.

Appendix 9. Rheological data processing and analysis.

Example of rSpace dataset obtained via frequency sweep rheological testing (Methods 3.3.1).

G' and G'' highlighted as data of interest.

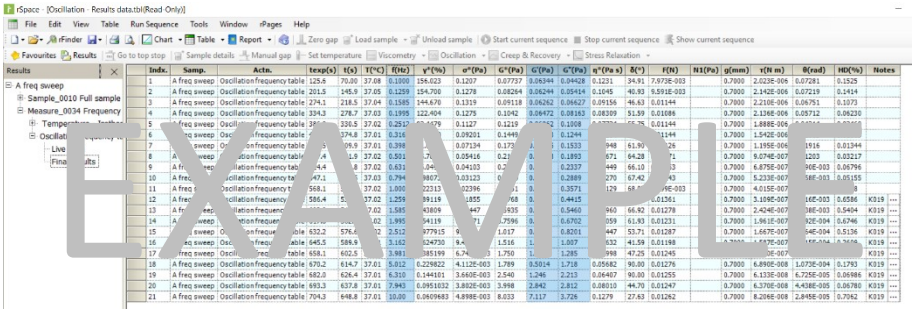

Frequency sweep testing is repeated in triplicate for each sample to provide a batch average across frequencies 0-10 Hz.

	Index	Sample	Action	t(exp)	t(s)	T(C)	F(Hz)	γ*(%)	δ*(Pa)	G*(Pa)	G'(Pa)	G''(Pa)	η*(Pa s)	δ(°)	F(N)	N1(Pa)	g(mm)	T(N m)	eabs(rad)	HD(%)
n1	1	A freq swe	Oscillation	125.6	70	37.08	0.1	156.023	0.1207	0.07737	0.06344	0.04428	0.1231	34.91	7.97E-03		0.7	2.02E-06	7.28E-02	0.1525
	21	A freq swe	Oscillation	704.3	648.8	37.01	10	0.060968	4.90E-03	8.033	7.117	3.726	0.1279	27.63	0.01262		0.7	8.21E-08	2.85E-05	0.7062
n2	1	A freq swe	Oscillation	78.7	70	37.29	0.1	79.183	0.11	0.1389	0.08065	0.1131	0.2211	54.5	-0.0467		1	1.84E-06	5.28E-02	1.21
	21	A freq swe	Oscillation	657.5	648.8	37	10	0.04309	6.35E-03	14.73	12.48	7.834	0.2345	32.12	-0.05047		1	1.06E-07	2.87E-05	0.4391
n3	1	A freq swe	Oscillation	81.62	70	37.18	0.1	2.46E+01	0.1005	4.08E-01	4.55E-02	4.05E-01	6.49E-01	83.59	-6.28E-04		1	1.68E-06	1.64E-02	0.03066
	21	A freq swe	Oscillation	660.4	648.8	37	10	4.40E-02	0.01195	2.71E+01	1.82E+01	20.13	0.432	47.88	-1.67E-03		1	2.00E-07	2.94E-05	0.5169

EXAMPLE

n1	n3	G' av	n1	n	n3	G
0.06	0.08065	4.55E-02	0.04428	0.	5E-01	.8
0.06	0.125	5.74E-02	0.05414	0.	5104	.22
0.06	0.1205	7.44E-02	0.06627	0	166	0.28
0.06		3.87E-02	8163	0.	63	0.35
0.06	0.1149	1.33E-01	1008	0		0.
0.07	0.1168	1.80E-01	244		1.	0.55
0.08	0.1249	2.47E-01	33	0.	1.5	0.68
0.09	0.1356	3.42E-01	0.	0.	1.96	0.84
0.1		73E-0	0.242	0.	0.	2.421	1.
0.1201	0.1708	6.53E-01	0.314567	0.2889	0.5957	2.971	1.2852
0.1441	0.199	8.98E-01	0.413767	0.3571	0.7433	3.626	1.575467
0.1799	0.2486	1.22E+00	0.5495	0.4415	0.9259	4.413	1.9268
0.2326	0.3056	1.66E+00	0.732733	0.546	1.159	5.319	2.341333
0.3575	0.3286	2.19E+00	0.9587	0.6702	1.461	6.42	2.8504
0.6022	0.3181	2.90E+00	1.274433	0.8201	1.84	7.662	3.4407
1.134	0.8413	4.07E+00	2.014433	1.007	2.264	8.981	4.084
1.188	1.371	5.87E+00	2.81	1.285	2.834	10.44	4.853
0.5014	1.425	8.31E+00	3.4108	1.718	3.633	12.17	5.840333
1.246	0.829	1.17E+01	4.591667	2.213	4.703	14.21	7.042
2.842	0.8948	1.64E+01	6.7156	2.812	6.201	16.63	8.547667
7.117	12.48	1.82E+01	12.599	3.726	7.834	20.13	10.56333

EXAMPLE

Batch averages are averaged again to provide an average for each condition across frequencies 0-10 Hz.

G'	N1	N2	N3	G' avg	G''	N1	N2	N3	G''
	0.02877	0.05692	0.03819	0.041293		0.09873	0.3678	0.1171	0.194543
	0.02938	0.06555	0.05501	0.04998		0.1248	0.4778	0.135	0.245867
	0.02998	0.08055	0.05729	0.05594		0.1587	0.6172	0.1666	0.314167
	0.03168	0.1027	0.0616	0.065327		0.2012	0.7859	0.2068	0.397967
	0.03579	0.1362	0.0666	0.07953		0.2543	0.9919	0.257	0.501067
	4.19E-02	0.1833	0.07283	0.099353		0.3207	1.245	0.3202	0.628633
	0.05097	0.2512	0.08099	0.12772		0.4036	1.551	0.3993	0.784633
		0.246	0.1 28	0.167513		0.5	924	.4987	0.976567
	40E-02	0.47	.108	0.223397		0.6 7	2 75	.6232	1.2113
	12E-01	0.657	0.1297	299833		0.7 8	1 16	.7794	1.497067
	54E-01	0.90	0.1621	107133		0.9	.552	.9748	1.840367
	20E-01	1.23E+	.215	54733		1. 8	4.32	1.217	2.258333
	92E-01	1.67 00	296	0. 3167		1. 7	5.2	1.519	2.755333
	4.22E-01	2.32E+00	0.3889	1.042733		1.92	6.18	1.903	3.334333
	3.76E-01	3.01E+00	0.5668	1.3165		2.419	7.432	2.375	4.075333
	7.64E-01	3.92E+00	0.8679	1.849933		2.965	8.839	2.967	4.923667
	1.92E+00	4.50E+00	2.054	2.825667		3.593	10.62	3.637	5.95
	2.70E+00	4.18E+00	3.563	3.481333		4.489	12.79	4.54	7.273
	9.23E-02	1.13E+01	5.796	5.71275		5.896	13.9	5.719	8.505
	7.12E+00	1.54E+01	10.38	10.969		7.088	16.35	7.247	10.22833
	2.656	23.99	15.03	13.892		9.481	18.99	9.483	12.65133

EXAMPLE

GraphPad Prism is used to plot this in the form of two continuous datasets whereby averages for G' and G'' are presented as mean ± SEM, against increasing frequency.

Appendix 10. NPC differentiation on PORN-Laminin coated slips.

Coating procedure followed method 3.1.1. Differentiation protocol was carried out following seeding at 150,000 cells/cm^2 on coated slips. NPCs were left to recover in NMM containing 10μM Rock Inhibitor for 24-48 hours until 90%+ confluent. Following this, media changes were performed with STEMCELL technologies differentiation media; BrainPhys™ Basal medium, 2% (v/v) SM1 supplement, 20ng/mL brain-derived neurotrophic factor (BDNF) & 20ng/mL glia-derived neurotrophic factor (GDNF). The differentiation medium was stored at 4°C and pre-warmed to RT before use. Following recovery, a full media change was performed, with the addition of 2mM Compound E (Sigma-Aldrich, UK, 565790) at a ratio of 1:1000 to provide a working concentration of 2μM, to induce synchronised differentiation of cells. Full media changes were carried out every 2 days, with fresh compound E, for a total of 7 days. Cultures then underwent full differentiation media changes every other day, with compound E, until day 14. Staining via ICC followed method 5.1.5.1 and antibodies shown in Table 2.

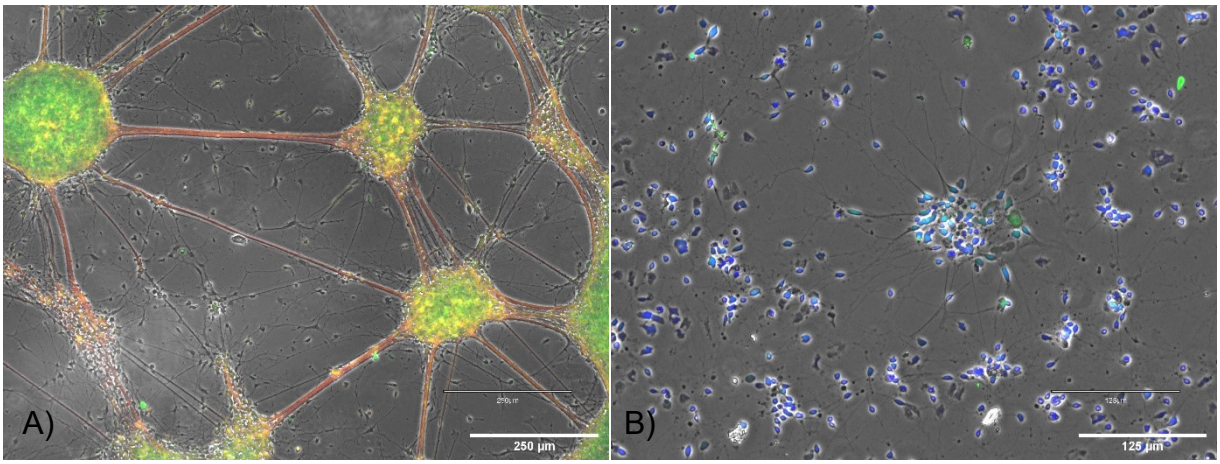

Appendix 10. Representative images of L5 NPC differentiation to neurons after fifteen days. A) Cells are stained via ICC staining of Tujj (Red) and Ki67 (Green). B) Cells are stained via ICC staining of Pax6 (Green) and Sox2 (Red). N=1.

Images of NPC differentiation here are preliminary N=1. Differentiation was not successful, as shown by off-target differentiation and inconsistency within antibody staining. Figure A shows aggregation of cells to form bundles with thick projections, alongside heightened Ki67 expression. This is indicative of off-target differentiation, as neuronal differentiation should reduce expression of Ki67. Figure B demonstrates a smaller magnification of a non-bundled area, displaying a fine network of individual neurons and their projections. Loss of Sox2 expression (B) indicates a departure from pluripotency, while the increased expression of Tujj (A) signifies the development of neuronal cells.